Characterisation of the 2D and 3D density and connectivity attributes of fracture systems in carbonate reservoir analogues: implications for fluid flow

SAGI, DAVID,ADAM

DEPARTMENT OF EARTH SCIENCES, DURHAM UNIVERSITY

Characterisation of the 2D and 3D density and connectivity attributes of fracture systems in carbonate reservoir analogues: implications for fluid flow

---

A Thesis Submitted to Durham University
for the Degree of Doctor of Philosophy in the
Faculty of Science

DAVID ADAM SAGI
September 2012

Abstract

Fault zones, hosted in fractured carbonate reservoirs, can behave as either high porosity and permeability conduits, favouring the migration of fluids; or, conversely, as low porosity and permeability barriers, retarding fluid flow, due to the presence of fine-grained fault gouges (Agosta and Aydin, 2006, Agosta and Kirschner, 2003). Due to these reasons, fault zones can have great economical importance for the hydrocarbon industry. Furthermore, within fault zones, the cyclic accumulation and sudden release of trapped, high pressure fluids can trigger earthquakes and aftershocks (Miller et al. 2004).

In this project, we referred to the classical fault zone architecture models defined by Sibson (1977) and Chester et al. (1993), in which faults are built up of a fault core (where most of the displacement is localised), a damage zone (containing fractured host rocks) and the protolith (the unfractured host rock). Faults, with displacements ranging from cm- to km-scale have been studied within two study areas, Flamborough Head, UK and the Gubbio fault in the Northern Apennines, Italy. Flamborugh Head is a peninsula in East Yorkshire, which represents analogues for hydrocarbon rich, fractured North Sea chalk reservoirs; whereas the Gubbio fault is a regional scale, seismically active normal fault, characterized by complex fault zone architectures, cutting through different types of carbonates.

At both study areas, field-based, outcrop-scale structural observations were completed in order to explore the internal architecture and infer the fluid transmissibility of the fault zones. Additionally, microscale structural observations were made using representative thin sections, collected from the different fault zone domains of the studied fault zones. Qualitative structural observations were complemented with quantitative analyses to study the variation of fracture and vein density and connectivity patterns across the fault zones, which were later used as a proxy for fluid transmissibility. These analyses included established 1D (transects) and 2D (image analysis) methods and a newly developed workflow for the modelling of fracture networks in 3D, based on LiDAR data. 3D modelling of fracture networks was developed using different fracture height/length aspect ratios. The quantitative comparison of different aspect ratio 3D models with established 1D and 2D results, by using misfit graphs, enabled to validate the different 3D models and to estimate the mean aspect ratio of fractures within the fault zones. Qualitative and quantitative results were integrated in conceptual fault zone architecture and fluid flow models.

At Flamborough Head small (cm-scale) and larger (up to 20 m) displacement normal faults were studied in two different types of chalks: one characterized by cm-scale interlayered marl horizons and another one, absent of it. Within the marl-free host rock, in the fault zones of both the small and the large displacement faults, fluid assisted deformation features, such as veins, are often observed. On the contrary, in marl-rich units, fluid assisted deformation features are absent, while fractures filled with intruded marl from the interlayered horizons are common. This suggests that the occurrence of fluid flow in this lithology is primarily controlled by the protolith.

1D quantitative analysis at Flamborough Head showed that, as also predicted by classical fault zone models, vein density progressively increases in the damage zones of faults moving from the protolith towards the fault core. 2D quantitative analysis showed that fracture connectivity remains as low as background values in the outer parts of the damage zones,

whereas it increases rapidly in the inner parts. By comparing the fracture density and connectivity patterns measured from different aspect ratio 3D models with results measured from 1D and 2D analyses showed that the most realistic model is the 1/5 fracture aspect ratio one.

The Gubbio fault cuts through a carbonatic multilayer containing carbonates with different marl content. In the Marne a Fucoidi formation marl is homogenously distributed, while in the overlying Scaglia Group marl is absent. Within the damage zone, hosted in the Marne a Fucoidi formation, fluid assisted deformation features are rare and are only present in the damage zones of subsidiary faults that entirely cut through the formation, linking the under and overlying marl free carbonates. On the contrary, within the damage zone, hosted in the Scaglia Group, fluid assisted deformation features are common, especially close to the fault core of the Gubbio fault and in the damage zone of subsidiary faults. Similarly to Flamborough Head, this suggests that the occurrence of fluid flow is primarily controlled by the nature of the protolith.

As predicted by classical fault zone models, 1D quantitative analysis across the Gubbio fault showed that vein density increases in the damage zone moving from the protolith towards the fault core. Similarly to results from Flamborough Head, 2D quantitative analysis showed that fracture connectivity is low in the outer parts of the damage zones, but increases rapidly within the inner parts, and the comparison of 3D models with 1D and 2D results showed that the most realistic model is the 1/5 aspect ratio one.

The conceptual fluid flow models, built for the study areas, highlights: a) the importance of different marl content host rocks controlling the initiation of fluid flow; b) the development of smaller and larger displacement normal faults and the effects of their displacements on fluid transmissibility; c) the effects of fault damage zones, positioned in an overlapping geometry, resulting in the development high and low fracture connectivity subdomains and fracture corridors; d) the differences in the relative variation of fracture/vein density and connectivity throughout the damage zone compared to background values; e) the fluid transmissibility of the different fault rocks, located within different subdomains of the fault core and f) the anisotropy of fluid transmissibility in the fault core.

Table of contents:

List of figures:

Chapter 1

Chapter 2

Chapter 3

Chapter 4

Chapter 5

List of Tables

Acknowledgement

I would like to thank my supervisors, Nicola "Nic" De Paola, Robert "Bob" Holdsworth and Ken "Ken" McCaffrey for their support and guidance throughout my project. Also a big thank to other research, admin and IT support staff at the Department who made my Durham experience a lot easier by helping to find my way through scientific problems, bureaucracy and never-ending printing issues.

I would also like to say many thanks to Maersk Oil for funding this research topic and for giving me the opportunity to do a summer internship with them. Special thanks to John Francis Karlo and Michael Engberg who made it happen and helped me throughout my time in Copenhagen. Thanks for the AAPG who provided additional support for the project by awarding the Norman H. Foster Memorial Grant as part of their Grants-in-aid program.

Big thanks to all my friends and colleagues from Durham, who made my work and my free time a lot more enjoyable. Special thanks to Max Wilkinson and Dave Ashby, who were also great housemates and were able to cope with me for 2 entire years. Also thanks to Izzy, Alodie, Wanda, Femke, Ben, Jen, Jon, the guys at Leeds Uni and my childhood friends from Budapest, especially Balázs, who finally came to visit me in the North of England and found that it is actually very nice.

Sorry, the rest of this paragraph is in Hungarian. Apa, Anya, Mama, Mirjam: Köszönöm a segítségeteket, a támogatásotokat és hogy végig mellettem álltatok. Bocsánat, ha néha kicsit idegesebb voltam a kelleténél, de már ezen is túl vagyunk. Apa, hogy megy be az a nagy elefánt az oroszlán barlangjába? Apa hogy megy, Apa hogy megy be ha meghívják teára…

I left the single most important person to the end of this list. Hanni, thank you for the motivation you gave me to apply for the PhD and for inspiring me and helping me through the good and the bad times. Without you I would never have got this far.

Declaration

No part of this Thesis has previously been submitted for a degree at this or any other university. The work described in this Thesis is entirely that of the author, except where reference is made to previously published or unpublished work.

David Adam Sagi

Durham University

Department of Earth Sciences

September 2012

1. Introduction

1.1.Project rationale

Fault zones in fractured carbonate reservoirs can act as high porosity and high permeability conduits, and can accommodate large volumes of migrating fluids, or conversely, behave as impermeable seals that are barriers for fluid migration (e.g. Agosta and Aydin, 2006; Agosta and Kirschner, 2003). As a result, fault zones are of great importance for the hydrocarbon industry (e.g. Aydin, 2000), for Carbon Capture Storage (CCS) studies (e.g. Wilson et al., 2007) and for water management companies (e.g. Price, 1987). Additionally, the cyclic accumulation and sudden release of trapped, high-pressure fluids, can trigger earthquakes and aftershocks (Miller et al., 2004 and references therein), providing interests from seismologists.

Quantitative fault zone attributes, related to fracture properties, such as orientation distribution (Sleight, 2001), density (Faulkner et al., 2011; Mitchell and Faulkner, 2009), connectivity (Ghosh and Mitra, 2009; Micarelli et al., 2006a; Odling, 1992, 1997) and height/length aspect ratio (Schultz and Fossen, 2002) are known to show great complexity, heterogenity and high anisotropy in all three directions relative to the orientation of the fault (across-fault, dip-parallel, strike-parallel directions). As these fault zone attributes can strongly influence the fluid transmissibility of faults (Aydin, 2000), the quantitative characterization of their nature and distribution should be studied, in order to obtain a better understating of fluid flow.

The importance of fault zones in controlling fluid flow is widely recognized, and several detailed case studies (e.g. Agosta and Aydin, 2006; Agosta and Kirschner, 2003; Agosta et al., 2007; Billi, 2005; Koukouvelas and Papoulis, 2009; Micarelli et al., 2006a; Micarelli et al., 2003; Micarelli et al., 2006b; Questiaux et al., 2010) and models (e.g. Caine et al., 1996) exist that link fault zone architecture (Agosta and Aydin, 2006; Graham et al., 2003; Micarelli et al., 2006a) with fluid transmissibility (Knipe et al., 1998). Such case studies and models are based upon detailed structural field observations (e.g. Faulkner et al., 2003), laboratory experiments (e.g. Evans et al., 1997; Faulkner, 2004), numerical modelling (e.g. Zhang et al., 2009) and field-based quantitative analysis of fault zone attributes, with data collected across a range of scales (e.g. Mitchell and Faulkner, 2009).

This study aims to describe fault/fracture patterns in low-porosity, low permeability carbonate reservoirs by qualitatively and quantitatively analysing the complexity, heterogeneity and 3D anisotropy of fault zone attributes; explicitly fault/fracture orientation, density and connectivity. Quantitative data have been used to create reality-based models that describe the 3D structural architecture of the studied fault zones. Finally, an attempt to conceptually model fluid transmissibility in 3D, along and across fault zones, and for scales ranging from micro to outcrop scales and different height/length aspect ratios of fractures has been made.

1.2.Thesis outline

This Thesis structures as follows:

Chapter 1.3 describes the scientific and methodological approaches followed during the research project, including the collection and analysis of quantitative data such as 1D

structural transects, 2D numerical photo analysis and LiDAR based, 3D modelling. Here, the detailed description of the new methodology, developed during this project to quantify fracture density and connectivity in 3D is presented and discussed.

Chapter 2 is a literature review, summarizing findings of previous studies related to the topics discussed in this Thesis. The chapter is divided into four parts. In the first section, a summary of existing fault classifications is discussed, based on the geometry and relative displacement between the two wall rocks. The second section contains the principles of fault mechanics, including modes of fault initiation and reactivation. Within the third part of the chapter, classical fault zone models are introduced, where faults are described as structures of finite width, comprised of different fault zone domains and characterized by complex fault zone architectures. Finally, the fourth and last section concerns fluid flow within fault zones, and provides detailed descriptions on the control exerted by fault zone deformation features, fault attributes and anisotropy on fluid flow.

Two case studies are presented in Chapters 3 and 4, in which detailed structural observations were carried out using the 1D, 2D and 3D quantitative methods, explained in Chapter 1.3, to obtain a better understanding of the architecture of the studied fault zones. These findings were used to build conceptual fault zone and fluid flow models. Chapter 3 is a case study from Flamborough Head, UK; a setting containing a well-known outcrop, which represents analogues for hydrocarbon rich, fractured North Sea chalk reservoirs. Chapter 4 is a case study of the Gubbio fault in the Northern Apennines of Italy, which is a regional scale, seismically active normal fault in carbonate rocks, characterized by a complex fault zone architecture. The Gubbio fault is a good analogue for large scale, complex, folded and faulted carbonate reservoirs.

Finally, in Chapter 5 the results obtained from studies and analyses from both of the field areas are discussed. Here, the main conclusions of this PhD Thesis are also presented. This chapter is divided into five sections. In the first one, structural observations related to the fault zone architecture if the studied faults are summarized and discussed. In the second one, 1D and 2D quantitative results, gained from the different study areas, are compared and discussed. The third part provides details on the procedures adopted to use 3D LiDAR data to build fracture networks and how the results gained from this new methodological approach compare to results obtained from 1D and 2D established, quantitative methods. Within the fourth section, the complexity of fault zone architectures, found in the study areas, are discussed, in terms of the variations in fracture and vein density and connectivity, particularly for those situations where the observed trends do not follow the trends predicted by classical fault zone models. Finally, in the last section, conceptual fluid flow models, developed for each case study, are discussed in terms of the main deformation features that induce fault zone anisotropy controlling 3D fluid transmissibility.

1.3. Methodological approach

During this research project multi-scale, field-based structural observations were complemented with microscale structural analysis performed on thin sections, obtained from rock samples collected in the field from different fault zone domains. Quantitative fault attribute data were collected using: 1) traditional paper based methods along 1D structural transects (for details see Chapter 1.3.1.), 2) semi-digital methods by using 2D outcrop photos and table top scans of thin sections (based on Ghosh and Mitra, 2009; Odling, 1992, 1997; Sleight, 2001, for details see Chapter 1.3.2.), 3) modern, digital technologies, by the acquisition of 3D, LiDAR data (based on Jones et al., 2009; Jones et al., 2008; McCaffrey et

al., 2008; Wawrzyniec et al., 2007). Detailed descriptions of the LiDAR data acquisition, and the method of building fracture networks, developed for this study to estimate 3D across-fault variation in fracture density and connectivity, can be found in Chapter 1.3.3 and 1.3.4, respectively. Finally, the method developed for the comparison of 1D, 2D and 3D datasets, used to validate the 3D models and to estimate the mean aspect ratio of fractures in the studied damage zones, is described in Chapter 1.3.5.

1.3.1. 1D quantitative analysis

Orientation data of structural features (e.g. fractures, veins and subsidiary faults) were collected along 1D structural transects, to quantify the density of fracturing across the fault zones (Fig. 1.1a-b). Fracture density was defined as the number of structural features intersecting the transect over a unit length (m), and this parameter has the unit of X/m, where X is the number of intersected features.

Quantitative data were collected along transects that were oriented orthogonal to the strike of the studied faults (Fig. 1.1c). The transects ranged between 2 and 40 m in length, depending on the size of the accessible outcrops. The coordinates of the termination points of the transects were recorded with a handheld GPS (Fig. 1.1c). For each structural feature that intersected the transect, the strike, dip, dip direction and width were measured as well as recording the distance along the transect. Where appropriate, the nature of the filling materials was characterized, and, where observed, the fault offsets and the rakes were also measured.

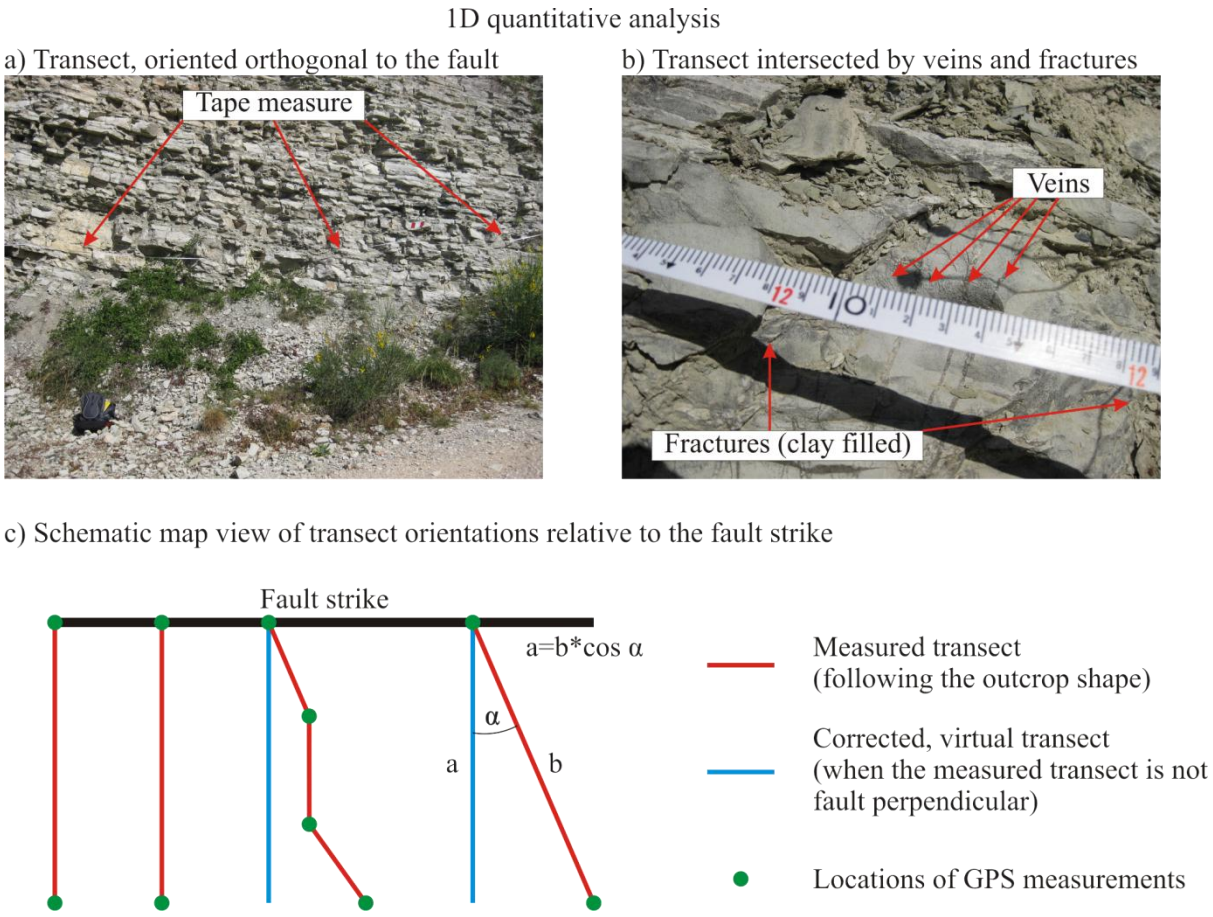

Figure 1.1 - 1D quantitative analysis

a) 1D transect across the damage zone of a fault (large scale view), b) 1D transect across the damage zone of a fault (small view), c) Schematic map view showing the orientation of the measured and the virtual transects in respect to the fault strike, with the trigonometric equations used for calculating the length of the virtual transects and the locations of the GPS measurements at the termination and break points of the transects

For the measured structural features, distance along the transect was converted to distance from the fault core-damage zone boundary (Fig. 1.1c). In some cases, due to the orientation of the outcrops, the studied sections were oriented oblique to the fault strike (Fig. 1.1c). In these cases, the measured distances of features along the transect were corrected using trigonometric equations to account for the obliquity between the transect orientation and the orientation of the fault strike. The resulting virtual transects are shorter than the original transects, but they are oriented perpendicular to the fault strike, therefore representing the across-fault variation in fracture and vein density more accurately. Using a GPS to measure the termination points and breakpoints of the transects ensured a more accurate determination

of the locations of the transects, and therefore a more accurate estimation of the distance between the individual structural features and the fault core-damage zone boundary (Fig. 1.1c).

1.3.2. 2D quantitative analysis

2D image analyses were used to quantify structural feature (e.g. fracture, vein and subsidiary fault) density and connectivity across the fault zones, using high resolution, outcrop scale digital photos. These photos were taken from the exposed fault zones in the field (Fig 1.2a), and from thin sections obtained from samples collected from different fault zone domains.

Mesoscale fractures, veins and bedding surfaces were digitized from outcrop photos (Fig. 1.2b). The photos, used for the analysis, were always oriented parallel to the outcrop direction and, therefore, to the 1D transect directions as well, and were taken from 0.5 m, 2 m, and 5 m distances from the outcrop, respectively. At these distances, the narrowest features that could be resolved were approximately 1 mm, 2 mm and 5 mm wide, respectively. The scaling issues arising from the use of different outcrop-camera distances, which will affect the results of quantitative analyses, have been explained in details in Chapter 4. The identified fractures, veins and bedding surfaces were picked as polylines using CorelDRAW© software (Fig. 1.2b). Fractures, veins and bedding surfaces were separated into three groups, so that each type of features could be separately analysed.

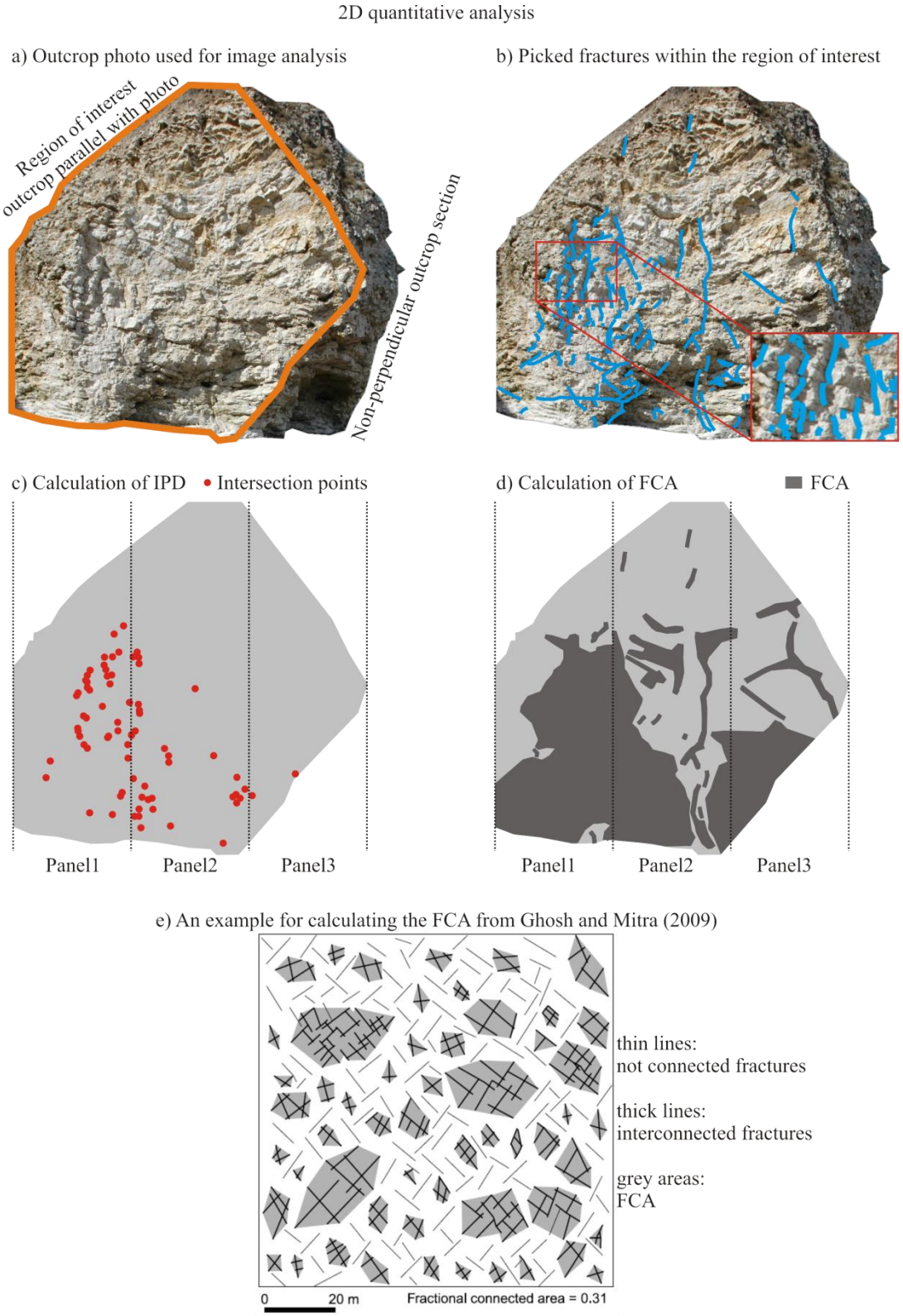

Figure 1.2 - 2D quantitative analysis

a) Outcrop photo of a fault zone section with the region of interest highlighted, b) Outcrop photo with the picked fractures (inlet showing a zoomed view, c) area of the region of interest (grey area), separated into panels, with the intersection points (red dots) highlighted, f) area of the region of interest (light grey area), separated into panels, with the fractional connected area highlighted (dark grey area), e) schematic view of the FCA by Ghosh and Mitra (2009)

The digitized images were exported into ImageTOOL©, an image analysis software, to quantify their density and connectivity, using the default object analysis options of the software. To quantitatively analyse the variation of fracture and vein density and connectivity across the faults, the distances between the fault core and the studied outcrop sections were recorded. In some cases, to achieve higher across-fault resolution during quantitative image analyses, the photos were divided into several fault zone parallel panels (Fig. 1.2c-d)

Stylolites, microfractures and veins were digitised from greyscale images obtained from digital scanning of thin sections by a high resolution table-top scanner. The greyscale images were imported into ImageTOOL©, where they were analysed using the same method used for the outcrop scale photos.

Fracture/vein density was quantified as the total length (m) of these features over a unit area (m^2). This has a unit of m/m^2 in case of outcrop photo analysis, or mm/mm^2 in the case of thin section analysis (Odling, 1992, 1997). Another way of quantifying fracture density in 2D is calculating the average fracture length per unit area (Singhal and Gupta, 2010). However, this method does not account accurately for the across-fault variation of fractures/veins present, as it gives different results in case of numerous short fractures or a few long fractures present in the region of interest, even though these two options can provide the same amount of migration paths for fluids. Moreover, this method is difficult to use when veins with anastomosing geometries are present, as it is difficult to distinguish the individual veins from each other, therefore the length of the individual veins cannot be measured.

Fracture/vein connectivity was quantified using two separate methods: the intersection point density (IPD) and the fractional connected area (FCA) methods. The IPD is the number of

intersection points between fractures and/or veins (n) over a unit area (Fig. 1.2c) thus has units of n/m^2 in case of outcrop photos and n/mm^2 in case of thin section analysis (Odling, 1992, 1997). The FCA is the summed area of all the clusters of interconnected fractures, divided by the total sample area, expressed as percentage (Ghosh and Mitra, 2009, Fig. 1.2e). The FCA was calculated by drawing enveloping polygons around clusters of intersecting fractures (Fig. 1.2d-e), measuring the areas of these surfaces and then summing them before dividing the result for the total area of the region of interest.

A comparison between these two methods of quantifying fracture/vein connectivity in 2D was carried out at one of the studied faults at Selwick Bay, Flamborough Head. Fracture/vein connectivity was calculated in the fault damage zone of one of the main faults using both methods on the same cliff face, that was divided into fault parallel panels on the photos (for the outcrop photo and the panels see Fig. 3.10a-b). The fracture/vein connectivity values obtained by using the different methods were plotted against each other on a graph, and a linear cross-correlation was found with an angular coefficient of about $m=1$ (best fit equation: $y=0.95x-0.34$ and R^2 value of 0.90, Fig. 1.3). This relatively strong, linear cross-correlation suggests that both methods can be applied to quantify fracture/vein connectivity in 2D.

It should be noted that in this study no box counting methods were used to determine the spatial characteristics of fracture patterns. Although box counting methods are widely used in characterizing the fracture patterns; however, Gillespie et al. (1993) argued that box counting methods do not yield the power-law relationship between box sizes and number of boxes that would be expected from fractal geometries. They suggested that the method is too insensitive because there are other important parameters as well.

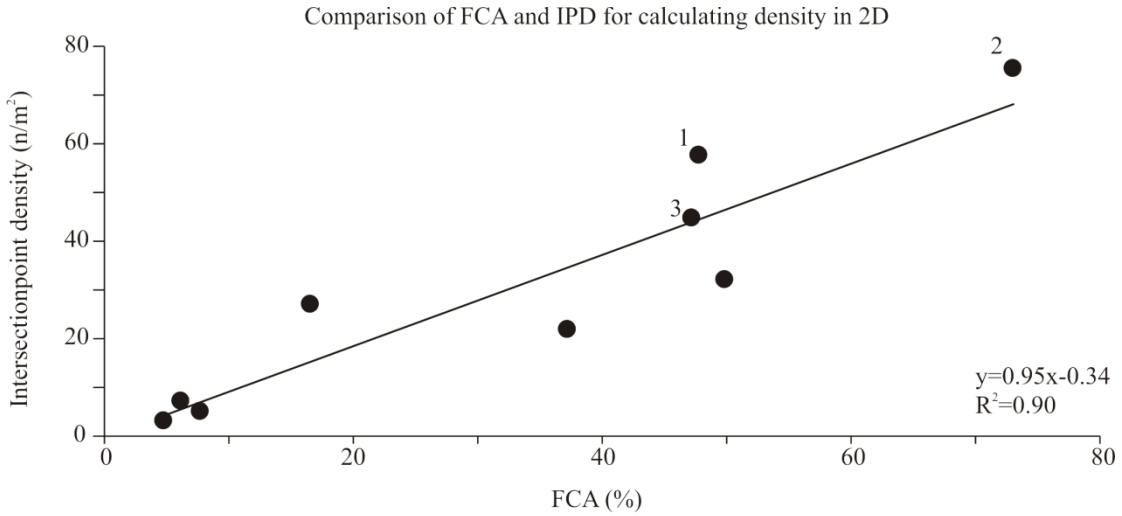

Figure 1.3 - Correlation between the two methods (IDP and FCA) to quantify fracture and vein connectivity in 2D

Each datapoint represents connectivity values from an across fault section (photo panel) at one of the fault zones at the Selwick Bay study area at Flamborough Head (Numbered dots represent the panels from Fig. 1.2c-d)

1.3.3. 3D data collection

Laser scanning is a quick and effective way to collect field-based digital 3D data. The terrestrial Laser Scanning (or ground-based LiDAR, Light Detection And Ranging) is a relatively new technology used in Earth Sciences aiming to display and model geological features in 3D (e.g. Jones et al., 2009; Jones et al., 2008; Kokkalas et al., 2007; McCaffrey et al., 2008; Wawrzyniec et al., 2007). It is an instrument that emits a laser pulse towards, and records the reflecting laser pulse from an outcrop surface. The measured travel time of the reflected light is used to calculate the distance and the 3D coordinates of the reflecting point (McCaffrey et al., 2008), and, for each point, an intensity value, equal to the ratio of the laser energy reflected back from the reflecting surface, compared with the initially emitted energy, is calculated. The scanner used for data collection in this study was a Riegl LMS-z420i, with a mounted Nikon D300 camera (Fig. 1.4a). This type of LiDAR can emit up to 12 000 laser pulses per second while it rotates 0-360° in the horizontal plane, and 80° vertically (±40°

from the horizontal plane). Laser scan datasets are characterized by clusters of points with xyz coordinates in 3D space known as pointclouds.

As only surfaces in the line-of-sight of the scanner are recorded, outcrops, characterized by complex, concave shapes, have to be scanned from several different scan positions. Different scan positions can be tied together into one project by using multiple (at least 4) purpose-designed highly reflective objects. These objects are usually cylinder shaped for even reflectivity in every horizontal direction (Fig. 1.4a). These large reflectors (up to 40 cm radius) are kept at the same location during the survey, while the scanner is moved to different scan positions along with the field laptop that operates the scanner. When the network of reflectors is scanned and recognized by the software, it calculates the orientation and position of the different scan positions with respect to each other. To achieve a georeferenced dataset, dGPS data can be collected for the location of the reflectors, and the locational data can be added to the project.

Finally, a camera on top of the scanner is connected to the field laptop and takes high resolution, RGB (red, green, blue) photos of the outcrops during the survey. With the use of the camera the point cloud can be converted into real colour, using another set of small reflectors (5 cm diameter, Fig. 1.4a) that are identified both by the scanner and also on the photos, helping the software to accurately tie together the points with colours. The result of the survey is a high resolution, georeferenced pointcloud, usually referred to as Virtual Outcrop Models (VOM) (Trinks et al., 2005; Xu et al., 2000; Xu et al., 1999) or Digital Outcrop Models (DOM) (Bellian et al., 2005), with up to millions of points, each point characterized by georeferenced, xyz 3D coordinates and RGB colours (e.g. Fig. 1.4b).

3D data collection

a) Equipment setup

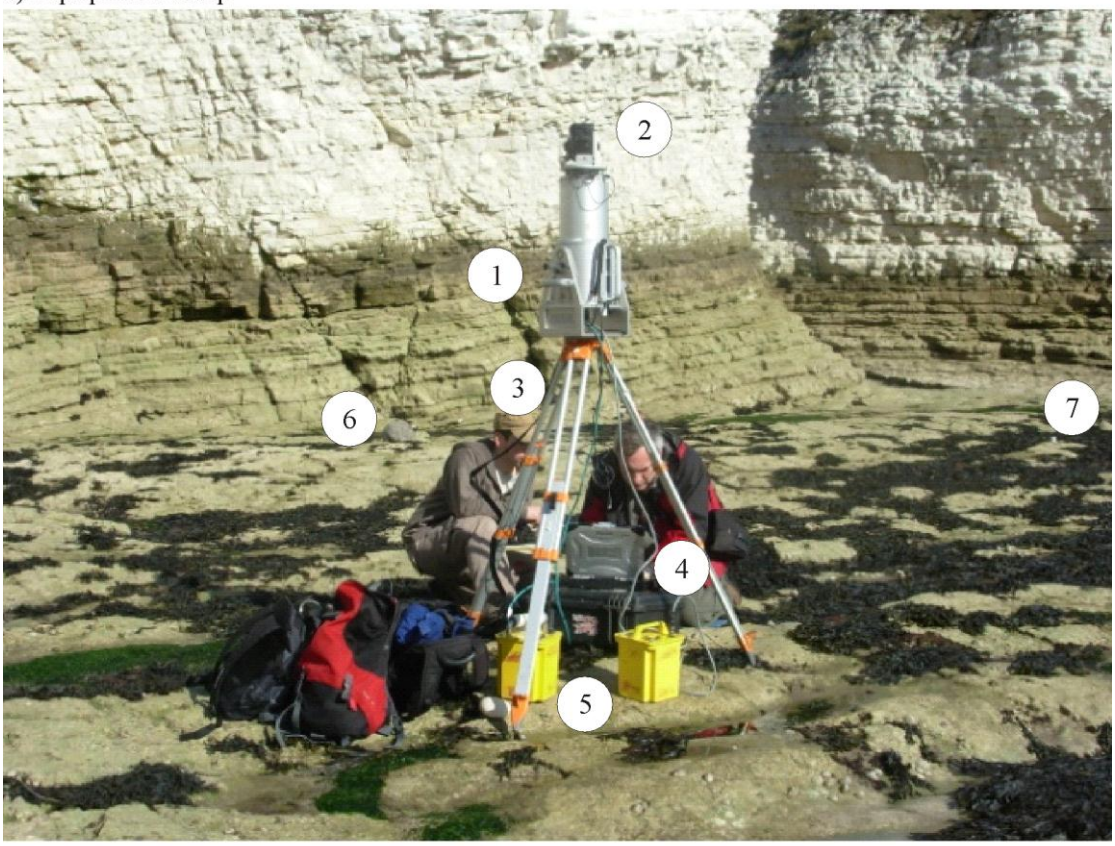

1: LiDAR, 2: Camera, 3: Tripod, 4: Field laptop, 5: Batteries,
6: Reflector (for different scan positions), 7: Reflector (for camera)

b) Visualization of pointcloud in the RiSCAN - Virtual Outcrop Model

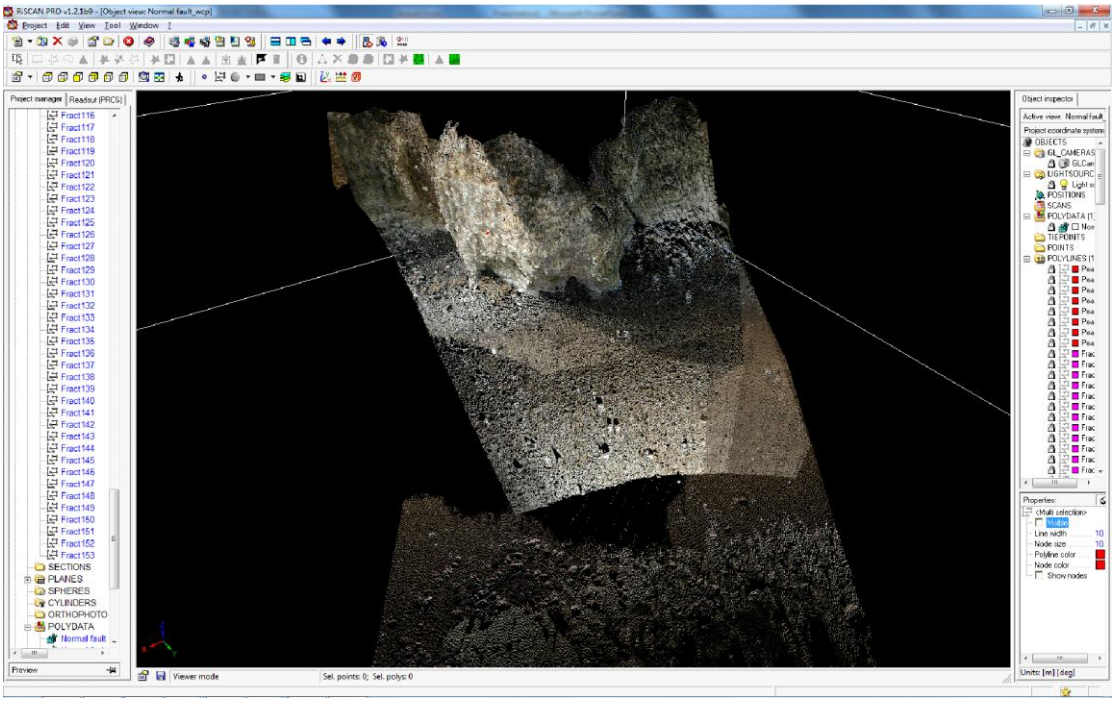

Figure 1.4 - 3D data collection
a) equipment setup, b) visualization of pointcloud in RiSCAN

1.3.4. 3D quantitative analysis

A new method was developed (see below) during this study to create 3D models of the fracture networks, in order to obtain quantified values of fracture/vein density and connectivity across fault zones. The fracture/vein density and connectivity values gained from these models are strongly dependent on the assumed aspect ratio of the fractures. Additionally, the orientations of the fractures/veins could also be determined within the digital 3D dataset by using this method. The output of the method is fracture/vein density and connectivity. In 3D, fracture/vein density can be quantified as the total fracture surface area of the fractures/veins (m^2) over a unit volume (m^3), which is (m^2/m^3), while fracture/vein connectivity can be quantified as the total length of intersection lines between fractures (m) over a unit volume (m^3), which is (m/m^3). These units are in agreement with the units of the measure of fracture density in 1D, 2D and 3D suggested by Dershowitz and Herda (1992).

Data processing was performed using a new method developed for this project (Fig. 1.5-1.7). The 3D, georeferenced, RGB pointclouds were used to identify the primary structural features, such as fault core-damage zone boundaries and other principal slip surfaces; and secondary features, such as fractures, veins and subsidiary faults within the damage zones. The thickness of the narrowest features, possible to identify from the pointclouds depends on the resolution of the pointcloud, which is a function of the distance between the LiDAR and the outcrop. The particular resolutions of the different 3D datasets of this study are quantified in the particular chapters. All these structures were picked as polylines in the pointclouds using the scanners own software, RiSCAN Pro© (Fig. 1.5a-b, for the same pointcloud without any interpreted features see Fig. 1.4b). The polylines were exported as DXF files (suffix .dxf) to GoCAD©, where the fracture models were then made (Fig. 1.5c). All the polylines consisted of at least 3 points, so that a best fit plane could have been fitted to these in 3D space, using default processing tools in GoCAD (Fig. 1.5d-e). It was possible to measure the

3D quantitative analysis (modelling)

a) Fault core-damage zone boundaries (red) and fractures (purple) picked from the pointcloud (large scale view)

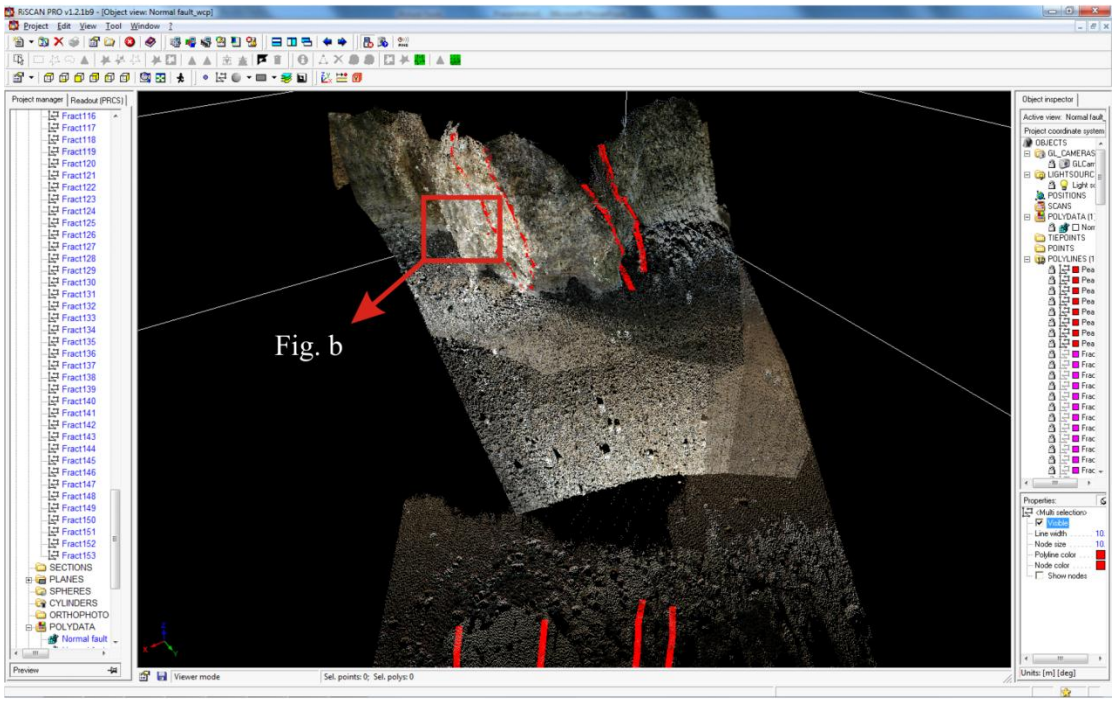

b) Fault core-damage zone boundaries (red) and fractures (purple) picked from the pointcloud (zoomed view)

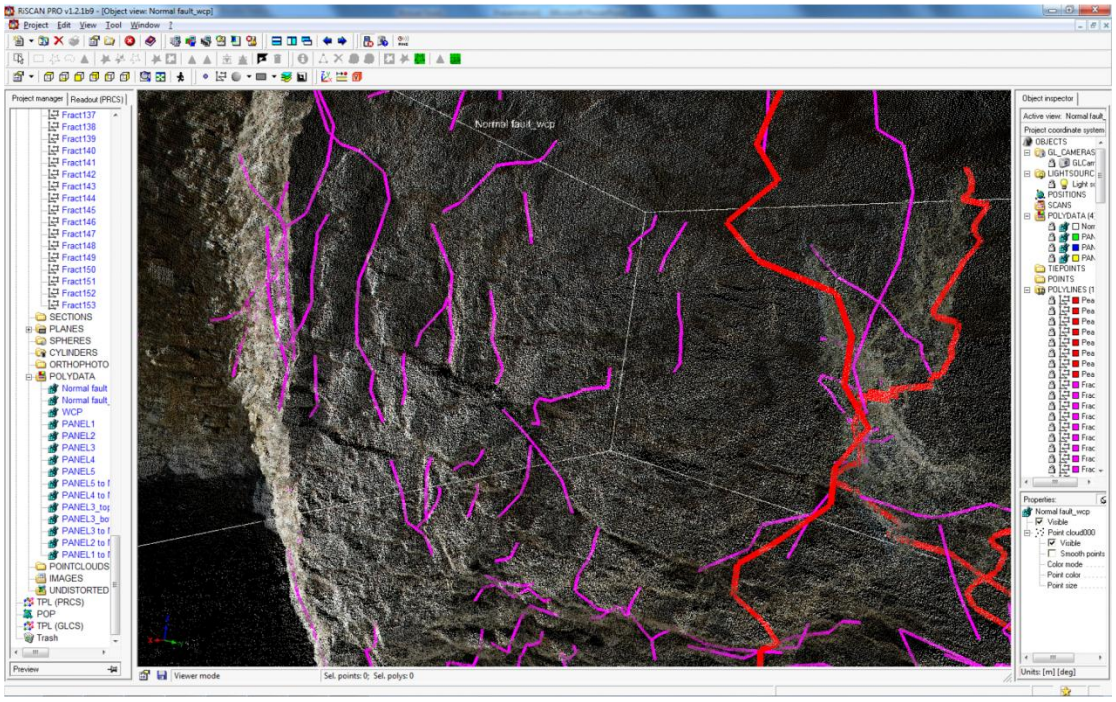

c) Fault core-damage zone boundaries and fractures modelled in GoCAD (large scale view)

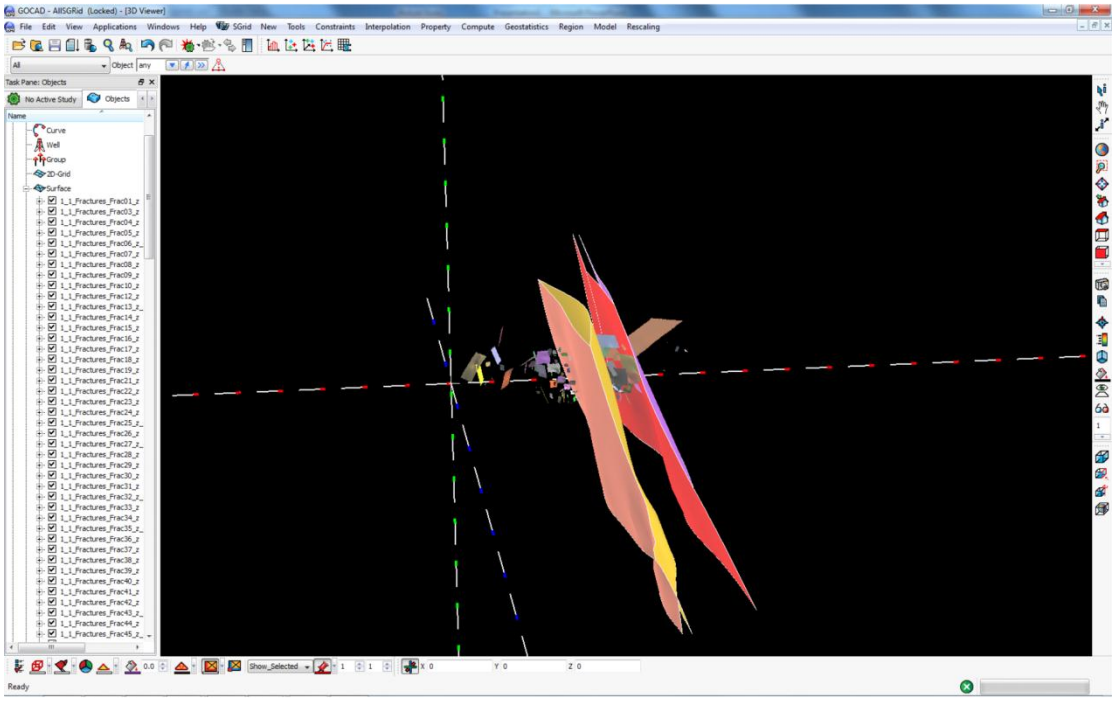

d) Fracture netowrk modelled in GoCAD (zoomed view, 1/1 aspect ratio)

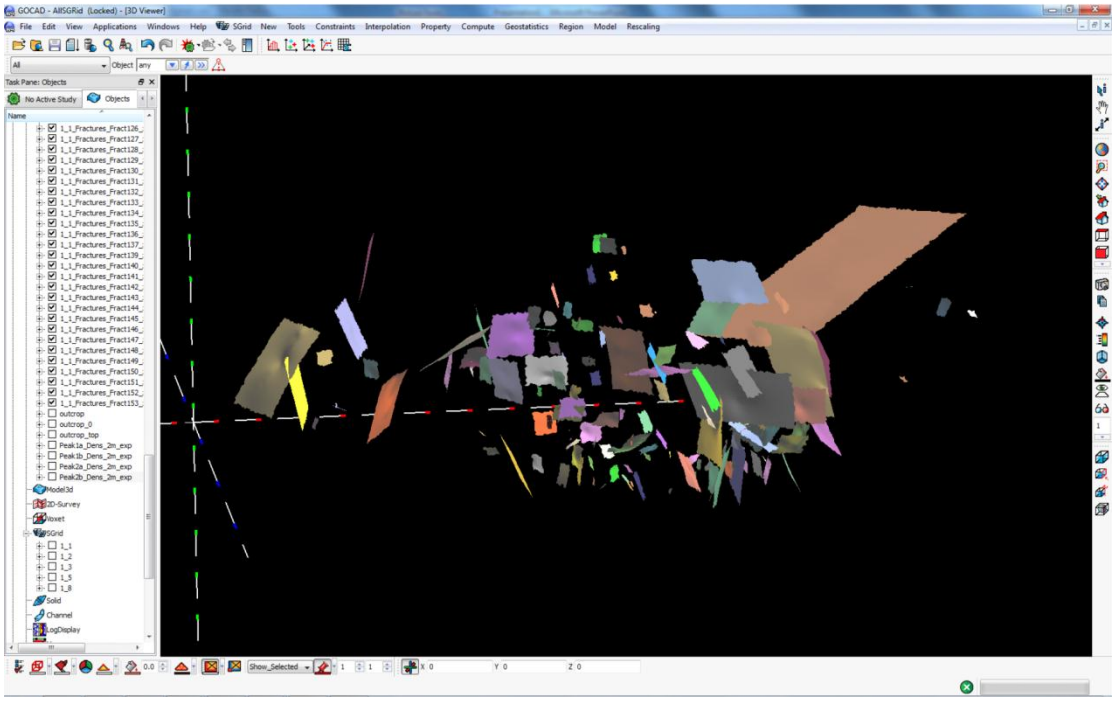

e) Fracture netowrk modelled in GoCAD (zoomed view, 1/8 aspect ratio)

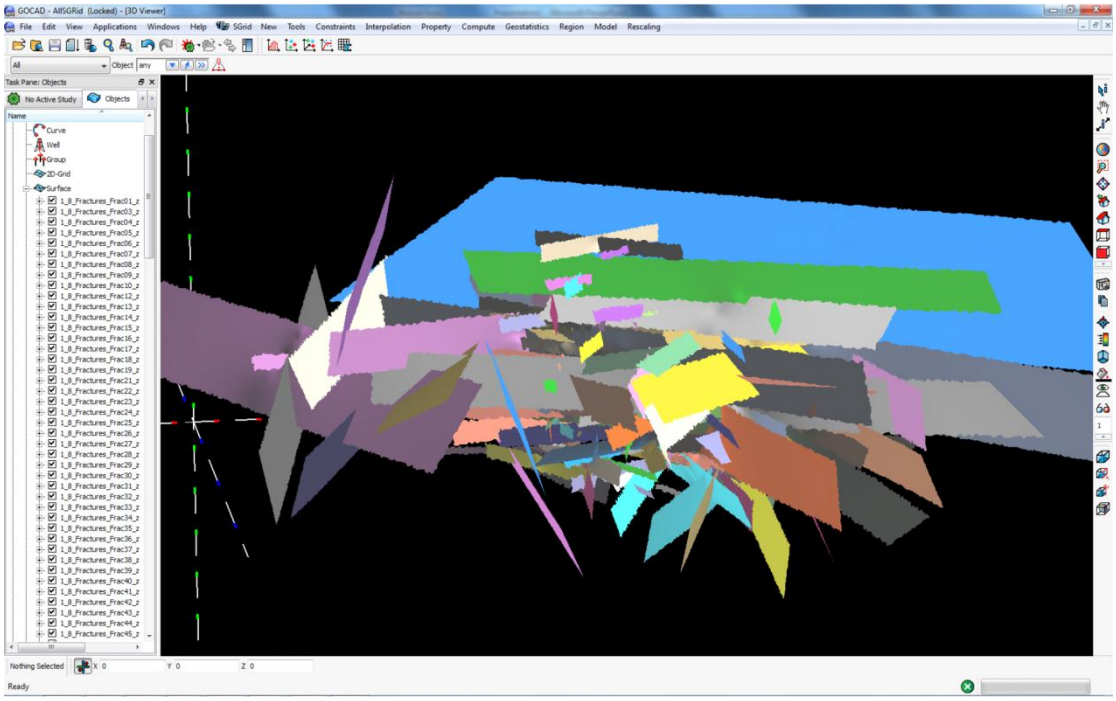

Figure 1.5 - 3D quantitative analysis (modelling)
a) fault core-damage zone boundaries (red) and fractures (purple) picked from the pointcloud (large scale view, for the same pointcloud without any interpreted features see Fig. 1.4b), b) fault core-damage zone boundaries (red) and fractures (purple) picked from the pointcloud (small scale view, for the same pointcloud without any interpreted features see Fig. 1.4b), c) fault core-damage zone boundaries and fractures modelled in GoCAD (large scale view), d) fracture network modelled in GoCAD (zoomed view, 1/1 aspect ratio), e) fracture network modelled in GoCAD (zoomed view, 1/8 aspect ratio)

orientations of these fitted planes using default processing tools in GoCAD, as the datasets were georeferenced. The measured orientations were plotted on stereonets, so that they could be compared with the orientations, measured in the field.

To produce realistic fracture networks, from which the across-fault variation of fracture density and connectivity can be quantified and that filled a 3D volume, it was necessary to define finite dimensions of the initially infinite planes, both in the vertical and in the horizontal directions (Fig. 1.6). In this respect, the following assumptions were made:

Considerations for surface building in 3D

a)Fractures usually terminate against bedding surfaces, vertical extent of modelled fractures determined based on the outcrop trace length

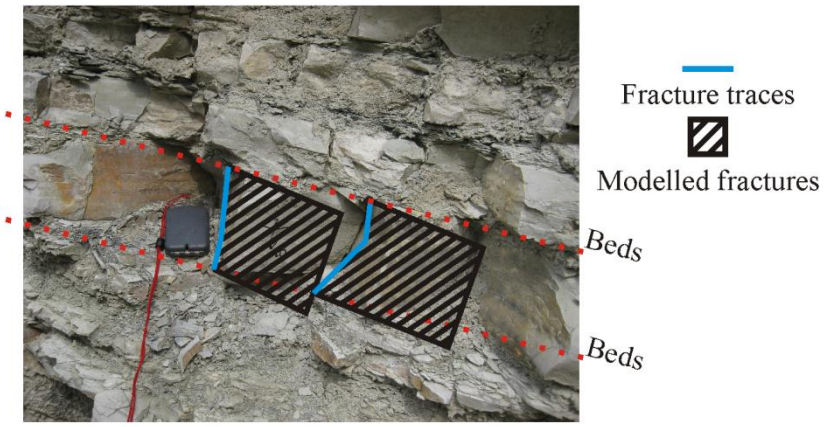

b) Fractures are modelled as squares and half of their surface is "behind" and the other half is "in front of" the outcrop surface regardelss their aspect ratio

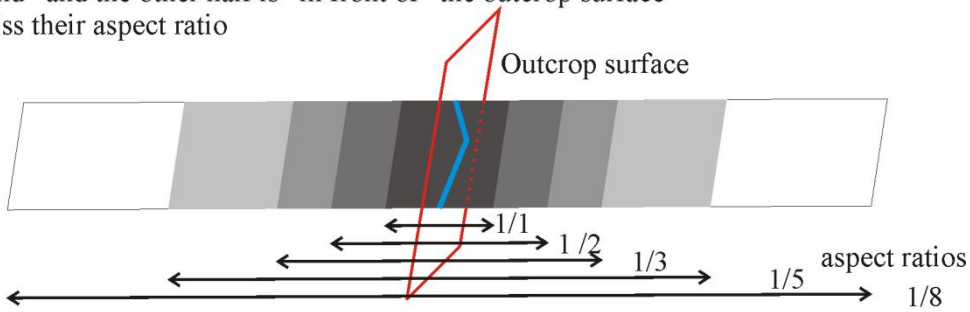

c) Intersection between fractures:
a smaller outcrop trace length fracture is fully crosscut by a larger one

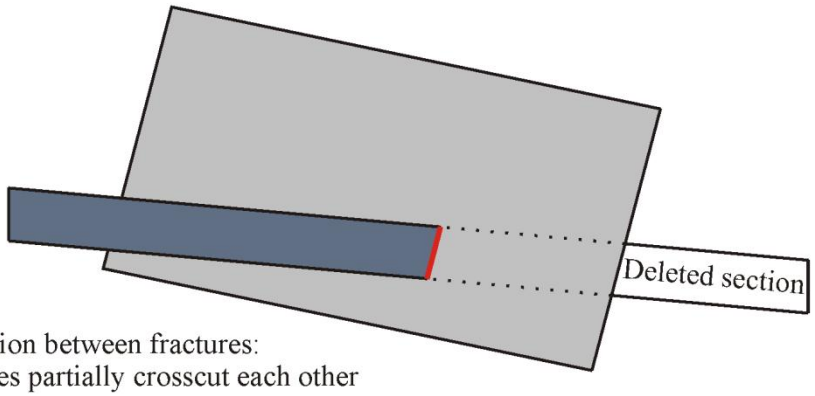

d) Intersection between fractures:
two fractures partially crosscut each other

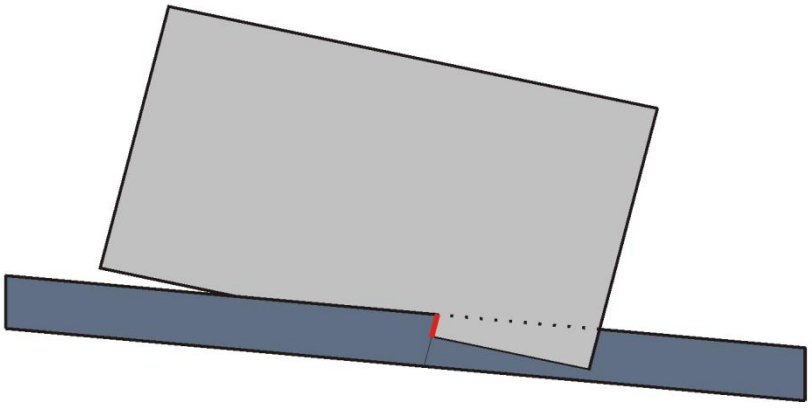

Figure 1.6 - Considerations for surface building in 3D
a) as the fractures usually terminate against bedding surfaces, fractures are modelled as rectangles and their vertical extent is determined based on their outcrop trace length, b) Fractures are modelled as squares and half of their surface is "behind" the other half is "in front of" the outcrop surface regardless their aspect ratio, c) intersection between fractures: a smaller outcrop trace length fracture if fully crosscut by a larger one, d) intersection between fractures: two fractures partially crosscut each other

1) The studied damage zones were located in well-bedded country rocks, and structural observations showed that fractures and veins mostly terminate against bedding surfaces. As a result, the modelled fractures were chosen to be square shaped with their heights determined from their outcrop trace length, observed on the pointcloud (Fig. 1.6a).

2) The modelled fractures were constructed with the picked polylines located in the centre of the plane, regardless of their aspect ratios. Half of the surface area was extended outside the real outcrop, whist the other half was continued within the outcrop (Fig. 1.6b).

3) Based on structural observations of nearby vertical and horizontal outcrops Schultz and Fossen (2002) suggested that the typical aspect ratio of fractures ranges between 1/1 (square) and 1/10 (horizontally elongated). In this study, in case of each study area, 5 different 3D models were built. In each 3D model the fracture aspect ratios were assumed to be constant with values of: 1/1, 1/2, 1/3, 1/5 1/8 (Fig. 1.6b).

4) The intersections between two fractures, when happen, can occur in two ways: a) a smaller height fracture is fully crosscut by a larger height one (Fig. 1.6c), or b) the two fracture planes, regardless of their height, partially crosscut each other (Fig. 1.6d). In the first case, the smaller fracture was terminated against the larger one, and the part that did not contain the originally picked polyline was deleted. In the latter, case the fractures were not terminated against each other, consistently with outcrop observations.

5) Based on structural field observations it was observed that all secondary features in the damage zone, such as fractures, veins and subsidiary faults, do not crosscut the fault core-damage zone boundary and other principal slip surfaces, such features have been terminated against the fault core-damage zone boundary, or the principal slip surface. The secondary features were cut at their intersection line with the fault core-damage zone boundary or principal slip surfaces, and the part which did not contain the initially picked polyline was deleted (e.g. Fig. 1.6d.)

6) Only the fractures intersecting the surface of the outcrops (i.e. real fractures, visible on the pointclouds of the digital outcrop) were modelled. No fractures were created "behind" and "in front of" the outcrop by using statistical methods.

These assumptions were not applied for the modelled damage zone-fault core boundaries and other principal slip surfaces, as these main features were extended far beyond the fractured outcrop surfaces, both in the horizontal and in the vertical directions, in accord to field observations. In this way, the geocellular models used for quantifying density and connectivity (see text below) could be fitted to these surfaces, providing a more accurate quantification of the distance from these primary features.

Given these assumptions, the initially infinite length fractures were cut along the horizontal direction at the lowest and highest (z) values of the picked polylines (the top and bottom point of the fracture trace on the outcrop). Parts of the surfaces that were above the highest point, and parts that were below the lowest point were deleted, making the fractures as long stripes (Fig. 1.6a-b). In order to reduce the length of the fractures to the specific aspect ratios chosen, the fractures were cut in the horizontal direction both "behind" and "in front" of the

picked polylines (Fig. 1.6b). The coordinates of the fracture edges were calculated based on the mean x and y coordinates of the picked polylines and by using the Pythagoras-equation.

Once the fractures were produced, a geocellular model (SGrid in GoCAD) was built (Fig. 1.7) using the following criteria:

1) The side length of the individual cells is 1 m or 10 cm depending on the size of the initial data. For datasets extending to approximately 10 m, 10 cm cell sizes were chosen and for datasets exceeding 50 m, 1 m cell sizes were chosen. These lengths were chosen so that one cell always contains only one fracture intersecting the cell, except for the near proximity of intersection lines of two fractures. Studying the datasets showed that the amount of cells intersected by more than one fracture is less than 2%. The fact that most of the cells are intersected by only one fracture, allowed the quantification of fracture/vein density and connectivity across the fault using the SGrid (see text below).

2) Along directions, parallel to the outcrops, the model was extended to create a volume where all the picked polylines are within the volume, but not any further. Not letting the SGrid to extend any further than the furthest polyline from the fault core-damage zone boundary minimalizes the "edge-effect" at the side of the model, where fracture/vein density and connectivity values would decrease because of the bias in the model, not because of the representation of real variations.

3D quantitative analysis (quantification)

a) Sgrid with long axis oriented parallel with the fault strike (red arrow)

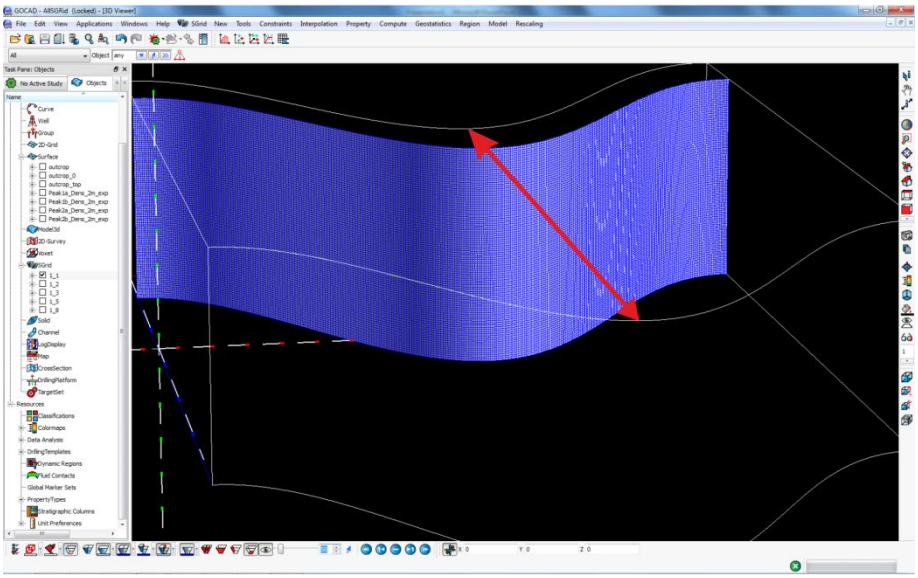

b) Cells of Sgrid intersected by fractures

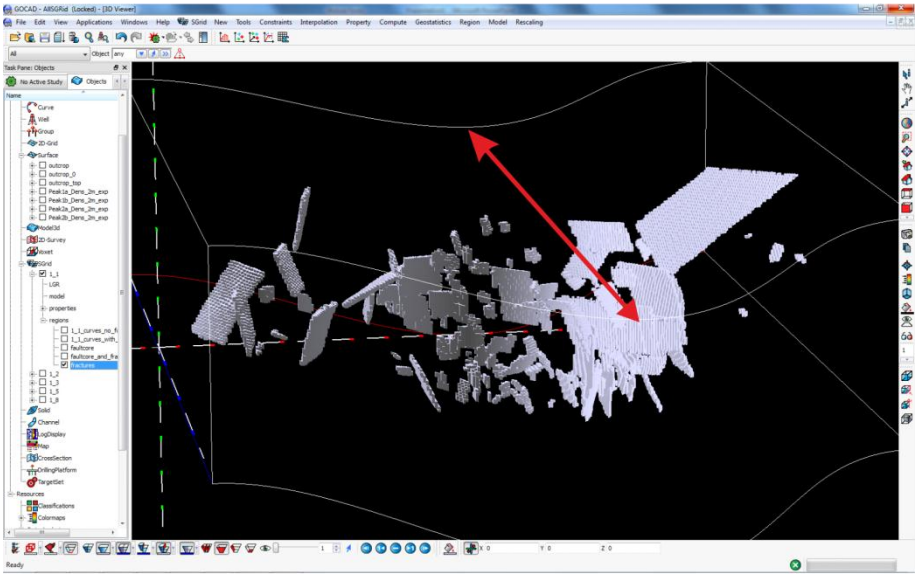

c) A fault parallel slice of the Sgrid with parts of a region highlighted

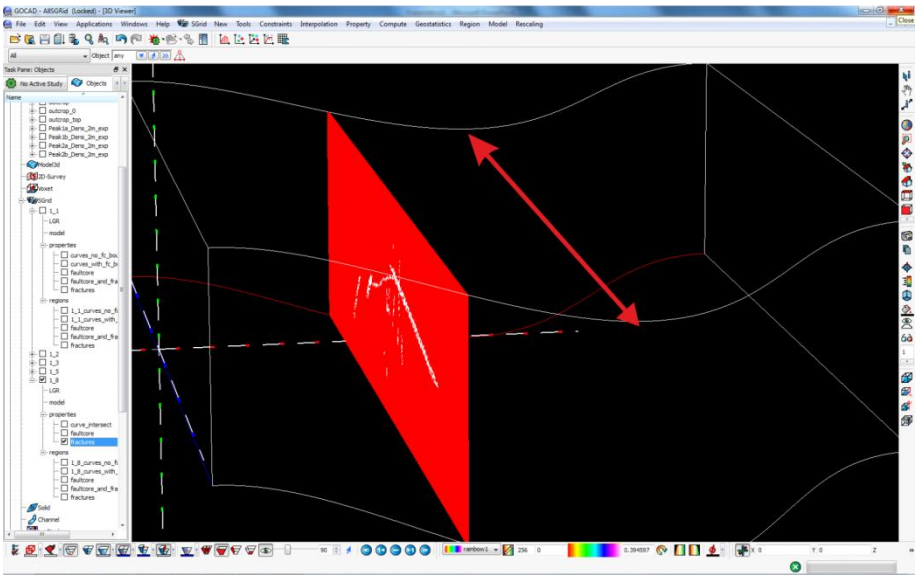

Figure 1.7 - 3D quantitative analysis (quantification)
a) SGrid with long axis oriented parallel with the fault strike, b) Cells of SGrid intersected by fractures, c) A fault parallel slice of the SGrid with parts of a region highlighted

3) The fault core-damage zone boundaries and the other principal slip surfaces fully crosscut the SGrids. This allowed the SGrid to be slightly modified in shape by fitting the slices of the SGrid onto fault core-damage zone boundaries and principal slip surfaces. This modification of the SGrid allowed a more accurate quantification of distance from these features.

4) One axis of the different geocellular models (and therefore the individual cells) is oriented vertical, another one is oriented parallel with the fault strike, and the third one is oriented perpendicular to it (Fig. 1.7a). Using these orientations the variation of fracture/vein density and connectivity across the fault and along its dip can be quantified more accurately.

Once the SGrid was produced, it was slightly modified in shape to better fit the geometry of the outcrop and the dip of the principal slip surfaces (Fig. 1.7a). However, these modifications did not modify the total volume of the model and did not modify the volume of the individual cells by more than 5%.

Within the SGrid, regions can be created that contain a collection of cells as defined by the user (Fig 1.7b). A region can contain any number of cells, and the cells do not have to border each other. Several regions can be made for any given SGrid, and these regions can overlap with each other. With the SGrid, used for the models at each study area, 10 regions were made, 2 for each aspect ratio models, one containing cells intersected by fracture planes (as a measure of density) and one containing cells intersected by intersection lines of fracture planes (as a measure of connectivity). To calculate the across-fault variation in density and

connectivity for a given aspect ratio model the number of cells within a given SGrid region were counted in fault parallel slices (Fig. 1.7c).

The conversion from number of cells per fault parallel slices to SI units of fracture/vein density and connectivity was accomplished using geometrical considerations (Fig. 1.8). Density is calculated using the following geometrical considerations (Fig. 1.8a): If the sidelength of a cube shaped cell is 1, than the largest surface it can be cut within is a rhombus that connects the two opposite corners of the cell, and also intersects two other edges of the cell at their halfheight. The area of the rhombus, by definition, can be calculated as the product of its two diagonals divided by 2. Its first diagonal is connecting two opposite corners of the cube therefore the length of it is given by using the Pythagoras-equation twice, resulting in a value of $\sqrt{3}$. The other diagonal is connecting two opposite edges of the cube, both at their halfheight, giving a length of $\sqrt{2}$ by using the Pythagoras-equation once; therefore the area of the maximum size surface that can cut a 1 sidelength cube is $(\sqrt{3}*\sqrt{2})/2=\sqrt{6}/2\approx1.225$. Since all cells of the 3D models, which are crosscut by a surface, can be intersected by any surface sizes ranging from infinitesimally small values to $\sqrt{6}/2$, a mean value of these possible surface areas were taken, that is $(\sqrt{6}/2)/2=\sqrt{6}/4\approx0.612$. According to this calculation, if the sidelength of the cell in the model is 10 cm, than the conversion from number of cells to fracture/vein density values is 1 cell=6.12 cm^2/cm^3; while if the sidelength of the cells is 1 m, than the conversion is 1 cell=0.612 m^2/m^3.

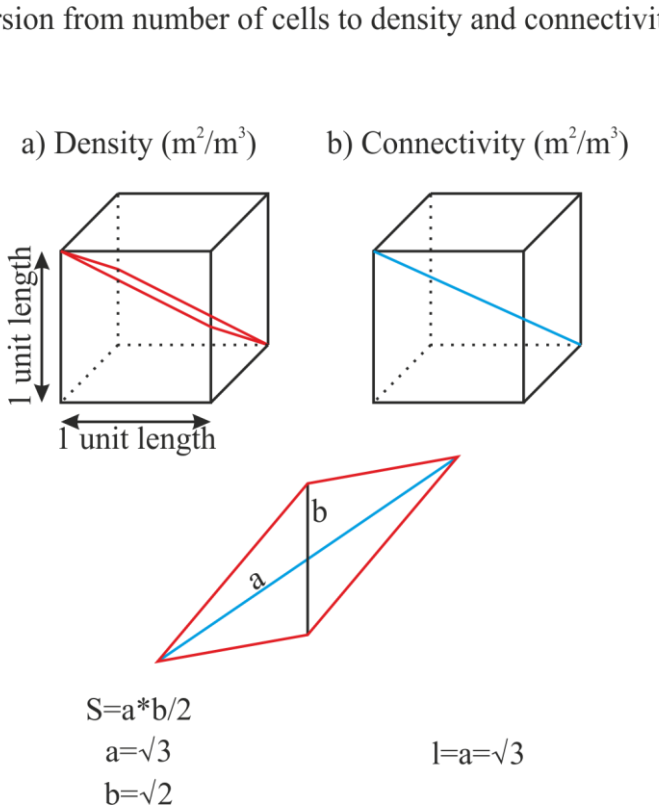

Figure 1.8 - Conversion from number of cells
to a) fracture/vein density and b) fracture/vein connectivity in SI units

Using similar considerations, fracture/vein connectivity values were also converted to SI units from the number of cells intersected by intersection lines of fractures (Fig. 1.8b). The longest possible line intersecting a 1 sidelength cube runs through its two opposite corners. The length of this line has been calculated already, as it is the longer diagonal of the rhombus calculated for fracture/vein density, and it is $\sqrt{3}\approx1.732$. Using similar considerations as for the fracture/vein density values, as a line intersecting a cell can have any length between infinitesimally small values to $\sqrt{3}$; a mean value of $\sqrt{3}/2\approx0.866$ was calculated. According to this calculation, if the sidelength of the cell in the model is 10 cm than the conversion from number of cells to connectivity values is 1 cell=8.66 cm/cm^3; while if the sidelength of the cells is 1 m, than the conversion is 1 cell=0.866 m/m^3.

1.3.5. Validating 3D models, estimating the mean aspect ratio of fractures

The model parameter chosen to test the validity of the different 3D fracture models obtained was the mean aspect ratio of fractures/veins. 3D fracture/vein patterns have been modelled for different values of fracture/vein aspect ratios. Across-fault variation of fracture/vein density and connectivity values, gained from different aspect ratio, 3D models were quantitatively compared with across-fault fracture/vein density and connectivity profiles gained from different 1D and 2D methods. The comparison between results obtained with different methodologies is based on the assumption that the relative variation of fracture/vein density and connectivity values across a given fault zone should be independent of the particular method adopted to quantify them.

Comparison of fracture/vein density values gained from the different 3D models and the 1D transect data was achieved by taking virtual transects (line of cells) across the different 3D models and comparing the across-fault, relative variation of fracture density, measured along these virtual transects with the relative variation of fracture density along the real 1D transects (Fig. 1.9a). However, within the geocellular model any fault-orthogonal transect (line of cells) can be chosen for comparison, regardless of its along-dip and along-strike position (Fig. 1.9b). To account for this possible bias in the comparison of datasets, the sum of all the possible 1D fault orthogonal transects (line of cells), obtained for the different 3D models, was made, regardless of their along-dip and along-strike position, and was divided by the number of possible virtual transects, in order to get an average value. The relative across-fault variation of this summed virtual transect is comparable with the real 1D transect, and it is directly proportional to the density values calculated in 3D, because the cell sizes of the geocellular models were chosen in a way that a single cell is only intersected by one fracture.

Using similar considerations, comparison of the fracture/vein density and connectivity values, gained from the different 3D models and the 2D image analysis data was carried out by taking virtual, fault orthogonal 2D panels across the different 3D models and comparing the across-fault, relative variation of fracture/vein density and connectivity along these virtual panels with the relative variation of fracture/vein density along the real 2D panels. However, within the geocellular model any fault-orthogonal panel can be chosen for comparison, regardless of its along-strike position. To account for this possible bias in the comparison of the datasets, the sum of all the possible 2D fault orthogonal panels, obtained from the different 3D models, was made, regardless of their along-strike position, and was divided by the number of possible panels in order to get an average value. The relative across-fault variation in fracture/vein density and connectivity of these summed sections of panels is comparable with the real 2D panels, and it is directly proportional to the fracture/vein density and connectivity values calculated in 3D, for the same reason that were explained above.

a) randomly selected fault orthogonal transect (red line) across the fault zone (fault core lense boundaries displayed with yellow, orange and purple)

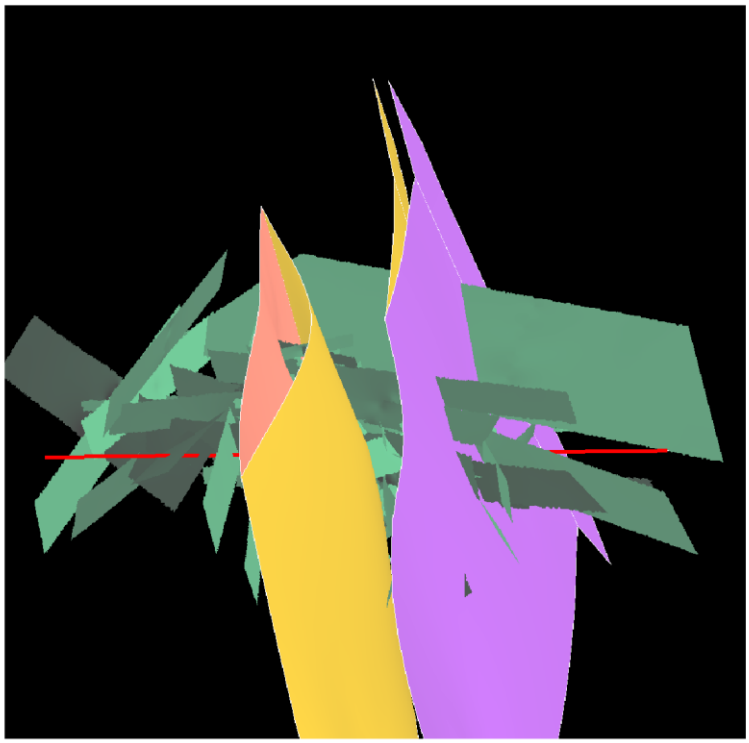

a) line of cells at the transect location, with cells intersected by fractures highlightes and marked with arrows

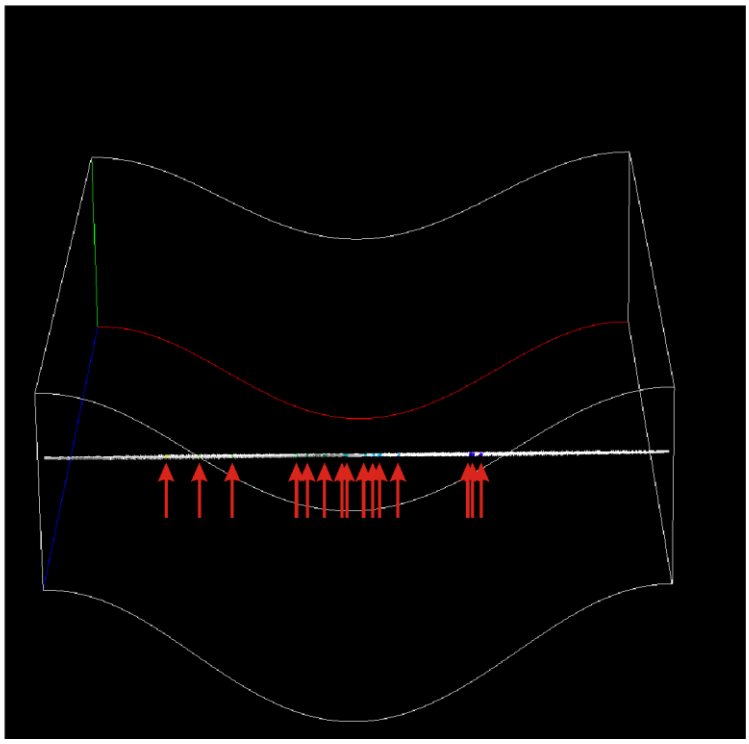

Figure 1.9 - Calculating fracture/vein density and connectivity
a) randomly selected fault orthogonal transect (red line) across the fault zone (fault core lens boundaries displayed with yellow orange and purple), d) line of cells at the transect location, with those cells intersected by fractures highlighted and marked with arrows

In order to be able to validate the different 3D models and, as a result, to estimate the mean aspect ratios of fractures, all datasets have been normalized in a way that the fracture/vein density and connectivity values in the protolith were 1. This normalization allowed an easier visualization of the relative increase in fracture/vein density and connectivity from the protolith to the fault core-damage zone boundary and, in this way, the normalized 1D and 2D (outcrop and microscale) fracture/vein density values were comparable with fracture/vein density values gained from sampling 3D models for different aspect ratios, while the normalized 2D fracture/vein connectivity values (outcrop and microscale) were comparable with fracture/vein connectivity values gained from sampling 3D models for different aspect ratios.

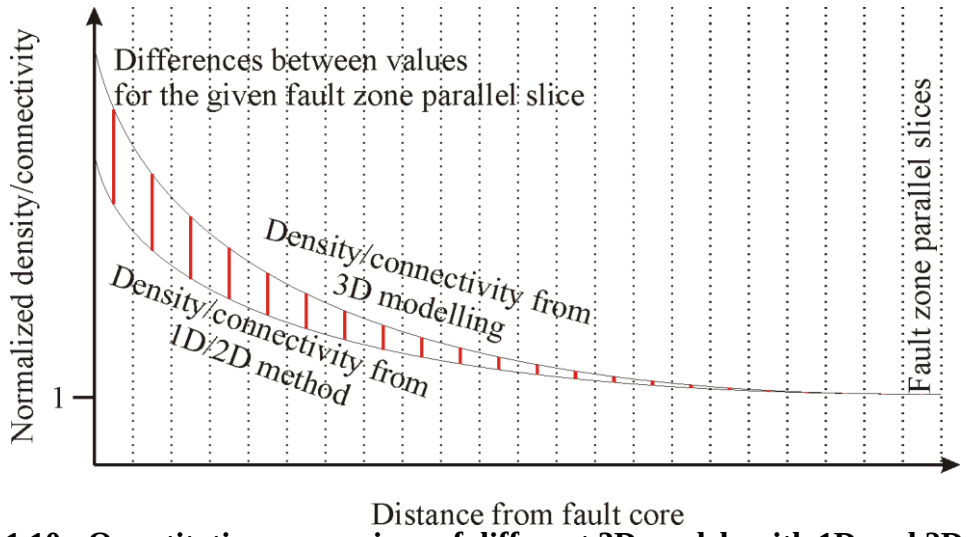

Figure 1.10 - Quantitative comparison of different 3D models with 1D and 2D results using misfit graphs

Quantitative comparisons were made by using misfit graphs (Fig. 1.10): differences between normalized fracture/vein density or connectivity values from the different fault parallel, across-fault sections were added up. This summed value between any given 3D model and any given 1D or 2D method is the misfit value that quantitatively characterizes the mismatch between any two datasets. These misfit values (calculated individually for fracture/vein

density and connectivity) can be compared individually or summed for any 3D model. The 3D model with the aspect ratio that fits better the 1D and 2D values of fracture/vein density and connectivity is the most valid and realistic one within the approximation of the method and, therefore, this model contains fractures that best-correspond to the mean aspect ratio of fractures in the fault zone.

2. Internal architecture and transport properties of fault zones

2.1.Classification of faults

Faults and fractures are brittle discontinuities in rocks, which can form across a range of scales from micron to kilometre-scales. Based on the relative displacement between their wall rocks, fractures can be classified as Mode I, Mode II and Mode III fractures (e.g. Atkinson, 1987, Fig. 2.1a). Mode I fractures are tensile fractures with no shear (e.g. joints, extension veins), while Mode II and Mode III fractures (e.g. faults) are sheared features, with the shearing being in-plane and anti-plane, respectively.

Faults can be classified using Anderson`s fault classification (Anderson, 1951, Fig. 2.1b), that is based on the relative orientation of the fault planes with respect to the maximum, intermediate and minimum principal stress axes (σ_1, σ_2 and σ_3, respectively), which are oriented perpendicular to each other, with one of the principal stress axes being vertical and the two other being horizontal. According to Anderson`s fault classification, when σ_1 is vertical normal faults form, when σ_3 is vertical reverse faults (thrusts) form and when σ_2 is vertical strike-slip faults form.

Faults can also be classified based on the relative movement of the two faulted blocks (McClay, 1987, Fig 2.1c). According to this kinematic fault classification, faults can be split into five types: a) normal faults, when the fault hanging wall moves downward along the dip direction (extensional faults), b) reverse faults, when the fault hanging wall moves upwards along the dip direction (compressional faults), c) strike-slip faults, when displacement of the wall rocks occurs along strike direction (in the horizontal plane), d) oblique-slip fault (combined strike- and dip-slip displacement) and e) rotational faults, when the direction and values of the displacement along the fault plane is a function of the location along the plane.

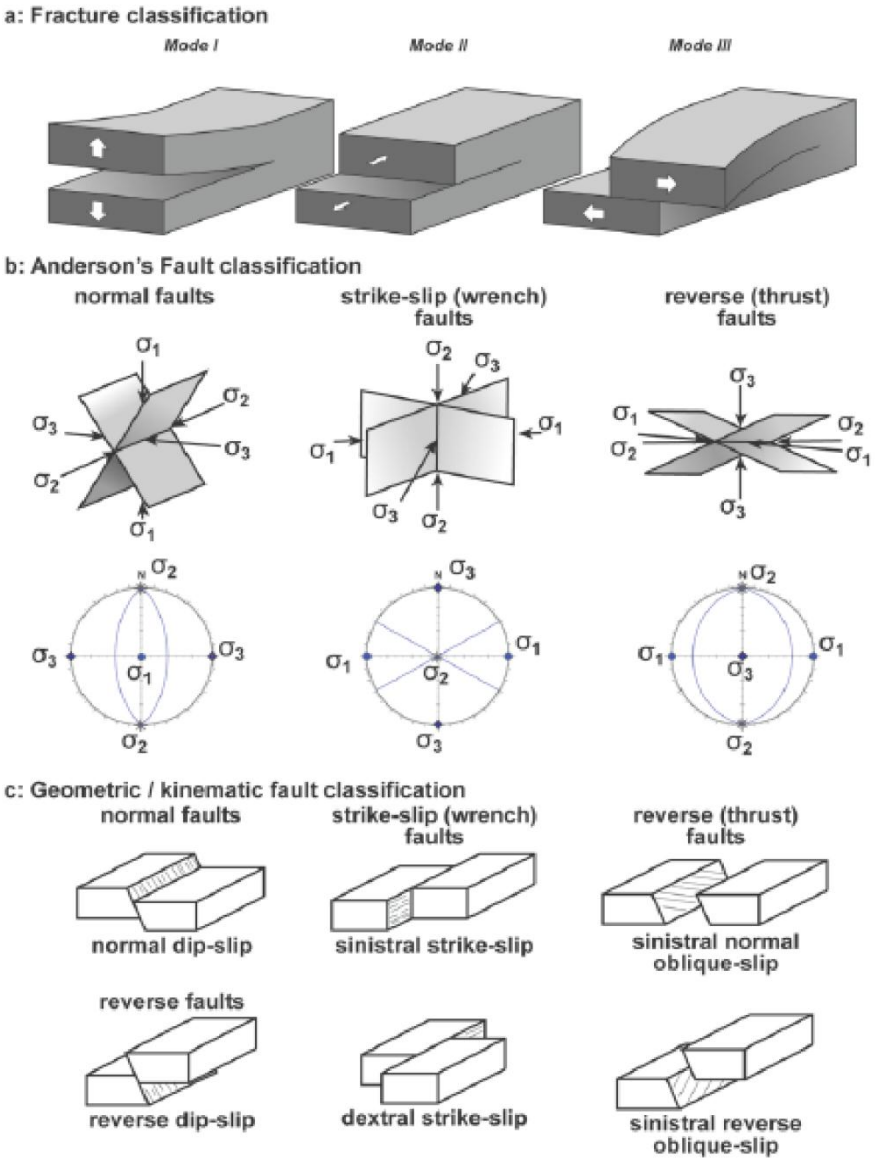

Figure 2.1 - Fault and fracture classification
a) fracture types (*Mode I*, *II*, and *III*) based on the relative displacement of material on either side of a fracture, b) Andersonian and c) geometric fault classification schemes (from McClay, 1987, edited by Walker, 2010)

The direction of motion along the fault planes can be identified using kinematic indicators that can be fault plane striations, fault plane undulations and secondary fracture systems (e.g. Walker, 2010 and references therein). Due to their abundance in the study area, in this Thesis only fault plane striations have been used as kinematic indicators. Striations can appear in two forms (Petit, 1987 and references therein, Fig. 2.2): a) slickenlines, that are striations

(grooves) produced by the sliding of fragments and asperities on the fault planes (Fig. 2.2a), b) slickenfibres, due to crystals growing on shear planes, during aseismic movement on the fault (Fig. 2.2b), where the growth of fibers is facilitated by gaps opened during displacement of the two irregular fault blocks (Twiss and Moores, 1992). Both slickenlines and slickenfibers are elongated features, and their long axes are parallel with the direction of motion along the fault. The amount of displacement along faults can be quantified by using marker points from the opposite sides of the fault, which were originally coincident before the fault plane was created.

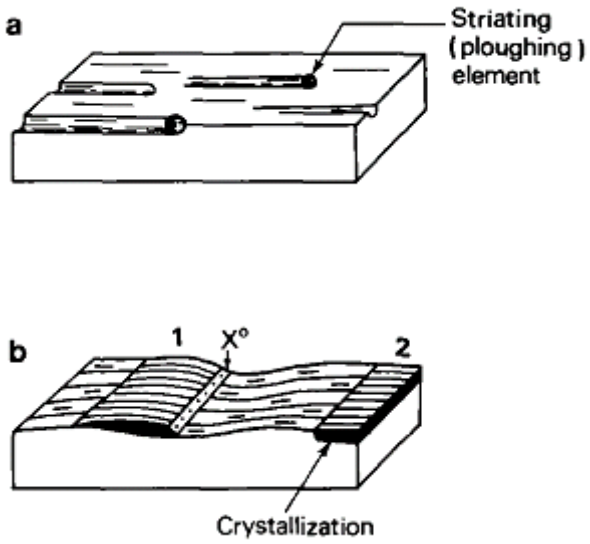

Figure 2.2 - Kinematic indicators
a) striation due to a ploughing element (asperity ploughing), b) crystallization on the asperities (from Petit, 1987)

2.2.Principles of rock and fault mechanics

Initial fracturing of intact rocks initiates when the value of the applied stresses reaches the rock`s strength, as described by the Mohr-Coulomb failure criterion:

$$\tau = C + \mu_i \sigma_n \quad \text{or,} \quad \tau = C + \mu_i(\sigma_n - P_f), \qquad \text{Eq. 1 and Eq. 2}$$

where τ is the shear stress, *C* is the cohesive strength of the intact rock, μ_i is the coefficient of internal friction, σ_n is the normal stress, σ_n` is the effective normal stress and P_f is the pore fluid pressure.

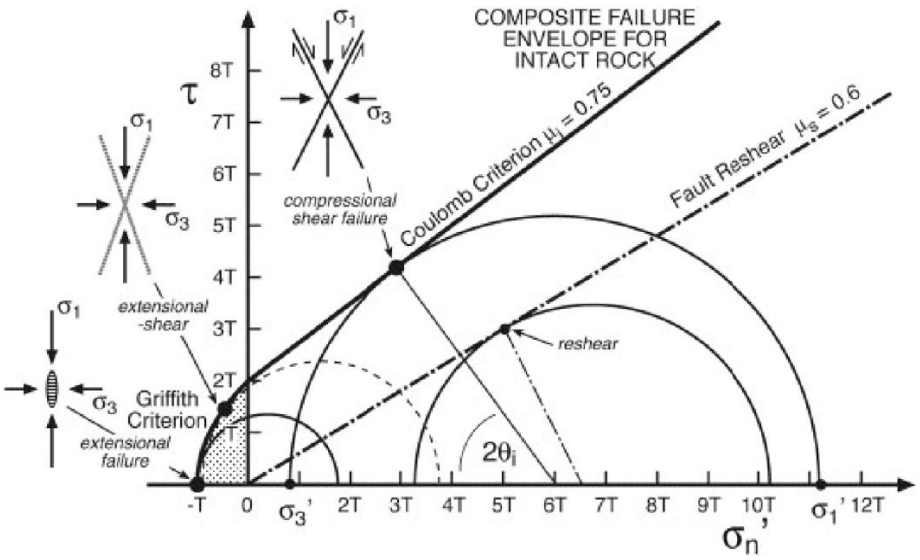

Figure 2.3 - Composite failure envelope for intact rock

Composite failure envelope for intact rock (bold line) plus the reshear condition for a cohesionless fault (dash–dot line) plotted on a Mohr diagram of shear stress, *τ*, against effective normal stress, σ'_n, normalised to rock tensile strength, *T*. Critical stress circles are shown for the three macroscopic modes of brittle failure and for the reshear of an optimally oriented cohesionless fault. Expected orientations with respect to the principal stress axes of new-formed compressional shear, extensional-shear, and extension fractures are shown in the attached cartoons (from Sibson, 2004)

Failure envelopes describing the mode of failure can be drawn on τ, shear stress vs. σ_n, normal stress diagrams, called Mohr-diagrams (e.g. Fig. 2.3). Mohr-diagrams can be used to infer the level of stresses required for failure at different conditions of normal stress (Fig. 2.3). Sibson (2004) summarized the three macroscopic modes of brittle failure that can occur within intact, isotropic rocks (Fig. 2.3): compressional shear failure ($\sigma`_n > 0$), extensional shear failure ($\sigma`_n < 0$, and $\tau \neq 0$) and extensional failure ($\sigma`_3 = -T$, where *T* is the

tensile strength of the rock) (Brace, 1960; Jaeger and Cook, 1979; Secor, 1965; Sibson, 2004).

When $\sigma`_n > 0$ faults form by compressional shear failure in accordance with the linear Coulomb criterion:

$$\tau = C + \mu_i \sigma_n` \approx 2T + \mu_i(\sigma_n - P_f), \quad \text{Eq. 3}$$

where $C \sim 2T$ is the cohesive strength of the rock. In this case faults tend to form along planes containing the σ_2 direction at angles $\theta_i = 0.5\, tan^{-1}(1/\mu_i)$ to the σ_1 directions (typically $25° < \theta_i < 30°$).

In the tensile field ($\sigma`_n < 0$), when $\tau \neq 0$ failure is governed by the macroscopic Griffith criterion,

$$\tau^2 = 4(\sigma_n - P_f)T + 4T^2, \quad \text{Eq. 4}$$

which describes the stress conditions for extensional shear failure along planes oriented at $\theta<\theta_i$ to σ_1. Eq. (4) reduces to the tensile fracture criterion in case of $\sigma`_3 = T$:

$$\sigma_3` = -T \quad \text{Eq. 5}$$

and

$$P_f = \sigma_3 + T, \quad \text{Eq. 6}$$

which describe those conditions, necessary for the formation of pure tensile (Eq. 5) and hydraulic fractures (Eq. 6), oriented perpendicular to σ_3 (Sibson, 2004).

The mode of failure of intact rock depends on the value of differential stress, ($\sigma_1 - \sigma_3$), expressed in terms of tensile strength, T. For values of $\mu_i = 0.75$, typical of most rocks, compressional shear failure occurs when $(\sigma_1 - \sigma_3) > 5.66T$, extensional shear requires $4T < (\sigma_1 - \sigma_3) < 5.66T$, and hydraulic tensile fracturing requires $(\sigma_1 - \sigma_3) < 4T$ (Secor, 1965).

Amonton`s Law defines the sliding friction coefficient of a pre-existing fault as the ratio:

$$\tau = \mu_s \sigma_n`, \qquad \text{Eq. 7}$$

where μ_s is the sliding friction coefficient (Jaeger and Cook, 1979). Results from laboratory experiments show that the value of μ_s, for most rock types ranges between 0.85, at normal stresses lower than 2 kbar (200 MPa), and 0.6, at normal stresses higher than 2 kbar (Byerlee, 1978, Fig. 2.4).

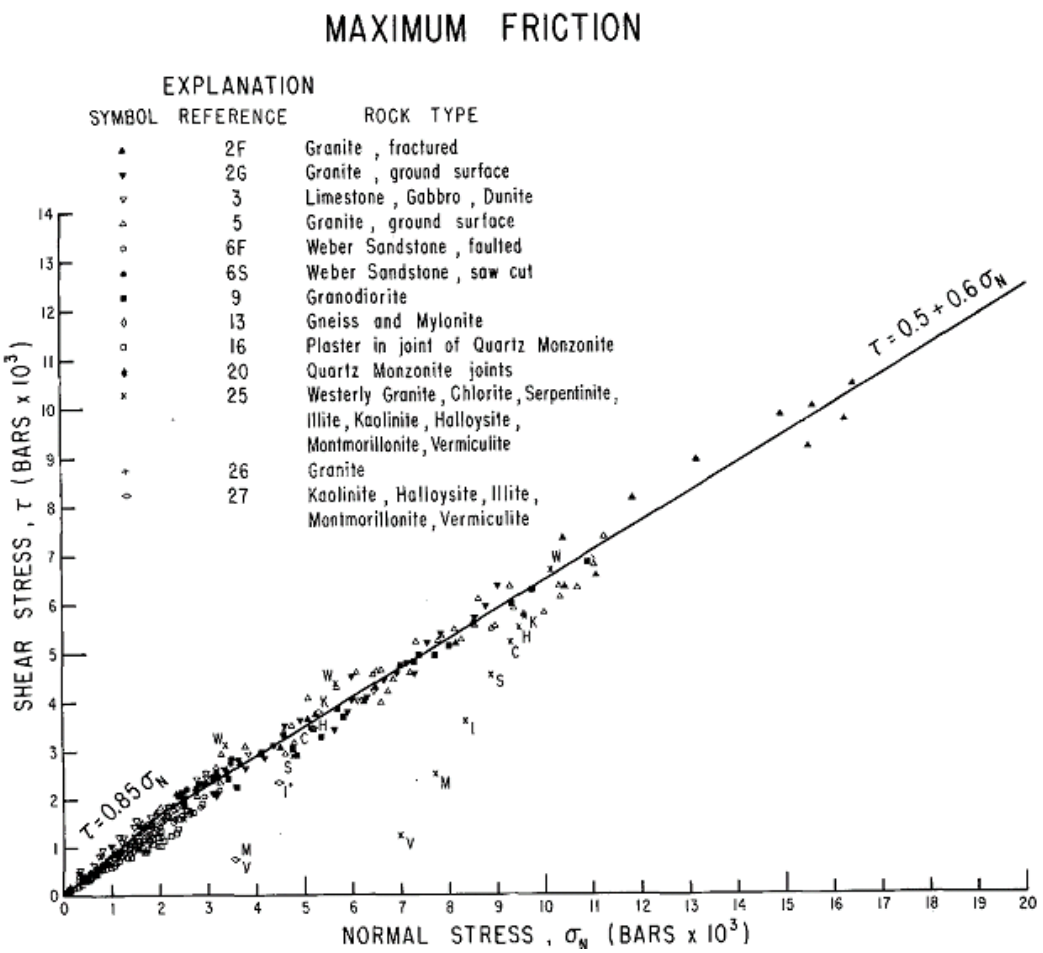

Figure 2.4 - Shear stress plotted as a function of normal stress

Shear stress plotted as a function of normal stress at the maximum friction for a variety of rock types at normal stresses to 20 kb (from Byerlee, 1978)

2.3.Fault zone architecture

Although, from a mechanical point of view faults may be considered as simple planes, field-based structural observations showed that fault zones are structures of finite width, with complex 3D architectures (Chester et al., 1993; Sibson, 1977; Wallace and Morris, 1986). Highly simplified models of mature fault zone architectures predict the presence of three main domains, each with its own characteristic suite of fault rocks (Fig. 2.5): 1) a *fault core* made of single or multiple strands of fine- to ultra-fine grained rocks (e.g. gouges, cataclasites and ultra-cataclasites), where most of the displacement is localised; 2) a *damage zone* of fractured host rocks, where the intensity of the fracturing progressively decreases as one moves away from the fault core; 3) a *protolith* made by the host rock, where the effects

of fault-related deformations are minor or absent, only background fracturing is present, due to previous faulting events. The geometry, width, intensity and nature of fracturing within each different fault zone domain can vary significantly, and is likely to be influenced by the lithology of both the host and the associated fault rocks (Antonellini and Aydin, 1994; De Paola et al., 2008; Faulkner et al., 2003).

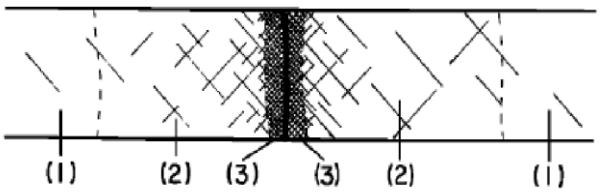

(1): Protolith (2): Damage zone (3): Fault core

Figure 2.5 - Internal structure of faults
Not to scale (from Chester et al., 1993)

2.3.1. Deformation features in the different fault zone domains

The development of the fault zone domains and the deformation features within these domains is related to the P/T conditions, velocity mode of faulting (Sibson, 1977), lithology, fault displacement and the presence of circulating fluids in the fault zone (e.g. Micarelli et al., 2005; Micarelli et al., 2006a). Fault damage zones usually consist of rock volumes affected by intense fault-related fracturing, but bedding surfaces and inherited structural fabrics are commonly preserved (Billi et al., 2003). With strain localisation, a fault core develops within fault zones, and the damage zone accommodates relatively little further shear displacement (Micarelli et al., 2005). Faults with cumulative displacements less than 1 m usually lack a fault core, faults with displacements between 1 to 5 m may have discontinuous cores and finally, faults with displacements over 5 m may have continuous cores (Micarelli et al., 2005). Fault rocks in the proximity of the fault slip surface, within the fault core, develop due to porosity reduction that is controlled by three main mechanisms such as a) pore collapse due to localised compaction and re-organisation along grain boundaries, b) rotation-enhanced particle abrasion of larger particles during shear and c) precipitation of calcite cement in newly formed fractures (Micarelli et al., 2005 and references therein).

Sibson (1977) produced a fault rock classification, based on their cohesion and fabric, developed at different depth and controlled by environmental p/T conditions (Table 2.1). At depth above the greenschist transition, typically 10-15 km, rocks behave in a brittle way, as deformation is friction dominated; this regime is called *elasto-frictional*. At larger depths, where a major rock constituent (usually quartz) can readily deform by crystal plasticity, the rheological behaviour may change and be

			Random-fabric		Foliated	
Incohesive			**Fault breccia (visible fragments > 30% of rock mass)**		?	
			Fault gouge (visible fragments < 30% of rock mass)		?	
Cohesive	Nature of matrix	Glass/devitrified glass	Pseudotachtylyte		?	
		Nature of matrix Tectonic reduction in grainsize dominates grain growth by recrystallisation & neomineralisation	Crush breccia		(fragments > 0.5 cm)	0-10%
			Fine crush breccia		(0.1 cm>fragments > 0.5 cm)	
			Crush microbreccia		(fragments < 0.1 cm)	
			Protocataclasyte	Cataclasite series	Protomylonite	10-50%
			Cataclasite		Mylonite	50-90%
			Ultracataclasite		Ultramylonite	90-100%
		Grain growth pronounced	?		Blastomylonite	

Proportion of matrix

Mylonite series

Table 2.1 - Textural classification of fault rocks
Highlighted with yellow are the types of fault rocks studied in this Thesis (after Sibson, 1977)

described as *quasi-plastic* (Sibson, 1977). Fault rocks, formed in the quasi-plastic regime are typically cohesive, foliated rocks of the mylonite series and blastomylonites, produced by quasi-plastic shearing and transient seismic shearing (Sibson, 1977). On the other hand, fault rocks, formed in the elasto-frictional regime are fault gouges and breccias, in the top few kilometres of the crust (up to 4 km), and cataclasites and ultra-cataclasites at larger depths, between 4 to 10 km. These type of fault rocks are characterized by the development of a weak and random fabrics (Sibson, 1977). In particular, breccias and gouges are incohesive fault rocks, with visible fragments of the original host rock being >30%, and <30% of the rock mass, respectively; cataclasites are (partially) recrystallized, cohesive fault rocks originated by tectonically induced, intense grain size reduction (Table 2.1, Sibson, 1977). More recently other authors have suggested a review of Sibson's fault rock classification. For example Woodcock and Mort (2008) and Mort and Woodcock (2008) suggested that breccias should be reclassified based on the size of the largest clasts (i.e. larger than 2 mm) in their matrix into crackle breccias (>75%), mosaic breccias (>60%) chaotic breccias (>30%) and cataclasites (<30%).

Several different models exist for explaining the development of damage observed around fault zones, based on different mechanical process (Blenkinsop, 2008; Mitchell and Faulkner, 2009; Wilson et al., 2003). These models are (Fig. 2.6): a) the Andersonian model of fault formation (Anderson, 1942), b) the interaction of multiple fault tips model (Blenkinsop, 2008), c) the fault tip model for growth by tip propagation (Scholz et al., 1993; Vermilye and Scholz, 1998), d) the fault model along wavy, frictional fault surfaces (Chester and Chester, 1998; Scholz, 1987) and finally, e) the model of off-fault damage due to due to the propagation of dynamic rupture (Rudnicki, 1980; Wilson et al., 2003).

The Andersonian model of fault formation assumes simple, homogenous stress states in the crust, and that failure of intact rocks occurs in accord with the Coulomb failure criterion (Eq. 1, Fig. 2.6a). According to this model, faults will form at angles of ~25-30° with respect to the maximum principal stress driving the deformation (Sibson, 2004).

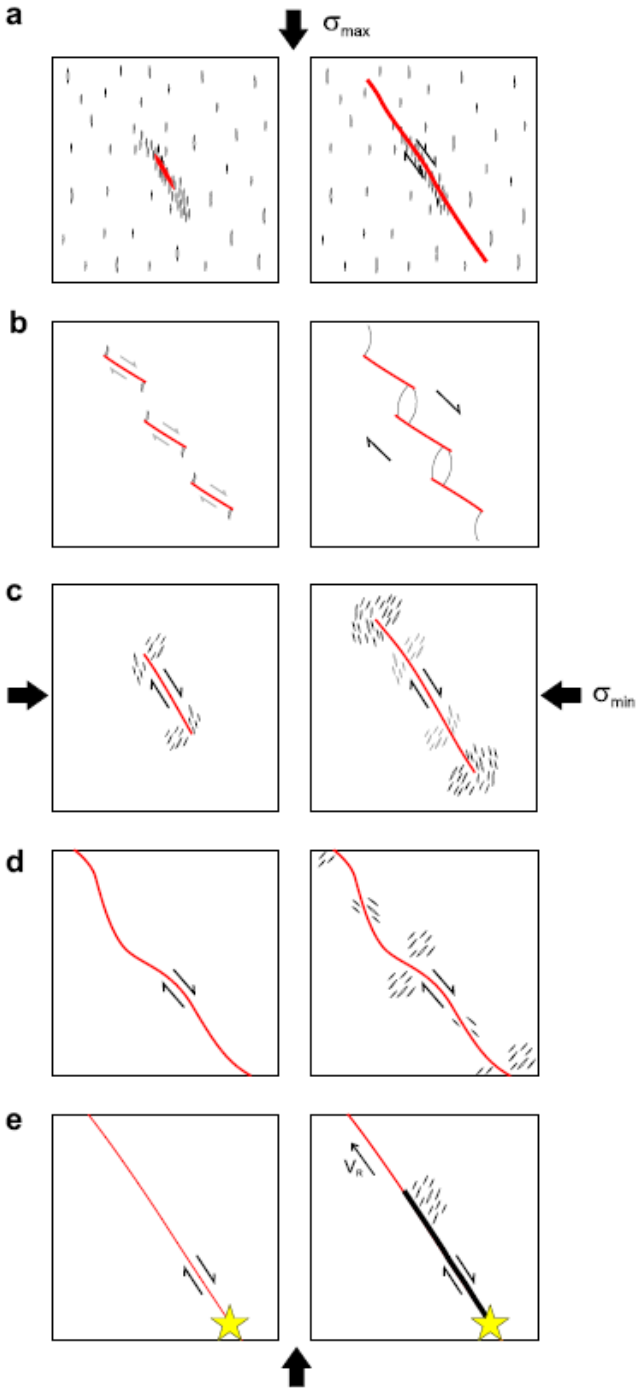

Figure 2.6 - Schematic diagram illustrating various models that may be responsible for creating off-fault damage

Schematic diagram illustrating various models that may be responsible for creating off-fault damage, modified from Wilson et al. (2003) and Blenkinsop (2008). (a) Fault model assuming homogeneous stress, where the Andersonian model of fault formation predicts microfracture orientation at approximately 30_ to the fault. Fault forms through the interaction and coalescence of many tensile microcracks. (b) Interaction of multiple fault tips model, where extension fractures formed at the tips of separate individual faults interact with each other. (c) Fault tip model for growth by tip propagation. Microfractures form in the region of the fault tip stress concentration. (d) Fault model for wear along wavy, frictional fault surfaces. (e) Off-fault damage due to the propagation of a dynamic rupture tip, with Vr being the rupture velocity that controls the form of fracturing. (from Mitchell and Faulkner, 2009)

The interaction of multiple fault tips model suggests that extensional fractures may form at the tips of individual interacting faults (Fig. 2.6b). Field evidence, experiments and theory have shown that extensional fractures form around the tips of isolated fractures when loaded in shear (Blenkinsop, 2008; Engelder, 1989; Pollard and Segall, 1987; Rispoli, 1981). Such fractures are referred to as wing, and faulting may occur by the linkage of such features when two or more fault tips interact (Fig. 2.6b). Faults developing according to this model may produce fracture sets in the damage zones with the same orientation as the Andersonian model (Blenkinsop, 2008).

The fault tip propagation model suggests that the bulk of the fracturing in the damage zone is produced immediately prior to the main fault formation in the ‘process zone’ surrounding the fault tip (Fig. 2.6c). The model is based on non-linear and post-yield fracture mechanics models (Scholz et al., 1993; Vermilye and Scholz, 1998). In this case, fracture orientations are expected to range from high to low angles to the main fault plane, dependent on whether they are in the tensile or compressive region of the fault tip, respectively (Fig. 2.6c, Scholz et al., 1993).

In the fault model along wavy, frictional fault surfaces (Fig. 2.6d) fracture damage may occur due to the juxtaposition of fault irregularities during stress cycling (Chester and Chester,

2000; Scholz, 1987). In this model the bulk of the fault damage is related to fault wear and due to cumulative fracturing, resulting from continued slip on pre-existing fault surfaces (Chester and Chester, 2000; Scholz, 1987). The maximum compressive stress orientations can vary locally, from parallel to perpendicular to the fault plane (Chester and Fletcher, 1997; Saucier et al., 1992) and, as such, controlling the orientation of fractures (Fig. 2.6d).

Finally, the off-fault damage model explains the damage observed in the damage zone of faults as due to the dynamic propagation of seismic ruptures (Fig. 2.6e, Rudnicki, 1980; Wilson et al., 2003). The fractures that are created by the propagation of an earthquake at the rupture tip are expected to be formed in a similar orientation to the fractures formed by the migrating fault tip model, shown in Fig. 2.6c.

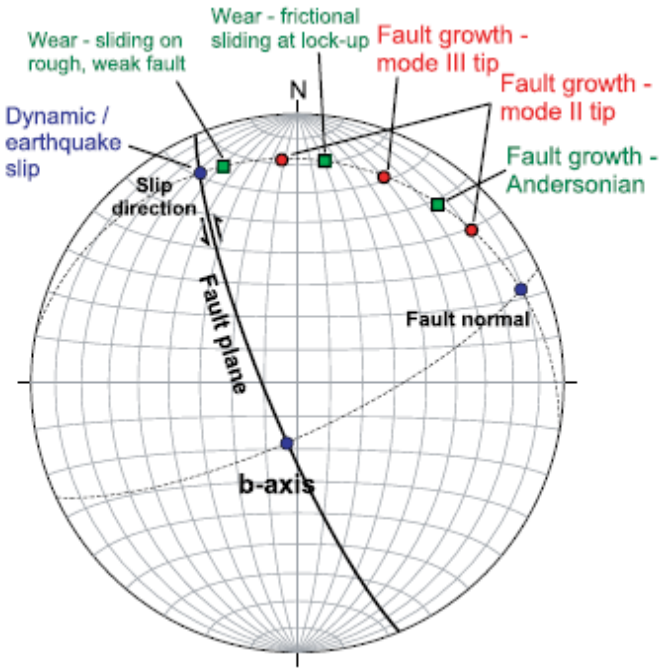

Figure 2.7 - Expected orientation of microfractures of the various models
(from Wilson et al., 2003)

A summary of the different fracture orientations in the damage zone of faults, predicted by these five different models is shown in Fig. 2.7 (Mitchell and Faulkner, 2009; Wilson et al., 2003). The range of orientations of fractures in the damage zone of faults is an important

fault attribute, as it can determine important parameters as fracture connectivity, which may ultimately control fluid flow (Manzocchi et al., 1998; Odling et al., 1999; Sleight, 2001).

2.3.2. Quantitative fault zone attributes

Scaling relations

A scaling relation between fault displacement and the width of the damage zones is suggested by existing datasets (Knott et al., 1996; Micarelli et al., 2006a; Mitchell and Faulkner, 2009; Torabi and Berg, 2011 and references therein). Field studies have shown that displacement scales with damage zone width according to a positive empirical relationship (Fig. 2.8).

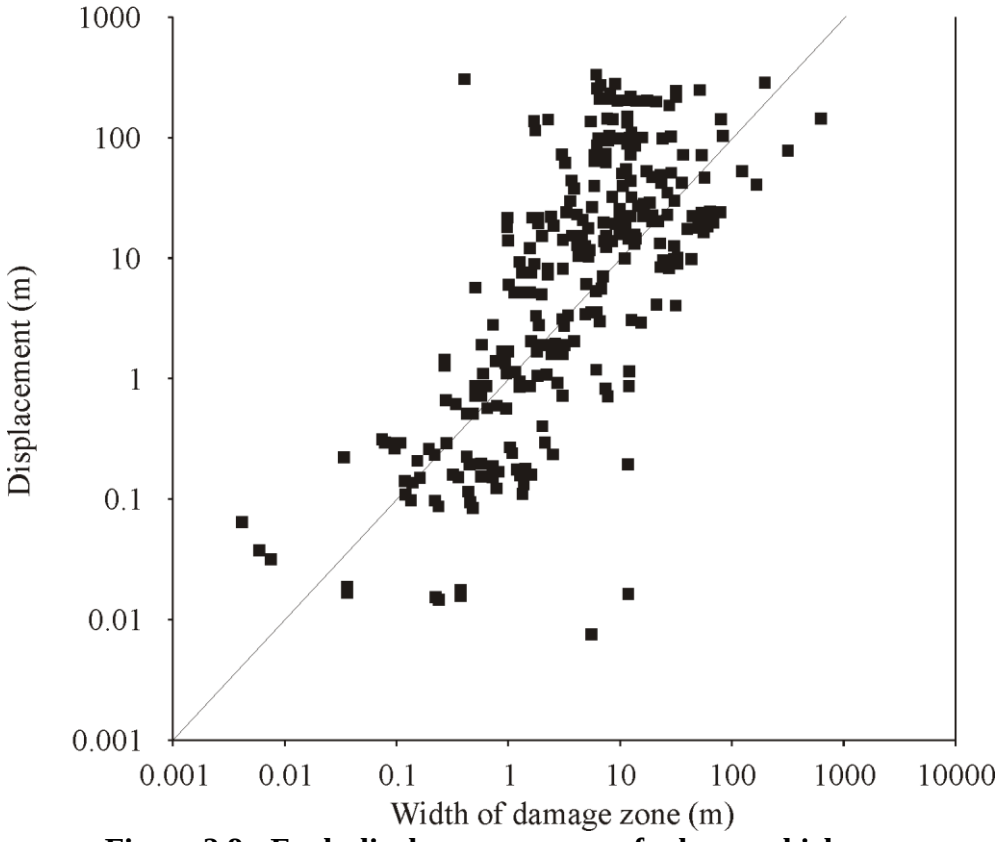

Figure 2.8 - Fault displacement versus fault core thickness
(after Torabi and Berg, 2011)

The observed scattering of the data has been interpreted as due to the lithological variations of the host rocks (Torabi and Berg, 2011). All studies found that for faults with displacements

less than 1 km the displacement scales with damage zone width according to the following empirical relationship:

$$D=W, \qquad \text{Eq. 8}$$

where D is the displacement on the fault and W is the width of the damage zone.

However, it has been suggested that for displacements larger than 1 km, the width of the damage zone may reach a critical value (e.g. 150 m), beyond which it does not increase anymore with fault displacement (Faulkner et al., 2011, Fig. 2.9). Additionally, positive, linear correlations have been suggested between fault displacement and the thickness of the fault core (Torabi and Berg, 2011 and references therein, Fig. 2.10), and between fault length (Needham et al., 2008; Torabi and Berg, 2011, Fig. 2.11). These relationships have been interpreted as due to the cyclic reactivation of faults, including during the propagation of earthquakes, that repeatedly enlarges the length and displacement of the fault and thickens its fault core (Torabi and Berg, 2011).

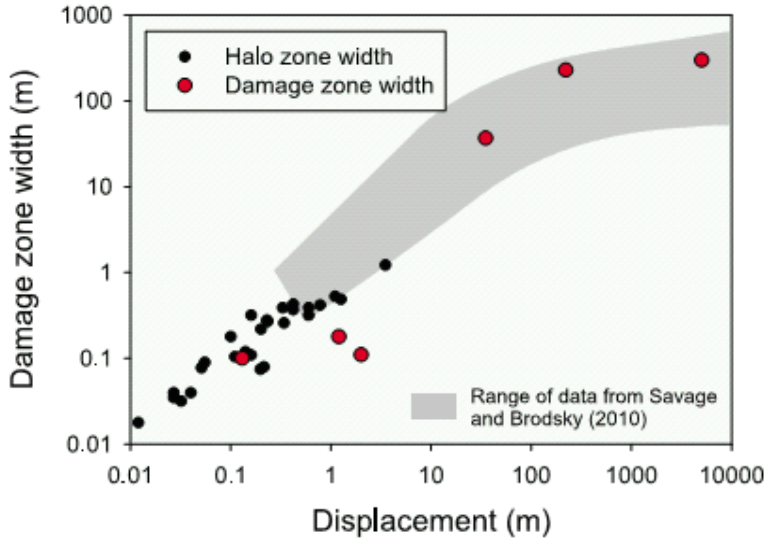

Figure 2.9 - A compilation of data for damage zone width versus displacement Microfracture data from Mitchell and Faulkner (2009 and this work and macro-fracture data (shown by the shaded area) compiled by Savage and Brodsky (2011) (from Faulkner et al., 2011)

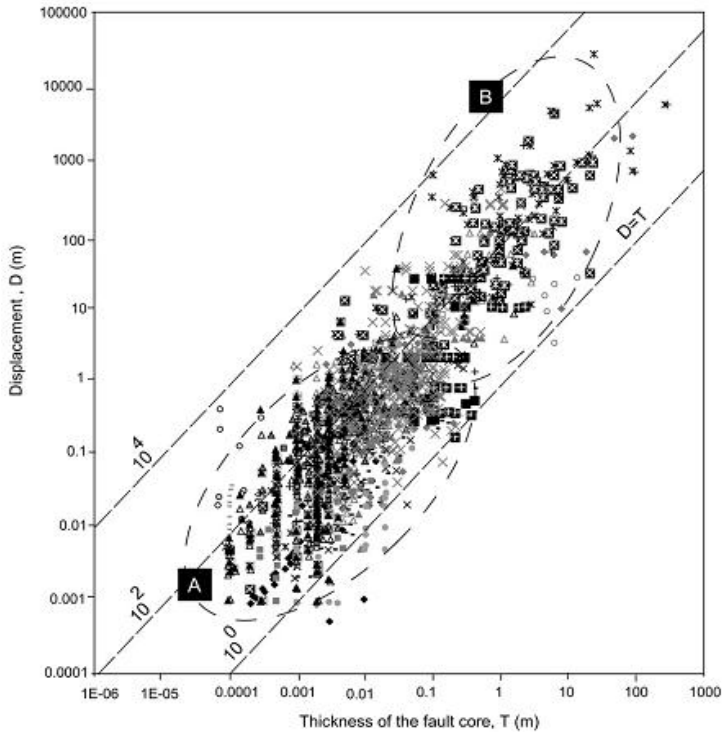

Figure 2.10 - Fault displacement versus fault core thickness
the different symbols refer to data from different studies and, the two areas marked "A" and "B" refer to "small" and "large" faults (from Torabi and Berg, 2011)

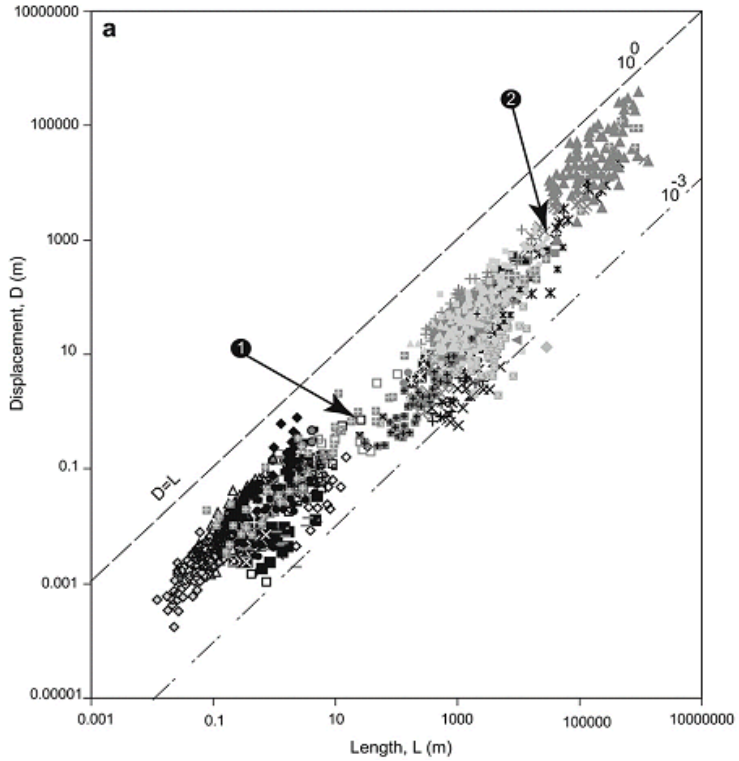

Figure 2.11 - Relationship between maximum displacement and length for faults at different tectonic settings
the different symbols refer to data from different studies, and the two arrows marked "1" and "2" are pointing to the boundaries between small, medium and large faults, where a break of slope in the data can be found (from Torabi and Berg, 2011)

Fracture density and connectivity

Faults and associated fracture patterns, developed within different lithologies and at different scales, are known to exhibit a great variability of fault zone attributes such as fracture density and connectivity (Agosta and Aydin, 2006; Aydin, 2000; Tondi, 2007). Regardless of the scale of observations, previous studies found that fracture density decreases when one moves away from the fault core-damage zone boundary towards the protolith (Chester et al., 1993; Faulkner et al., 2011; Knott et al., 1996; Micarelli et al., 2003; Micarelli et al., 2006b; Mitchell and Faulkner, 2009; Savage and Brodsky, 2011; Scholz et al., 1993; Sibson, 1977). The decrease in fracture density is generally approximated with a power-law relationship. However, Nicol et al. (1996) argued that this relationship may only be an apparent one, due to sampling biases caused by transect lengths, data resolution and differences in sampling methodology. Due to large number of datapoints, the best fit trendlines are usually characterized by relatively low R^2 values. Another factor that might have a complicating effect on the quantitative description of fracture patterns is the existence of single and multiple strand fractures (Vermilye and Scholz, 1994). Single strand fractures are easier to describe and usually follow a clearer trend.

Regardless of the type of best-fit trendline, the decreasing trend of fracture density, generally observed in the damage zones, can be locally altered due to the presence of subsidiary faults; in these cases, damage zone fracture density can be anomalously higher than in their surroundings (Mitchell and Faulkner, 2009, Fig. 2.12). Although the width of the damage zone is considered as a function of the displacement along the fault, field-based quantitative studies showed that fracture intensity close to the fault core is independent from fault displacement it (Mitchell and Faulkner, 2009, Fig. 2.12).

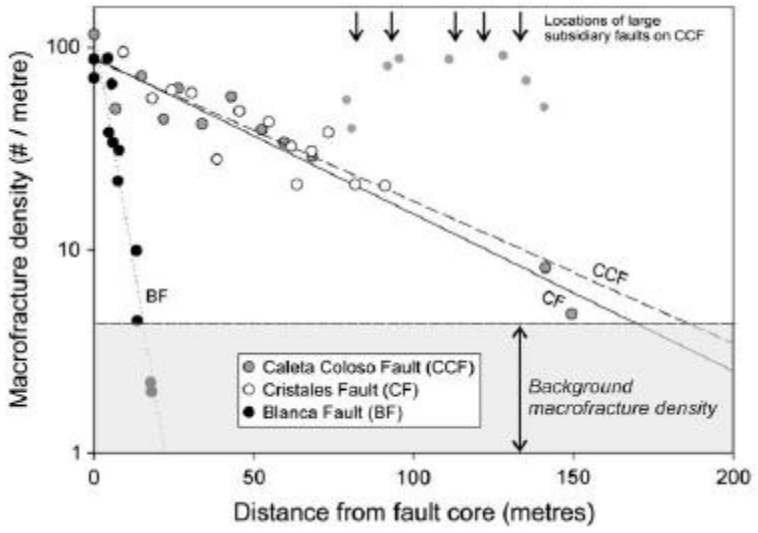

Figure 2.12 - Graph showing macrofracture density versus perpendicular distance from the fault core

Locations of large subsidiary faults around the Caleta Coloso fault are marked with arrows. Data points where the subsidiary faults appear to have a clear effect on the density are ignored for the least square lines of best fit (represented as the points with no border) (from Mitchell and Faulkner)

Fracture connectivity is defined by the degree to which the fracture network provides continuous pathways through the rock (Stauffer, 1985). It is dominantly controlled by the density, length, orientation and spatial distribution of fractures (Odling, 1992). It can be quantified using percolation theory (e.g. Odling, 1992, 1997; Odling et al., 1999; Stauffer, 1985; Stauffer and Aharony, 1991; Zhang et al., 2009; Zhu and Wong, 1999) that is a concept describing the behaviour of connected clusters in a random graph (Broadbent and Hammersley, 1957). Within the graph the studied objects (in this case fractures and/or veins) intersect to form clusters and at a certain density of objects a theoretically infinitely large cluster is formed (Stauffer, 1985). Using percolation theory, connectivity can be quantified in 2D or 3D by analysing the clusters of intersecting fractures. If an intersecting cluster of fractures intersects all sample boundaries, the cluster reached its percolation threshold values (p_c, Reynolds et al., 1980), or in other words, it is fully connected. Micarelli et al. (2006a) studied the variation of fracture connectivity across fault zones, and found that the outer parts

of the damage zones are characterised by low connectivity, while the inner parts of the damage zones and the fault cores are characterised by higher connectivity.

In 2D, for a given area, fracture connectivity can be measured as the fractional connected area (FCA), that is the area within the clusters of interconnected fractures compared to the total sampling area in per cent (Ghosh and Mitra, 2009, Fig. 1.2e). Fracture connectivity can also be quantified using intersection point density (e.g. Manzocchi, 2002; Micarelli et al., 2006a; Sleight, 2001, Fig. 1.2c). Intersection point density can be quantified for: a) each interconnected cluster, b) unit area, or c) each fracture.

Another important fault zone parameter is the aspect ratio of fractures within the damage zone. The aspect ratio is the ratio between the height and the length of the fractures (Kim and Sanderson, 2005; Schultz and Fossen, 2002, Fig. 2.13). This parameter can control modelled values of fracture connectivity as, for example for two fractures with equal heights, the one that is more elongated than the other is more likely to intersect other fractures producing higher fracture connectivity values. Based on structural observations of 3D exposures of fractures in damage zones, of faults located within sandstones, in the Goblin Valley, Utah, Schultz and Fossen (2002) estimated that the aspect ratio of fractures typically ranges between 1/1 and 1/10.

Other authors who studied the quantitative properties of fracture and vein patterns found that the cumulative frequency versus vein thickness and cumulative frequency versus aperture show a power-law distribution, while vein spacing is following an exponential function with negative slope (McCaffrey et al., 2003).On the contrary, Gillespie et al. (2001) found that

veins also show power-law spatial distribution; however, veins and fractures can have very different spatial and scaling properties.

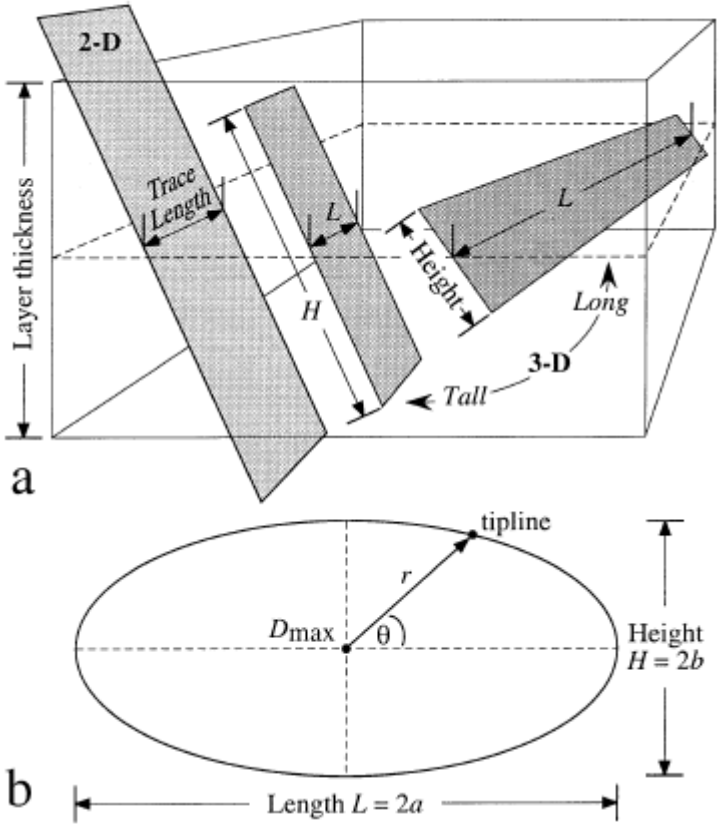

Figure 2.13 - 3D visualization of fractures with different aspect ratios
(from Schultz and Fossen 2002)

2.3.3. Complex fault zone architectures

Although classic fault zone models describe fault zones as being made of three distinct fault zone domains (fault core, damage zone, protolith, Chester et al., 1993), many faults in nature were observed to display more complex architectures due to the development of multiple strands of fault cores (e.g. Faulkner et al., 2003), by the presence of subsidiary faults in the damage zones (e.g. Mitchell and Faulkner, 2009), due to fault zone asymmetry and fault attribute variations along strike and dip (e.g. Billi et al., 2003).

Complex fault cores

Based on structural observations at the Carboneras fault in Spain Faulkner et al. (2003) described a fault zone with anastomosing strands of fault gouge interlocked with heavily fractured country rocks (Fig. 2.14). The development of this complex, more diffuse fault zone is due to the host rock, as the Carboneras fault is located within phyllosilicate-rich material, as opposed to fault zones displaying more localised and less complex architectures in quartzofeldspathic host rocks, suggesting that the geometry of the fault zone is strongly influenced by the host rock (Antonellini and Aydin, 1994).

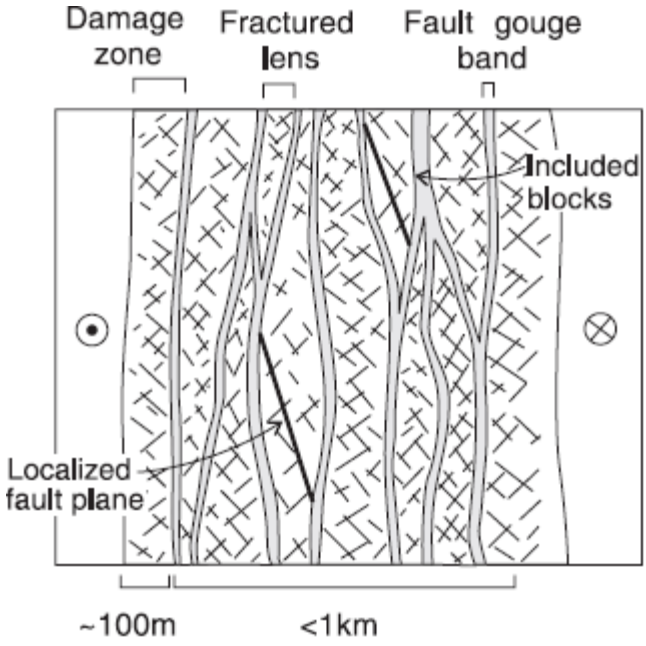

Figure 2.14 - A conceptual model of a fault zone containing a large proportion of phyllosilicate-rich material

The fault is wide and contains anastomosing strands of fault gouge which contain lenses of country rock. The fault may also contain blocks of rock that are more competent than the country rock, and this material may respond differently to the deformation, developing localized fault planes. (from Faulkner et at., 2003)

Complex damage zones

It has been observed that the damage zone of a fault zone, in this case located within carbonates and characterized by a displacement of approximately 800-1000 m, can be subdivided into a weakly deformed damage zone (WDDZ) and an intensely deformed

damage zone (IDDZ) (Micarelli et al., 2003; Micarelli et al., 2006b). The subdivision is based on the values of fracture density. The IDDZ is usually located close to the fault core and is characterised by 3-6 times higher fracture density than the WDDZ, which is located further away from the fault core.

Berg and Skar (2005) were able to subdivide the damage zones of normal faults hosted in sandstones into an inner and an outer zone based on differences in deformation band frequencies. They found that deformation bands are up to a magnitude higher in the inner damage zone, which is located close to the fault core, than in the outer damage zone, located further away from the fault core. Kim et al. (2004) introduced a general subdivision of the damage zones of faults into tip, wall, and linking damage zones based on their relative position to the fault.

Fault damage zones can also display an asymmetric geometry, as described by (Billi et al., 2003), resulting from the development of a *master fault*, the major slip surface, that bounds the fault core on one side; in this case the damage zone can be considerably narrower and less fractured on one side of the principle slip zone than on the opposite one (Fig. 2.15, Berg and Skar, 2005). On the contrary, other authors have suggested that the fault core is bounded by principal slip surfaces on both sides (e.g. Childs et al., 1996, Bonson et al., 2007). The development of these asymmetric patterns can be due to the asymmetric stress field that develops during fault propagation (Berg and Skar, 2005), the irregularities on the fault trace (Aarland and Skjerven, 1998), or the different stress conditions in the footwall and in the hanging wall during faulting (Knott et al., 1996).

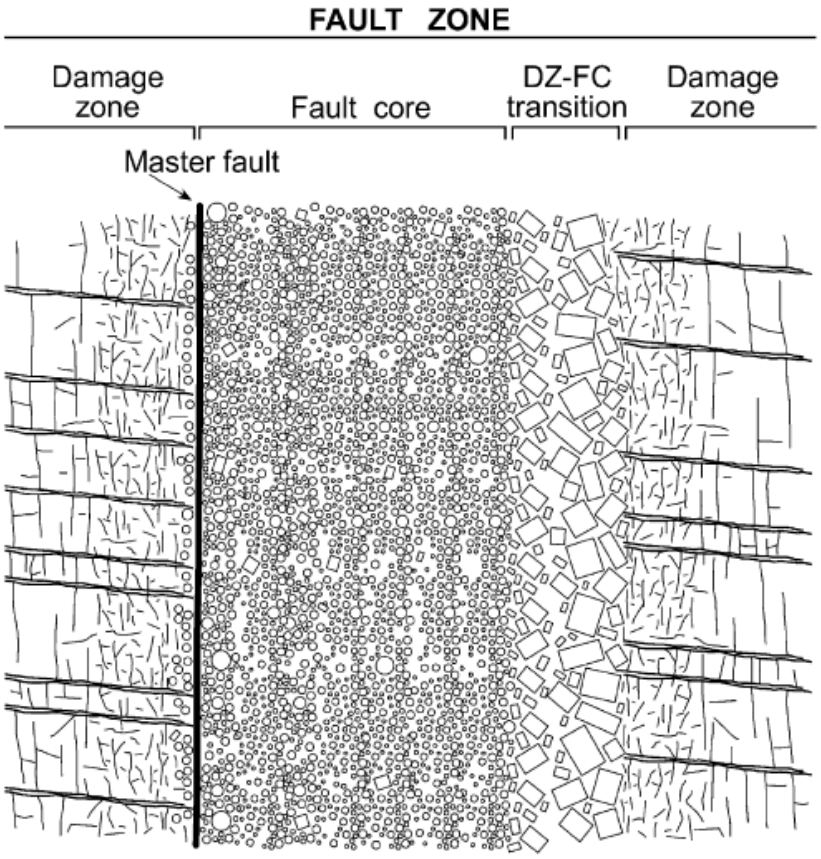

Figure 2.15 - : Conceptual sketch of a fault zone sectioned perpendicular to the shear direction
(not to scale) (from Billi et al., 2003)

Fault zone architecture can vary both along the strike, as a function of displacement, and along the dip of fault planes, as these cut through different lithology. According to models of fault propagation (e.g. in Wilson et al., 2003), where displacements are larger at the centre than at the tip of the faults the damage zone in the central portion of the fault is the most developed when compared to sections which are closer to the tip of the fault. The central segments of faults have been used as good analogues of faults in their mature stage of deformation, whilst the tip segments have been considered as good analogues for the early stages of fault development (Billi et al., 2003; Micarelli et al., 2006a). This assumption can be made because a fault zone is a four dimensional system involving slip along the main fault surface and deformation within a volume around that surface, both of which accumulate through time (Shipton and Cowie, 2001). Lithological control on the fault zone architecture

can be studied by observing dip-parallel variations in quantitative fault attributes, such as the thickness of the damage zone and across-fault variation in density as done by Berg and Skar (2005) within damage zones of a fault located in various Carboniferous to Cretaceous sandstones in Utah, finding different damage zone widths in different lithologies along the same fault.

2.3.4. Fault zones in carbonates

Fault zones in low-porosity, low-permeability carbonates can somewhat differ from fault zones in other lithologies (e.g. Agosta and Aydin, 2006; Agosta et al., 2007) due to the significant role of pressure solution features (Alvarez et al., 1978; Graham et al., 2003; Groshong, 1988; Peacock and Sanderson, 1995; Willemse et al., 1997), peculiar pore types, such as vugs, molds, fractures and channels (Lucia, 1999; Wang, 1997) and finally their unique deformation mechanism related to dissolution, transportation and deposition of host rock materials (e.g. Agosta et al., 2007; Graham et al., 2003; Salvini et al., 1999; Willemse et al., 1997). However, it is important to note that the general architecture of faults, developed within carbonate host rocks are similar to faults developed in other host rocks and the classical fault zone models of Sibson (1977) and Chester et al (1993) can be applied to these faults as well.

Mimran (1975) highlighted the importance of mechanical compaction in chalk samples, collected at the Dorset coast of the UK. It has been shown that mechanical compaction due to differential stresses can lead to a loss of approximately 20% of the initial porosity. This process can also be seen on the amount of complete coccoliths, whose number significantly reduced during mechanical compaction. Furthermore, Mimran (1975) also highlighted the importance of pressure solution. During the deformation of chalk pressure solution is usually

following mechanical compaction as the pore space is reduced and further compaction can only be achieved by pressure solution, leading to transportation of the calcite within the host rock. The total volume loss achieved by the two deformation stages can be as high as 70% (Mimran, 1975).

Graham et al. (2003) refer to a pre-phase and four syn-phases of normal fault development in thrust fault carbonates. The pre-phase is the development of pressure solution surfaces, whose orientation is always perpendicular to σ_1. The actual faulting process is summarized in four stages. The first one is the shearing of bed-parallel and bed-perpendicular solution surfaces and the formation of oblique solution surfaces. This stage does not produce significant offset. The second stage is a an increased slip that results in fragmented rock by linkage of pre-existing solution surfaces with the oblique solution surfaces, produced during stage 1. This stage can produce a total offset of approximately 20 cm. Stage three is the shearing and linkage of fragmentation zones in adjacent mechanical layers and formation of breccias and eventually discrete slip surfaces. This stage can lead up to 10 m of offset. The final, fourth stage is the development of a mature fault zone with well-defined fault surface(s), cutting across multiple mechanical layers and forming a fine-grained fault rock. This stage can lead to offsets well over 10 m, and in some cases it can lead up to km-scale displacements (Graham et al. 2003).

Fluids present in carbonates can highly enhance the transportation of calcite and this can lead to the healing of the fractures present (e.g. Agosta et al., 2007; Graham et al., 2003; Salvini et al., 1999; Willemse et al., 1997). Egeberg and Saigal (1991) showed that the calcite that healed fractures in North Sea oil fields are locally derived from the host rock that has precipitated in the fractures spaces.

Finally, Agosta and Aydin (2006) summarized three main deformation features that can develop along faults in carbonates such as a) throughgoing slip surfaces and fault breccia that initiated by echelon joints and were later sheared, producing cross joints, which broke up the joint-bounded bridges (Mollema and Antonellini, 1999), b) faults developed entirely by pressure solution-based mechanism (Graham et al., 2003) with the shearing of the pre-existing bed-parallel and bed-perpendicular pressure solution seams, producing oblique pressure solution seams in their contractional quadrant; and by continued deformation, the isolated blocks were linked together by thoroughgoing breccia and slip surfaces, and finally c) are deformation features developed as a combination of the previous two cases occurred (Willemse et al., 1997). Although these deformation features are unique to carbonate hosted faults, faults in carbonates can also be host other deformation features discussed further up in the text.

2.4.Transport properties of fault zones

The main attributes controlling fluid flow in a finite volume of faulted rocks are the fault zone transport properties. Fluid flow across and parallel to fault zones is a function of the host rock permeability (e.g. Mallon, 2008; Mallon et al., 2005), and the fault rock permeability in the fault core and in the damage zone (Wibberley and Shimamoto, 2003). Hence, fluid flow is significantly influenced by the fault zone internal architecture and, in particular, by the nature and distribution of fault rocks in the different fault zone domains (Caine et al., 1996; Chester and Chester, 1998; Chester et al., 1993; Collettini et al., 2009; Lockner and Beeler, 1999; Seront et al., 1998). Specific sets of faults and associated deformation features may act as conduits or barriers for fluids migrating through the upper crust (Caine et al., 1996; Sibson, 2000). Based on field observations and laboratory

experiments, fault cores are generally considered as barriers for migrating fluids, whilst damage zones are considered as conduits (Caine et al., 1996, Fig. 2.16). Fluids may be preferentially transmitted along fault-parallel fracture corridors, forming conduits, whilst, at the same time, being retarded by across-fault barriers, such as fine-grained fault gouges developed in the fault core (Byerlee, 1993). This is due to the fact that fault cores are often characterized by reduced porosity and permeability, compared to the surrounding damage zone and protolith rocks, due to the intense grain size reduction and/or mineral precipitation; on the other hand, fractures developed within the damage zones (e.g. veins, fractures, subsidiary faults) may enhance the porosity and permeability, favouring fluid flow. However, the assumptions of Caine`s (1996) conceptual model are oversimplified and can be significantly flawed in the presence of heterogeneity and anisotropy in the distribution of fracture patterns within natural fault damage zones and fault cores.

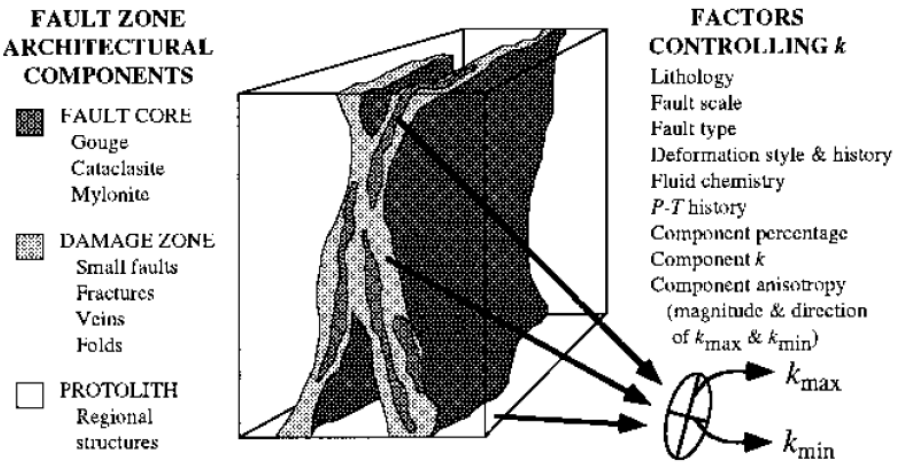

Figure 2.16 - Conceptual model of fault zone with protolith removed
(after Chester and Logan, 1986; Smith et al., 1990). Ellipse represents relative magnitude and orientation of the bulk twodimensional permeability (*k*) tensor that might be associated with each distinct architectural component of fault zone (from Caine et al., 1996)

A key role in controlling fluid flow in damage zones is played by the attributes of fracture patterns such as the orientation distribution (Sleight, 2001), the fracture density (McQuillan, 1973) and connectivity (Ghosh and Mitra, 2009; Odling, 1992), and the fractures aspect ratio

(Schultz and Fossen, 2002). Fault-parallel fracture corridors are usually located in the damage zones, close to the fault cores (Agosta et al., 2007; Micarelli et al., 2006a; Micarelli et al., 2006b) however, fracture corridors can also develop as the initiation of subsidiary faults (Micarelli et al., 2003) and as the damage zone of subsidiary faults (Questiaux et al., 2010). Additionally, high permeability karstic cavities, bedding surfaces an sinkholes can also develop in damage zones (Billi et al., 2007). On the contrary, fault cores are usually assumed to be barriers for fluids due to the presence of fine-grained fault rocks; however, certain fault rocks, such as breccias, can behave as conduits on the microscale (Evans et al., 1997).

Complex fault zone architectures, discussed in Chapter 2.3.3 can largely modify and complicate the relatively simple fluid transmissibility model of Caine et al. (1996) (e.g. Agosta et al., 2007; Bussolotto et al., 2007; Chester and Chester, 1998; Chester et al., 2000; Needham et al., 2008), resulting in fluid transmissibility models showing a great degree of heterogeneity and anisotropy in all directions (e.g. De Paola et al., 2009; Evans et al., 1997; Rowland and Sibson, 2004). Detailed structural analysis of individual faults have led many authors to elaborate fluid flow models which differ significantly from the relatively simple fluid transmissibility model proposed by Caine et at. (1996). These models consider the effects of the development of pulverised fault rocks in the damage zone (Agosta et al., 2007), karstic cavities and sinkholes of the host rock (Billi et al., 2007) and the development of an intensively connected damage zone (Micarelli et al., 2006a). These features can either contribute to the increase fluid transmissibility on one hand, or reduce fluid transmissibility due to the presence of interlayered marl rich units (Billi, 2005), lenses of illite, smectite and previously precipitated large grains of calcite and quartz (Koukouvelas and Papoulis, 2009) and mylonites (Wibberley and Shimamoto, 2003) on the other hand.

Impermeable seals can also develop along subsidiary faults and associated fractures within the damage zone creating compartments that can contain fluids under different pressures (Byerlee, 1993). Brittle cataclasis during faulting causes grain size decrease, reducing the overall porosity and permeability in the fault core. The sealing properties of faults play an important role in creating reservoirs (Yielding et al., 1997). Faults can act as seals in the four following cases: 1) juxtaposition in which reservoir rocks are juxtaposed against a low-permeability unit, 2) clay smear into the fault plane, 3) cataclasis that causes grain size reduction therefore a decrease in permeability, 4) diagenesis (Knipe, 1992; Watts, 1987). Fault seals can lead to fluid overpressure in the fault zones, causing hydrofracturing and hydraulic brecciation of the host rocks. Although this classification is widely accepted it should be noted that due to the presence of several slip surfaces within the same fault smearing might not be that effective, therefore compartmentalization of fault zone might not occur that effectively.

Fracturing in the damage zone, and cataclasis in the fault core can lead to the development of the dual, conduit-barrier behaviour of faults (Caine et al., 1996). Aydin (2000) lists three different fault zone permeability structures (Fig. 2.17) that can develop within a fault zone. The first type of structure is pure permeability decrease (barrier-type behaviour, Fig. 2.17a). The amount of decrease is a usually a function of the host rock (Caine et al., 1996; Knipe et al., 1998), and in high porosity sandstones it can be as high as two to four magnitudes (Antonellini and Aydin, 1994; Antonellini et al., 1999). The second structure is a dual model (conduit-barrier-type behaviour, Fig. 2.17b). This model is similar to the one introduced by Caine et al. (1996) with the fault core behaving as a barrier, while the surrounding damage zone behaving as a conduit. The permeability in the fault core can be up to 4 orders of magnitudes lower than the surrounding host rock, while the damage zone permeability can

increase by 1 order of a magnitude compared to the host rock (Jourde et al., 2002). Finally, the third structure describes pure increase (conduit-type behaviour, Fig. 2.17c) where the amount in permeability increase depends on porosity of the fault zone (Aydin, 2000).

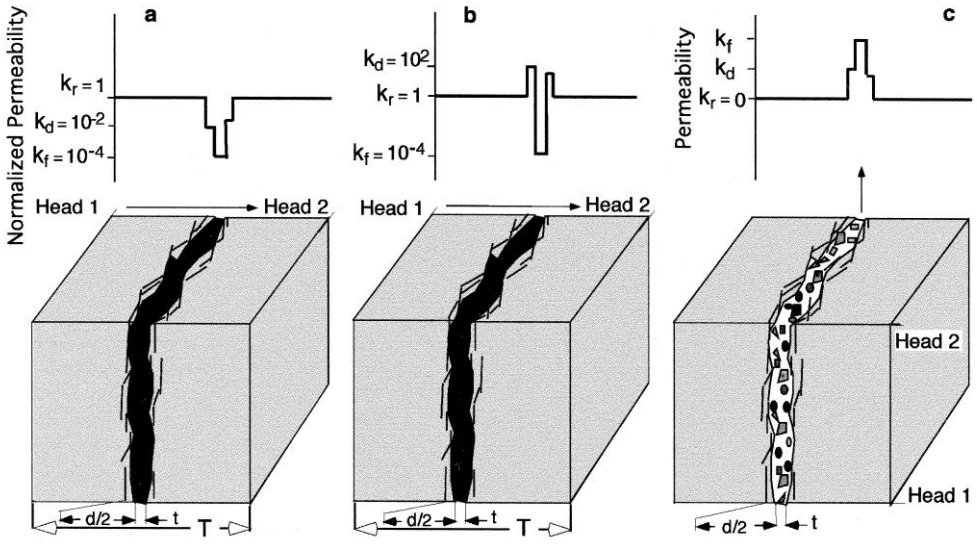

Figure 2.17 - Idealized fault architectures and corresponding permeability structures (a) A deformation-band fault zone with reduced permeability in a direction perpendicular to the fault. The degree of permeability reduction depends on the lithology of the rock but on average the reduction is two to four orders of magnitude with respect to that of the rock matrix. (b) A fault developed by shearing across a joint zone. Fault rock formed by this process is similar to that of the deformation band process but it is surrounded by a damage zone, more permeable than the parent rock. (c) A brecciated fault zone filled with hydrocarbon. The permeability depends on the porosity of the zone and the ratio of the fault thickness to particle radius (after Aydin, 2000)

Laboratory measurements on samples, collected from different fault zone domains, showed that the permeability of fault cores, built up of gouges and cataclasites, can reduce 3-4 orders of magnitudes compared to the host rock, while breccias in the fault cores can increase permeability by up to two magnitudes (Antonellini and Aydin, 1994; Mizoguchi et al., 2008). In comparison, the permeability of the damage zone is sometimes measured to be increasing with one magnitude compared to the host rock (Evans et al., 1997), while in other cases it is measured to be slightly decreasing (Seront et al., 1998).

The transport properties of faults are not constant, but evolve with time and space (Allan, 1989; Bouvier et al., 1989; Harding and Tuminas, 1988; Knipe et al., 1998; Smith, 1980).

Faults are initially forming as conduit fracture corridors, but as their fault core develops they evolve into barriers (Roberts et al., 1996). The permeability of seismically active fault zones is also strongly affected by the fault's position in the earthquake cycle. During earthquakes permeability increases, but then fault rocks, such as breccias, reseal the system. Woodcock et al. (2007) studying the Dent fault in NW England found that may breccias reflect only a single phase of brecciation. After reseal the newly developed breccias get stronger than the intact country rocks and subsequent brecciation is inhibited within the newly deformed rock volume.

Carbonates are typically low porosity (5-20%), low permeability ($< 4 \times 10^{-20}$ m^2) rocks and can act as an effective seals for fluids in the subsurface (Mallon et al., 2005). Once fractured, however, chalk can develop significant amounts of fracture porosity and may become highly permeable, up to 10^{-12} m^2 (e.g. Frykman, 2001; Scholle, 1977).

Understanding the complex internal architecture and transport properties of fault zones has a great scientific and economic importance. Overpressure of fluids in fault zones can lead to (periodic) earthquake nucleation (Miller et al., 2004), and also earthquake nucleation can lead to the migration and release of fluids (Sibson, 1992; Sibson, 2000; Sibson et al., 1975; Sibson and Rowland, 2003). High permeability fault zone domains can provide flow paths for fluids migrating in the upper crust, but also can behave as fractured hydrocarbon reservoirs or aquifers. In onshore, fractured chalk forms an important aquifer for water suppliers, for example in East Yorkshire (Price, 1987), while some large oil reservoirs occur in highly fractured rocks chalk (e.g. Ekofisk, Skjold and Dan fields, North Sea, Egeberg and Saigal, 1991; Jensenius, 1987), and some reservoirs are also potential sites for sub-surface CO_2 sequestration and storage in the future (Wilson et al., 2007).

3. Flamborough Head

3.1.Introduction

Natural fault zones are thought to comprise three main domains a fault core, a damage zone and a protolith (Chester et al., 1993; Sibson, 1977). Dip-slip fault systems, hosted in low-porosity carbonates, can display significant differences in the extent and intensity of fracturing in the footwall and the hanging wall damage zones. Such asymmetric patterns may develop through fault propagation (Berg and Skar, 2005), resulting from different stress field conditions in the footwall and hanging wall during faulting (Knott et al., 1996), or from the varying displacements occurring along faults, with irregular traces (Aarland and Skjerven, 1998).

Classical fault zone models predict that fracture density and connectivity monotonically decreases moving away from the fault core (e.g. Chester et al., 1993, Sibson, 1977). However, based on structural observations and quantitative analyses of the variation of fracture density along 1D structural transects. Micarelli et al. (2003, 2006a, 2006b) found that in faults hosted in carbonate rocks, these parameters may vary in a more complex fashion. They subdivided the damage zone of a fault zone, hosted in low-porosity carbonates, into a weakly deformed damage zone (WDDZ) and an intensely deformed damage zone (IDDZ), based on the variation of fracture density values. According to their subdivision, the IDDZ is located closer to the fault core and it is characterised by higher fracture density values than the WDDZ, located further away from the fault core.

It is well known that the transport properties of fault zones are controlled by their internal architecture, and fluid transmissibility can vary significantly within the different fault zone domains (Caine et al., 1996). Fluid transmissibility is primarily controlled by the nature and

distribution of both the host and the associated fault rocks (Antonellini and Aydin, 1994; Caine et al., 1996; Chester and Chester, 1998; Chester et al., 1993; Collettini et al., 2009; De Paola et al., 2008; Faulkner et al., 2003; Lockner and Beeler, 1999; Seront et al., 1998), and also by the density (McQuillan, 1973), connectivity (Odling, 1992) and orientation distribution (Sleight, 2001) of fractures within the different fault zone domains.

Specific sets of faults and associated fractures may act as conduits or barriers for fluids migrating in the upper crust (Caine et al., 1996; Sibson, 2000). Fluids may be preferentially transmitted along fault-parallel fracture corridors that can provide migration routes for fluids, i.e. acting as conduits (Evans et al., 1997); as well as being retarded by across-fault barriers. In this latter case, brittle cataclasis, which causes grain size reduction, can reduce the overall porosity and permeability of the fault core (Antonellini et al., 1994; Byerlee, 1993).

Chalk is typically a low porosity (5-20%) and low permeability ($<4x10^{-20}$ m^2) carbonate rock and it can act as an effective seal for hydrocarbons in the subsurface (Mallon et al., 2005). However, once fractured, chalk can develop significant amounts of structural porosity and may become highly permeable, up to 10^{-12} m^2 (e.g. Frykman, 2001; Scholle, 1977). The faults and associated fracture patterns developed within chalks are known to exhibit great variability in fault attributes such as fracture density and connectivity e.g.(Agosta and Aydin, 2006; Aydin, 2000; Tondi, 2007). This has important applications for the hydrocarbon industry, as some large, North Sea oil reservoirs occur in fractured chalk (e.g. Ekofisk, Dan, Skjold fields). Laboratory measurements showed that structural porosity in fractured chalks can be as high as 30%, and heavily fractured chalk is generally accepted to be a good reservoir rock (e.g. Odling, 1999, Egeberg and Saigal, 1991). These reservoirs can also be potential target sites for sub-surface CO_2 sequestration and storage in the future (Wilson et

al., 2007). In onshore regions, adjacent to the North Sea, chalk forms an important, strategic aquifer for water suppliers, for example in East Yorkshire (Price, 1987).

In this chapter a case study from coastal exposures of fractured chalk at Flamborough Head, Yorkshire is presented. These outcrops are likely to be representative of sub-surface chalk reservoirs in nearby onshore and offshore regions, e.g. the North Sea. The architecture, geometry and associated fracture and vein density and connectivity patterns of naturally developed fault zones and fracture/vein networks in chalk were characterized. These fracture networks comprise small (cm-scale offsets) and large displacement faults (offsets up to a few tens of meters).

Field and microstructural observations on fault patterns at a range of scales and in different lithological host rocks were integrated with quantitative analyses of fracture/vein density and connectivity across the studied fault zones using 1D, 2D and 3D methods (see Chapter 1.3). These data are discussed in terms of their potential controls on subsurface fluid flow in fractured reservoirs. Additionally, LiDAR based 3D models of fracture/vein networks, characterized by different aspect ratios, were created. The variations of fracture/vein density and connectivity were compared to 1D and 2D results, in order to validate the different 3D models and to estimate the mean aspect ratio of fractures/veins in the fault damage.

3.2.Geological setting and study areas

Flamborough Head forms part of the Yorkshire coast in the UK, located north of Bridlington (Fig. 3.1), at the eastern termination of the E-W trending, extensional Howardian-Flamborough Fault Belt (Fig. 3.1a). This fault belt forms the southern boundary of the inverted, Mesosoic Cleveland Basin and the northern boundary of the Market Weighton

Block (Hawkins and Aldrick, 1994; Kirby and Swallow, 1987). The Howardian-Flamborough Fault Belt was initially active during the Late Jurassic-Early Cretaceous, and was later reactivated as a network of thrust fault between the Late Cretaceous and the Tertiary (Kirby and Swallow, 1987).

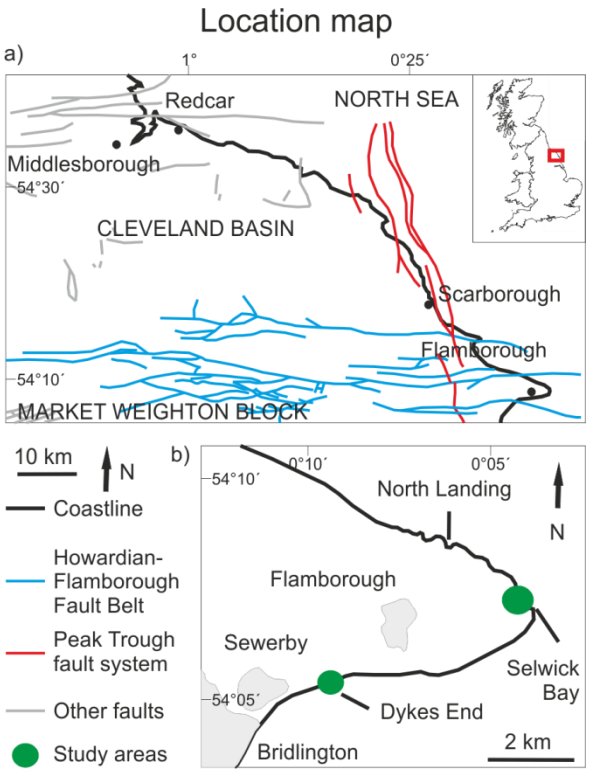

Figure 3.1 - Location map

a) Location map and geological setting of Flamborough Head, b) study areas (modified after Peacock and Sanderson, 1994)

The southern termination of the Peak Trough faults is also located close to Flamborough Head (Fig. 3.1a). This N-S trending extensional fault system was also reactivated during the inversion of the Cleveland Basin, during the early Tertiary (Milsom and Rawson, 1989). The Flamborough Head area, being located at the intersection of the Howardian-Flamborough Belt and the Peak Trough, has experienced deformation phases including both N-S (during the Late Jurassic-Early Cretaceous) and E-W (during Tertiary) extension and inversion related reactivation.

The well exposed cliff sections at Flamborough Head make it a particularly suitable site for studying fault and associated fracture systems in chalk. First studied geologically by Lamplugh (1895), the high (>20 m) cliffs and foreshore are made up entirely of well stratified Upper Cretaceous chalk. The fine grained, low porosity, homogenous beds are between 2 mm and 1.5 m thick (Childs et al., 1996) and at certain areas, are typically interlayered with thin (1-80 mm) clay-rich marly horizons (Lamplugh, 1895).

Outcrop scale, field-based structural studies and microscale diagenetic studies suggest that, after burial to a depth of about 0.8-1.5 km (Hillis, 1995; Stewart and Bailey, 1996), the rocks present in the area, experienced several phases of deformation, producing a wide range of deformation features (Childs et al., 1996; Starmer, 1995). Both Peacock & Sanderson (1994) and Starmer (1995) refer to several phases of Late Cretaceous to Cenozoic extensional and contractional, brittle deformation, based on cross-cutting relationships observed in the field.

Based on preferential cross-cutting relationships and orientation of faults, Peacock & Sanderson (1994) suggested that the small displacement normal faults developed in a triaxial paleostress system, with σ_1 oriented sub-vertical, and the far-field σ_3 is interpreted to have been approximately N-S, but stress release on the large normal faults caused approximately equal horizontal paleostresses in the areas between these large faults, resulting in an approximately 1% extension in all horizontal directions (Peacock & Sanderson, 1994). In comparison, Starmer (1995) interpreted the small displacement normal faults to be Late Cretaceous (100 Ma) to Paleocene ("post-Laramide", 60 Ma) age, developed in a stress field characterized by isotropic horizontal stresses.

Peacock and Sanderson (1994) observed that the characteristic flat-ramp-flat geometries, developed in association with the small displacement normal faults (<20 cm), are lithologically controlled by the presence of marly horizons that are interlayered with the chalk beds in some areas. Additionally, Childs et al. (1996) showed that the offsets of the small displacement normal faults, across adjacent chalk beds, can be controlled by the presence of marl-rich layers, producing a range of different fault geometries, including contractional and extensional jogs, overlaps and bends.

The present study focuses on two locations, where detailed structural observations and 1D and 2D quantitative data collection have been carried out: Selwick Bay and Dykes End (Fig. 3.1b). These localities were selected based on the quality of the exposures which best represents faulting relationships in the region. At Dykes End the cliffs can be studied over a length of several kilometres, while at Selwick Bay the cliffs and foreshore sections are exposed for several hundreds of meter and are extensively incised, providing a good 3D exposure of the structures preserved. Additionally, due to the good 3D exposure of fault zones and fracture patterns, the Selwick Bay study area was chosen to collect LiDAR data for 3D modelling of fracture networks.

At Selwick Bay (which is stratigraphically lower than Dykes End), two main large displacement (up to 20 m of cumulative displacement, Lamplough, 1895), ENE-WSW trending normal fault zones can be observed, which are 4 m apart. At Dykes End, only one large displacement normal fault zone (approximately 1 m of offset) was observed. At both locations, widespread, brittle deformation is accommodated by many small displacement (up to a few cm) normal faults and associated fractures and veins.

3.3.Structural observations

3.3.1. The protolith

The Upper Cretaceous chalk at Flamborough Head is well bedded with an average bed thickness of approximately 25 cm. At Dykes End the chalk beds are often interlayered with clay-rich, marl horizons that have a thickness between a few mm and 3 cm, and their combined thickness makes up approximately 5% of the total outcrop height (Fig. 3.2a). By contrast, at Selwick Bay (Fig. 3.2b), interlayered marl horizons are rare (< 1% by volume) and, when present, have a maximum thickness of 2 mm. At the same time bedding-parallel stylolites are common features at Selwick Bay, but rare at Dykes End (Fig. 3.2a-b). Closer to the fault zones of the larger displacement faults a few sub-vertical to inclined stylolites can also be found at Selwick Bay. Clay-rich, mm-thick films of residual material are commonly observed on stylolitic surfaces.

Optical microscope (OM) observations show that the matrix of the chalk is very fine grained (Fig. 3.2c); the individual grains cannot be resolved even under 50x magnification. Brighter, circular or ellipsoidal zones, with sizes ranging from 10 to 100 µm, have been observed (Fig. 3.2c). These generally appear to be randomly dispersed in the matrix, although they occasionally show a preferential alignment. These brighter spots may represent recrystallized regions of chalk.

Scanning electron microscope (SEM) images show that the matrix is very homogenous, comprising grains with an average size of 50 microns in diameter (Fig. 3.2d). The individual grains do not appear to contain any intragranular fractures.

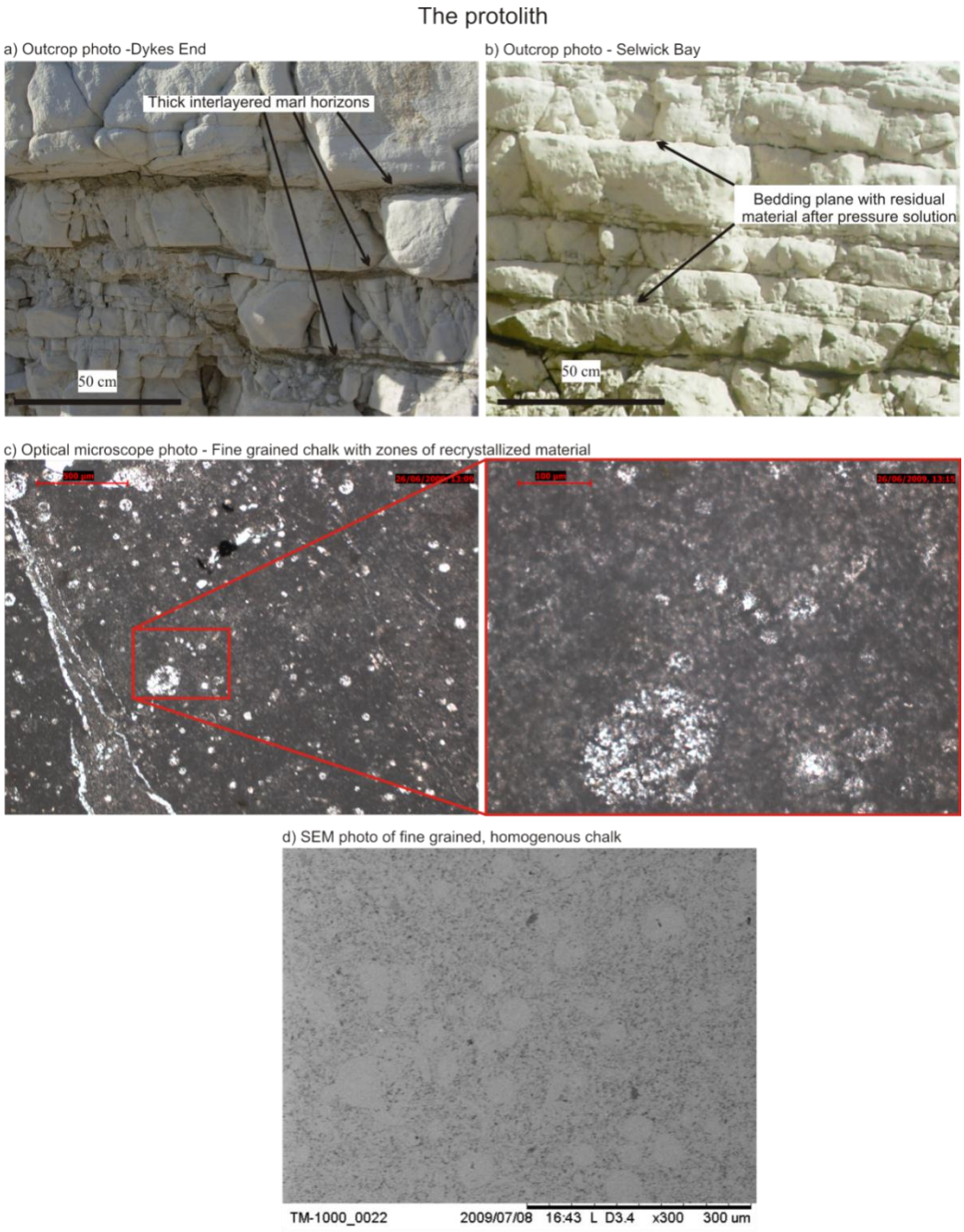

Figure 3.2 - The protolith

at a) Dykes End and b) at Selwick Bay: the thickness of the chalk beds varies from a few mm up to 50 cm. Some sub-horizontal, bedding parallel stylolites are present. Bedding surfaces at Dykes End (a) usually contain interlayered marl horizons with a thickness up to 2-3 cm. At Selwick Bay (b) no interlayered marl horizons are present but those bedding planes that are stylolitic surfaces as well contain residual clay material from pressure solution processes, c) Optical microscope photo showing the protolith with examples of recrystallized chalk, d) SEM photo of the fine grained, homogenous chalk

3.3.2. Small displacement normal faults

The displacements of the small normal faults range from 1 mm to 20 cm. Both at Selwick Bay and at Dykes End they are often organized into apparently conjugate sets of Andersonian fault systems (Fig. 3.3a), where individual faults are observed to be mutually crosscut (Fig. 3.3a-b). At both localities these faults are often characterized by flat-ramp-flat geometries (Fig. 3.3c-d) resulting in the development of dilational and compressional jogs related to the ramp and flat sections, respectively.

Dykes End

The orientations of small displacement normal faults at Dykes End are scattered (Fig. 3.4a), with one major fault set striking NW-SE. Many fractures contain filling of marl (Fig. 3.4b-c, see text below), with no kinematic indicators. It was only possible at a few places to observe some slickenlines that suggest dip-slip to slightly oblique slip, normal kinematics (Fig. 3.4a).

Most of the small displacement normal faults are characterised by flat-ramp-flat geometries (Fig. 3.4b). The ramp sections are mostly located in the chalk beds, while the flat sections follow the interlayered marl horizons (Fig. 3.4b), that represent mechanically weak layers. Dilational jogs, developed along the ramp sections, are either open features, or, partially, filled with clay-rich materials, due to injection and smearing from the interlayered marl horizons (Fig. 3.4c). Compressional jogs, related to the flat sections of the faults, are characterized by intense, local fracturing of the chalk in the hanging wall, with the fractures characteristically organized in a radial pattern (Fig. 3.4d-e). There were no veins or other deformation features suggesting fluid assisted processes at Dykes End.

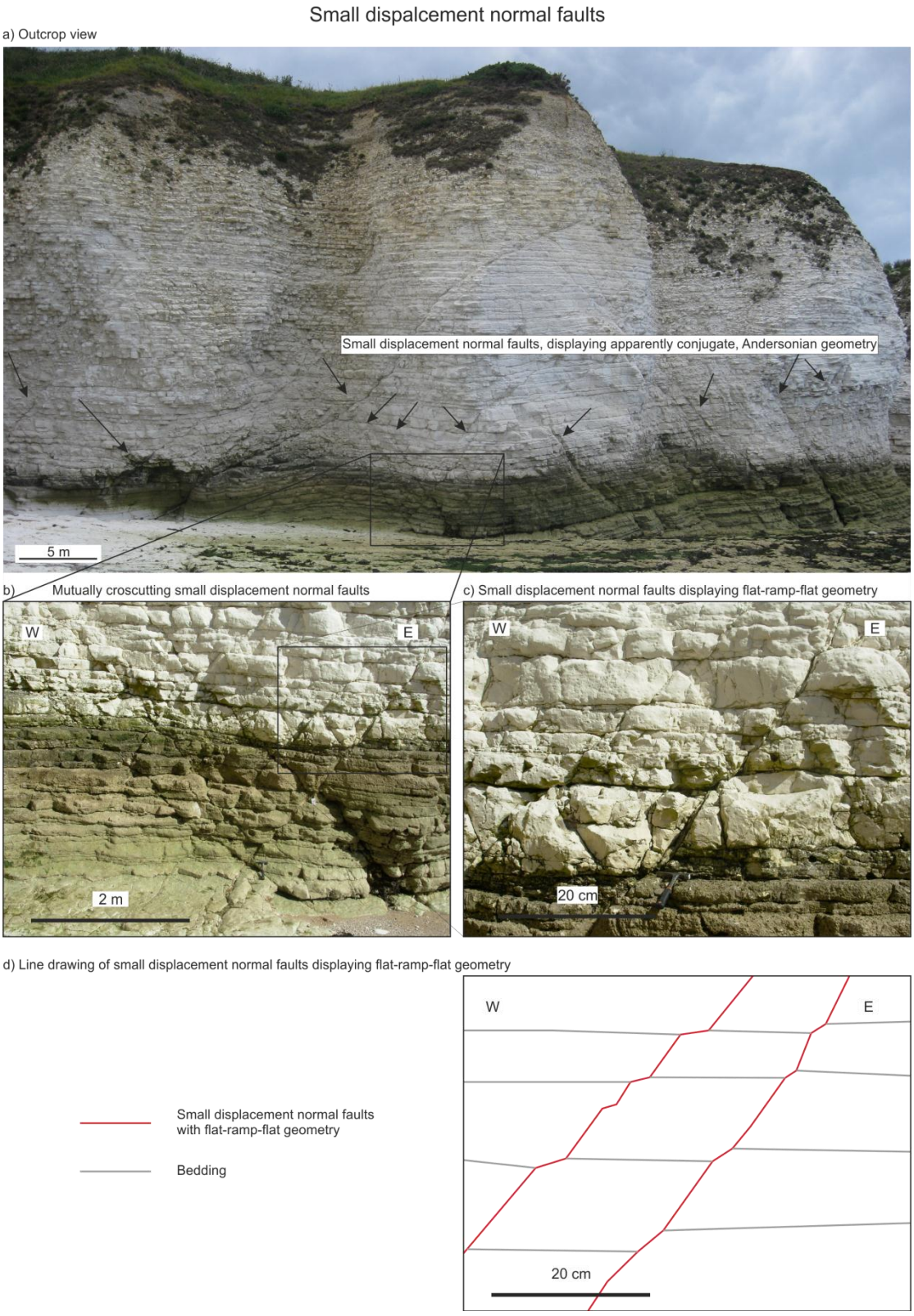

Figure 3.3 - Small displacement normal faults

a) outcrop view with the most prominent small displacement faults (northern cliff, Selwick Bay), b) view of apparently conjugate sets of Andersonian faults on the cliff, c) small displacement normal faults with flat-ramp-flat geometry, d) line drawing of the small displacement normal faults

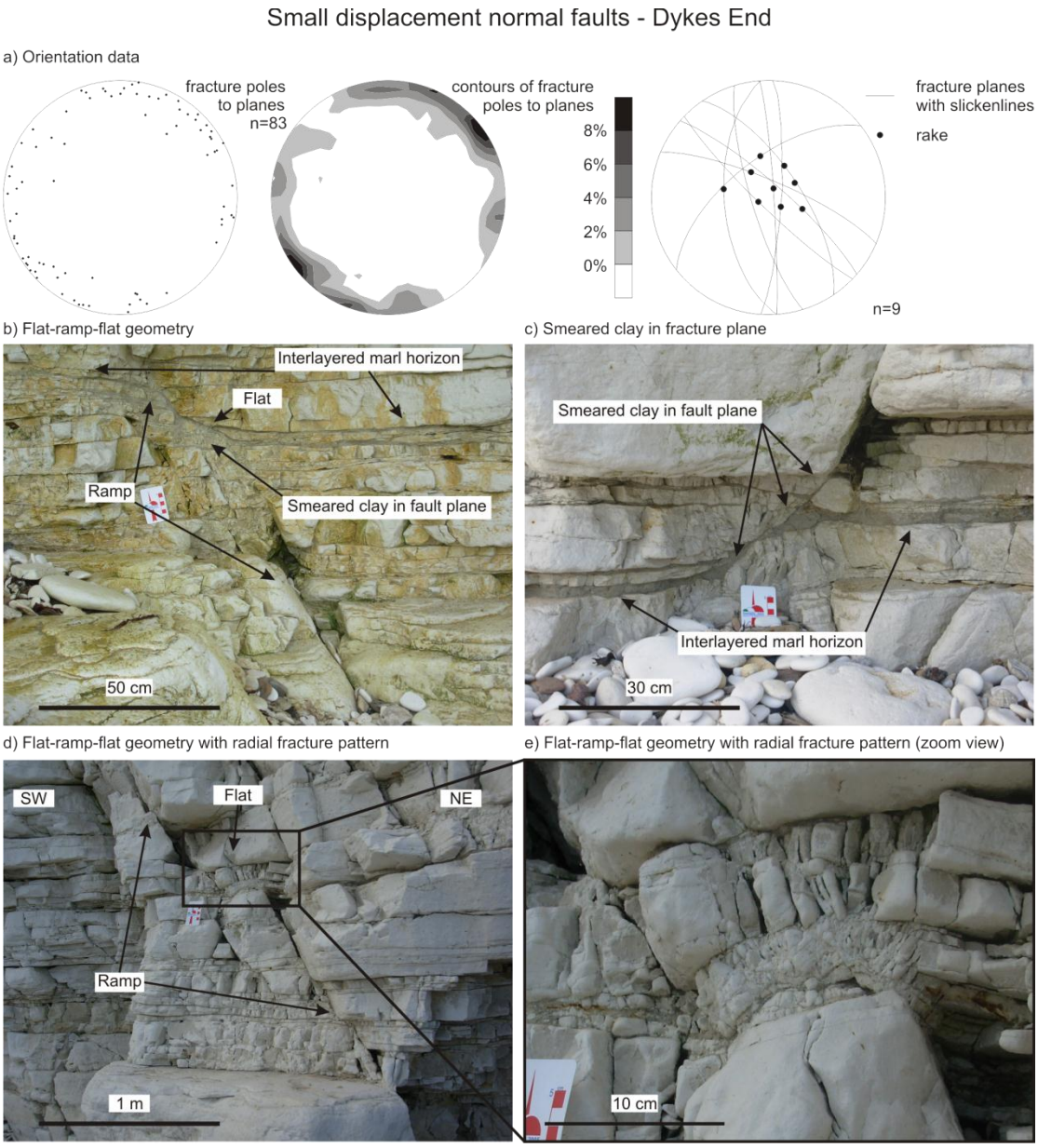

Figure 3.4 - Small displacement normal faults at Dykes End

a) stereonet of the small displacement normal faults at Dykes End with scattered orientation, and one minor NW-SE striking trend, and the slickenline data indicating dip-slip kinematics, b) forming flat-ramp-flat geometry while cutting through chalk and interlayered marl horizons, c) smearing of the interlayered marl horizons into the fracture plane, d, e) open fractures organised in a radial pattern around the flat section

Selwick Bay

The orientations of small displacement normal faults at Selwick Bay are scattered (Fig. 3.5a). Similarly to Dykes End, there is one major set of NW-SE striking fractures, with dips typically greater than 70° (Fig. 3.5a). Kinematic indicators on the fault planes are rarely observed, obliterated by the calcite filling of fractures (Fig. 3.5b-c). Similarly to Dykes End, the few slickenlines, observable on small fault planes, suggest dip-slip to slightly oblique slip kinematics (Fig. 3.5a).

The flat sections of the small displacement normal faults are often located on bedding planes, which are also reactivated as stylolitic surfaces due to pressure solution (Fig. 3.5b-c). Dilational jog structures, developed along small displacement normal faults are almost always (>90%) filled with crystalline calcite (Fig. 3.5c). The widths of the jogs are up to 30 cm, and the individual calcite crystals within the jogs can grow up to 5 cm in length. Angular chalk clasts, found within calcite veins, are 2-3 cm long. Compressional jogs are usually characterized by pressure solution features (Fig 3.5c), with some residual, clay-rich material left undissolved on the stylolite surfaces.

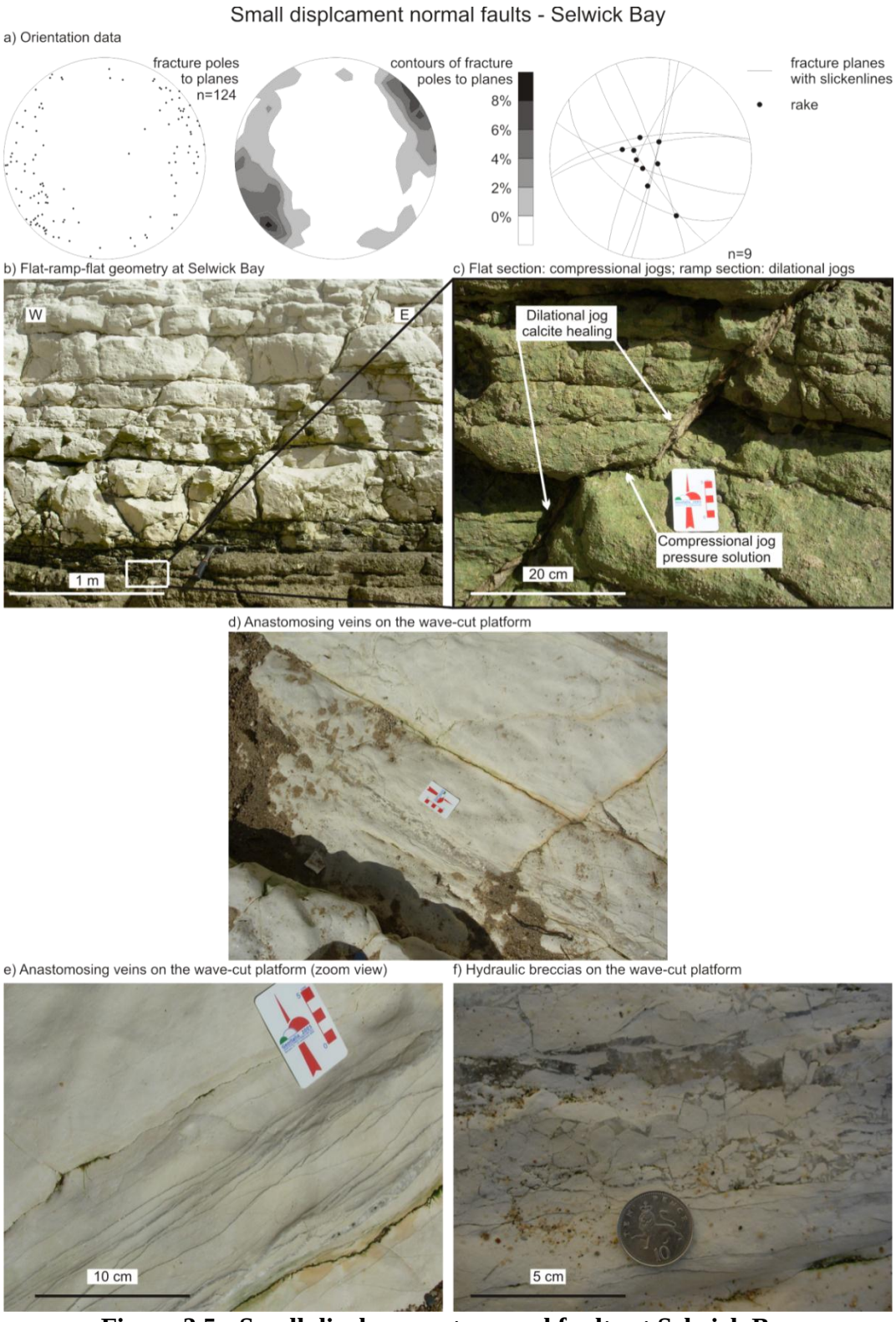

Figure 3.5 - Small displacement normal faults at Selwick Bay

a) stereonet of the small displacement normal faults at Selwick Bay with scattered orientation, and one minor NW-SE striking trend, and the slickenline data indicating dip-slip kinematics, b) flat-ramp-flat geometry, c) ramp section dilational jogs are healed with calcite veins, while flat section compressional jogs are showing evidence for pressure solution with some residual material, d e,) veining zone on the wave cut platform indicating crack-seal mechanism, f) vein with hydraulic brecciation, (notice how the damage increases from the bottom towards the top of the photo)

The small displacement normal faults can also be observed in plain view, on the wave-cut platform in front of the cliffs (Fig. 3.5d-f). Typically, these are made of a braided, up to 0.5 m wide zones of veining (Fig. 3.5d-e), terminating by a series of en-echelon calcite filled fractures. These geometries are very similar to those seen in the "zebra rocks" described by Holland and Urai (2010) in low porosity limestones in Oman. Most individual veins have an average thickness of 1-2 mm, but the thickest can, locally, reach widths of up to 30 cm, and show clear evidences for hydraulic brecciation processes, with white angular wall-rock clasts dispersed in a crystalline calcite matrix (Fig. 3.5f). These textures are thought to form due to the hydraulic brecciation of the host rock, followed by rapid drop in fluid pressure, which causes instantaneous calcite precipitation (Sibson, 2000). In most of the thin veins, the individual calcite crystals cannot be seen with the naked eye, but in the thickest veins they can grow up to 6 cm in length. The orientations of the crystals within the veins do not clearly define weather the veins were formed as hybrid shear/extensional or pure tensile features.

3.3.3. Large displacement normal faults

Dykes End

At Dykes End, a larger, thoroughgoing fault with about 1 m displacement has been observed (Fig. 3.6). The fault has an orientation of 169/50 NE, does not display a flat-ramp-flat geometry, and is characterised by a well developed fault core, where most of the displacement was accommodated (Fig. 3.6a). The fault core is continuous (Fig. 3.6b-c), and varies from 5 to 20 cm in thickness. It is mostly made of a clay-rich gouge, which developed from the smearing of the original marl horizons along the fault plane, but also contains cm-scale clasts of the original host rock dispersed within the clay (Fig. 3.6c-d). Within the gouge a localised slip surface displays several well-developed slickenlines, indicating pure dip-slip kinematics (Fig. 3.6d).

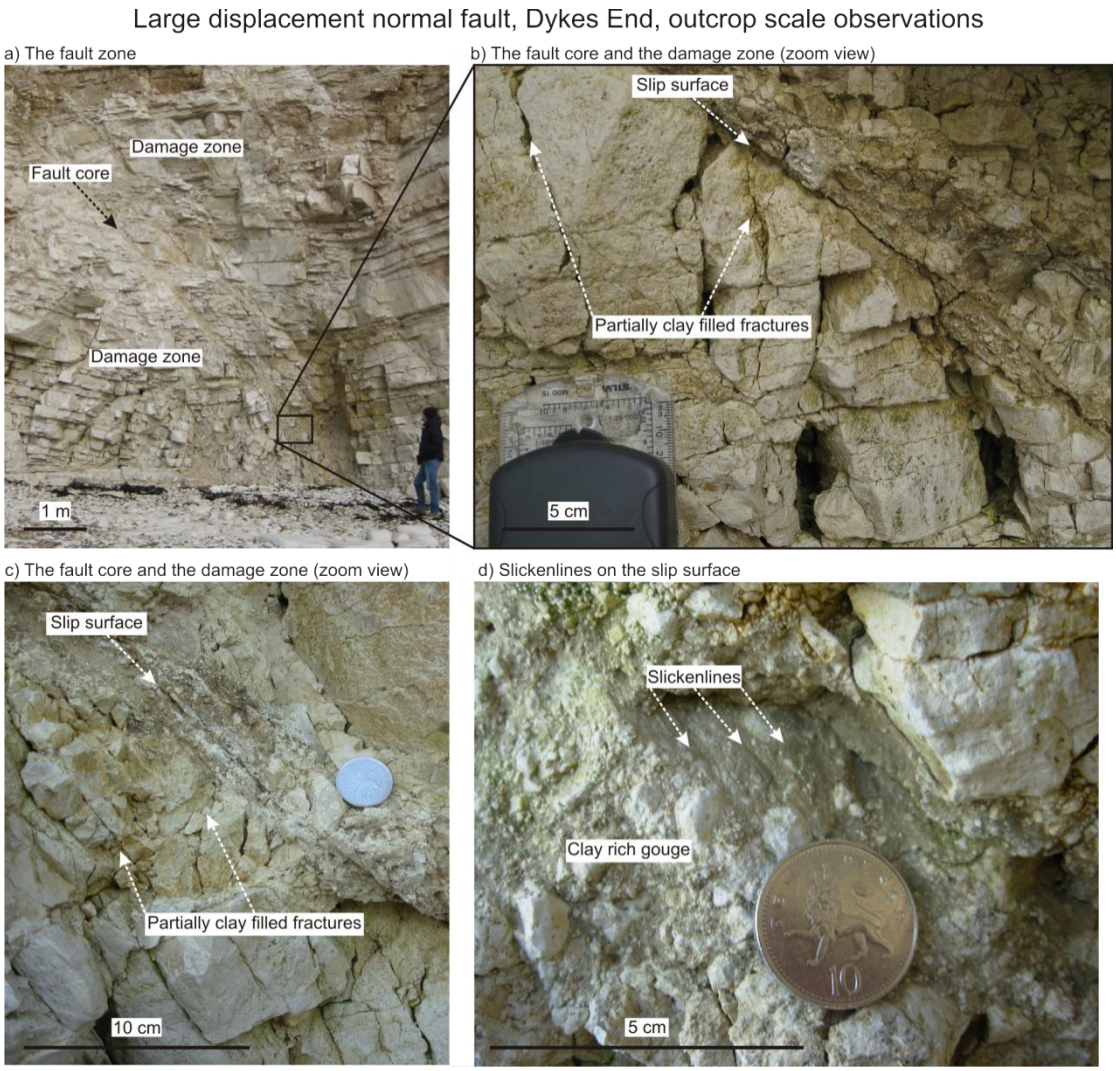

Figure 3.6 - Large displacement normal faults at Dykes End – outcrop scale
a) Fault zone with narrow (<20 cm) fault core and surrounding 3-4 m wide damage zone, b) sharp fault core – damage zone boundary, c) well defined slip surface within the gouge of the fault core, d) slickenlines on the slip surface showing dip slip kinematics

Adjacent to the fault gouge layer, both in the hanging wall and the footwall, a 2-3 m wide zone of damage occurs, characterized by intense fracturing (Fig. 3.6a-b). There is a sharp transition between the gouge layer in the fault core and the surrounding damage zone (Fig 3.6b). Most of the fractures in the damage zone are open and a large proportion of them is sub-vertical (Fig. 3.6a-b). Some of the fractures in the damage zone, particularly those closer to the fault core and/or to the interlayered marl horizons, are partially filled with clay,

intruded into the fracture planes both by smearing and injection. There is no field evidence for veining or other fluid-assisted fracturing processes within the fault core and damage zone.

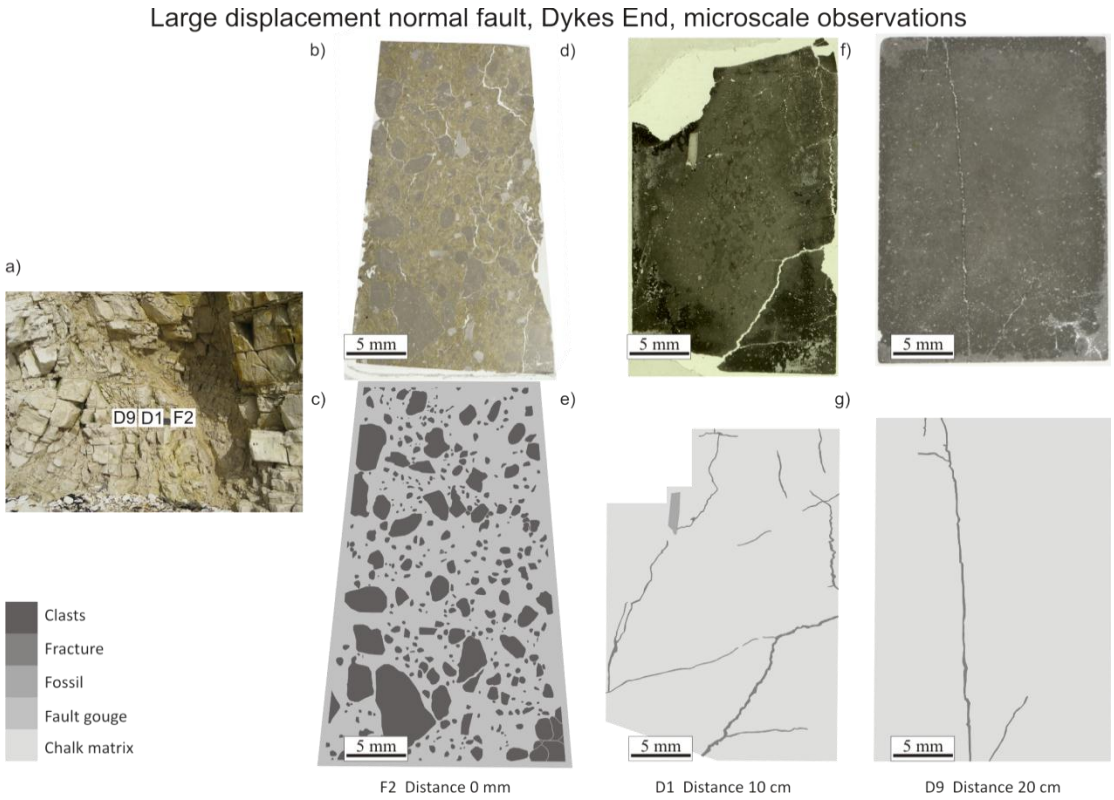

Figure 3.7 - Large displacement normal faults at Dykes End– microscale
a) original location of the thin sections on the outcrop: b, c) F2 sample from the fault core, containing fault gouge and some mm-scale clasts of the host rock, d, e) D1 sample, collected 10 cm away from the fault core, containing some fractures that are clay filled due to the injection on the fault plane, and some stylolites, f, g) D9 sample collected 20 cm away from the fault core, showing one clay filled fracture

Microstructural observations, made on thin sections cut from representative rock samples of the different fault zone domains of the large displacement normal fault show that the fault gouge of the fault core contains chalk clasts up to 4 mm in diameter (Fig. 3.7), dispersed in a very fine-grained matrix made of clays and fine-grained chalk (sample F2, Fig. 7b-c; for sample location see Fig. 3.7a). The chalk clasts are slightly elongated, with rounded edges and are homogenously distributed in the matrix showing no preferred orientation (Fig. 3.7b-c). Thin sections cut from samples taken from the heavily fractured damage zone, 10 cm away from the core (sample D1 in Fig. 3.7a), show the presence of open fractures (Fig. 3.7d-

e). Some of these fractures have originated by the reactivation of stylolitic planes, which can be observed from the 2-3 mm stylolite teeth on the digitized images (Fig. 3.7e). Optical microscope images from samples collected 20 cm away from the slip zone (sample D9 in Fig. 3.7a) showing the presence of less fractures and stylolites (Fig. 3.7f-g).

Selwick Bay

Two large displacement normal faults have been observed at Selwick Bay, both striking ENE-WSW, and dipping steeply (>70°) to the NNW (Fig. 3.8). The fault zones of the normal faults together form a promontory on the cliffs (Fig. 3.8). The faults are located about 4 meters apart, diverging from each other slightly across the foreshore, towards the NE (Fig. 3.8). The north facing fault has a well-defined fault core (hereafter referred as FC) characterized by a slip surface, located within a narrow (up to 10 cm) domain of fault gouge (Fig. 3.8a-b), whilst the south facing fault instead of a fault core, is characterized by an intensely brecciated zone (hereafter referred as IBZ), without a well-defined slip surface (Fig. 3.8a, c). The two faults are surrounded by damage zones that are 4-5 m wide in the footwall, but less than 1 m wide in the hanging wall. The damage zones are characterised by a higher density of calcite veins, when compared to the surrounding regions.

Figure 3.8 - Large displacement normal faults at Selwick Bay – outcrop scale
a) the headland forming the fault zone with the FC and IBZ, b) The FC, with a slip surface and sharp contact with the dragged beds of the hanging wall, c) fault breccias in the IBZ, d) thick (> 5 cm) veins with coarse grain crystals cross-cutting braided, narrow veins, e) thick (10 cm) vein with clear median line

In the hanging wall of the FC, the beds are almost vertical, possibly due to the drag along the fault (Fig. 3.8a-b). Calcite veins are less common in this region compared to the nearby cliff sections. The sub-vertical beds in the hanging wall are in direct contact with the FC. The FC

is made up of two parts: a) a sharp and narrow, 10-15 cm wide, zone of fault gouge with dispersed small (cm-scale) clasts of the original host rock (Fig. 3.8b), containing a slip surface, on which slickenlines indicate dip-slip kinematics; b) an approximately 0.5-1 m thick zone of highly brecciated chalk, which exhibits a transitional boundary with the damage zone that separates the FC and IBZ.

The IBZ is more than 1 m thick, and lacks an obvious slip surface (Fig. 3.8c). The intensity of veining and calcite precipitation in the IBZ is lower than in the surrounding damage zone. The damage zone between the FC an IBZ is characterised by tensile, intense veining in the chalk (several times higher than in the nearby rocks), where veins with both fault synthetic and antithetic dips are present. The present rocks display evidences for intense hydraulic brecciation with 2-3 cm large chalk clasts embedded within calcite cement (Fig. 3.8c). Open fractures are rare, less than 5% of all fractures. The geometry and infilling calcite structure of these veins are similar to those, observed at the small displacement faults at Selwick Bay (Fig. 3.5c-d; Fig. 3.8d). Larger veins have coarse grained crystals that can grow up to 5 cm, and are sometimes characterised by either a well-defined median line in the centre (Fig. 3.8e), or by the development of vuggy textures and cavities. Most of these large veins and vuggy fills locally crosscut the typically braided, smaller veins (Fig. 3.8d).

Like the damage zone between the FC and IBZ, the footwall damage zone of the IBZ is characterized by intense veining and fracturing, which gradually decreases towards the protolith. Further away from the large displacement normal faults, in the protolith, the rocks do not appear to be intensely deformed on the macroscopical scale.

Thin sections, cut from representative rock samples of the different fault zone domains, show the distribution and features of veins across the fault zone (Fig. 3.9, for sample location see Fig. 3.10b). In the samples studied, the width of the veins varies between 5 microns and 10 mm. The samples from the FC (sample S3) and the IBZ (sample S4) contain veins that branch out with an anastomosing, braided geometry, forming fan shapes. These are similar to the veins observed at the small displacement normal faults in other parts of Selwick Bay (Fig. 3.5c-e), and to the zebra rocks described by Holland and Urai (2009) in limestones, in Oman.

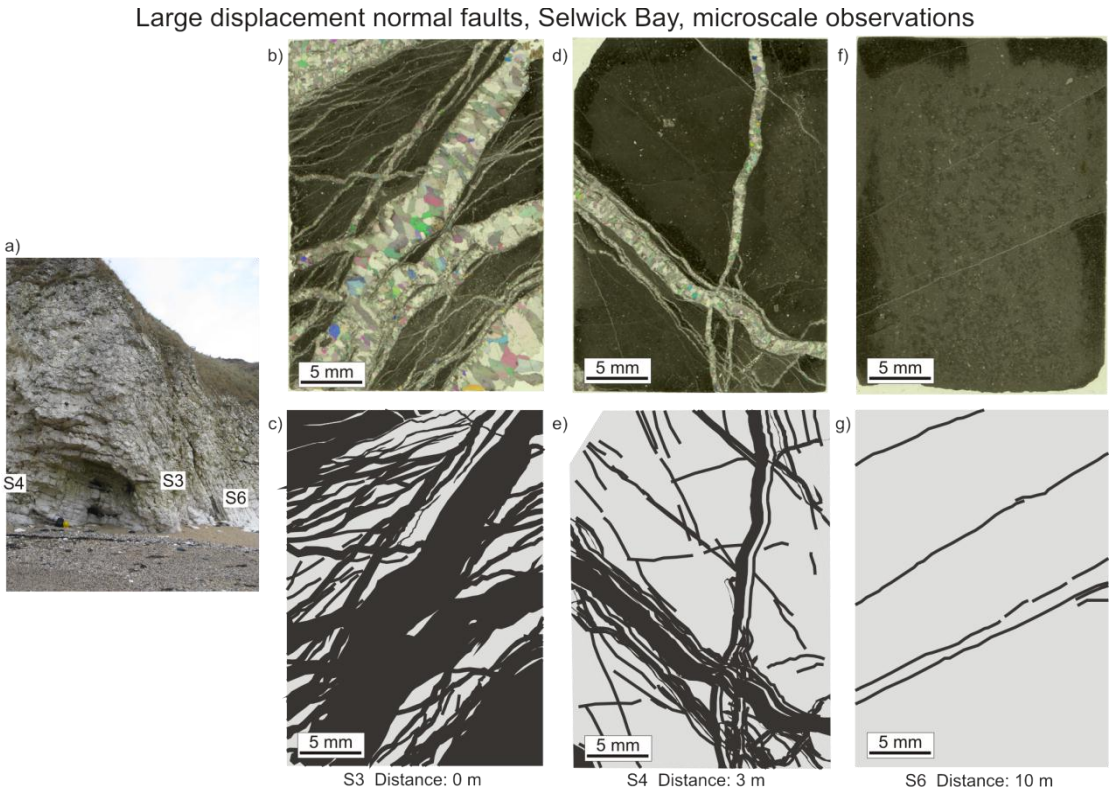

Figure 3.9 - Large displacement normal faults at Selwick Bay – microscale
a) original location of the thin sections on the outcrop b, c) S3 sample from the brecciated part of the FC, showing very high vein density, d, e) S4 sample from the IBZ with intense veining , f, g) S6 sample from the hanging wall protolith with only minor veining

Sample S3 is from the brecciated part of the FC, located in the footwall of the slip surface (Fig. 3.9a-c). It contains several anatomising veins with thicknesses ranging from 0.5 mm to

7 mm (Fig. 3.9b-c). Due to the anatomising geometry, the veins form a fully connected network. Sample S4 was collected from the IBZ (Fig. 3.9a), and contains fewer and thinner veins than S3 (Fig. 3.9d-e). The average width of the veins here is around 1 mm and the average crystal size is around 0.5 mm. In this sample two major vein zones are seem to mutually cross-cut each other (Fig. 3.9d-e). Finally, sample S6 was collected 4 m away from the fault core in the hanging wall (Fig. 3.9a). It shows only a few veins oriented sub-parallel with each other, which do not intersect (Fig. 3.9f-g). In this case the connectivity is low compared to both previous samples described.

3.4. Quantitative analysis of fracture/vein density and connectivity in the fault zones of large displacement faults

3.4.1. Methodological approach

Quantitative fault attribute data, such as fracture/vein orientation, density and connectivity, were collected across the large displacement normal faults at Dykes End and Selwick Bay using three different methods: a) 1D line transects orthogonal to the main fault trend, b) 2D image analysis from high resolution, outcrop scale and microscale photos, c) 3D, Virtual Outcrop Models using LiDAR data.

1D quantitative data were collected along sub-parallel transects, following the procedures explained in Chapter 1.3.1. Most transects were oriented orthogonal to the strike of the faults, both near to the cliffs and, where possible, on the wave-cut platform (N1-N3 at Selwick Bay and N4-N5 at Dykes End, Fig. 3.10). The length of the transects ranged between 10 and 20 m, depending on the thickness of the particular damage zones. For each structural feature (e.g. fractures and veins) intersecting the transect the distance along the transect, the strike,

dip, dip direction, width and nature of the filling material were recorded. Where observed, the fault offset and the rakes were also recorded.

The N1 transect, along the cliff face at Selwick Bay was irregular, due to the shape of the outcrop, with some sections oriented oblique to the fault strike. In this case, the fracture density data were corrected to account for the obliquity between the transect trend and the fault strike, as explained in Chapter 1.3.1. The original transect was divided into three sections, each characterised by a specific acute angle oriented with the fault strike (Fig. 3.10b). The middle section, located in the front of the headland, was oriented orthogonal to the fault strike, therefore no correction was needed. The data collected along the other two sections, running at an angle to the fault strike, were corrected so that they became consistent with those of the middle section. In the two corrected sections the fracture/vein spacing distances, measured along the transect, were modified, as explained in Chapter 1.3.1, resulting in a shorter, virtual transect that runs orthogonal to the fault strike.

2D quantitative image analyses were performed on: a) high resolution digital photos, taken from the exposures of the large displacement normal faults with a constant camera-outcrop distance of 5 m (Fig. 3.10), and b) from thin sections obtained from samples collected from different fault zone domains along the N1 and N5 transects (Fig. 3.10b, d).

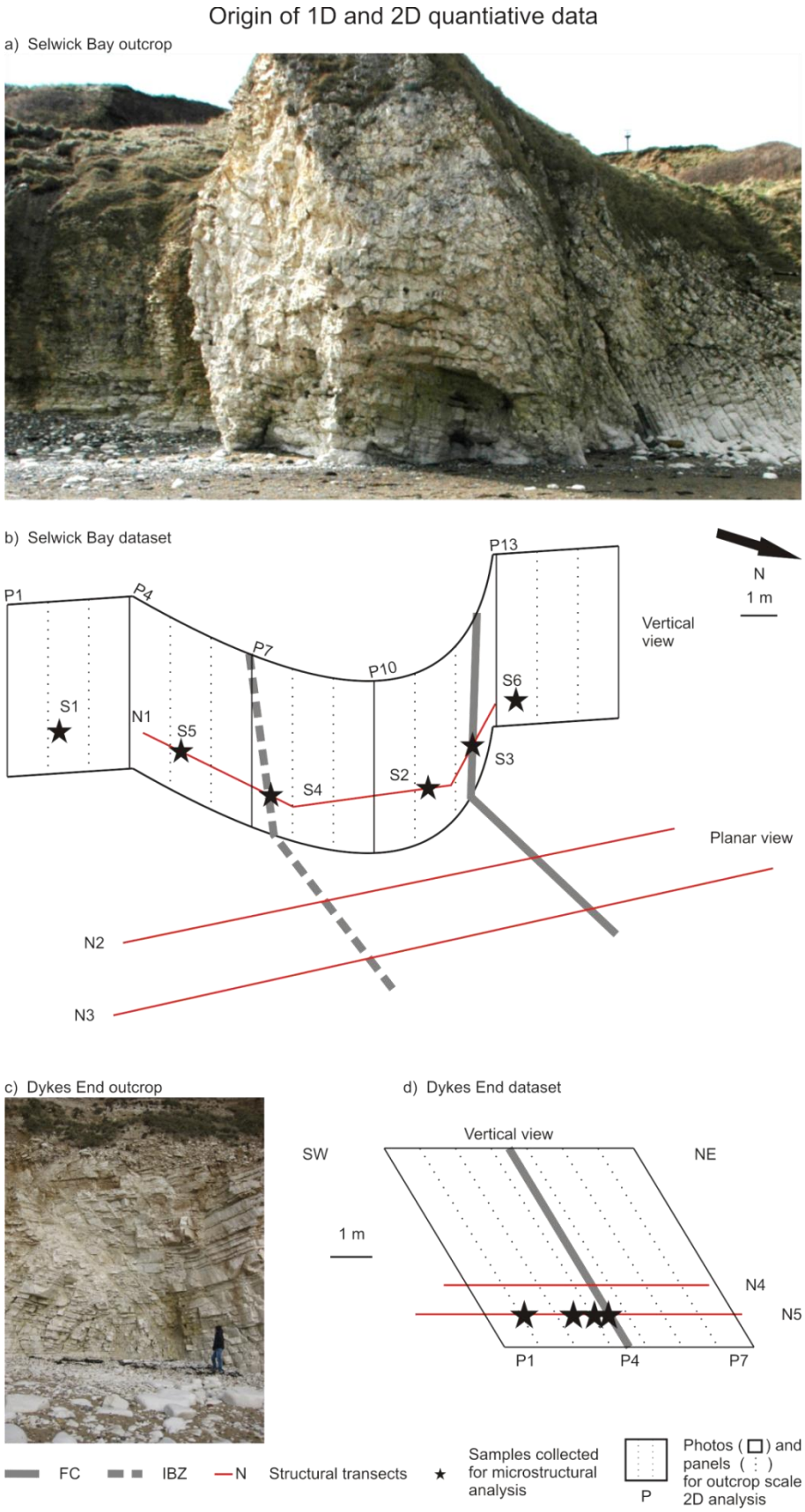

Figure 3.10 - : The 1D and 2D quantitative dataset (transects, photo panels, thin sections)

at a, b) Selwick Bay, c, d) at Dykes End with respect to the location of the large displacement normal faults

In case of Selwick Bay, each photo was divided into 3 different panels ("P"), each panel representing an approximately 1 m wide cliff section (Fig. 3.10a-b) At Dykes End one photo was divided into 7 fault zone parallel panels, each panel representing an approximately 1 m wide cliff section (Fig. 3.10c-d). The fracture and vein density was measured using the total length of fractures/veins within the sampling area (m/m^2), and connectivity was calculated using two different methods: a) intersection point density (IPD) and b) the fractional connected area (FCA), as explained in Chapter 1.3.2.

3D LiDAR data have been only collected for the Selwick Bay large displacement normal fault (Fig. 3.11, for clear pointcloud see Fig. 1.4b). After picking the bounding surfaces of the IBZ and FC as primary features (Fig. 3.11a), the veins of the damage zone were also picked, as secondary features (Fig. 3.11b). Since the IBZ and FC boundaries (i.e. the primary features) were identifiable both on the cliff face and on the wave-cut platform, their bounding surfaces were merged at both places, in order to better constrain their orientations and geometry in 3D. Veins of the damage zone were only picked at the cliff face, as these features were impossible to follow and trace on the wave-cut platform, due to the presence of seaweed. The smallest veins picked from the point cloud were approximately 5 mm wide.

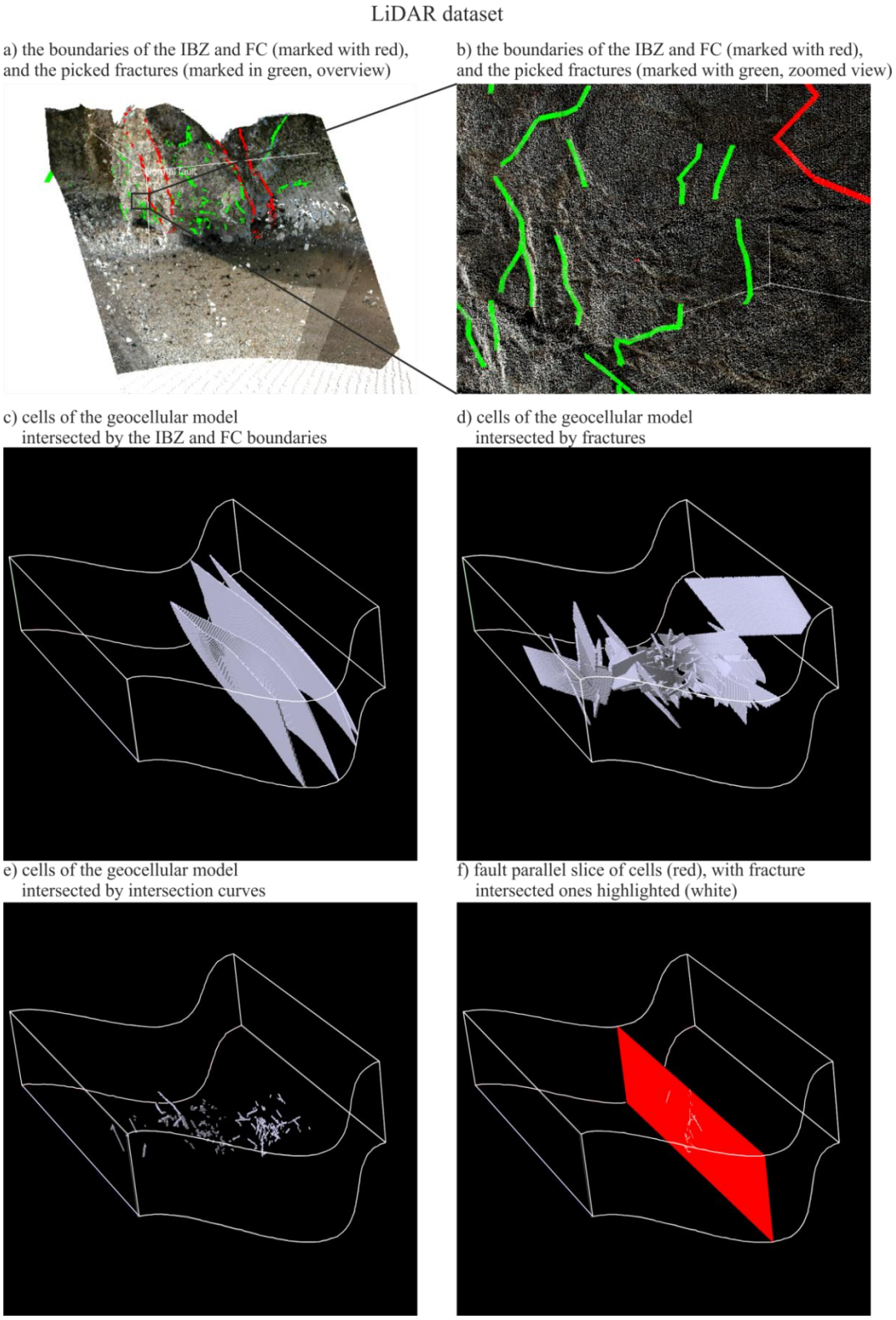

Figure 3.11 - The 3D dataset

a) the boundaries of the IBZ and FC, and the picked fractures (overview); b) the boundaries of the IBZ and FC, and the picked fractures (zoomed view); c) boxes of the geocellular model intersected by the IBZ and FC boundaries; d) boxes of the geocellular model intersected by fractures; e) boxes of the geocellular model intersected by intersection lines; f) fault parallel slice of boxes with those that are intersected by fractures being highlighted

By following the procedure explained in Chapter 1.3.4, the picked polylines were imported to GoCAD, where surfaces were built from them to model the fracture network. First the boundary surfaces of the IBZ and the FC were constructed, in order to be able to create the SGrid with the correct orientation relative to the fault (Fig. 3.11c). The SGrid was oriented parallel with the strike of the faults and one axis was modified with a sin function in order to better fit the shape of the outcrop. Before modifying the shape of the SGrid, the lengths of each side of the cells were 10 cm, and the model was built up of 300 (across fault) x 100 (dip parallel) x 400 (strike parallel) cells. The modification of the shape of the SGrid did not affect the length of the cells in across-fault directions.

Following this step, the planes, representing the veins, were created. Within the SGrid, regions of cells were created that contained either the modelled fracture planes for different aspect ratio models (Fig. 3.11d, as a measure of density) or the intersection lines of fractures planes (Fig. 3.11e, as a measure of connectivity). Across-fault quantification of vein density and connectivity for different aspect ratio models was achieved by using these regions. For every fault parallel slice of the SGrid, and for all the different regions created, the number of cells was counted (Fig. 3.11f). Conversions for number of cells to SI units of vein density (m^2/m^3) and vein connectivity (m/m^3) were done using geometrical considerations explained in Chapter 1.3.4. Because the edge length of the cells was 10 cm, one intersected box was converted into 6.12 cm^2/cm^3 for density values, and 8.66 cm/cm^3 for connectivity values.

Vein density and connectivity across the fault zones were modelled using five different vein aspect ratios models that were 1/1, 1/2, 1/3, 1/5, 1/8. These different models were quantitatively compared with 1D and 2D results, by following the procedures described in

Chapter 1.3.5. Comparison was done in order to validate these different models and to estimate the most realistic aspect ratio of fractures within the damage zone of these models.

Additionally to vein density and connectivity data, orientation data were also collected from the 3D models. Due to problems with data collection on the field, dGPS data were not available for this dataset. As a result, strike data was only available relative to the fault. The strike direction distribution of veins in the damage zone was obtained relative to the strikes of the IBZ and FC. However, dip data were collected in absolute values, as it was possible to define the horizontal plane without the use of dGPS data. In order to make this limited dataset comparable with field-based orientation measurements, orientation data, gained from the LiDAR data, were rotated into an orientation, where the IBZ and FC orientation overlapped with the field measurements. After the rotation, the dip distribution and the scattering of strike values of the veins were compared to field measurements.

3.4.2. Results

3.4.2.1. 1D transect results

Dykes End

The orientation of fractures in the damage zone of the large displacement normal fault at Dykes End is similar to that of the large displacement normal fault itself (Fig. 3.12a). The fault and most of the fractures in the damage zone are oriented NW-SE, with dips greater than 60° (Fig. 3.12a). The few kinematic indicators, observable on the fracture planes within the damage zone of the large displacement normal fault, suggest dip-slip to slightly oblique slip, normal kinematics (Fig. 3.12a).

Quantitative 1D fracture density data are plotted on Figure 3.12b-e, where fracture density variation was plotted with a 1 m window (for transect locations see Fig. 3.10d). Note that the fault cores in Fig. 3.12b-e are represented by a wider zone than its real width, therefore those sections of the graphs are strictly not to scale. Based on measurements further away from the fault zone, the background fracturing was estimated to be approximately 5/m. The damage zone in the footwall (left from the fault core, on the graphs) is 3 m and 2 m wide according to data from N4 transect (Fig. 3.12b) and N5 transect (Fig. 3.12d), respectively. The width of the hanging wall damage zone is 2 m on both transects (Fig. 3.12d). Fracture density, close to the fault core, is higher in the hanging wall (approximately 20/m) than in the footwall (approximately 10/m), (Fig. 3.12b-c).

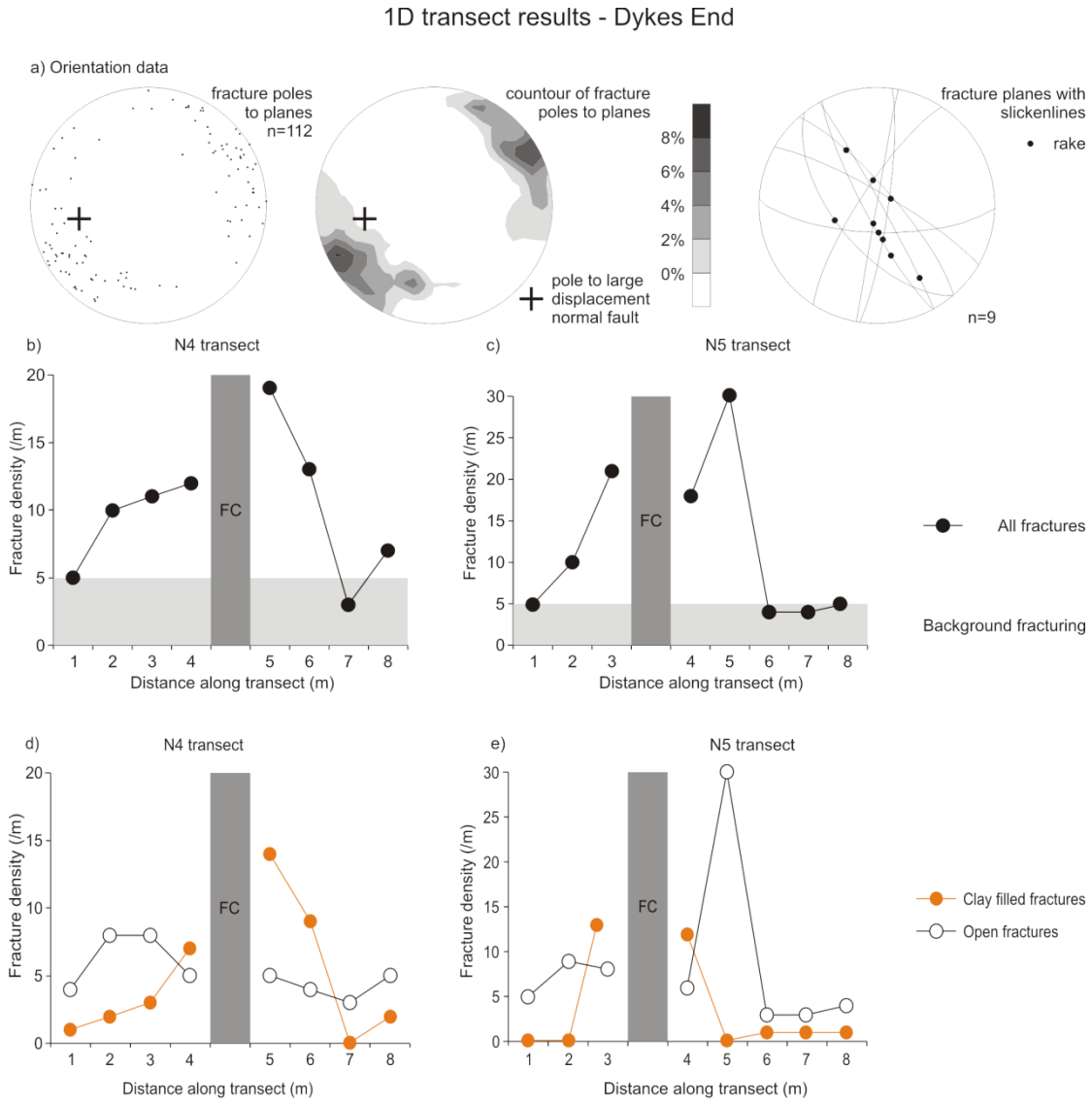

Figure 3.12 - 1D transects at Dykes End

a) orientation of the fractures in the damage zone, and the kinematic indicators on their surfaces, b) fracture density across the fault zone (N4 transect), c) fracture density across the fault zone (N5 transect), d) variation in the density of open and clay filled fractures across the fault zone (N4 transect), e) variation in the density of open and clay filled fractures across the fault zone (N5 transect)

Some fractures of the damage zone are clay filled, due to clay being intruded into the fracture planes from the interlayered marl horizons during/after the fracture opening. If the density of open and clay filled fractures are plotted separately, their variation across the fault zone can be studied independently (Fig. 3.12d-e). The number of open fractures slightly reduces closer to the fault core, where values, which are comparable to the background fracturing, are observed (except for the second meter on the N5 transect). Conversely, the density of clay-

filled fractures is significantly higher in the near vicinity of the fault core, compared to the outer parts of the damage zone and the protolith.

Selwick Bay

The fractures associated with the large displacement normal faults at Selwick Bay are almost all calcite filled, i.e. veins (>90%). Vein density was calculated along three transects orthogonal to the fault zones (Fig. 3.13a, for transect locations see also Fig. 3.10b). Veins in the damage zone have a dominant trend, oriented parallel to the large faults, and they dip between 50° and sub-vertical (Fig. 3.13b). The few shear planes observed display slickenlines with dip-slip to oblique slip kinematics (Fig. 3.13b).

Based on measurements further away from the fault zone, the background density of veins was found to be approximately 2/m (Fig. 3.13c-e). The footwall damage zone of the IBZ is approximately 3 m wide, beyond which the intensity of damage gradually decreases towards the background vein values (Fig. 3.13c-e). In the hanging wall of the FC, the vein density is low and comparable to background veining values (Fig. 3.13c-e). In between the FC and the IBZ, vein density is more than six times higher, where the FC and IBZ are located 4 m apart (Fig. 3.13c, N1 transect). The distance between the FC and IBZ increases towards the wave-cut platform, where the fault cores are 5 m and 10 m apart (Fig. 3.13d-e, N2 and N3 transects, respectively). The damage zone appears to be relatively narrow on N2, only 1-2 m wide, however, the highest vein density was recorded on this transect, in the footwall damage zone of the IBZ (Fig. 3.13d). On the N3 transect (Fig. 3.13e) both of the footwall damage zones are 1 m wide, while the hanging wall damage zones are 3 m wide. Within the wider

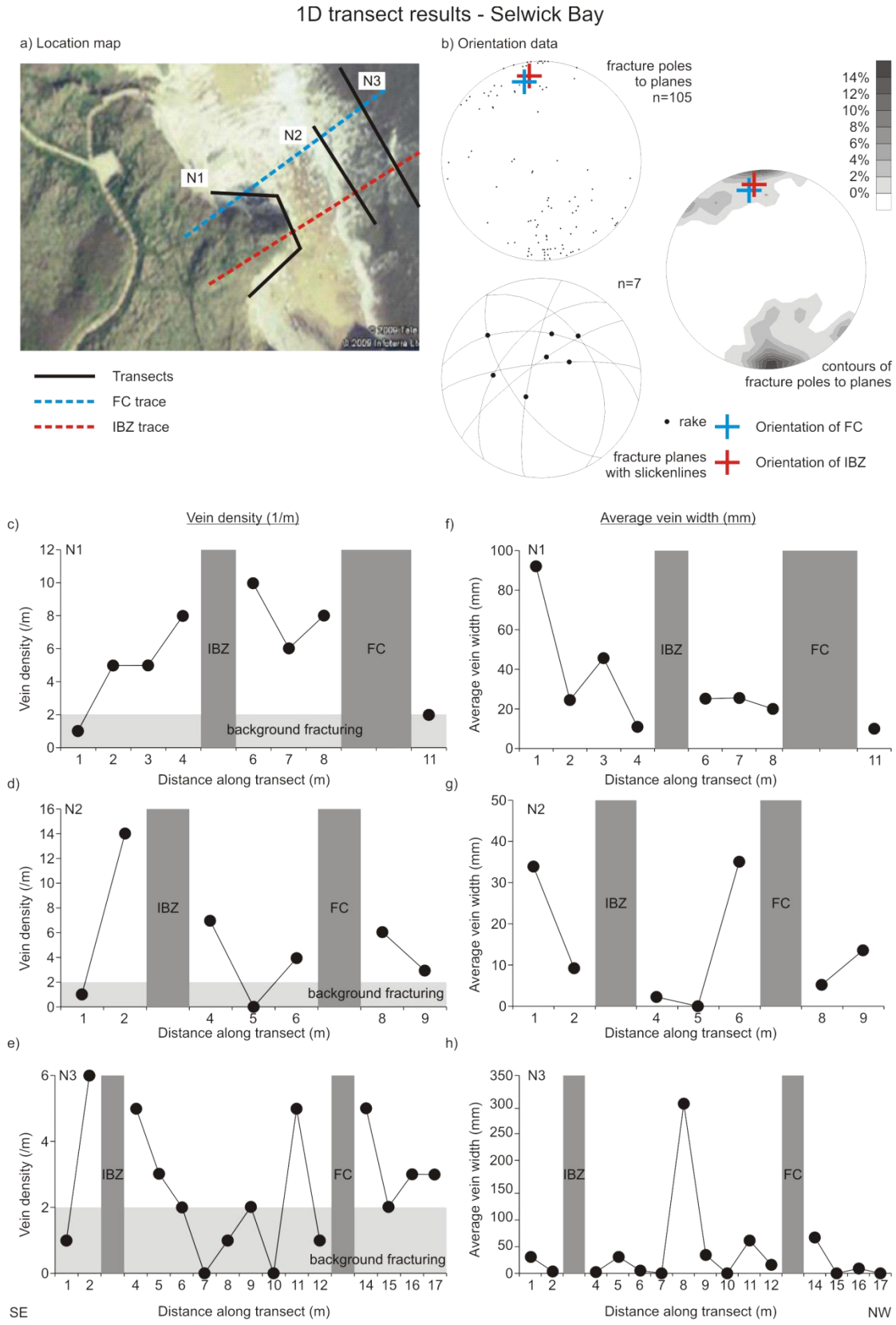

Figure 3.13 - 1D transects at Selwick Bay

a) location of transects in respect to the FC and IBZ, b) orientation of veins in the damage zone, and the kinematic indicators on their surfaces, c, d, e) vein density across the fault zone along the three transects, N1-N3, respectively, f, g, h) average vein widths across the fault zone along the three transects N1-N3, respectively

hanging wall damage zones, vein density gradually decreases towards the background values, typical of the protolith (Fig. 3.13e). The average vein width was also measured for each meter of the three transects (Fig. 3.13f-h), but these values do not show a systematic variation across the fault zones.

3.4.2.2. 2D Image analysis

Dykes End

2D fracture density and connectivity data at the Dykes End large displacement normal fault was collected from 6 fault zone parallel panels, each approximately 1 m wide (Fig. 3.14a-b). Fracture density, in the damage zone of the large displacement normal fault, increases when moving from the protolith towards the fault core (Fig. 3.14c). In the footwall, fracture density values close to the fault core (3.5 m/m^2) are 4 times higher than those measured outside the damage zone (< 1 m/m^2). Fracture density values in the footwall, close to the fault core (P3) are twice as high as in the hanging wall (2 m/m^2, P5).

Fracture connectivity across the damage zone, measured as FCA also shows significantly higher values in the footwall damage zone (up to 60%) than in the hanging wall damage zone (up to 20%), (Fig. 3.14d). Finally, fracture connectivity values, measured as IPD (Fig. 3.14e) also show higher values in the footwall (up to 90 n/m^2), than in the hanging wall (up to 40 n/m^2). Fracture connectivity, measured as IPD (Fig. 3.14e), monotonically increases towards the fault core, as opposed to the fracture connectivity values, measured as FCA (Fig. 3.14d), where the monotonicity cannot be observed.

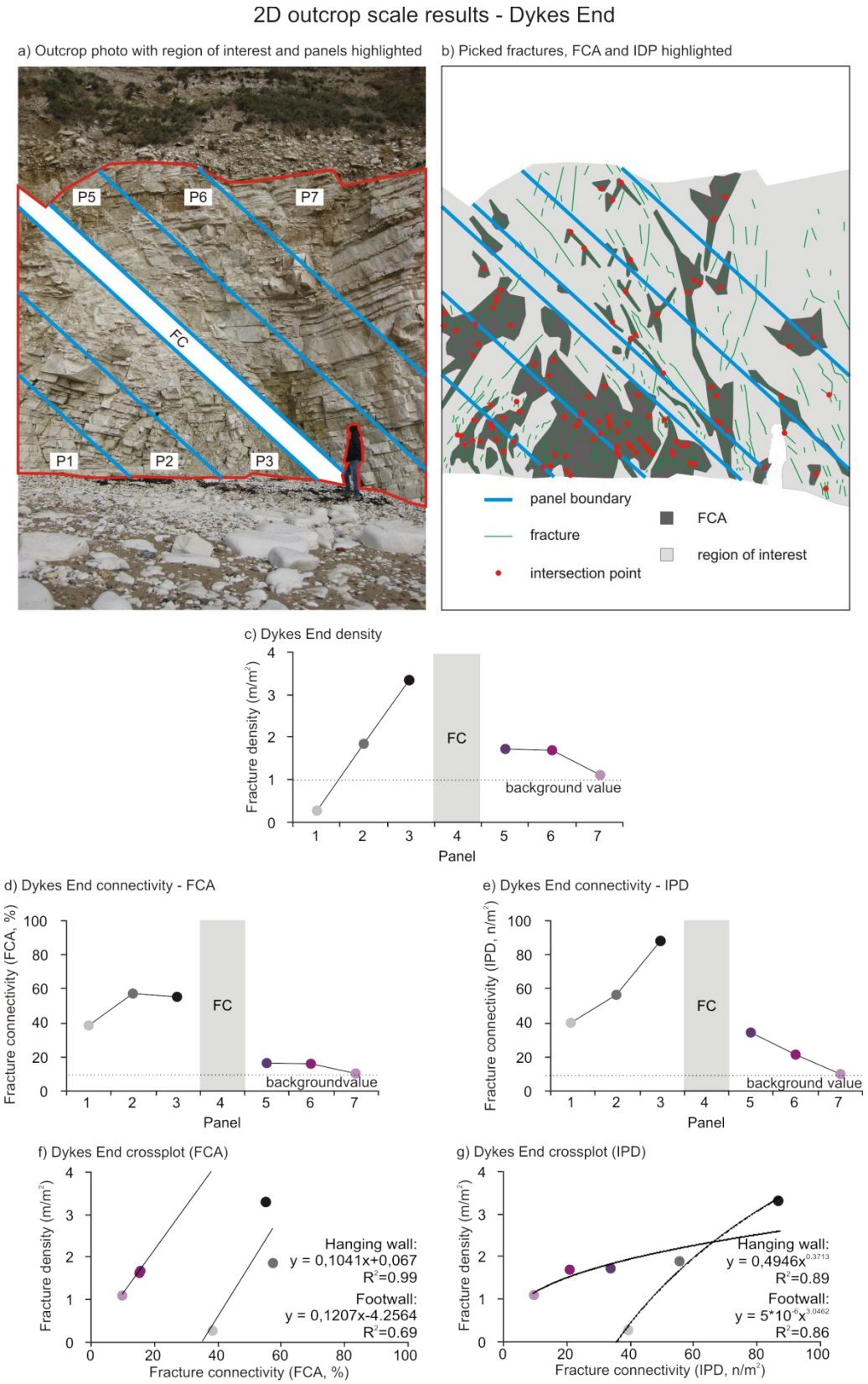

Figure 3.14 - 2D outcrop scale results – Dykes End

a) Outcrop photo with the region of interest and panels highlighted, b) Picked fractures with the FCA and intersection points highlighted, c) Fracture density across the fault zone, d) Fracture connectivity across the fault zone (FCA), e) Fracture connectivity across the fault zone (IPD), f) Fracture density vs. connectivity (FCA) crossplot, g) Fracture density vs. connectivity (IPD) crossplot

Fracture density versus connectivity cross-plots, based on the data from Dykes End show the relation between fracture density and connectivity (Fig. 3.14f-g). Regardless of the method used for quantifying connectivity, FCA or IPD, respectively, panels of the damage zone, which are closer to the fault core (e.g. P2-3, P5-6 in Fig 3.14a-b), are characterised by higher fracture density and connectivity values than panels of the damage zone, located further away from the fault core (e.g. P1, P7 in Fig. 3.14a-b).

Best-fit trendlines can be fitted to the footwall and hanging wall datapoints separately (Fig. 3.14f-g). When fracture connectivity is calculated as FCA, the best fit trendline is linear (Fig. 3.14f). The equation of the trendline is

$$y=0.1041x+0.067,\ R^2=0.99,$$

in the hanging wall (where y is the fracture density and x is fracture connectivity) and

$$y=0.1207x-4.2564,\ R^2=0.69,$$

in the footwall (Fig. 3.14f). When fracture connectivity is calculated as IPD, the best fit trendline is power-law (Fig. 3.14g). The equation of the trendline is

$$y=0.4946x^{0.3713},\ R^2=0.89,$$

in the hanging wall and

$$y=5*10^{-6}x^{3.6462},\ R^2=0.86,$$

in the footwall (Fig. 3.14g).

Selwick Bay – outcrop scale analysis

In the case of Selwick Bay, five photos were taken to cover the entire fault zone of the large displacement normal fault (Fig. 3.15a; Fig. 3.10a-b). Each photo was divided into 3 panels, for a total of 15 panels, each of them representing an approximately 1 m long section of the cliff. Vein density and connectivity were calculated within each panel. An example of the

procedure applied can be seen on Fig. 3.15b, where the photo was taken on a view, perpendicular to the outcrop, approximately 5 m away from it and, subsequently, divided into 3 separate panels (namely P4-P6). Within each panels, following the method explained in Chapter 1.3.2, the veins and the bedding surfaces were marked with black lines and the FCA was marked with dark grey, while the intersection points of fractures were marked with red dots.

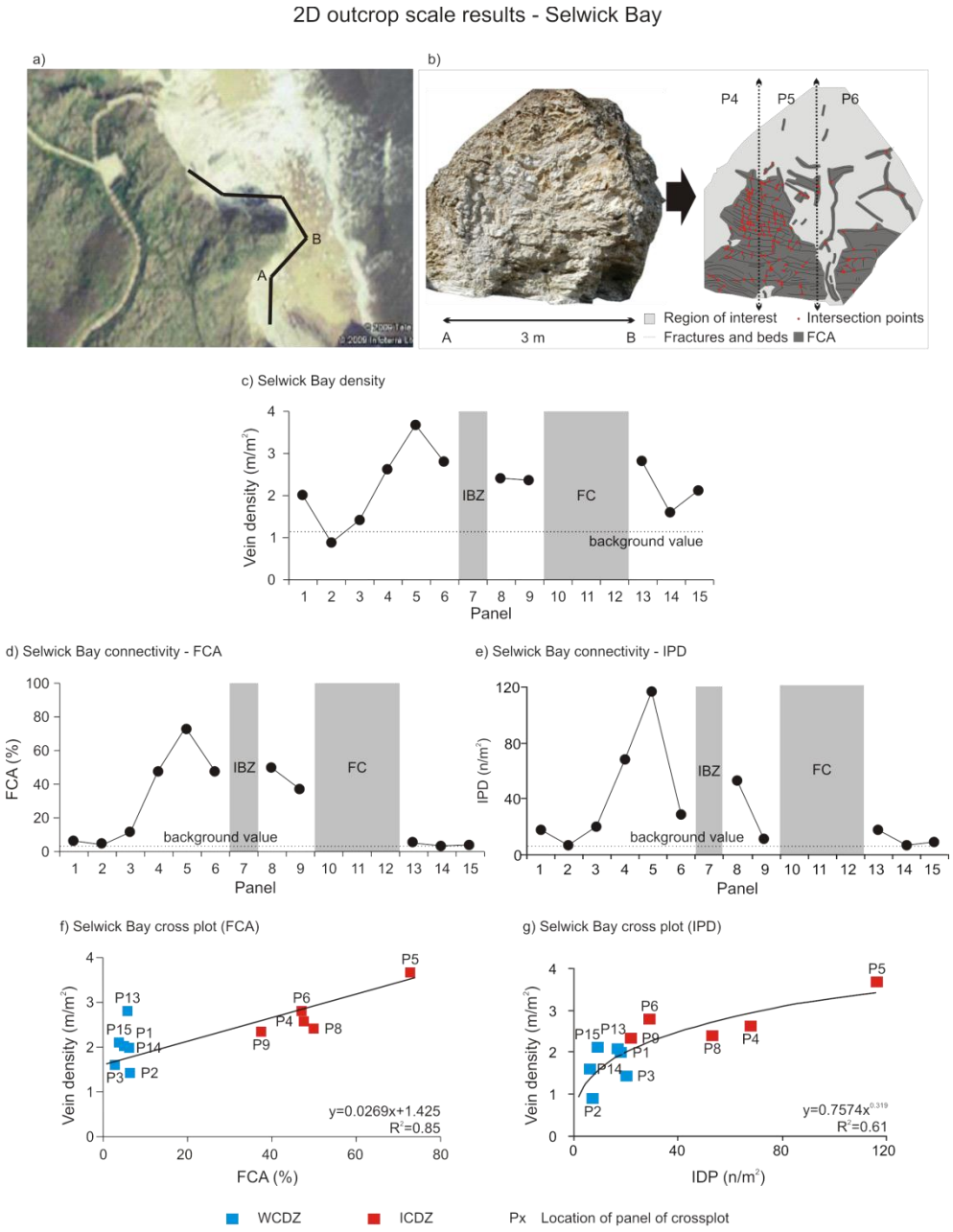

Figure 3.15 - 2D outcrop scale results – Selwick Bay

a) Location of photos used for analysis across the headland, b) Example photo showing the panels (P4-P6) used for the analysis with the picked veins, FCA and vein intersection points, c) Changes in vein density along the Selwick Bay large displacement normal faults along all the panels, d) Changes in vein connectivity along the Selwick Bay large displacement normal faults along all the panels (calculated as FCA), e) Changes in vein connectivity along the Selwick Bay large displacement normal faults along all the panels (calculated as IPD), f) Vein density vs. connectivity crossplot (calculated as FCA), g) Vein density vs. connectivity crossplot (calculated as IPD)

The variation of vein density in 2D across the IBZ and FC at Selwick Bay is plotted on Fig. 3.15c. High vein density fault zone domains are located close to the IBZ and FC in 3 panels (P4-6) of the footwall damage zone of the IBZ, in the damage zone between the FC and the IBZ (P8-9) and in the first panel in the hanging wall damage zone of the FC (P13) (Fig. 3.15c). Vein density values in these domains are up to 4 times higher (4 m/m^2) than in the outside parts of the damage zone, where background values are approximately 1 m/m^2. In other sections of the damage zone (e.g. P1-3, P13-P15) density values are up 2 times higher (2 m/m^2) than the background values.

Vein connectivity values, measured as FCA, vary across the fault zone in a similar fashion than vein density (Fig. 3.15d). However, their relative increase, when compared to background values, can be as high as one order of a magnitude (Fig. 3.15d). Panels, located in the footwall, close to the IBZ (P4-6), and between the FC and IBZ (P8-9) are characterized by connectivity values between 50% and 80%. Panels in the footwall, further away from the IBZ (P1-3), and in the hanging wall of the FC (P13-15) are typically characterized by low vein connectivity values, less than 10%. This suggests that the damage zone can be divided into sub-domains, based on high and low values of vein connectivity. Following the subdivision of damage zones proposed by Micarelli et al. (2005), who subdivided the damage zones of faults hosted in carbonates into weakly and intensively deformed damage zones (WDDZ and IDDZ), based on the variation of fracture density, hereafter damage zone domains, characterized by high connectivity values will be referred to as intensively

connected damage zones (ICDZ), and damage zone domains, characterized by low connectivity values will be referred to as weakly connected damage zones (WCDZ).

When vein connectivity values are measured as IPD, the trend across the fault zone is similar to that shown by the values, calculated as FCA (Fig. 3.15e, for correlation see also Fig. 1.3). The only panel that shows a significantly different pattern is P9, where the vein connectivity value measured as IPD (10 n/m^2) is significantly lower when compared to the other panels, whereas vein connectivity, measured as FCA, was relatively high (40%).

The vein density and connectivity data can be plotted against each other on vein connectivity versus vein density cross-plot in case of both methods used for measuring connectivity (Fig. 3.15f-g). The crossplot, when connectivity is calculated as FCA (Fig. 3.15f), shows that the datapoints for the ICDZ and WCDZ, respectively, group into two distinct clusters (Fig. 3.15f). A linear trendline can be fitted to these points, with an equation of

$$y=0.0269x+1.425, (R^2=0.85),$$

where y is vein density and x is vein connectivity, measured as FCA. The weakly connected damage zone (WCDZ) is characterised by moderate to high vein density and relatively low vein connectivity values and the intensely connected damage zone (ICDZ) is characterised by high vein density and high vein connectivity values. The ICDZ domains are located in the region between the FC and the IBZ (P8-9) and in the footwall damage zone of the IBZ, close to it (P4-6); while the WCDZ domains (P1-3, P13-15) are located further away from the FC and IBZ.

When vein connectivity is measured as IPD, the vein connectivity versus vein density cross-plot shows some different characteristics, compared to the previous one (Fig. 3.15g). The best-fit trendline to this data is a power-law trendline:

$$y=0.7574x^{0.319},\ R^2=0.61,$$

where y is vein density and x is vein connectivity measured as n/m^2, conversely to the previous cross-plot where it was a linear trendline. Additionally, although datapoints representing the ICDZ and WCDZ are clustering separately, the clustering in this case is more gradual than in the case, when vein connectivity was calculated as FCA. However, the ICDZ is still characterized by higher vein connectivity values than the WCDZ (Fig. 3.15g).

Selwick Bay – microscale analysis

Vein density values have also been obtained by digital quantitative analysis performed on thin sections, collected in the different fault zone domains (for sample location see Fig. 3.10b). In case of microscale analysis, vein density and connectivity was also possible to be measured accurately in the IBZ and FC. The results show that the background fracturing in the protolith is approximately 200 m/m^2 (Fig 3.16a, data refer to S1 and S6 samples in Fig. 3.10b). This value is significantly lower than the values gained from thin sections collected from the damage zones, in the IBZ and in the FC. Vein density in the entire fault zone ranges between 700-1000 m/m^2. The highest values are measured in the brecciated parts of the FC (S3 sample, 1000 m/m^2), and the intensity decreases gradually in the ICDZ (S2 sample, 900 m/m^2), in the IBZ (S4 sample, 800 m/m^2), and, finally, the lowest values are measured in the WCDZ (S5 sample 700 m/m^2). The differences between the values measured from samples within the fault zone are not significant when compared to the increase observed with respect to the background values calculated for the protolith.

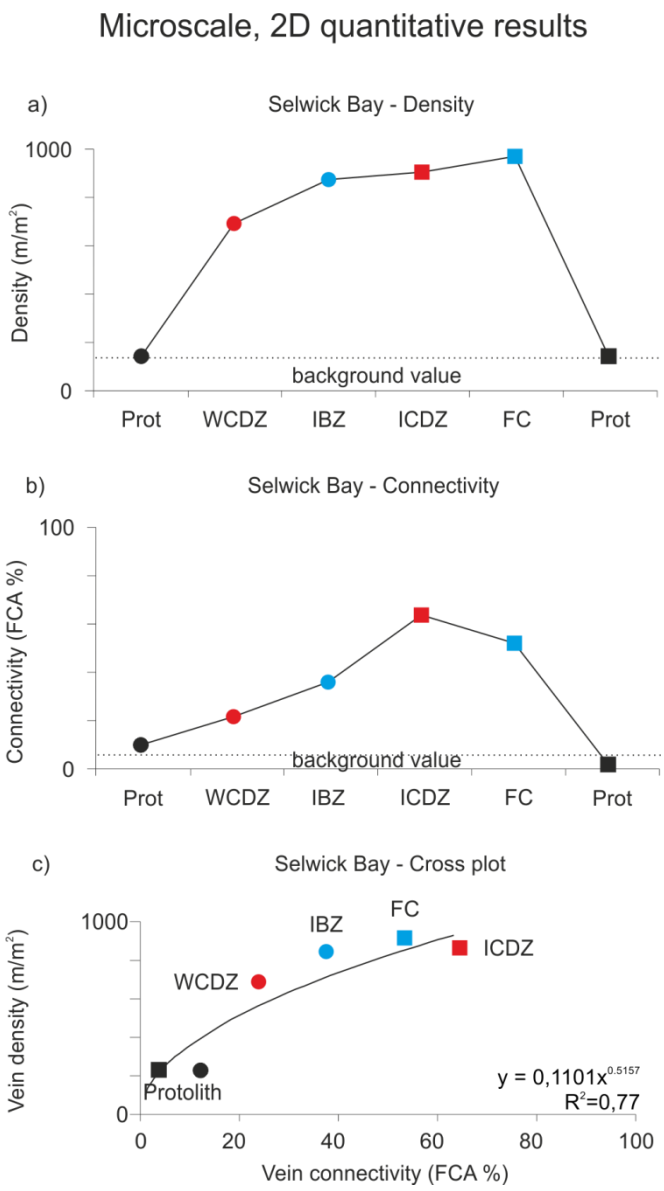

Figure 3.16 - 2D microscale image analysis

a) Vein density in the different fault zone domains at Selwick Bay, b) Vein connectivity in the different fault zone domains at Selwick Bay, c) Vein density vs. connectivity crossplot of the different fault zone domains at Selwick Bay

Vein connectivity values, gained from the same thin sections, can be plotted on a similar graph as vein density (Fig. 3.16b). Vein connectivity in the protolith was found to be low (<10%), compared to the damage zones and fault cores, where vein connectivity values range between 20% and 60% (Fig. 3.16b). In the FC and IBZ vein connectivity values are 50% and 40%, respectively; while in the ICDZ and WCDZ they are 60% and 20%, respectively (Fig. 3.16b). The measured vein connectivity values in the IBZ and FC are very similar, and

are also comparable with vein connectivity values measured for the ICDZ (Fig. 3.16b). On the other hand, vein connectivity values measured for the ICDZ and WCDZ differ significantly (Fig. 3.16b). Similarly to outcrop scale results the ICDZ is characterized by considerably higher connectivity values than the WCDZ.

Vein connectivity versus vein density cross-plots, for the microscale results, show a similar trend than observed for the outcrop scale results (Fig. 3.16c). A best fit, power-law trendline can be fitted to the data ($y=0.1101x^{5157}$, where y is vein density and x is vein connectivity, measured as FCA), characterized by a relatively high R^2 value (0.77). The datapoints do not cluster as much as seen on Fig. 3.15f in case of the outcrop scale results. However, the datapoints, representing the WCDZ and ICDZ are plotted respectively at the same sections of the graph as seen in case of the outcrop scale data. In summary, the protolith is characterized by low vein density, and low vein connectivity, the WCDZ is characterized by high vein density, but relatively low vein connectivity and the IBZ, the brecciated parts of the FC and the ICDZ are all characterized by high vein density and vein connectivity values (Fig. 3.16c).

3.4.2.3. 3D LiDAR data

At Selwick Bay 3D LiDAR data were collected for the large displacement normal fault, to quantify vein density and connectivity values across the fault zone. Additionally, orientation data were also gained from the 3D models with the limitations explained in Chapter 3.4.1.

Orientation data

Orientation data show that veins are dominantly sub-parallel to the main fault zones (Fig. 3.17a). However, orientation data gained from LiDAR data is more scattered than the orientation data measured in the field both in terms of dips and strike directions (Fig. 3.17b).

Qualitative comparison between orientation data, collected from the same fault zone using 1D transects and 3D LiDAR suggests that the latter methods results in similar peak orientations, but more scattered distribution (Fig. 3.17).

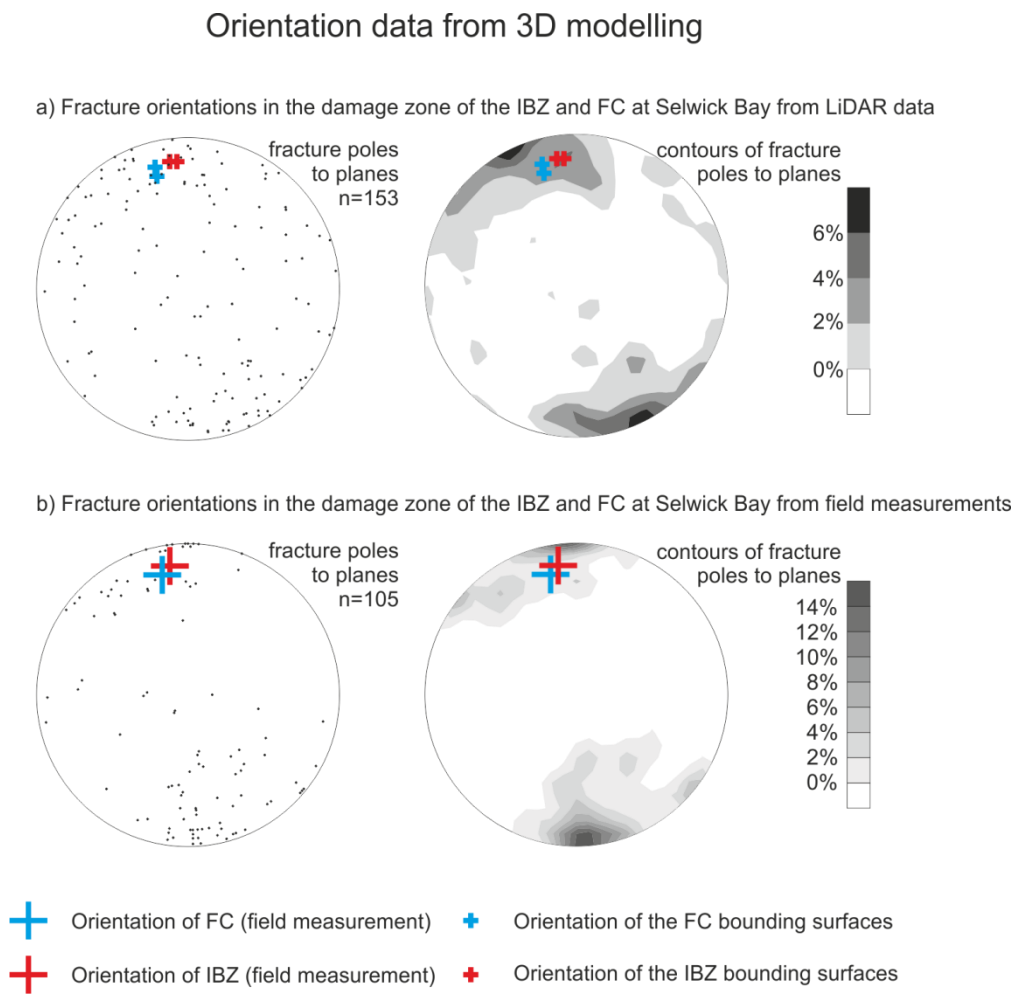

Figure 3.17 - 3D results – orientation of veins in the damage zone of the Selwick Bay large displacement normal fault

a) Plotted based on 3D LiDAR data, b) Plotted based on field-based measurements

Vein density and connectivity data

Vein density and connectivity data were gained by modelling the veins in the fault zone using 5 different aspect ratio values that were 1/1, 1/2, 1/3, 1/5, 1/8 (Fig. 3.18). The highest aspect ratio values (1/1, 1/2, 1/3) do not show any systematic variation in vein density (Fig. 3.18a) and connectivity (Fig. 3.18b) values across the fault zone. On the other hand, lower aspect

ratio models (1/5, 1/8) revealed the internal structure of the fault zone (Fig. 3.18a-b). For these lower aspect ratio models, vein density values are increasing from the protolith, where background values of approximately 0.5 m^2/m^3 were measured, towards the IBZ, in the footwall damage zone, where the highest values of 12 m^2/m^3 and 8 m^2/m^3 for the 1/8 and 1/5 aspect ratio model, respectively, were observed at 5 m along the transect (Fig. 3.18a). Between the IBZ and the FC vein density values range from 6 to 9 m^2/m^3 and 5 to 7 m^2/m^3 for the 1/8 and 1/5 aspect ratio model, respectively. In the hanging wall of the FC, vein density values are only as high as 2 m^2/m^3, next to the FC, and these values quickly decrease to the background values within 1 m distance (Fig. 3.18a).

Vein connectivity values are 0 m/m^3 throughout the protolith and most of the WCDZ, regardless of the particular aspect ratio (Fig. 3.18b). Within the WCDZ only a few vein intersections are present, with the highest vein connectivity values of 1 m/m^3 obtained for the 1/8 aspect ratio model (Fig. 3.18b). Within the ICDZ, in the footwall of the IBZ, vein connectivity values are higher, ranging around 2 m/m^3 and 1.5 m/m^3 for the 1/8 and 1/5 aspect ratio models, respectively. In the ICDZ, between the IBZ and FC, the observed vein connectivity values are similar to those observed in the footwall of the IBZ (Fig. 3.18b). Finally, in the hanging wall of the FC, vein connectivity values are typically 0 m/m^3, which are similar to the protolith.

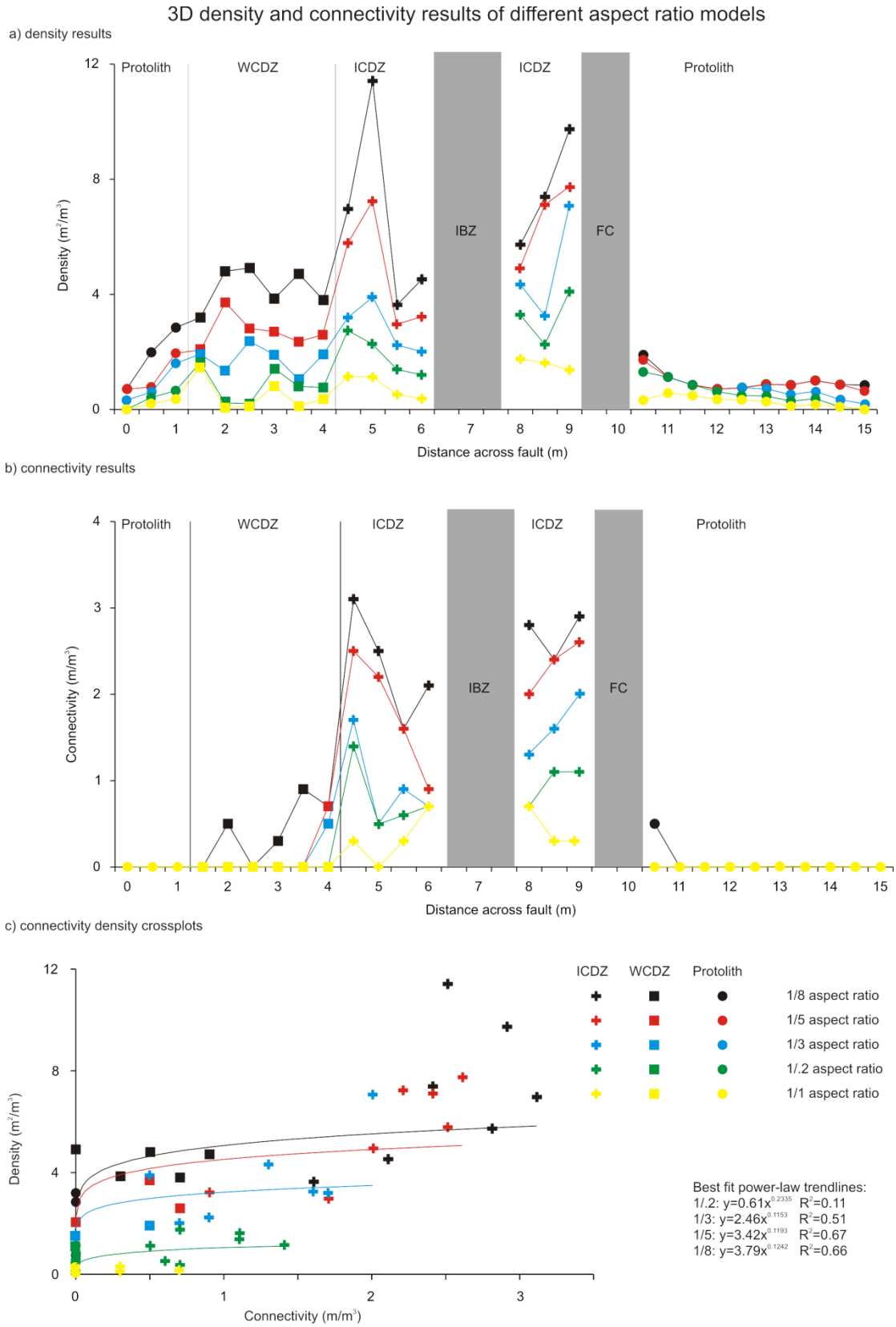

Figure 3.18 - 3D results

a) vein density across the Selwick Bay large displacement normal faults; b) vein connectivity across the large displacement normal faults; c) vein density connectivity crossplot of the the Selwick Bay large displacement normal faults

Vein density and connectivity values in the ICDZ are approximately one order of magnitude higher, when modelled by 1/8 aspect ratios (up to 12 m^2/m^3 vein density and 3 m/m^3 vein connectivity), than when modelled by 1/1 aspect ratio models (1.1 m^2/m^3 vein density and 0.3 m/m^3 vein connectivity). The differences in the vein density and connectivity values, obtained for different aspect ratio models decrease towards the protolith (Fig. 3.18b).

Vein density versus vein connectivity cross plots show that, regardless of the aspect ratios (Fig. 3.18c), datapoints representing the protolith are clustered around low vein density and vein connectivity values, datapoints from the WCDZ have higher vein density but low vein connectivity values and datapoints from the ICDZ have high vein density and vein connectivity values. Power-law, best fit trendlines can be fitted to the datasets, representing different vein aspect ratio values. These trendlines are

$$y=0.6097x^{0.2335}\ (R^2=0.11),$$

$$y=2.4578x^{0.1153}\ (R^2=0.51),$$

$$y=3.4171x^{0.1193}\ (R^2=0.67),$$

$$y=3.79x^{0.1242}\ (R^2=0.66)$$

for the 1/2, 1/3, 1/5, 1/8 aspect ratio models respectively. While the R^2 values are low for higher aspect ratio models (1/2, 1/3), they are higher for models with more elongated shapes (1/5, 1/8), suggesting a better power-law correlation.

3.5.Discussion

3.5.1. Lithological control on fault patterns and implications for fractured reservoirs: a simple conceptual model

Based on the field observations and the qualitative data collected and analysed, a simple conceptual model of fluid flow is proposed, which could apply to reservoirs, hosted in chalk with similar features as those, observed at Flamborough Head (Fig. 3.19).

Small displacement normal faults

The protolith at Dykes End is characterised by thick (cm-scale), interlayered marl horizons, whilst at Selwick Bay, interlayered marl horizons are either thin (mm-scale) or absent (Fig. 3.2a-b, 3.19a). Widespread, brittle deformation in both study areas is accommodated by patterns of small displacement normal faults, which display flat-ramp-flat geometries (Fig. 3.3-3.5, 3.19b). At Dykes End, the thick marl horizons, interlayered with the chalk, are smeared out and injected into many of the small displacement faults and associated fracture planes (Fig. 3.4b-c). Small fractures, further away from the small faults are open cracks with no filling material (Fig. 3.4d-e). No evidence for veining or other fluid assisted fracturing processes have been found at Dykes End. Conversely, at Selwick Bay, where interlayered marl horizons are absent, most of the fractures associated with small displacement normal faults are filled with crystalline calcite (Fig. 3.5c-f). These observations provide evidence for fluid assisted fracturing processes, e.g. hydrofracturing.

Thick (cm-scale), marl horizons, present at Dykes End, can act as effective barriers for fluids; in fact, the marl horizons themselves are barriers for fluids migrating along the vertical direction, while the marl material, smeared out along fault planes and injected into steeply dipping fracture planes, also form good barriers for fluids, migrating across the fault zones,

along the horizontal direction. Since the orientation distribution of the small displacement normal faults is very scattered (Fig. 3.4.a), they should behave as distributed barriers, limiting horizontal fluid migration in all directions (Fig. 3.19b). Conversely, at Selwick Bay, small displacement normal faults are also characterised by scattered orientation (Fig. 3.5a), but here they appear to behave as distributed conduits, favouring the migration of fluids in all directions due to the absence of the interlayered marl horizons in the host rock (Fig. 3.19b).

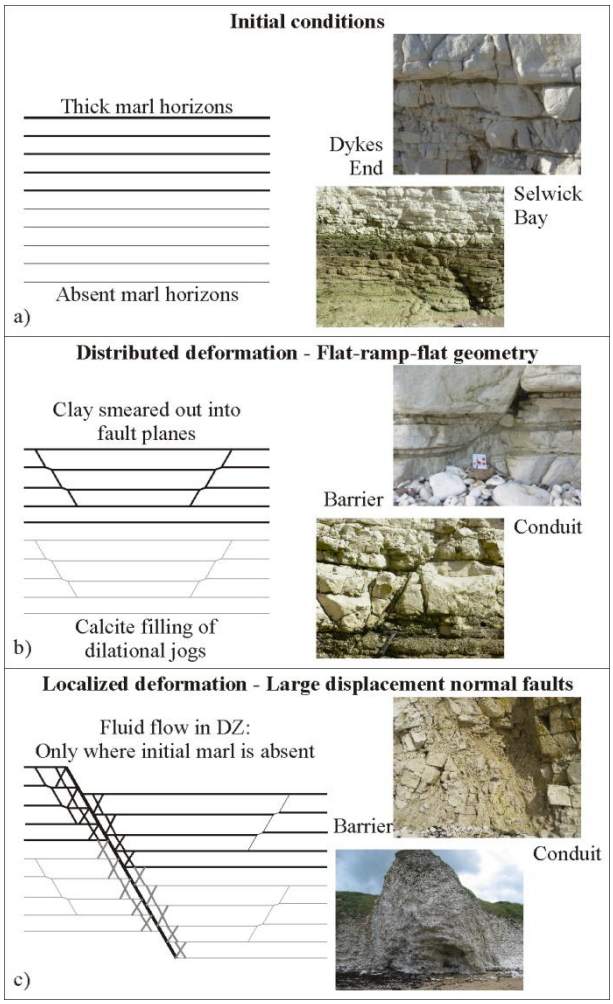

Figure 3.19 - Conceptual model of fault development at Flamborough Head
a) initially thick marl horizons deposited within the chalk at Dykes End, and thin to absent marl horizons at Selwick bay, b) distributed deformation developed the small displacement, flat-ramp-flat geometry faults; at Selwick Bay the fractures were healed by calcite as a result of fluid flow, while at Dykes End clay from the interlayered marl horizons were smeared out and injected into the fault planes forming barriers, c) localized deformation developed the large displacement normal faults; at Dykes End the development of the large faults resulted in an even stronger barrier for fluids while at Selwick Bay large faults channelized fluid flow

Highly fractured chalk is generally considered to be a good reservoir rock. However, the extrapolation to reservoir scenarios at depth of the field observations presented and analysed suggest that the presence of lithologies similar to that observed at Dykes End (e.g. > 5% cumulative thickness of the marl horizons) could potentially represent a highly compartmentalised and poor reservoir. On the other hand, lithologies similar to those observed at Selwick Bay (e.g. < 1% cumulative marl thickness) would potentially be a good reservoir, with the many small displacement normal faults providing high structural porosity and permeability, increasing fluid transmissibility (Fig. 3.19b).

Large displacement normal faults

Deformation is localised, in both study areas, along larger displacement normal faults (Fig. 3.19c, Fig. 3.6-3.9). At Dykes End, the large displacement normal fault comprises a narrow fault core, made of fault gouge, and an over 2 m wide damage zone surrounding the core, characterised by high fracture densities (Fig. 3.6). Many of the fractures, close to the fault cores, are (partially) filled with injected marls from the interlayered marl horizons (Fig. 3.6b-c). In the fault zone, no fluid assisted fracturing processes have been observed. Large displacement normal faults, similar to those observed at Dykes End, should behave as localised barriers to fluids migrating along the horizontal direction across the fault, due to the presence of fine grained gouges in the fault core and due to the injected marls in the surrounding fractures of the damage zone (Fig. 3.19c).

At Selwick Bay, the large displacement normal faults are characterized by a more complex internal architecture, with the FC and the IBZ separated by heavily fractured damage zones (Fig. 3.8). The observation of precipitated calcite in most fracture planes and within the FC

and IBZ provides extensive evidences for fluid assisted fracturing processes, e.g. hydrofracturing (Fig. 3.8c). At the same time, the presence of a narrow layer of fault gouge, observed on the slip surface in the FC (Fig. 3.8b), could act as a small barrier for fluids migrating across the fault core along the horizontal direction. This could explain the absence of veins observed in the hanging wall damage zone of this fault. Based on the field observations presented, it is inferred that the large displacement normal faults at Selwick Bay behaved as conduits, favouring the migration of fluids that were channelized in the fault zone. Based on the vein connectivity data (Fig. 3.15d-e) it is inferred that fluid flow was high in the following fault zone domains: 1) in the footwall damage zone, 2) in the IBZ, 3) in the damage zone between the FC and IBZ and 4) in the brecciated parts of the FC, specifically in the footwall of the slip surface, which is located on the fault core-hanging wall damage zone boundary.

In a potential subsurface reservoir scenario, large displacement faults, like the one studied at Dykes End, would behave as a localised barrier for fluid migration, strongly reducing fluid flow migration pathways and producing a compartmentalized reservoir. On the other hand, faults with similar features as the one at Selwick Bay, would behave as a localised conduits, enhancing fluid transmissibility within the reservoir (Fig. 3.19c).

3.5.2. The internal architecture of fault zones: 1D and 2D quantitative analysis

Results of the 1D and 2D quantitative analyses, of fracture/vein density and connectivity, revealed the details regarding the internal structure of the large displacement normal faults studied at both localities (Figs. 3.12-3.16). At Dykes End, both 1D and 2D outcrop-scale quantitative analyses showed a rather simple distribution of fracturing across the fault zone, with a gradual decrease in fracture density and connectivity within the damage zone, when

moving from the fault core towards the protolith (Fig. 3.12, 3.14). According to 1D results, the footwall damage zone is wider (> 2 m) than the hanging wall damage zone (< 1-2 m) (Fig. 3.12), but fracture density and connectivity values are higher in the hanging wall damage zone. According to 2D results fracture density and connectivity values are higher in the footwall (Fig. 3.14).

At Selwick Bay, results from the 1D and 2D quantitative analyses show a more complex distribution of fracturing, with the identification of across-fault domains and sub-domains, characterized by heterogeneous distribution and intensity of fracturing (Figs. 3.13, 3.15-3.16). According to outcrop scale 1D and 2D analyses, in the fault zone vein density is up to 6 times higher than in the surrounding protolith (Fig. 3.13). According to 2D microscale results, vein density in the fault zone can be nearly an order of magnitude higher than in the protolith. Vein connectivity values, regardless of the scale of observation and the method used for their quantification (e.g. FCA and IPD) are relatively low in the outer parts of the damage zone, where the values obtained are comparable with the protolith ones, but they rapidly increase, by over an order of magnitude, towards the inner parts of the damage zone (i.e. in the footwall damage zone, close to the IBZ, and between the FC and the IBZ). The terms intensely- and weakly connected damage zones have been used to define low and high vein connectivity damage zone sub-domains respectively (Fig. 3.20a, Fig. 3.15f). These terms were originally proposed by Micarelli et al. (2006b), who described similar fault zone sub-domains in carbonate hosted normal faults.

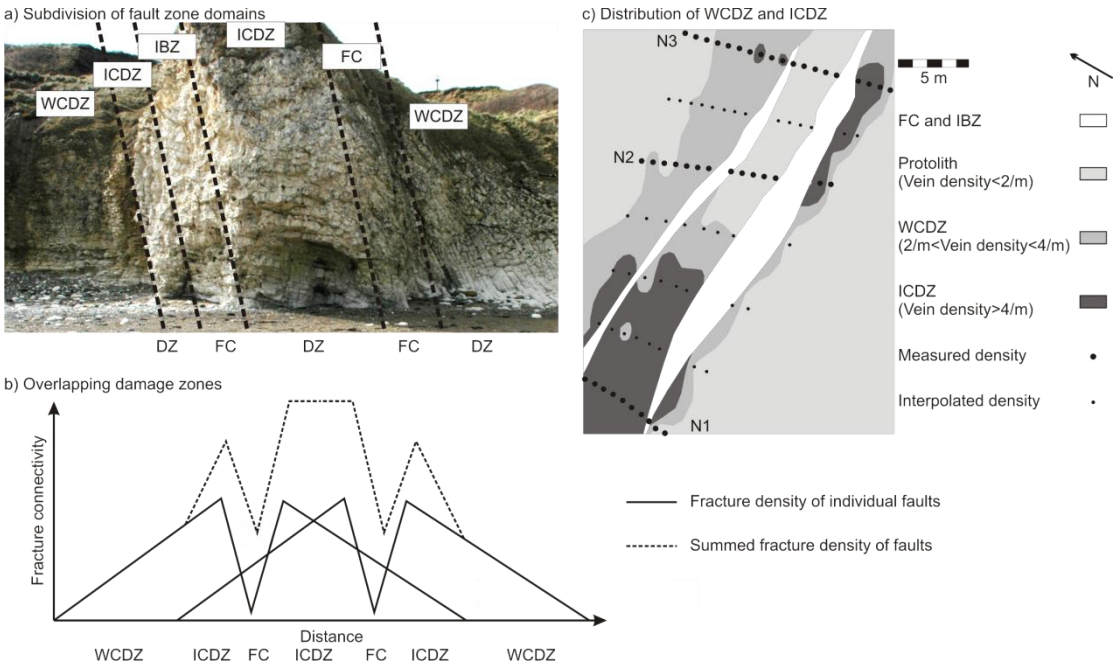

Figure 3.20 - Subdivision of the Selwick bay large displacement normal faults
a) damage zones separated into WCDZ and ICDZ on the cliff, b) interpretation for the development of the WCDZ and ICDZ: ICDZs are the results of two overlapping damage zones, c) damage zones separated into WCDZ (light grey areas) and ICDZ (dark grey areas) on the cliff and on the wave-cut platform

The development of the damage zone sub-domains may be explained by the partial overlap between the damage zones of the two closely spaced, large displacement normal faults (Fig. 3.20b). The two main fault zones are not exactly parallel with each other (Fig. 3.13b, 3.17a), therefore, the main fracture orientation in their damage zone are not parallel either. Where the two faults are close enough, the damage zones partially overlap (Fig. 3.20b). In this situation, within the overlapping areas, the vein connectivity is high because of the interaction between the two main faults and the interaction between individual fractures related to the two main faults, respectively, with slightly different orientations. The development of such intensely connected domains (ICDZ, Fig. 3.21b), at the overlap between the two fault zones, may help to channelize fluids along the fault zone.

1D vein density data, collected along 3 sub-parallel structural transects, N1, N2 and N3 (Fig. 3.10b), from Selwick Bay were used to create a map of the distribution of vein density around the fault (Fig. 3.20c). In the vein density map it was necessary to extrapolate values between two measured transects by taking their averaged vein density values. Between transects N1 and N2 this step was done twice, because of the larger distance between these two transects than N2 and N3 transects. The real measured datapoints (larger dots on Fig. 3.20c) and the extrapolated ones (smaller dots on Fig. 3.20c) were used to create the density map by kriging extrapolation in the ArcMAP© software. Based on corresponding vein density and connectivity values along N1 transect and 2D image analysis, values less than 2/m were classified as protolith, values between 2-4/m were classified as WCDZ and values larger than 4/m were classified as ICDZ. The interpolated data show how vein density increases by moving from the protolith towards the fault core. Vein density values are higher in the zones where the two damage zones overlap (Fig. 3.20c). Away from the cliff, on the wave-cut platform (N2, N3 transects), the two faults are slightly diverging from each other and their damages zones do not overlap (Fig 3.21c). At these locations, vein density and connectivity values are lower, suggesting less intense fluid transmissibility in the damage zones.

Both 1D and 2D fracture/vein density data show, in agreement with structural observations, that fluid assisted deformation features (e.g. veins) are common at Selwick Bay, but are absent at Dykes End. The 2D vein connectivity data show the development of high vein connectivity fault zone domains within the damage zone of the Selwick Bay large displacement normal fault. The extrapolation of the results of the 1D and 2D quantitative analyses to a potential subsurface scenario suggests that this type of fault zones can play an important role in the migration of fluids, primarily in fault parallel directions. On the

contrary, fracture connectivity values at Dykes End are generally lower, with no particularly high fracture connectivity fault zone domain developed. This implies that, although the level of fracturing is relatively high in the damage zone, they may still not act as conduits, due to the presence of interlayered marl horizons, clay filled fractures and the presence of gouges in the fault core, as these are all factors retarding fluid flow along both the vertical and the horizontal directions, respectively.

3.5.3. Modelling fractured reservoirs in 3D

LiDAR based 3D modelling of vein networks in the damage zone of the large displacement normal fault at Selwick Bay was performed by using a new method, developed for this project (see Chapter 1.3.4). The output of the method was vein orientation, density and connectivity across the fault zone.

Vein orientation data gained from 3D modelling (Fig. 3.17a) show a very similar distribution compared to data, collected in the field, using traditional methods (Fig. 3.17b). The relative orientation of the IBZ and FC was found to be the same in the case of 3D modelling as for field-based measurements (Fig. 3.17). The orientations of veins in the damage zone were also found to be similar to that measured in the field, with most of the veins oriented sub-parallel to the IBZ and FC (Fig. 3.17). An additional advantage of the use of LiDAR technology is that data can be collected and analysed for the total height of the outcrop, enabling to collect data more representative of the entire outcrop.

Vein density values, gained from 3D models, are strongly dependent on the particular aspect ratios chosen for the fractures (Fig. 3.18a). For high fracture aspect ratio (1/1, 1/2, 1/3) the models obtained are unable to resolve the internal architecture of the fault zone. However, for

the lowest aspect ratios (1/5, 1/8), the models obtained display the main characteristics of the fault zone that were also identified from the 1D and 2D quantitative data. The models show an increasing trend in vein density values towards the fault core, in the footwall damage zone, high vein density values throughout the damage zone between the FC and IBZ, and finally, no damage zone developed in the hanging wall of the FC. These trends are similar to the trends observed during 1D and 2D analyses of field data.

Similarly to the vein density data, the vein connectivity data, gained from 3D modelling (Fig. 3.18b), are strongly dependent on the particular aspect ratios used to model the collected dataset. 3D models, obtained by assuming high aspect ratios (e.g. 1/1, 1/2, 1/3) do not reveal the same internal architecture of the fault zone as shown by the 2D datasets. On the other hand, 3D models obtained by using lower aspect ratios (e.g. 1/5, 1/8) reveal the internal architecture of the fault zone, as the same sub-domains as those identified from 2D datasets can be recognised. Overall, vein connectivity values are generally low in the protolith (both in the hanging wall and footwall) and in the WCDZ, while several times higher in the ICDZs both in the footwall damage zone and between the IBZ and FC.

In general, the 3D modelling of vein networks within the damage zone of the Selwick Bay large displacement normal fault was proven to be a useful tool to study the orientation distribution of veins and the internal architecture of the fault zone. When using low aspect ratio models (e.g. 1/5, 1/8), all of the studied fault zone attributes (orientation distribution, vein density and connectivity) showed similar patterns than those shown by the analyses of 1D and 2D datasets. This suggests that LiDAR based 3D modelling is a useful tool to create fault zone models, and the method developed for this project can create realistic fault zone models.

3.5.4. 1D/2D versus 3D quantitative analyses: validating 3D models and estimating realistic fracture aspect ratios

Results from quantitative analyses of 1D and 2D data collected at the Selwick Bay large displacement normal fault have been used to validate the different 3D models, obtained for a range of vein aspect ratios. The different methods used to analyse the collected data (e.g. 1D and 2D) show that there is no fractured damage zone developed in the hanging wall of the fault; hence only data from the footwall have been used for comparison and validation of the models obtained from 3D datasets. From each different quantitative method (i.e. 1D and 2D) and 3D models an average vein density and connectivity value have been calculated for a series of fault orthogonal transects, located in the footwall protolith, the WCDZ and the ICDZ, respectively. Following the procedures described in Chapter 1.3.5, average vein density and connectivity values of the protolith, WCDZ and ICDZ have been normalized to the protolith values for all the methods. Finally, the normalized values obtained have been used to calculate the misfit values between the different methods.

The normalized vein density values are 5, 2 and 5 times higher in the WCDZ than in the protolith according to 1D, 2D outcrop scale and 2D microscale results, respectively (Fig. 3.21a). The normalized vein density values for the ICDZ are 8, 3 and 7 times higher than in the protolith for the 1D, 2D outcrop scale, and 2D microscale results, respectively (Fig. 3.21a). In comparison, 3D models obtained for fracture aspect ratios between 1/1 and 1/8 show that normalized vein density values for the WCDZ range between 0.8 and 1.6 and, for the ICDZ, range between 1.4 and 2.3 (Fig. 3.21a). The normalized results of 3D models give lower vein density values than the 1D and 2D results in the WCZ and ICDZ (Fig. 3.21a). They are more similar to the results obtained by the 2D outcrop scale digital image analysis study.

Normalized vein connectivity values show a different pattern (Fig. 3.21b). Regardless of the scale of observation (e.g. from outcrop to microscale), 2D vein connectivity values are approximately 2 and 10 times higher in the WCDZ and in the ICDZ, respectively, compared to the protolith (Fig. 3.21b). In comparison, high vein aspect ratio 3D models (1/1, 1/2, 1/3) show an increase in vein connectivity values between 32 and 41 times in the ICDZ compared to the protolith (Fig. 3.21b). Lower vein aspect ratio models, 1/5 and 1/8, in the ICDZ, show an increase in vein connectivity values of approximately 16 and 20 times compared to the protolith (Fig. 3.21b). These latter two 3D models give vein connectivity values that are more similar to the ones calculated by 2D analyses than the former three.

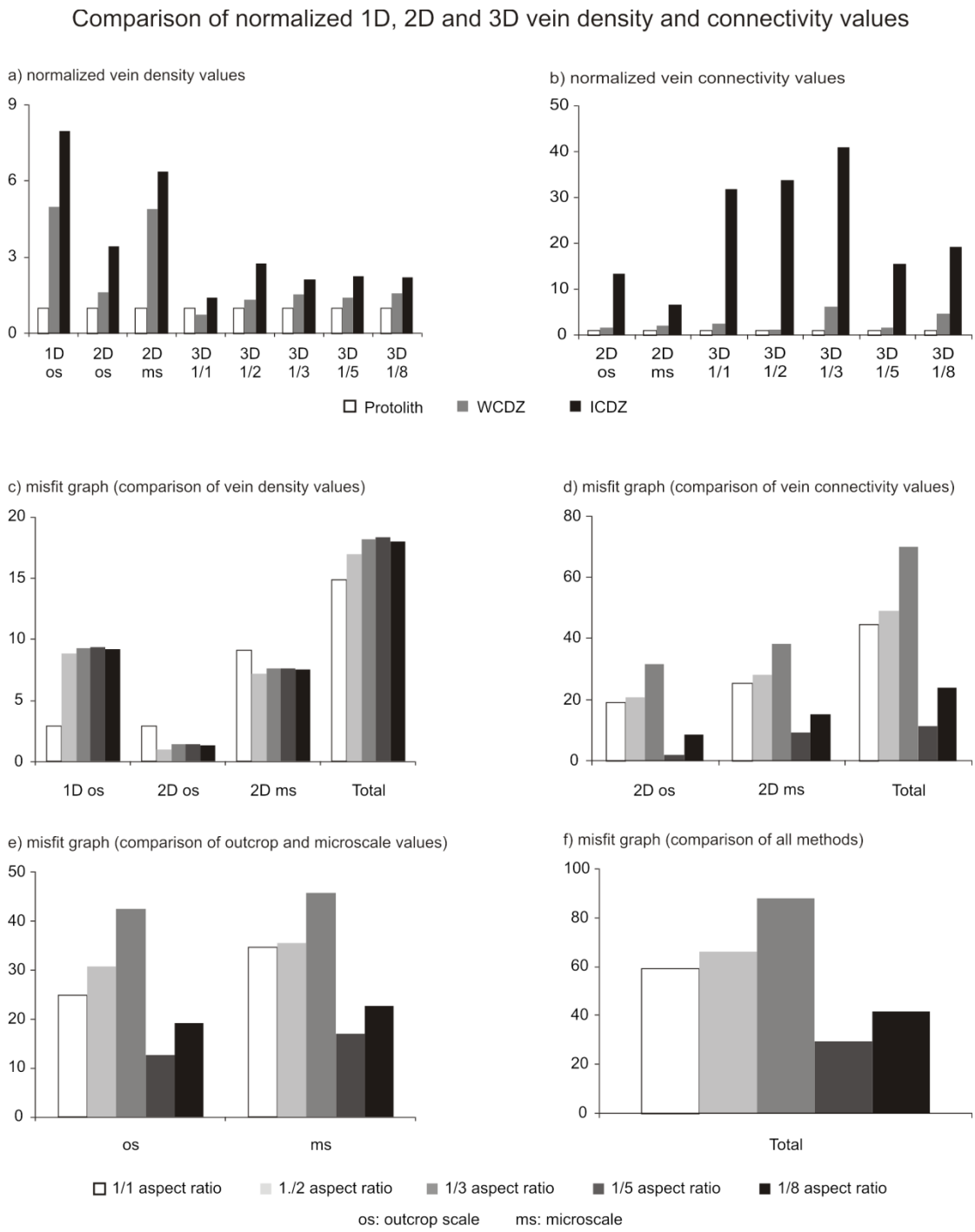

Figure 3.21 - : Comparison of normalized 1D, 2D and 3D vein density and connectivity values

a) normalized vein density values, b) Normalized vein connectivity values, c) Misfit graph (comparison of vein density values), d) Misfit graph (comparison of vein connectivity values), e) Misfit graph (comparison of outcrop scale and microscale results), f) Misfit graph (comparison of all methods)

For comparison, misfit graphs have been plotted for the results obtained from 3D models, for each different vein aspect ratio, and each of the 1D and 2D method results, respectively

(Fig. 3.21c-d). Misfit values range between 2.9 and 9.3 when the different vein aspect ratio models are compared to density values of 1D outcrop scale results (Fig. 3.21c). The lowest misfit value was calculated for the density of the 1/1 vein aspect ratio model, while all the other 3D models are characterized by misfit values ranging between 8.9 and 9.3 (Fig. 3.21c). In case of 2D outcrop scale results, vein density misfit values for the different vein aspect ratio models range between 0.9 and 2.9 (Fig. 3.21c). In case of vein density, for this method the highest misfit value was calculated for the 1/1 vein aspect ratio model (2.9), while the other ones are characterized by misfit values ranging between 0/9 and 1.4 (Fig. 3.21c). Finally, the third method, where misfit values were calculated for normalized vein density values is the microscale 2D analysis (Fig. 3.21c). In this case, misfit values range between 9.1 (1/1 vein aspect ratio model) and 7.2 (1/2 vein aspect ratio model, Fig. 3.21c). In summary, the total misfit values calculated for the vein density results for the different vein aspect ratio 3D models, range between 14.9 (1/1 fracture aspect ratio model) and 18.3 (1/5 aspect ratio model) (Fig. 3.21c). The difference between the smallest and largest misfit value is only 18%.

In general, misfit values calculated for the vein connectivity results, regardless of the particular 1D/2D method for comparison, are considerably higher and vary across larger ranges (Fig. 3.21d). Misfit values, in case of the 2D outcrop scale analysis for vein connectivity results range between 2.1 (1/5 vein aspect ratio) and 31.9 (1/3 vein aspect ratio) (Fig. 3.21d). While high vein aspect ratio models (1/1, 1/2, 1/3) are characterized by misfit values over 20, low vein aspect ratio models (1/5, 1/8) are characterized by misfit values lower than 9 (Fig. 3.21d). Misfit values of vein connectivity, when different vein aspect ratio models are compared to 2D miscroscale analysis, show a similar pattern (Fig. 3.21d). Misfit values range between 9.5 (1/5 vein aspect ratio model) and 38.3 (1/3 vein aspect ratio model), and high vein aspect ratio models (1/1, 1/2, 1/3) are characterized by misfit values over 25,

while low vein aspect ratio models (1/5, 1/8) are characterized by misfit values lower than 15 (Fig. 3.21d). In summary the total misfit values calculated for the vein connectivity results for the different vein aspect ratio 3D models, range between 11.6 (1/5 fracture aspect ratio model) and 70.2 (1/3 aspect ratio model, Fig. 3.21d). The biggest calcualted misfit value is more than 6 times higher than the smallest.

To quantify whether or not the scale of observation has an effect on the calculated misfit values, a sum of different outcrop scale and microscale analyses were calculated (Fig. 3.21e). In this case, 1D and 2D vein density and connectivity values were summarized. Summarized misfit values of outcrop scale analyses range between 12.7 (1/5 fracture aspect ratio model) and 42.5 (1/3 fracture aspect ratio model, Fig. 3.21e). The pattern is similar to the vein connectivity misfit values, as initially these were characterized by higher misfits than the vein density results. Summarized misfit values of microscale analysis range between 17.1 (1/5 vein aspect ratio model) and 45.9 (1/3 vein aspect ratio model, Fig. 3.21e). Again, the pattern is similar to the vein connectivity misfit values for the reason explained above.

Finally, to find the overall most realistic 3D model and to estimate the mean aspect ratio of veins within the damage zone a summary of the misfit values were calculated for each vein aspect ratio (Fig. 3.21f). In this case, vein density and connectivity misfit values, regardless of the methods used (e.g. 1D and 2D outcrop scale, 2D microscale), were summarized. These summarized misfit values range between 29.9 (1/5 vein aspect ratio) and 66.3 (1/3 vein aspect ratio, Fig. 3.21). High vein aspect ratio models (1/1, 1/2, 1/3) are typically characterized by summarized misfit values over 60, while low vein aspect ratio models (1/5, 1/8) are typically characterized by misfit values lower than 42 (Fig. 3.21f)

The plotted misfit graphs can be used to validate the different 3D models and by comparing their misfit values, estimate the mean aspect ratio of veins within the damage zone. When the vein density of different 3D models were compared to 1D and 2D (outcrop and microscale) vein density values, the differences between the misfit values, characterizing the different 3D models, did not differ from each other significantly. This suggests that using vein density values only is not enough to validate the different 3D models and to determine the mean aspect ratio of veins. In fact, vein connectivity values also have to be used and compared. Misfit values, calculated for vein connectivity data, significantly differ from each other for most of the 3D models. For higher aspect ratio models (1/1, 1/2, 1/3) misfit values are considerably higher than for lower aspect ratio models (1/5, 1/8), and these high aspect ratio models can be treated as non-realistic models. On the other hand, the higher aspect ratio models are the more realistic ones, characterized by lower misfit values, regardless of which 1D and 2D methods these are compared to.

The 3D model, characterized by the overall smallest misfit values, therefore the most realistic one is the 1/5 vein aspect ratio model. Accordingly, the method estimates that the mean aspect ratio of fractures within the damage zone is 1/5. Based on field observation, Schulz and Fossen (2003) concluded that the aspect ratio of veins typically ranges between 1/1 and 1/10. The 1/5 mean aspect ratio of fractures calculated in case of the Selwick Bay large displacement normal fault is in the middle of this range, confirming that this is the most realistic 3D model of the studied ones.

3.6.Conclusions

Qualitative and quantitative analyses of faults and fracture patterns in low porosity chalk at Flamborough Head show that:

(a) The infilling material of the small displacement normal faults is controlled by the protolith, in particular by the presence of interlayered marl horizons. When thick (cm-scale) interlayered marl/clay-rich horizons are present in the protolith rocks, no fluid assisted deformation features have been observed; conversely, in protolith rocks lacking the interlayered marls/clay-rich horizons, abundant evidence of fluid assisted deformation (e.g. hydraulic fracturing) has been observed. These observations suggest that small displacement normal faults, developed in highly fractured chalk, that contains interlayered marl horizons (Dykes End), can act as barriers for fluid flow, due to the sealing effect caused by the presence of clay that has smeared out along the fault planes and injected into the fractures of the damage zone. On the other hand, small displacement normal faults developed in chalk, where interlayered marl horizons are absent, can behave as conduits (Selwick Bay) for fluid flow, channellized within intensely fractured damage zones and within dilatant portions of the fault planes themselves (e.g. dilational jogs).

(b) In a predicted way, fracture vein increases gradually from the protolith towards the fault core, in the fault zone of the large displacement normal fault at Selwick Bay. However, vein connectivity has been observed to be much higher in the most inner parts of the damage zone, close to the fault core. As a result, the damage zone can be divided into two distinct domains, an intensively connected damage zone, close to the fault core, and a weakly connected damage, zone further away from it, towards the protolith rocks.

(c) High fracture density and connectivity domains are localized closer to the fault cores, where the damage zones of the large displacement normal faults are overlapping with each other. These intensively connected damage zones are the domains where most fluids are channelized and can represent critical sites of interest during reservoir analyses.

(d) Quantitative comparison of normalized vein density and connectivity values, gained from 1D and 2D methods, with 3D model results, obtained for different vein aspect ratios show that the most realistic model is the one which assumes 1/5 vein aspect ratio, suggesting that this value may be a realistic one to adopt when modelling reservoir fracture patterns and hydraulic transmissibility in chalk reservoirs with similar features as the one studied at Selwick Bay.

4. The Gubbio fault

4.1. Introduction

In general terms, fault zones can be described as objects with finite width, characterized by three main structural domains: a fault core, a damage zone and a protolith i.e. (Chester et al., 1993; Sibson, 1977). In faults, hosted in low porosity and low-permeability carbonates, the development of the different fault zone domains, each characterized by different fault rocks, such as cataclasites, breccias, gouges and other deformation features, such as subsidiary faults, fractures and vein can strongly influence fluid flow, causing the fault to behave as a conduit or a barrier (e.g. Agosta et al., 2009; Billi et al., 2007; De Paola et al., 2006; Micarelli et al., 2006a).

To better understand fluid flow within carbonate hosted faults, other authors performed a range of multiscale quantitative analyses. For example, (Gaviglio et al., 2009) studied microporosity in the fault core using SEM images and found that porosity and, therefore permeability, decreases towards the fault plane, reducing fluid transmissibility; while (Mitchell and Faulkner, 2009) studied the damage zone of fault zones, using outcrop scale data, collected along 1D structural transects and from thin sections. The former authors quantified fracture density across the damage zone and found that fracture and vein density decreases moving away from the fault core towards the protolith.

Understanding the internal architecture and fluid transmissibility of regional scale faults have both scientific and economic importance. Intensively fractured rock volumes can behave as fractured reservoirs, where the fracture patterns can accommodate large volumes of fluids, or conversely, localized fault zones can behave as impermeable seals retarding fluid migration

(Agosta and Aydin, 2006; Agosta and Kirschner, 2003). If these faults are seismically active, they can act as "valves" (e.g. Sibson, 2000), by suddenly releasing trapped, overpressured fluids, which would increase earthquake hazards (e.g. Miller et al. 2004).

In this chapter, outcrop scale to microscale structural observations were integrated with 1D, 2D and 3D quantitative data, collected along the Gubbio fault, in the Northern Apennines of Central Italy. The Gubbio fault is a regional scale, seismically active, normal fault, with over 3 km displacement at its centre. It cuts through a carbonate multilayer with interlayered marl formations. The aim of this study was to produce quantitative, fault orthogonal 1D, 2D and 3D fracture and vein density and connectivity profiles at different positions along dip (in different lithologies) and along strike (at the tip and at the centre of the fault zone), which would be used to create a conceptual fluid flow model of the fault zone. Additionally, 3D fracture models of the fault zone were built to estimate the variation in 3D of the fracture/vein density and connectivity of the fault zone, which has then been used to infer 3D fluid flow patterns.

4.2. Geological setting and study areas

4.2.1. Geological setting

The Gubbio fault is a regional scale, seismically active, normal fault located in the Northern Apennines of central Italy (Fig. 4.1a). The Northern Apennines is a NE verging fold and thrust belt, formed by NW-SE convergence between the Sardo-Corso block (part of the European plate) and the Adriatic block (part of the African plate) (Dewey et al., 1989, Fig. 4.1a).

The integration of field-based geological data and seismic data acquired by Agip in the 1980s and during the CROP03 project in 1993 (Pialli et al., 1998) showed four main stratigraphic units in the region. From bottom to top these are a) Paleozoic-phyllitic basement, that never crops out in the Umbria-Marche region, but has been identified in deep wells both offshore the Adriatic sea and onshore, next to Perugia, b) Triassic evaporites (Evaporiti di Burano formation) containing anhydrites and dolomites, that only crop out further west from the Gubbio fault, in Tuscany, in the core of a few partially eroded anticlines, c) Jurassic-Oligocene Carbonate multilayer, present in several outcrops in the NW region of the Gubbio area and d) Miocene turbidites (Marnoso Arenacea formation) cropping out in the SE region of the Gubbio area and in Western Umbria (Barchi et al., 1998b; Mirabella et al., 2004, Fig. 4.1b). The seismic data, shot by AGIP were calibrated with borehole data, using strong marker reflectors such as the Bisciaro formation at the base of the Moicene turbidites, the Marne a Fucoidi formation, interlayered within the carbonate multilayer, the top of the evaporates and the top of the Paleozoic basement (Anelli et al., 1994; Bally et al., 1986).

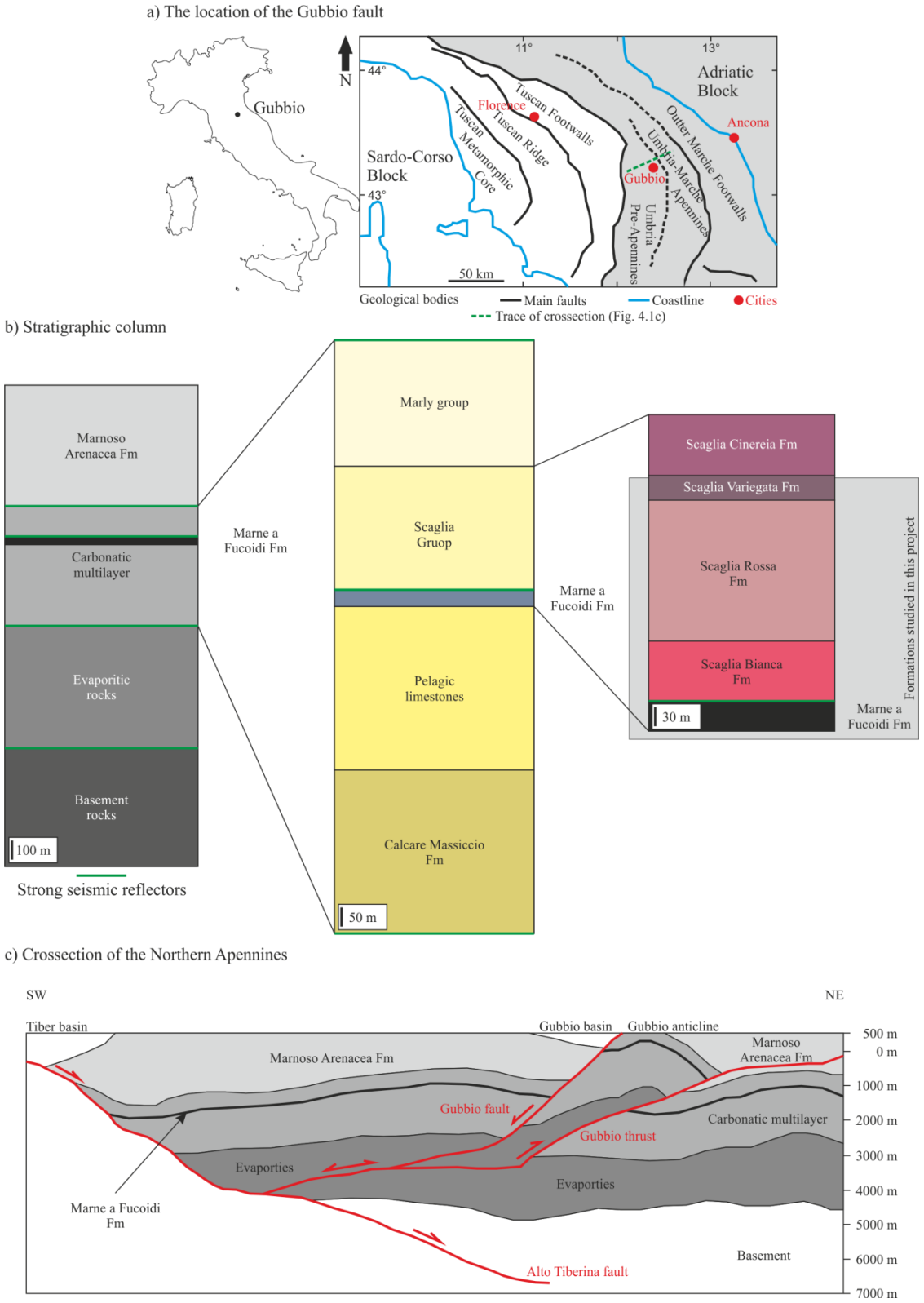

Figure 4.1 - Geological background I

a) Location of the Gubbio fault within Italy and within the fold and thrust belt of the Northern Apennines, b) Stratigraphic column of the different formations present in the study area; after Mirabella et al. (2004), c) Crossection of the Northern Apennines based on seismic data; after Mirabella et a. (2004)

In this chapter, data collected from the Marne a Fucoidi formation and the overlying Scaglia group (e.g. pelagic limestone) are presented. Both units are located stratigraphically within the carbonate multilayer (Fig. 4.1b). The Marne a Fuciodi is a 45-90 m thick, Aptian-Albian (100-125 My) formation with high organic content, containing black marly shale, representing an anoxic event (Alvarez et al., 1977; Alvarez and Montanari, 1988; Montanari and Koeberl, 2000 and references therein). The Scaglia group consist of four different formations that are from the oldest to the youngest: the Scaglia Bianca, Scaglia Rossa, Scaglia Variegata, and the Scaglia Cinerea formations. The Cenomanian Scaglia Bianca (93-100 My) lays directly above the Marne a Fucoidi formation. The contact between the two units is gradational, as the clay content of the rock decreases upwards. The Scaglia Bianca formation is a 50-70 m thick unit of well-layered, white, micritic limestones, with an average bedding thickness of approximately 15-20 cm. The Scaglia Bianca formation is separated from the overlying Scaglia Rossa formation by the Bonarelli Level, representing another anoxic event at the end of the Cenomanian (Alvarez and Montanari, 1988). The Turonian to Early Eocene Scaglia Rossa formation (40-93 My), similarly to the Scaglia Bianca formation, consists of micritic limestones, with 15-20 cm bedding thickness. Beds of the Scaglia Rossa formation are varying red, due to different oxidizing conditions. The total thickness of the Scaglia Rossa formation is up to 400 m. The Scaglia Rossa formation is divided into four members based on the variation in the presence of cherts. Additionally, the K/T boundary is also found within this unit. Above the Scaglia Rossa formation lays the Middle to Upper Eocene Scaglia Variegata formation, that is a chert free, marly limestone with a total thickness of up to 40 m. Beds within this greyish formation are only approximately 5 cm thick. The youngest member of the Scaglia group is the Oligocene, marl and clay rich, Scaglia Cinerea formation, but this formation does not crop out in the study areas.

The Gubbio fault is one of the many, seismically active, SW dipping normal faults in the Umbria-Marche region (Boncio and Lavecchia, 2000), antithetic to the regional scale, NE dipping, low angle Alto Tiberina normal fault (Fig. 4.1b). It extends from Cittá di Castello to Perugia, over 55 km (Boncio et al., 2000; Boncio et al., 1998; Collettini and Barchi, 2002). Other major SW dipping faults in the region are the Colfiorito and the Norcia faults. These faults are all seismically active, with recent large earthquakes, such as the 1979 Norcia (Mw=5.5, Deschamps et al., 1984), 1984 Gubbio (Mw=5.3, Dziewonski et al., 1985), and 1997 Colfiorito (Mw=6, Ekström et al., 1998) earthquakes (Fig. 4.2a).

The Umbria-Marche region has gone through three main phases of deformation in response to the north-eastward migration of the compressive stress field due to the collision between the Sardo-Corso block and the Adriatic block (De Paola et al., 2006) and references therein (Fig. 4.2b). The first phase of deformation affecting the Gubbio area was an early-orogenic extension in the foreland of the belt during the Lower Miocene (Mirabella et al., 2004). Such extension in the foreland is a result of the flexural bending of the lithosphere, which is also known as peripheral bulge (Doglioni, 1995). The extensional field migrated towards the NE through time, in response to the migration of the fold and thrust belt towards the same direction, and is currently active in the Adriatic Sea (Barchi et al., 1998a). In the Gubbio area, early-orogenic extension was followed by a syn-orogenic compression phase during the Upper Miocene (second deformation phase(De Paola et al., 2006). The third and final

a) Earthquake record of the Northern Apennines

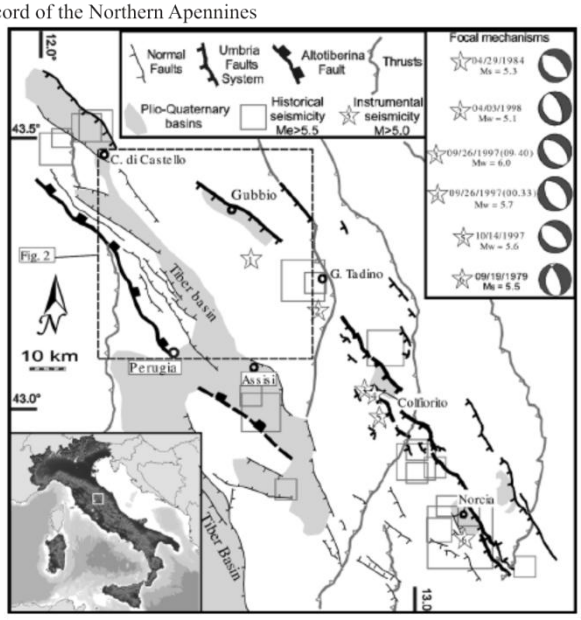

b) Extensional and compressional phases of deformation affecting the Gubbio area

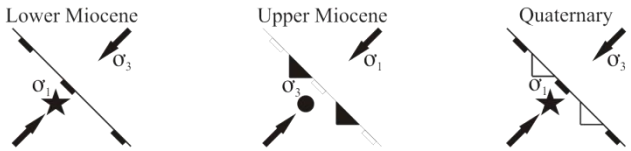

c) Displacement along the Gubbio fault based on seismic data

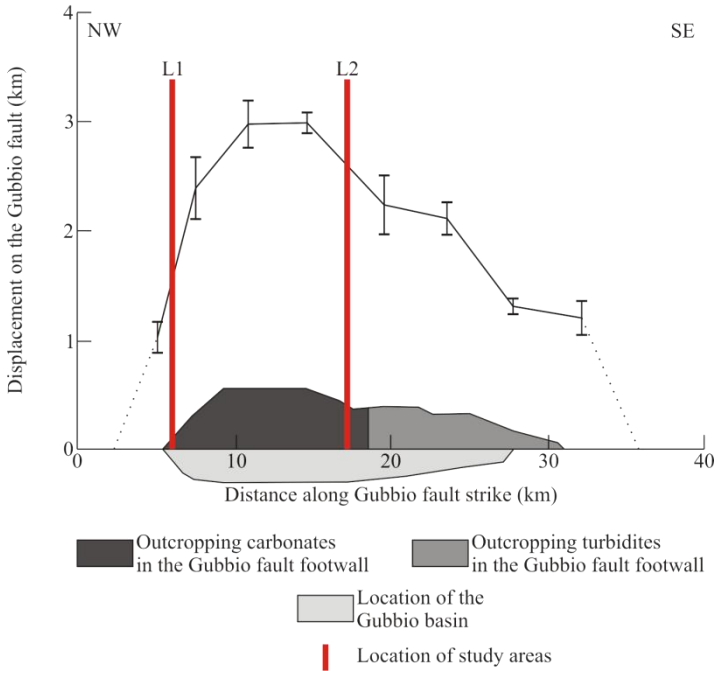

Figure 4.2 - Geological background II

a) Earthquake record of the Northern Apennines; after Mirabella et al. (2004), b) Phases of deformation affecting the Gubbio area; after De Paola et al. (2006), c) Displacement along the Gubbio fault based on seismic data; after Mirabella et al. (2004) with the study areas marked

phase of deformation affecting the Gubbio area is a late-orogenic extensional phase, currently occurring in the hinterland of the Northern Apennines fold and thrust belt. In the Gubbio area, this extensional phase started in the Quaternary and is responsible for the seismicity that still occurs in the region (Fig. 4.2b).

Based on interpretation of seismic profiles, Mirabella et al. (2004) found that the Gubbio normal fault initially formed during the first extensional phase, in the Miocene, and at depth it was linked to the Alto Tiberina low angle, normal fault (Fig. 4.1c). During the second phase of deformation, the compressional regime, the early Gubbio fault was reactivated at depth as a thrust and broke to the surface on the NE side of the Gubbio anticline, that itself was also a deformation feature, produced by the compressional event (Fig. 4.1c). At the last phase of deformation the early Gubbio normal fault reactivated, this time as a normal fault, producing the Gubbio basin in its hanging wall (Mirabella et al., 2004). During the different deformation phases the stress field was close to Andersonian with σ_2 always oriented NW-SE, while σ_1 oriented approximately vertical during the first and third phase and SW-NE during the second phase of deformation (De Paola et al., 2006, Fig. 4.2b).

The Gubbio fault can be traced at the surface for about 20 km (Fig. 4.3a), its hanging wall is downthrown to the SW and is currently buried under Quaternary, alluvial sediments forming the Gubbio basin SW from the fault (Fig. 4.1c). In the hanging wall, on the NW half of the fault the Scaglia Group crops out while towards the SW it is the Miocene Turbidites. Based on the seismic profiles, acquired by Agip, (Mirabella et al., 2004) studied the variation of displacement of the fault along strike (Fig. 4.2c). They found that the maximum displacement is approximately 3 km that decreases towards the tips of the fault. Maximum displacement is reached 2-3 km NW from Gubbio town. This point is closer to the NW tip of the fault than

the SE one (approximately 1/3 to 2/3), but located in the centre of that section of the fault where the Scaglia Formation crops out (Fig. 4.2c).

4.2.2. Study areas

In this chapter, data from two study areas are presented (Fig. 4.3a). The first locality studied is the Cemetery outcrop, located 2 km SE from Gubbio town (Fig 4.3a-b), where the displacement of the fault is 2.5 km (Fig. 4.2c, Mirabella et al., 2004). Hereafter this study area will be referred to as L1. The other study area is located 8 km NW from Gubbio town (Fig. 4.3a, c), and hereafter it will be referred as L2. This area comprises the "Cava Filippi" outcrop and a road section above Mocaiana village, where the displacement along the fault is estimated to be 1.5 km (Fig. 4.2c, Mirabella et al., 2004). The two localities at L2 are 200 m apart from each other along the strike of the Gubbio fault.

The fractures and veins, measured in the field can be classified based on their relative orientation to the Gubbio fault. Hereafter fractures and veins striking ±30º to the Gubbio fault (i.e. 105º-165º N) will be classified as fault parallel features, fractures and veins striking ±30º to the fault orthogonal direction (i.e. 15º-75º N) will be classified as fault perpendicular features and fractures and veins striking 0º-15º N, 75º-105º N, and 165º-180º N will be classified as features with other directions.

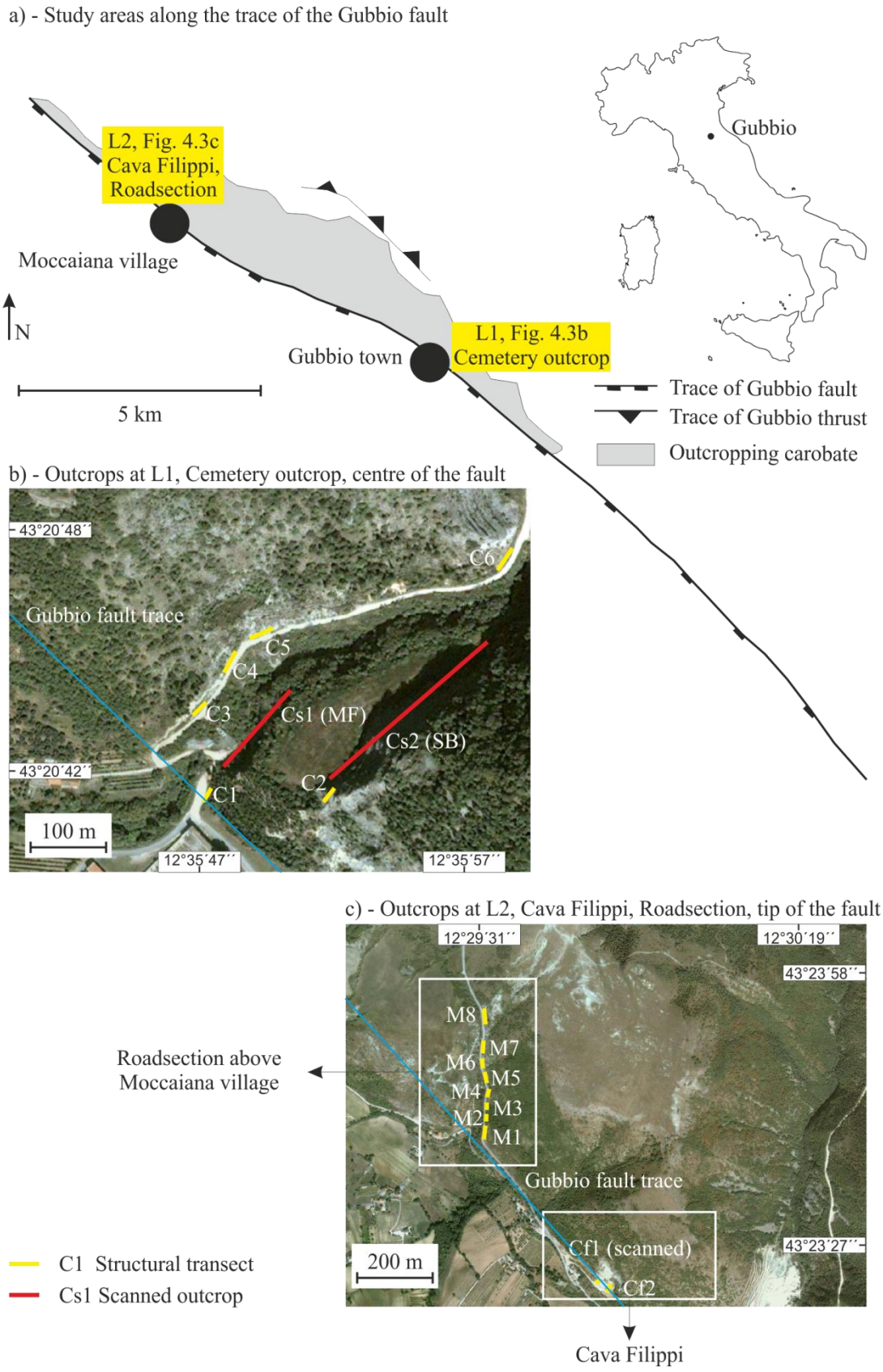

Figure 4.3 - Study areas

a) location of the Gubbio fault in the Northern Apennines and the study areas along the fault, after De Paola et a. (2006); b) studied outcrop sections at L1 (Cemetery outcrop); c) studied outcrop sections at L2 (Cava Filippi and Moccaiana roadsection)

Locality 1

At L1, structural data along 1D transects and outcrop photos for image analysis have been collected at 6 structural stations, located along both sides of a valley, running orthogonal to the strike of the Gubbio fault (Fig. 4.3b). On the SE side of the valley, the fault core-damage zone boundary can be observed in two small (up to 5-6 m) outcrop sections (C1 and C2 in Fig. 4.3b). Here, the most intensely fractured parts of the damage zone can also be observed. The first outcrop (C1) is located directly behind the cemetery, where the fault core is in contact with the Marne a Fucoidi formation. The second one (C2) is located on a plateau, approximately 30 m above C1, where the fault core is in contact with the Scaglia Bianca formation. On the NW side of the valley, outcrops with good exposures were studied along a minor road (C3-C6 transects on Fig. 4.3b). C3 transect is the closest to the fault core, it terminates only a few meters away from the fault core-damage zone boundary, exposing the Scaglia Bianca formation (Fig. 4.3b). Further to the NE, along the valley, the structural transects C4, and C5 are located about 40 m and 60 m away from the fault core respectively, both exposing the Scaglia Bianca formation. Finally, the structural transect C6 is located approximately 300 m away from the fault core, exposing the Scaglia Rossa formation.

3D LiDAR data were collected at the first locality (L1) along two different sections, both located on the SE side of the valley (Fig. 4.3b). The first one, CS1 located where the Marne a Fucoidi formation crops out along a 60 m section. This scanned section is bounded to the SW by the fault core-damage zone boundary. The second scanned section, CS2 is a 120 m long cliff section, located in a higher position than the previous section, exposing the Scaglia Bianca formation and being bounded by the fault core-damage zone boundary at its SW termination. These outcrops are well exposed, but, due to the high and steep cliffs, they were inaccessible for data collection using traditional methods.

Locality 2

The second study area, L2, at the tip of the fault (Fig. 4.3c), comprises the Cava Filippi outcrop, which is a quarry, where the fault core, the fault core-damage zone boundary and the most intensively deformed parts of the damage zone can be observed and studied along two continuous, NE-SW (fault perpendicular) trending outcrops, located on the opposite sides of the quarry (CF1 towards the NW, CF2 towards the SE, Fig. 4.3c). Structural data along 1D transects and outcrop photos for image analysis have been collected at these two localities.

Structural observations and quantitative data collected using 1D and 2D methods have also been collected at eight structural stations, located along the road section above Mocaiana village (Fig. 4.3c). These outcrops provide an almost continuous exposure of the entire damage zone of the Gubbio fault (M1-M6 transects, Fig. 4.3c) till the protolith (M7-M8 transects, Fig. 4.3c). Exposures of the damage zone lie within the Scaglia Rossa formation (M1-M6 transects) and exposures of the protolith lie within the Scaglia Variegata formation (M7-M8 transects), over 250 m away from the fault core.

At L2, 3D LiDAR data have been collected at the Cava Filippi outcrop, along the fault orthogonal, NE-SW trending CF1 transect (Fig. 4.3c). This section exposes the fault core and the most intensely deformed parts of the damage zone.

4.3. Structural field observations

4.3.1. The protolith

Field observations from four different lithologies, all affected by the deformation on the Gubbio fault, were collected and analysed. These lithologies belong to the Marne a Fucoidi, the Scaglia Bianca, the Scaglia Rossa and the Scaglia Variegata formations, from bottom to top in the stratigraphic sequence (for stratigraphic column see Fig. 4.1b).

The Marne a Fucoidi formation (observed at C1 section, on Fig. 4.3b) consists of interbedded carbonate and marl rich layers (Fig. 4.4a). The carbonates are usually organized in 5-10 cm thick beds. Each carbonate unit consists of 1-3 low porosity beds with light grey and light green colour. The marl units are usually 10-15 cm thick, with the thickest ones over 30 cm. Their colour varies from light green and grey to dark grey and black, possibly due to the changes in organic matter content. The marls are organised in small, slate-like sheets (Fig. 4.4b).

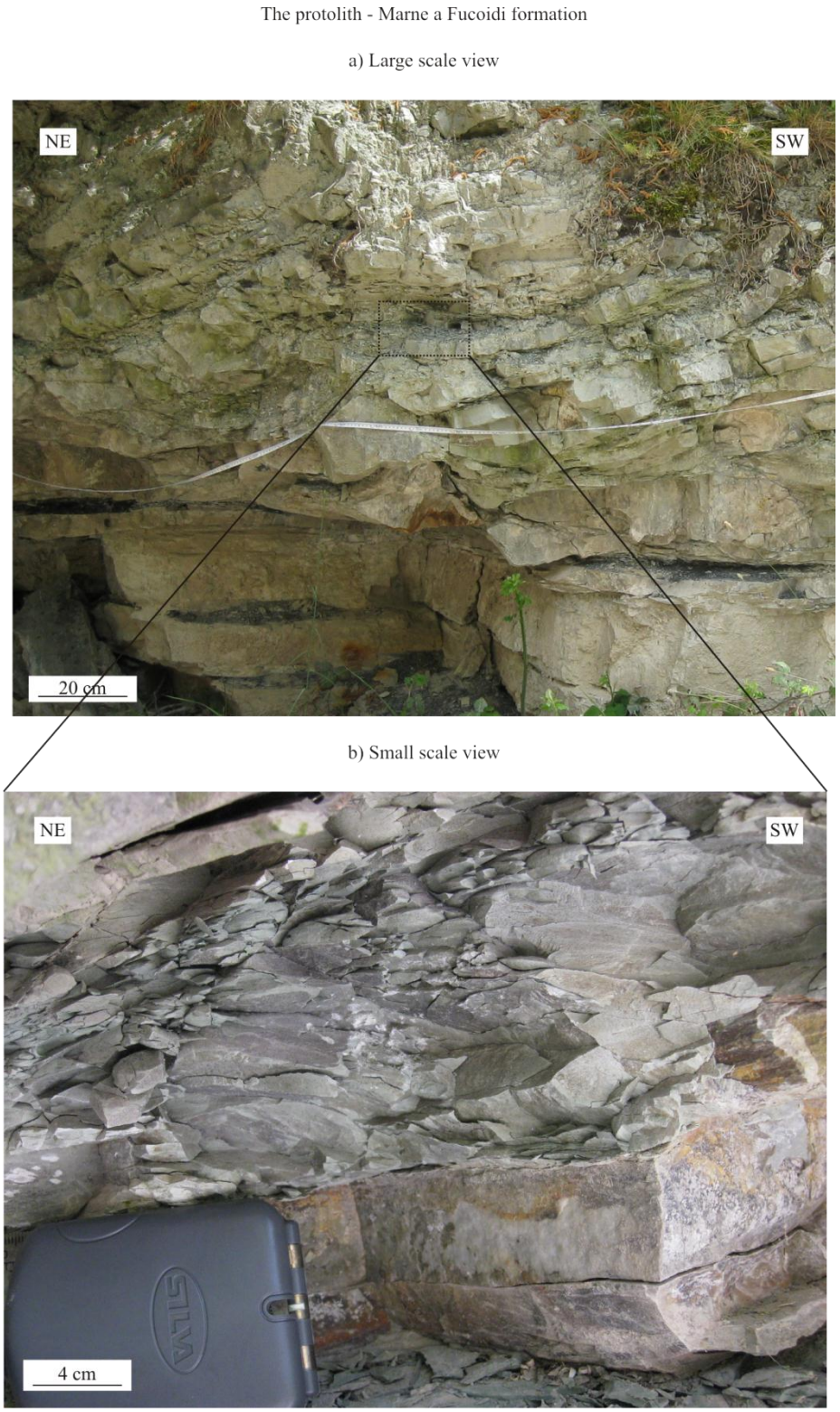

Figure 4.4 - The protolith - Marne a Fucoidi formation
a) large scale view, b) small scale view

The Scaglia Bianca formation (observed at C2-C5 sections on Fig. 4.3b) consists of low porosity carbonates and interlayered thin films of clay. The colour of the carbonates varies from bright white to light grey, and to yellow (Fig. 4.5a). Carbonate bed thicknesses range from 5 to 20 cm (Fig. 4.5b). Interlayered clays, representative of the gradual transition from the underlying Marne a Fucoidi formation to the Scaglia Bianca formation, are grey (Fig. 4.5c). Towards the bottom of the unit, close to the Marne a Fucoidi boundary, the presence of thin marl units can reach up to 40% of the total thickness (Fig. 4.5c).

The carbonates of the Scaglia Rossa formation (observed at C6, M1-M6 sections on Fig. 4.3b-c) are very similar to the Scaglia Bianca ones, apart from its colour that can vary on a wide scale from white to light pink and to dark red (Fig. 4.6a). Average bed thickness is between 15-20 cm and it appears to be uniform at all outcrops. Interlayered marl horizons are rare in the lower and upper members and are abundant in the middle part, which is almost entirely made of marls (Fig. 4.6b), sometimes with an undefined bedding.

The Scaglia Variegata formation (observed at M7-M8 sections, Fig. 4.3c) is characterised by interlayered, very thin limestone beds, with bed thicknesses ranging between 1 and 10 cm, and marls and clay rich thin layers, up to a few centimeters (Fig. 4.7a). The marly layers are affected by well-developed, pervasive, pencil cleavage fabric (Fig. 4.7b).

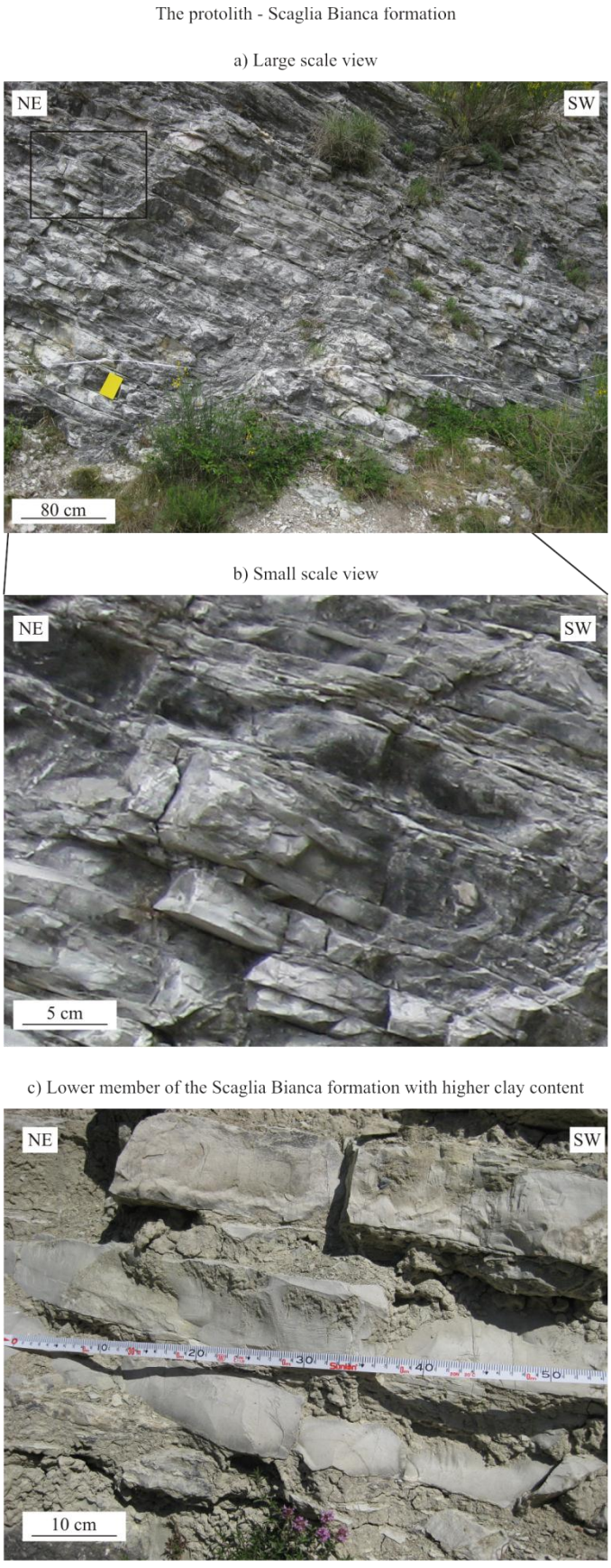

Figure 4.5 - : The protolith - Scaglia Bianca formation
a) large scale view, b) small scale view, c) lower member of the Scaglia Bianca with higher clay content

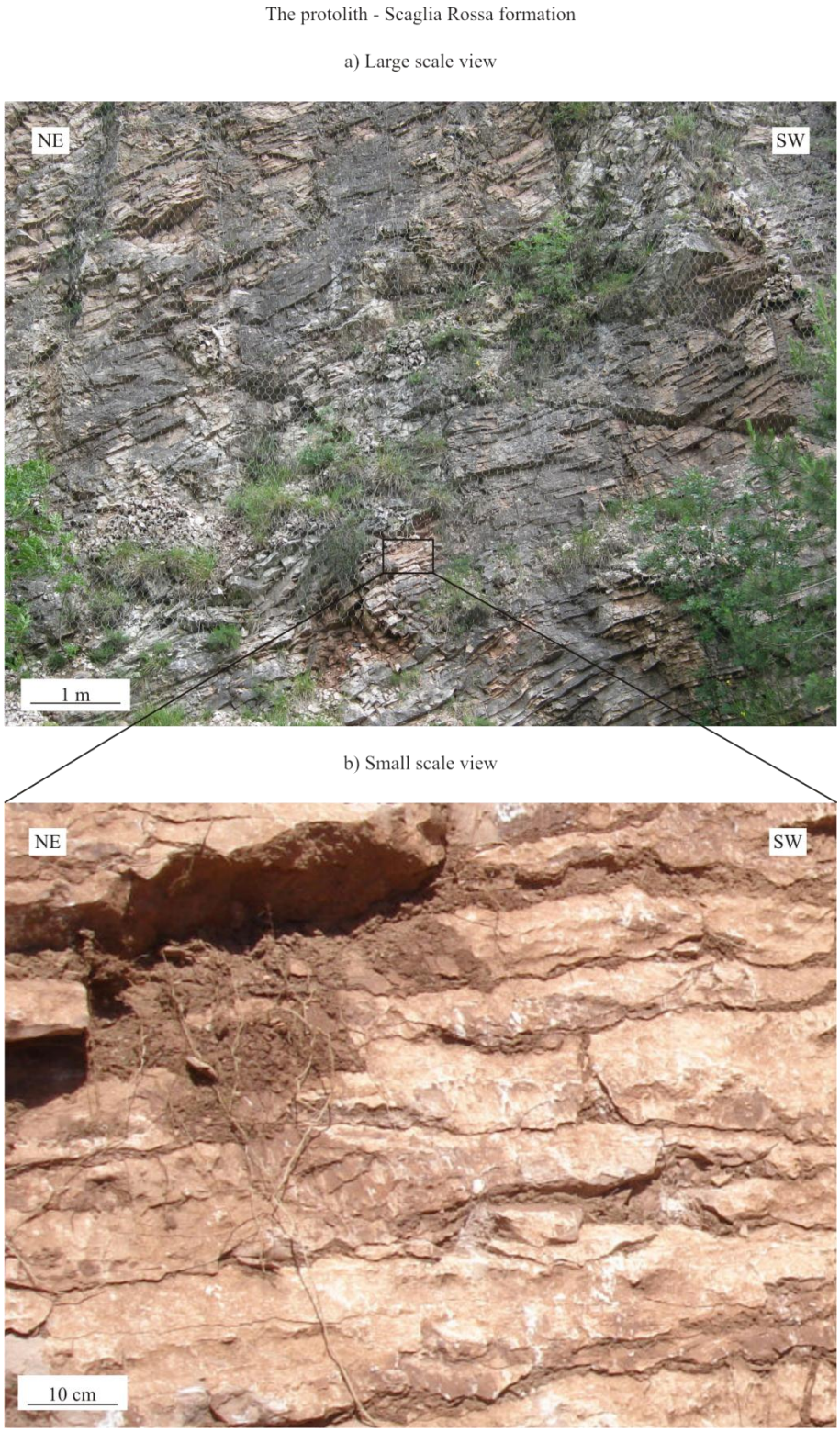

Figure 4.6 - The protolith - Scaglia Rossa formation
a) large scale view, b) small scale view

Figure 4.7 - The protolith - Scaglia Variegata formation
a) large scale view, b) small scale view

4.3.2. The damage zone

4.3.2.1. Locality 1

At L1 the damage zone of the Gubbio fault extends within the Scaglia Bianca formation from the fault core-damage zone boundary towards the protolith at outcrops C2-C5, and additionally, the most fractured parts of the Marne a Fucoidi formation can be observed on a short outcrop, C1, situated directly next to the fault core (Fig. 4.3b). Typical deformation features within the damage zone are fractures, veins, stylolites and subsidiary faults.

The Damage zone within the Scaglia Bianca formation

Within the Scaglia Bianca formation the damage zone is characterized by an increasing number of both fractures and veins as one moves from the protolith (beyond C5 on Fig. 4.3b) towards the fault core (before C2 on Fig. 4.3b). Orientation data shows that the fractures and veins are dominantly striking parallel to the Gubbio fault; however, fractures with other strike directions (e.g. fault perpendicular) are also present (Fig. 4.8a). The dips of the fractures and veins are larger than 60°. Most fractures and veins are pure extensional features and their thicknesses are typically 3-5 mm, although the widest ones can be up to 15 mm thick (Fig. 4.8b-c). The fractures and veins usually cut through more than 1 beds (Fig. 4.8c). Interlayered marl horizons, present in the lower parts of the Scaglia Bianca formation, are also affected by fractures and veins (Fig. 4.8c). These zones are characterized by several small cracks, mutually intersecting each other, opposed to one well defined fracture plane seen in the carbonate beds (Fig. 4.8c).

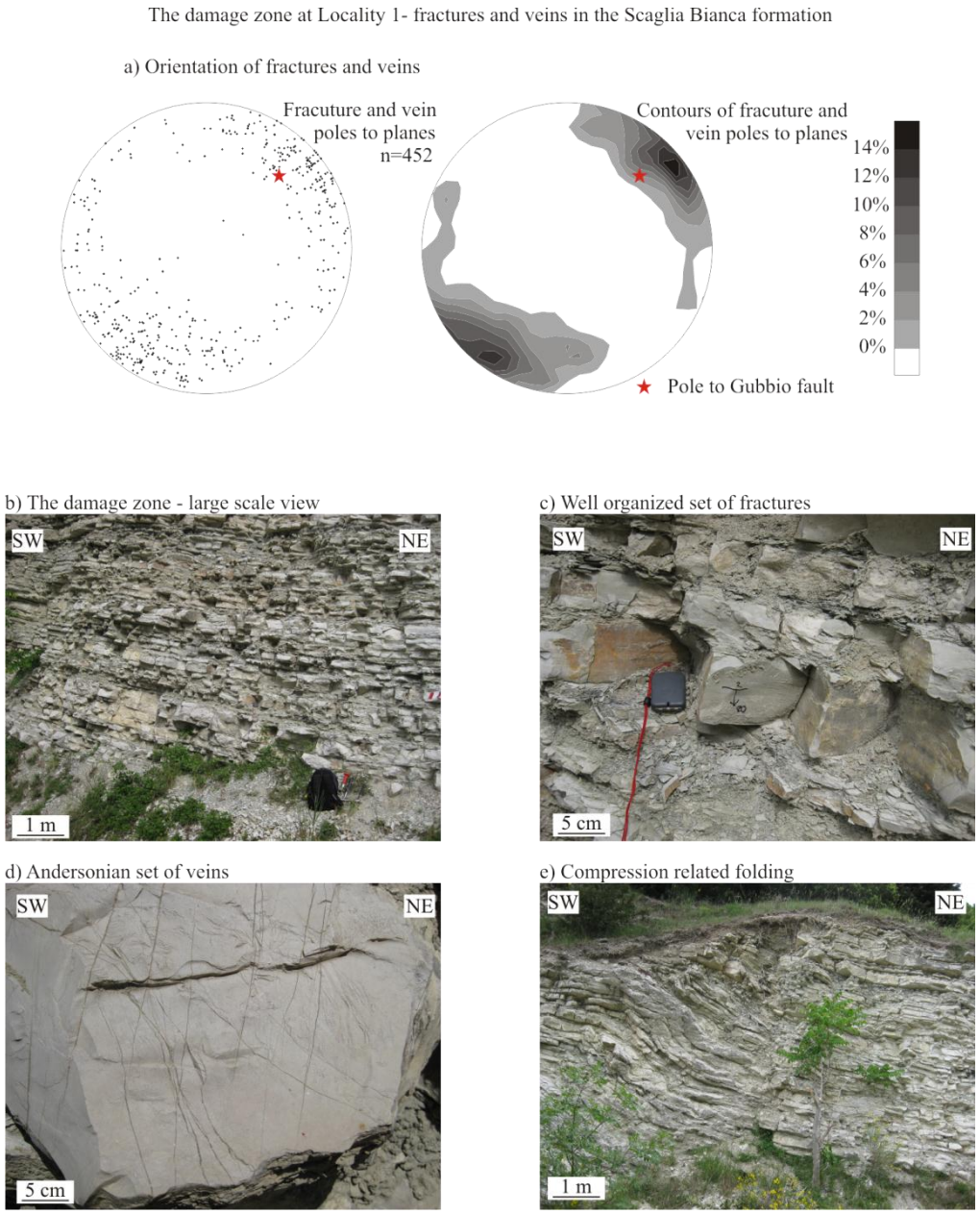

Figure 4.8 - The damage zone at L1 – fractures and veins in the Scaglia Bianca formation

a) orientation of fractures and veins, b) The damage zone – large scale, c) Well organised set of fractures, d) Andersonian set of veins, e) Compression related folding

Fracture/veins sets, striking sub-parallel to the Gubbio fault display an Andersonian geometry, with both Gubbio fault synthetic and antithetic dips. These are mutually intersecting each other (Fig. 4.8d). Additionally to fractures and veins, a few small folds are also present in the damage zone of the Gubbio fault (Fig. 4.8e). The hinge lines of these folds are sub-parallel to the Gubbio fault and are possibly related to the compressional phase of

deformation, also producing the Gubbio thrust and anticline. The presence of folds does not seem to affect the local values of density and connectivity.

Subsidiary faults are also relatively common features in the damage zone. Subsidiary faults, similarly to fractures and veins, can be subdivided based on their relative orientation to the Gubbio fault in parallel, orthogonal and different orientation ones, respectively (Fig. 4.9a). At L1, 13 subsidiary faults were observed in the damage zone, of which 8 (62%) are parallel to the Gubbio fault, 1 (8%) is perpendicular to it, while 4 (30%) are displaying different orientations (Fig. 4.9a). The slickenlines and relative offsets, observed and measured on the slip surfaces of the faults, show that fault-parallel subsidiary faults are always dip-slip normal faults (Fig. 4.9b); fault-perpendicular faults are always strike-slip faults (Fig. 4.9c); while subsidiary faults with different orientations show a range of kinematics from dip-slip to oblique-slip (Fig. 4.9d).

The normal displacement of the subsidiary faults ranges from 0.2-5 m. The subsidiary faults are characterized by a 10 cm to 1 m thick fault core and up to 1-5 m wide damage zone, surrounding the fault core (Fig. 4.9e). Fault rocks, found within their cores, are mostly cataclasites and breccias (Fig. 4.9f).

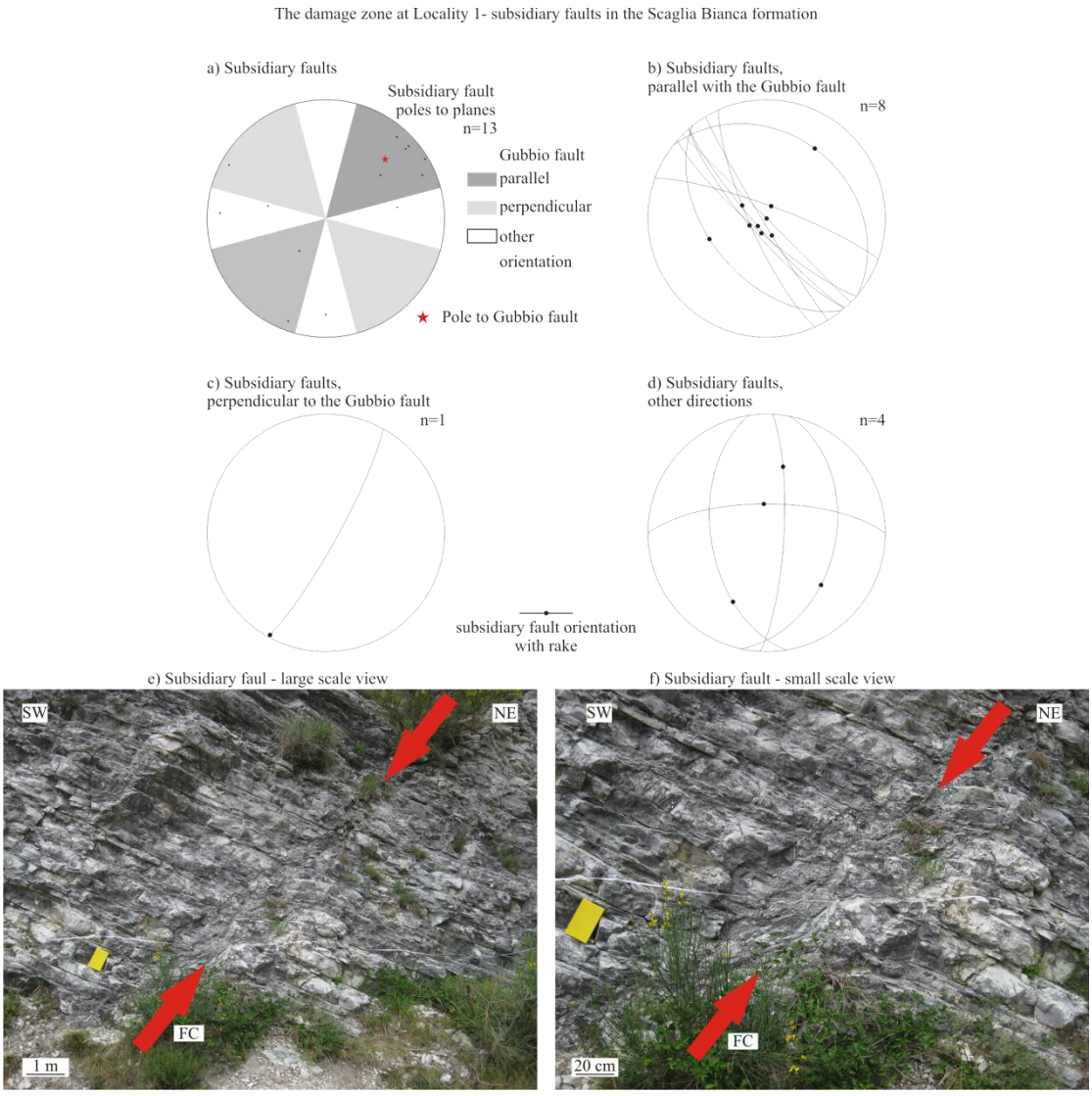

Figure 4.9 - The damage zone at L1 – subsidiary faults in Scaglia Bianca
a) Orientations of subsidiary faults, b) Subsidiary faults, parallel with the Gubbio fault with kinematic indicators, c) Subsidiary faults, perpendicular to the Gubbio fault, d) Subsidiary faults, other orientations, e) Subsidiary fault in Scaglia Bianca – large scale view, f) Subsidiary fault in Scaglia Bianca – small scale view

The Damage zone within the Marne a Fucoidi formation

The damage zone hosted in the Marne a Fucoidi formation was observed from a close distance along the C1 transect (for location see Fig. 4.3b), located next to the fault core. Additionally, parts of the damage zone within the Marne a Fucoidi formation can also be seen from the other side of the valley (Fig. 4.10a). From this distance the individual fractures cannot be seen, but some subsidiary faults can be observed. Some of these subsidiary faults are exposed on the over 20 m height of the cliffs. Since the

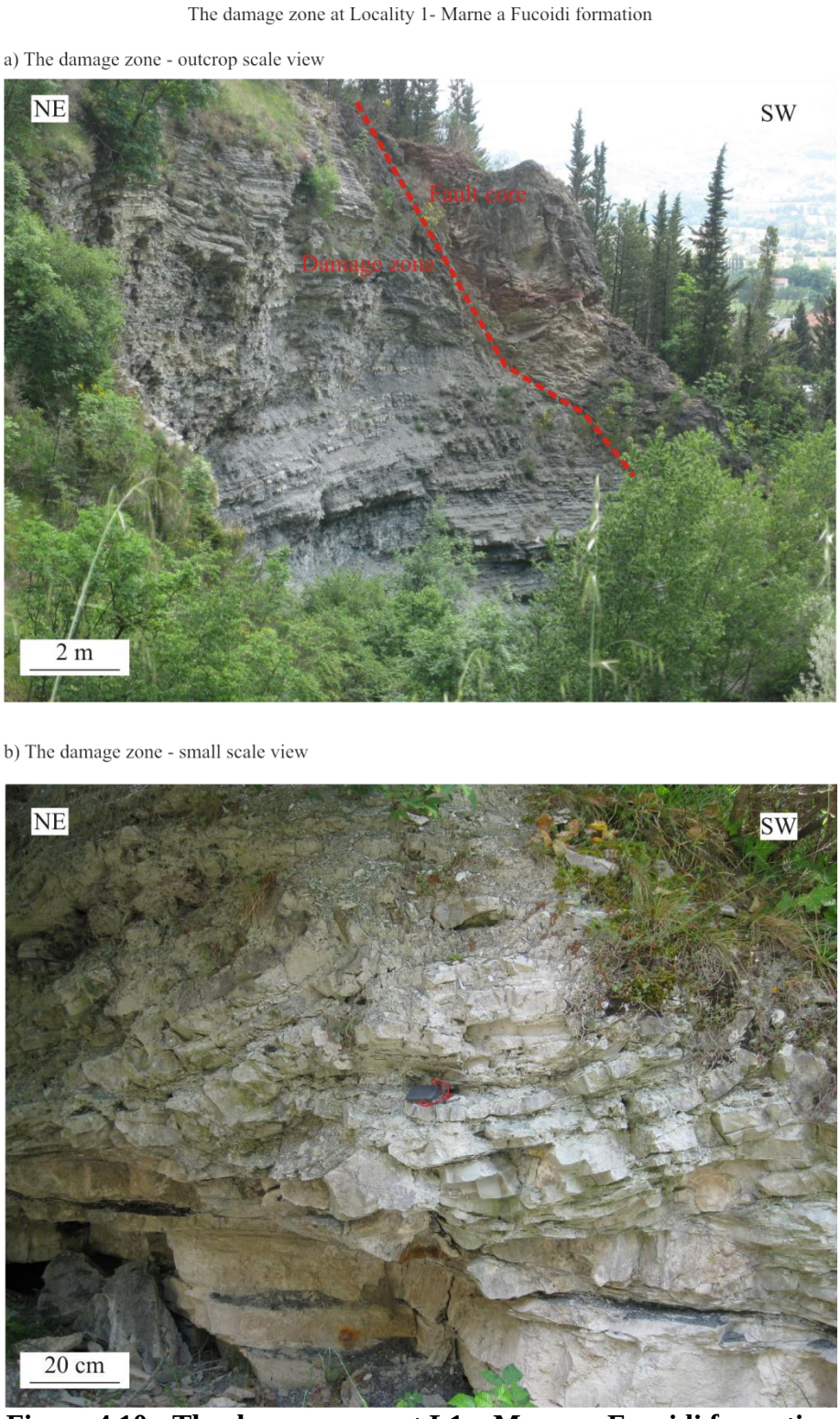

Figure 4.10 - The damage zone at L1 – Marne a Fucoidi formation
a) The damage zone – outcrop scale view, b) The damage zone – small scale view

total thickness of the formation is only between 45-90 m, it is possible that some of the subsidiary faults are cutting through the entire Marne a Fucoidi formation linking the Scaglia

Bianca formation with the Majolica formation, which underlies the Marne a Fucoidi formation.

Along the C1 transect, the Marne a Fucoidi formation shows that fracture density in this formation is high close to the fault core. These fractures are typically small cracks, not wider than 2 mm (Fig. 4.10b). Although fractures are very common features within the damage zone hosted within the Marne a Fucoidi formation, fluid assisted deformation features, such as veins have been very rarely observed.

4.3.2.2.Locality 2

The Damage zone within the Scaglia Rossa formation

At the second study area, L2, located closer to the tip of the fault, the damage zone in the Scaglia Rossa formation is displayed along outcrops M1-M6 (for location map see Fig. 4.3c). Fracture/vein orientations are scattered, with two mayor peaks, one being parallel with the Gubbio fault and the other one being perpendicular to it (Fig. 4.11a). The typical dips of the fractures and veins are larger than 60°. Both fracture and vein density appears to be increasing moving from the protolith (M6) towards the fault core (M1). Similarly to L1, most fractures and veins are pure extensional features, with only a few ones indicating hybrid shear-extensional behaviour, by displaying up to 5 mm offsets. Similarly to L1, fractures and veins cut through more than 1 bed (Fig. 4.11b). Fault-parallel and -perpendicular veins (related to the 1st and 3rd phases of extension and 2nd phase of compression, respectively at De Paola et al., 2006) are crosscutting each other (Fig. 4.11c). Some 3D exposures of beds allow the quantification of vein aspect ratios, that appear to be low (>1/5, Fig. 4.11d). A few folds are also present at L2. Within the folded sections some Gubbio fault sub-parallel veins are offset by up to 4 bedding planes within the fold (Fig. 4.11e).

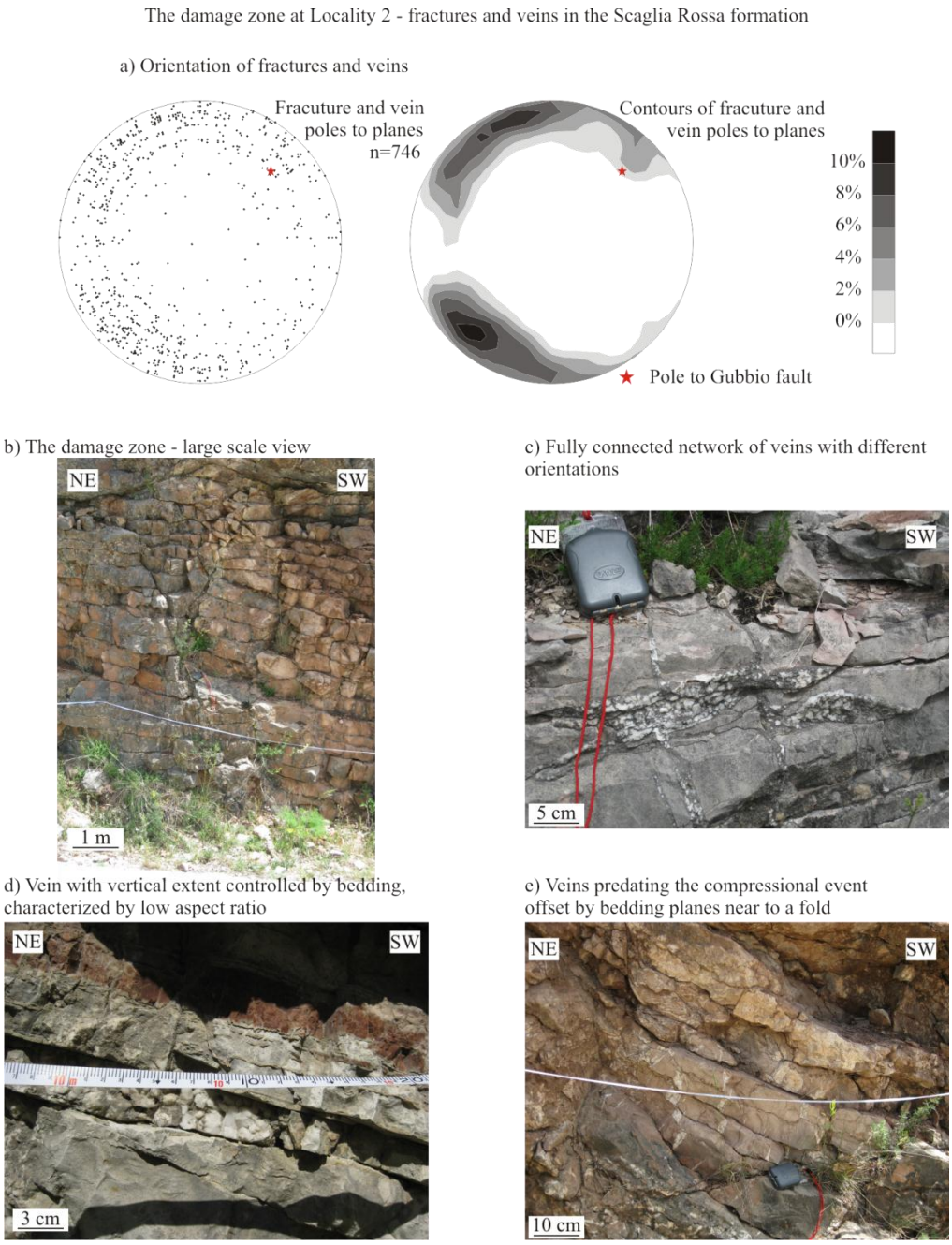

Figure 4.11 - The damage zone at L2 – fractures and veins in the Scaglia Rossa formation

a) orientation of fractures and veins, b) The damage zone – large scale view, c) Fully connected network of veins with different orientations, d) Veins with vertical extent controlled by bedding, characterized by low aspect ratio, e) Veins predating the compressional event, offset by bedding planes near to a fold

Subsidiary faults, developed at L2, are common features. These subsidiary faults can also be subdivided, as explained above, based on their orientation relative to the Gubbio fault, into

Gubbio fault-parallel, -perpendicular and other faults (Fig. 4.12a-d). At L2 a total of 35 subsidiary faults were observed (Fig. 4.12a), with 15 (43%) being parallel with the Gubbio fault (Fig. 4.12b), 14 (40%) being perpendicular to it (Fig. 4.12c) and a further 6 (17%) characterized by different orientations (Fig. 4.12d). Similarly to L1, kinematic indicators, observed on the slip surfaces of subsidiary faults, show that Gubbio fault parallel subsidiary faults are always normal faults (Fig. 4.12b), fault perpendicular faults are always strike-slip faults (Fig. 4.12c), while subsidiary faults with other orientations do not show a general sense of displacement (Fig. 4.12d).

The normal displacement of the subsidiary faults ranges from 0.5-5 m. The subsidiary faults are characterized by 10 cm to 1 m thick fault cores and 1 to 5 m thick damage zones, surrounding the fault core (4.12e). Fault rocks found in the fault cores of the subsidiary faults are cataclasites, breccias and sometimes gouges. The fault rocks are usually surrounding a well-defined slip surface (Fig. 4.12f). Occasionally, Gubbio fault parallel faults, characterized by synthetic and antithetic dips are cross-cutting each other displaying an Andersonian geometry (Fig. 4.12e) and high fracture density in their overlapping damage zones. The dip of these faults varies around 60°, one dipping to the SW, and one dipping to the NE, or one dipping approximately 80° to the SW and one 40° to the NE (Fig. 4.12e-f). In other cases, Gubbio fault parallel and perpendicular subsidiary fault can also mutually cross-cut each other.

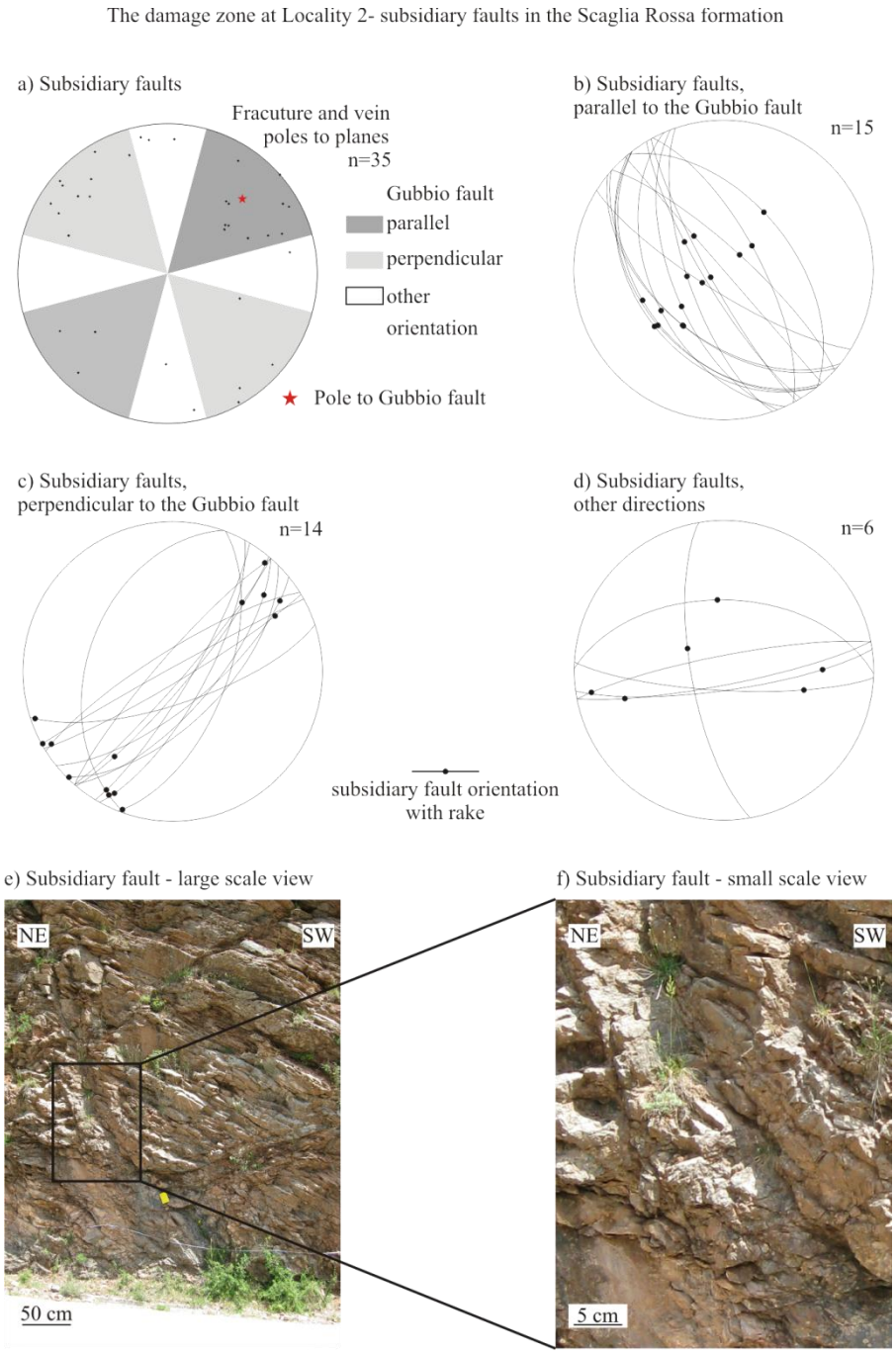

Figure 4.12 - The damage zone at L2 – subsidiary faults in the Scaglia Rossa formation
a) Orientation of subsidiary faults, b) Subsidiary faults, parallel to the Gubbio fault, c) Subsidiary faults, perpendicular to the Gubbio fault, d) Subsidiary faults, other orientations, e) Subsidiary fault in Scaglia Rossa – large scale view, f) Subsidiary fault in Scaglia Rossa – small scale view

4.3.3. The fault core

The fault core-damage zone boundary was observed at both studied localities, L1 and L2, as a sharp boundary, marked by a well-defined slip zone of gouges and fine grained cataclasites (Figs. 4.13, 4.14). At both localities, the fault core is more than ten meters thick and displays a complex internal architecture, made of different domains, bounded by discrete slip zones. Each fault core domain is characterized by its own suite of fault rocks.

4.3.3.1.Locality 1

At L1, the fault core-damage zone boundary and the fault core was observed at two locations, both at the SE side of the valley along C1 and C2 transects, where the damage zone is developed within the Marne a Fucoidi and the Scaglia Bianca formations, respectively (for locations see Fig. 4.3b).

Along the C1 transect, where the fault core is in contact with the Marne a Fucoidi formation, the fault core-damage zone boundary is represented by a 10 cm wide zone of dark gouges displaying s-c tectonites (Fig. 4.13a-b). Within the gouge a few, up to 1 cm long, clasts of carbonates from the host rock are visible. No evidences for fluid assisted deformation features have been observed here (Fig. 4.13b). The fault core at this locality is represented by up to 1 meter thick blocks of random fabric cataclasites, in which the carbonate clasts of the host rock are visible, up to 10 cm in size (Fig. 4.13a).

Along the C2 transect, where the fault core is in contact with the Scaglia Bianca formation, the fault core-damage zone boundary is a well-defined slip surface (Fig. 4.13c). Unlike the boundary along the C1 transect, here gouges are absent. In the damage zone side of the slip surface the Scaglia Bianca formation is heavily fractured and a few centimetre drag on the

beds can be observed. Within the fault core, towards the bottom of the outcrop, some bedding surfaces can still be recognised, but the rock is heavily brecciated (Fig. 4.13c-d). Within the fault core, the original beds of the host rock cannot be recognized and random fabric cataclasites are present (Fig. 4.13c).

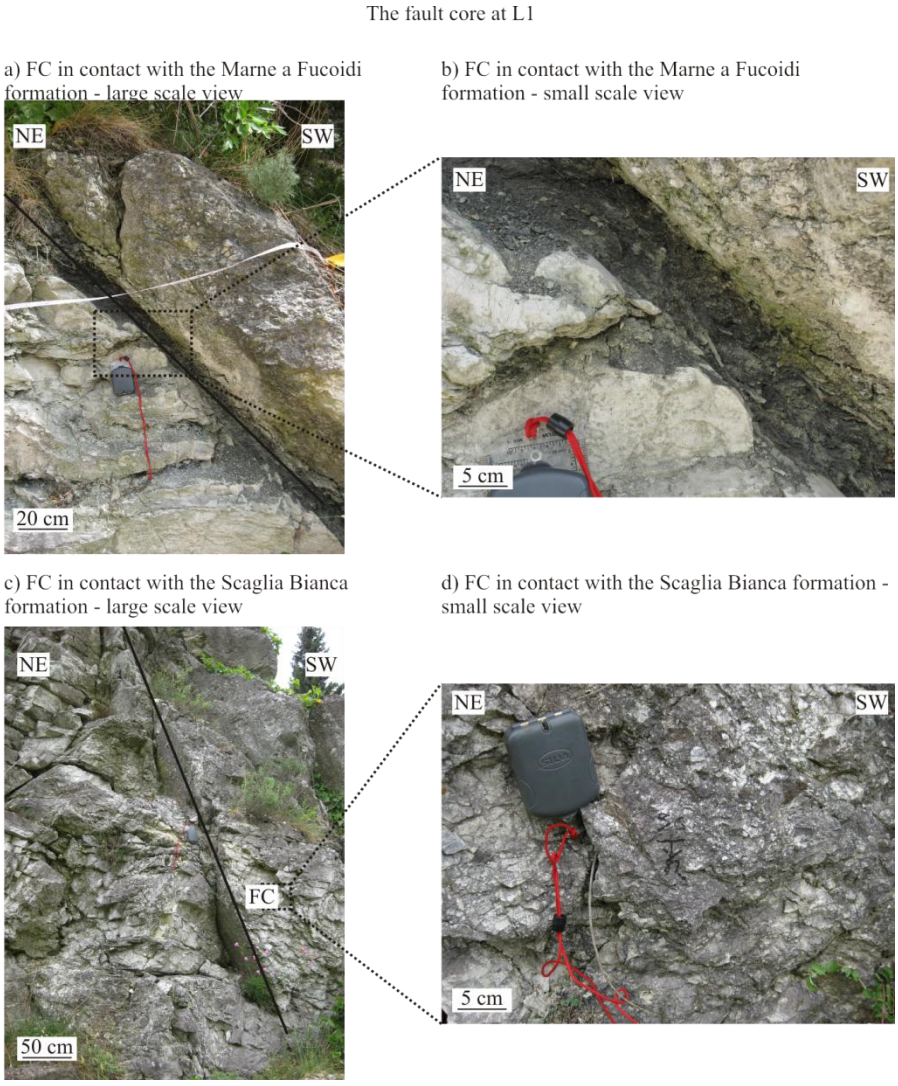

Figure 4.13 - The fault core at L1

a) The fault core in contact with the Marne a Fucoidi formation, large scale view, b) The fault core in contact with the Marne a Fucoidi formation, small scale view, c) The fault core in contact with the Scaglia Bianca formation, large scale view, b) The fault core in contact with the Scaglia Bianca formation, small scale view

4.3.3.2.Locality 2

At L2, at the Cava Filippi quarry, the fault core consists of five distinct domains, each bounded by well-defined slip surfaces (Fig. 4.14a). Hereafter these will be referred to as domain1 to domain5, progressively numbered from the fault core-damage zone boundary towards the hanging wall (Fig. 4.14a). The thicknesses of the fault core domains vary between 1 to 4 m (Fig. 4.14a-b). Due to the geometry of the quarry the fault core is exposed in two cliffs trending orthogonal to the main fault, one towards the NW (CF1 transect) and the other towards the SE (CF2 transect, for transect locations see Fig. 4.3c). The distance between the two cliffs is approximately 40 m. The fault core domains and the bounding slip surfaces identified on one cliff face can also be traced on the other one.

Along the CF1 transect the fault core-damage zone boundary is marked by a well-defined slip surface that shows a displacement of approximately 30±27 m (Bussolotto et al., 2007). This relatively small displacement can explain the small amount of fault rocks developed along this fault plane (Fig. 4.14a). Both in the hanging wall and footwall of the slip surface the beds of the host rock can still be recognized; however, these are tilted basinwards. The dips of the beds are approximately 10° and up to 40° in the footwall and hanging wall respectively (Fig. 4.14a-b). The rocks are characterized by intense veining with the veins orientated orthogonal to the bedding planes (Fig. 4.14b).

According to Bussolotto et al. (2007), the slip surface, separating domain1 and domain2, has a displacement of approximately 130±30 m. The host rocks, adjacent to the well-defined slip surface, are heavily brecciated, possibly due to the larger displacement along the plane. Small, cm-scale pores between the breccias are usually filled with crystalline calcite. Within domain2, that has a thickness of approximately 3 m, some bedding surfaces of the original

host rock are still recognisable (Fig. 4.14a). Interestingly, these beds are sub-horizontal (Fig. 4.14a). However, most of the domain is characterized by brecciated rocks that cover over 60% of the outcropping section. Similarly to the sections closer to the slip surfaces, in-between the breccias, pore spaces are usually filled with crystalline calcite.

The slip surface separating domain2 and domain3 has a displacement of 25±25 m (Busolotto et al. (2007). The exposed surface shows a planar geometry (Fig. 4.14a). Kinematic indicators suggest a pure dip-slip, normal displacement. Within domain3, foliated cataclasites are present, with the foliation plane striking parallel to the Gubbio fault itself. Within this domain none of the original beds are preserved (Fig. 4.14a).

Between domain3 and domain4 the displacement along the slip surface is less than 50 m (Busolotto et al., 2007). Close to the slip surface, within domain4, sc-tectonites are displayed alongside with minor slip surfaces that are sub-parallel to the Gubbio fault (Fig. 4.14d). Finally, the last slip surface observed along the CF1 transect has a displacement of approximately 60 ± 30 m (Busolotto et al., 2007). In the hanging wall of the slip surface, within domain5, the slip plane is bounded by an over 20 cm thick gouge layer, in which cm scale angular clasts of the original host rock can be observed (Fig. 4.14e). Along the CF1 transect the rest of the fault core, towards the hanging wall, has been artificially moved due to works in the quarry.

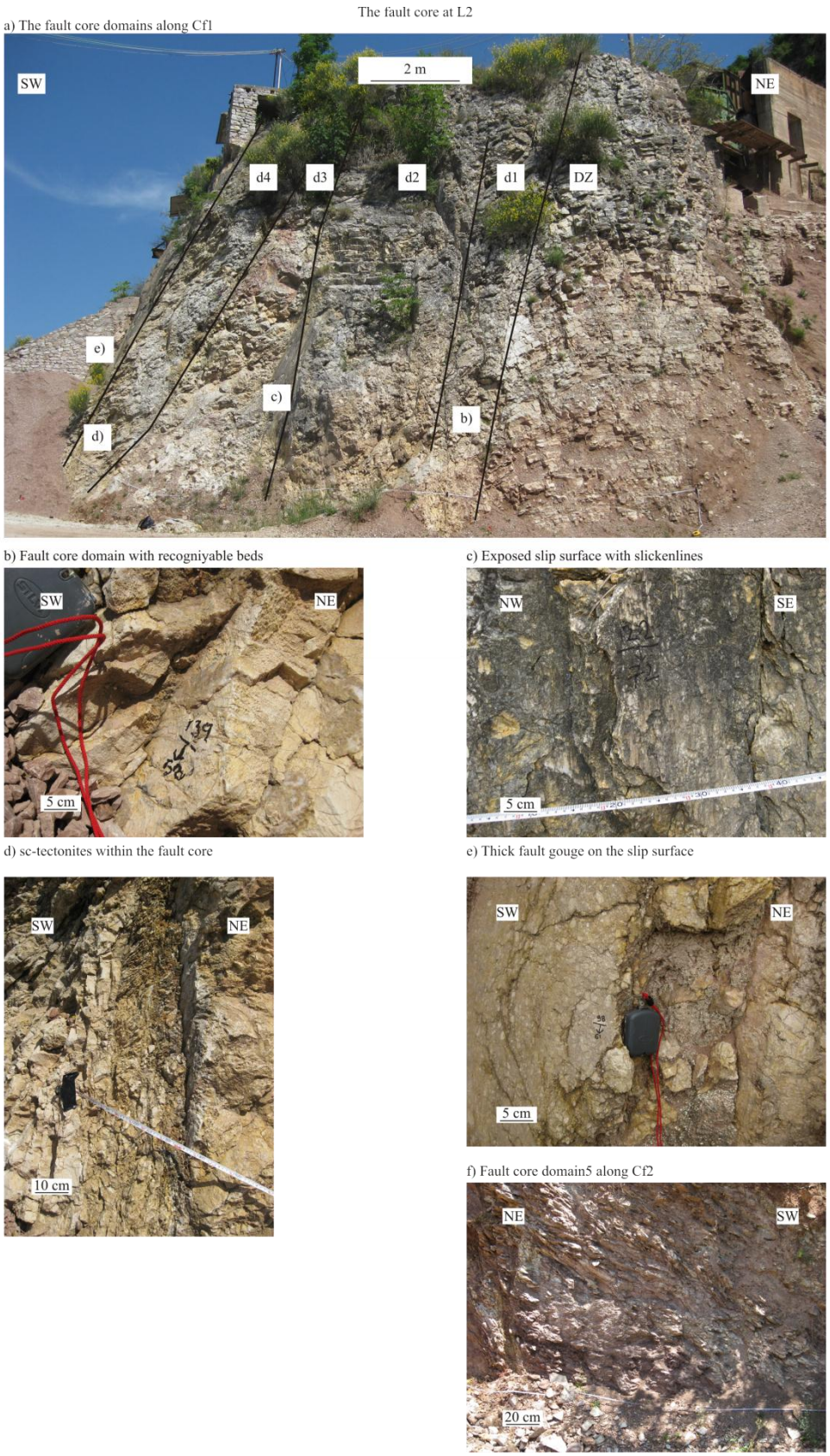

Figure 4.14 - The fault core at L2

a) The fault core and its domains along CS1 transect, with the fault core domains marked, b) Fault core domain with recognizable beds, c) Exposed slip surface with slickenlines, d) Sc-tectonites within the fault core, e) Thick fault gouge layer adjacent to a slip surface f) Fault core domain5 along CF2

Domain5 can be observed along the CF2 transect in the opposite side of the quarry. This domain is developed within red, marly carbonates (Fig. 4.14f). Some of the bedding surfaces are recognisable and are strongly tilted towards the SW. Cataclasites are also present within the domain, usually foliated ones, with the foliation plane striking parallel with the Gubbio fault. Veins and other fluid assisted deformation features are absent in this domain.

4.3.4. Microstructures

Microstructural observations were made on thin sections obtained from samples, collected from the fault core and from the damage zone at both study areas L1 and L2 (Fig. 4.15a, for detailed descriptions of the origins of samples see Table 4.2).

Fig. 4.15b is from a sample collected at L1, from the Scaglia Bianca formation, 110 m away from the fault core, representative of the protolith. The protolith is made of low porosity, low permeability micritic carbonates, with some fossil rich, bedding parallel bands. Thin (>0.1 mm) microcracks, sometimes filled with crystalline calcite, are commonly observed features.

Fig. 4.15c shows a picture of a sample that was collected at L1, within the Scalia Bianca formation, only 5 cm away from the fault core. It displays veins with anatomosing geometries, similar to the “zebra-rocks” observed by Holland and Urai (2010), in limestones, in Oman. The thickness of the veins varies between 0.01 mm and 2 cm, and the individual veins have a varying thickness that heavily depends on the intersections between the braids. Small clasts of the original host rock can be seen within the larger veins that are probably formed through hydraulic brecciation processes (Fig. 4.15c). The presence of styolites has an impact on the geometry of the veins present in the damage zone, as veins can be terminating

against stylolites (Fig. 4.15c, collected at L1, Scaglia Bianca formation, 42 m away from the fault core).

At L2, veins also display crack and seal textures, indicative of repeated openings along their median line (Fig. 4.15e sample CF17, collected at L2, Scaglia Rossa formation, 3 m away from the fault core). Within the fault core, at L2, precipitated calcite is common within the vuggy cavities between the brecciated rocks (Fig. 4.15g, samples CF25 and CF02, collected at L2 form domain2 and domain1, respectively). Minor slip surfaces and pressure solution structures are also common features on these samples.

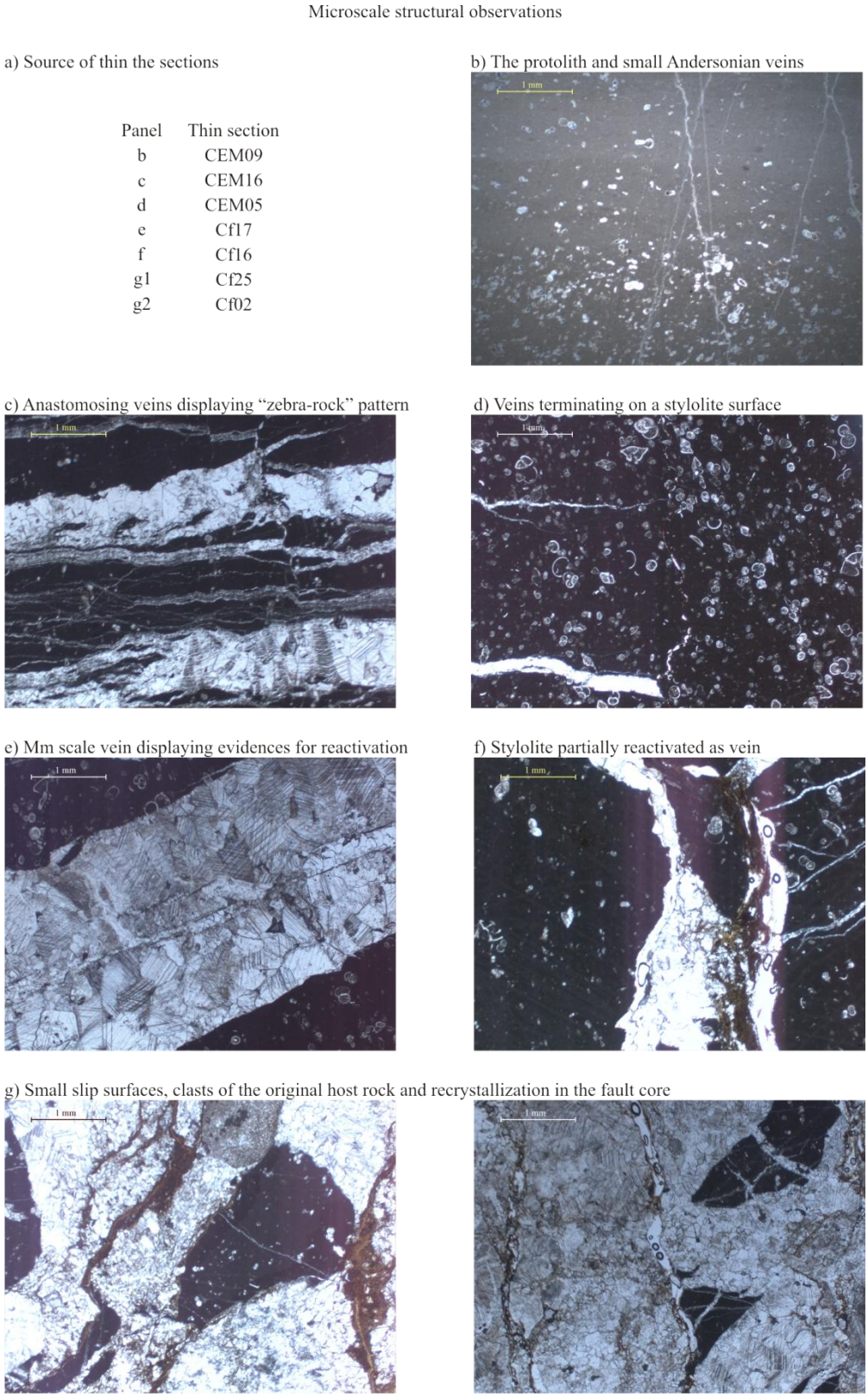

Figure 4.15 - Microscale structural observations

a) Source of the thin sections, b) The protolith and small veins; c) Anastomosing veins displaying "zebra-rock" pattern, d) Veins terminating on a stylolite surface, e) Mm scale vein displaying evidence for reactivation, f) Stylolite, partially reactivated as vein, g) Small slip surfaces, clasts of the original host rock and recrystallization in the fault core

4.4. Quantitative analysis

4.4.1. 1D Transects

4.4.1.1.Orientation data analysis (damage zone)

Orientation measurements of fractures and veins in the damage zone were made along structural transects at both localities, L1 and L2 (for transect locations at L1 and L2 see Fig. 4.3b and 4.3c respectively). As defined before, fractures and veins were classified based on their relative orientation to the Gubbio fault as fault-parallel, -orthogonal and other direction ones.

Locality 1

In the damage zone, at L1, 452 fractures and veins were measured (Fig. 4.16a). These features are characterized by scattered orientations, with a main set striking sub-parallel to the Gubbio fault (105°-165° N), with both synthetic and antithetic dips, and a secondary set of fractures and veins striking in a N-S orientation.

Fractures and veins were also studied separately from each other at L1 (Fig. 4.16b-c). Out of the total 452 features 312 (69%) were veins, compared to 140 (31%) fractures. Veins are mainly trending parallel to the Gubbio fault, with both synthetic and antithetic dips (53% of all veins); however, 11% of the veins show trends perpendicular to the fault and 36% are characterized with other orientations (Fig. 4.16b). In comparison to veins, fracture orientations are more scattered and characterised by three main orientations (Fig. 4.16c). A smaller peak is shown for fractures oriented perpendicular to the Gubbio fault (17 fractures, 12%), while two other peaks are oriented almost parallel to the fault (93 fractures, 67%). These two peaks are oriented about 15-20º away from the fault, and surrounding the peak of

fault parallel veins. The remaining 30 (21%) fractures are characterized by different orientations (Fig. 4.16c).

Fracture and vein datasets can be filtered based on their relative orientation to the Gubbio fault. If only fault parallel (105º-165º N) features are considered (Fig. 4.16d) the fractures and veins that are related to the Gubbio normal fault can be studied separately from other features forming the background fracturing, developed during the compressional phase, producing the Gubbio thrust and anticline (De Paola et al., 2006). At L1, a total of 193 Gubbio fault parallel fractures and veins were found along the transects (Fig. 4.16d), of which 111 (58%) were veins (Fig. 4.16d) and 82 (42%) were fractures (Fig. 4.16f). The Gubbio fault parallel veins show one main peak in their orientations, which strikes parallel with the Gubbio fault, but it is characterized by higher dips (>80º, Fig. 4.16e). In case of fractures, similarly to the observation made for the non-filtered data, there are two mayor peaks in their orientation, with strikes of 15-20º to the Gubbio fault and with dips, on average, slightly higher than the Gubbio fault itself (approximately 70º, Fig. 4.16f).

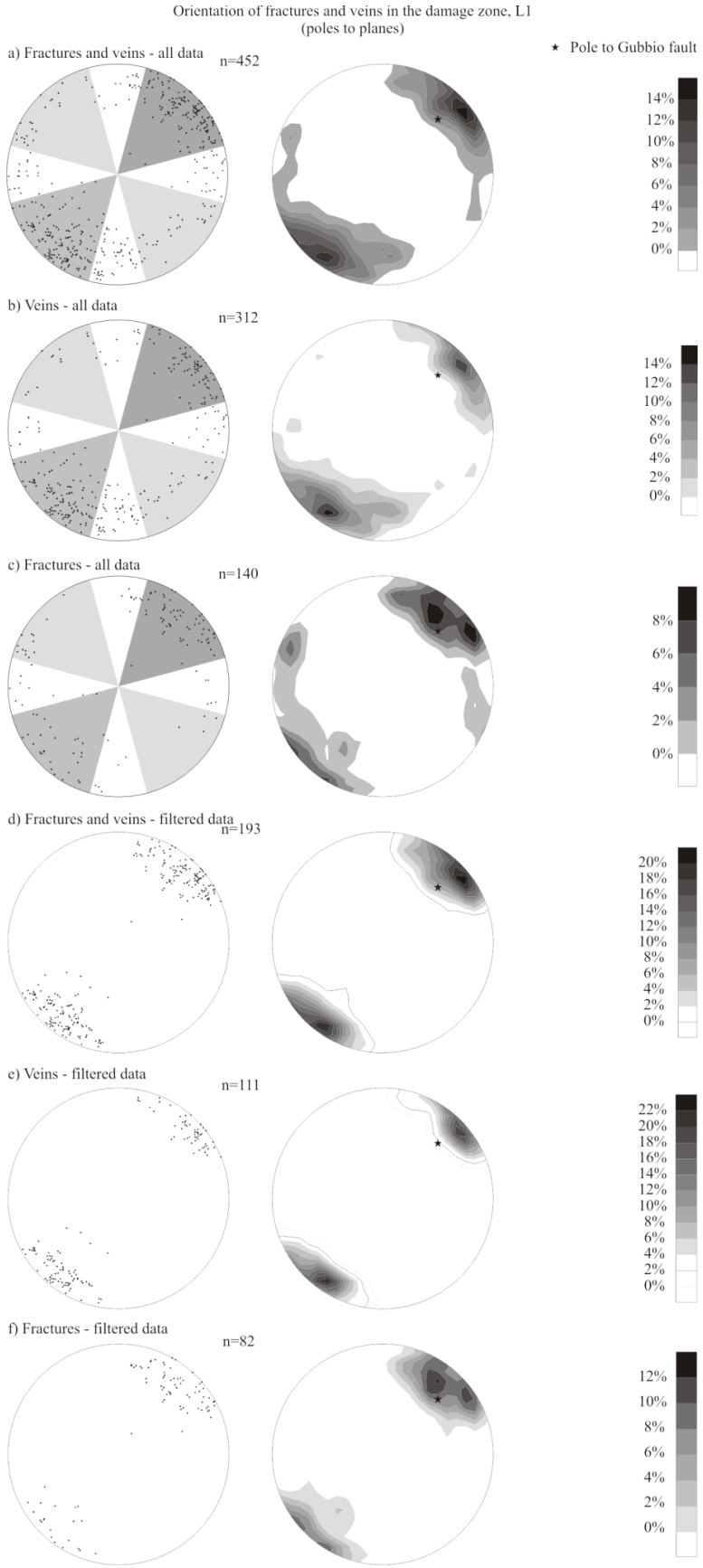

Figure 4.16 - Orientation of fractures and veins in the damage zone, L1
a) Fractures and veins – all data, b) Veins – all data, c) Fractures – all data, d) Fractures and veins – filtered data, e) Veins – filtered data, f) Fractures – filtered data

Locality 2

At L2, close to the tip of the fault, a total of 746 fracture and vein orientations were measured (Fig. 4.17a). Orientations at L2 are more scattered than at L1. There are two peaks in the data, one with Gubbio fault parallel strikes and with dips mainly antithetic to the Gubbio fault (dips >70º). The other peak shows fractures and veins striking approximately orthogonal to the Gubbio fault and dipping to the SE with dips larger than 75º (Fig. 4.17a). Between the two peaks there were several E-W striking fractures and veins measured but less N-S striking ones. Using the fracture and vein classification, based on their relative orientation to the Gubbio fault, 312 fractures and veins (42%) are striking parallel to the Gubbio fault, 230 (31%) are striking in the orthogonal direction and a further 204 (27%) are characterized by different orientation.

At L2 there were slightly more veins (396, 53%) found and measured than fractures (351, 47%). Orientation distribution of both features are more scattered here than at L1 (Fig. 4.17b-c). Veins are organized in two well defined sets: there are 204 (52%) veins parallel with the Gubbio fault and 105 (26%) perpendicular to it. The rest of the veins (87, 22%) are characterized with different strike directions (Fig. 4.17b). The orientations of fractures are characterized with one highly scattered peak (Fig. 4.17c). This peak ranges from NW-SE striking, fault zone parallel fractures, through E-W striking fractures to NE-SW striking, fault perpendicular fractures. On the contrary, N-S striking fractures are relatively rare. Using the fracture and vein classification, based on their relative orientation to the Gubbio fault, 126 (35%) fractures are fault parallel, 113 (33%) are fault orthogonal and a final 112 (32%) are characterized with different strike directions (Fig. 4.17c).

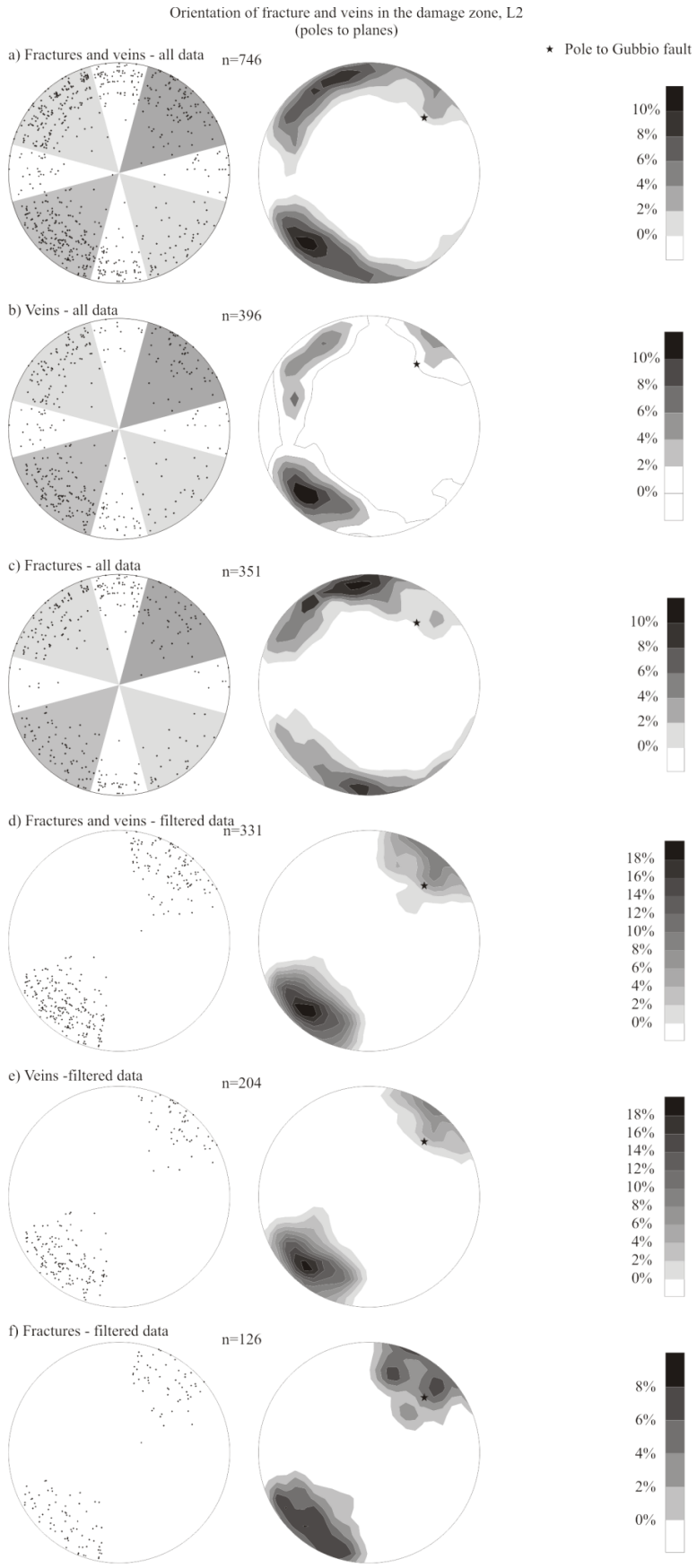

Figure 4.17 - Orientation of fractures and veins in the damage zone, L2
a) Fractures and veins – all data, b) Veins – all data, c) Fractures – all data, d) Fractures and veins – filtered data, e) Veins – filtered data, f) Fractures – filtered data

If fractures and veins are filtered based on their relative orientation to the Gubbio fault, then fault parallel ones can be studied separately from the other ones. If only fault parallel (105º-165º N) fractures and veins are considered, their orientation distribution shows that the orientation of these features are scattered around the orientation of the Gubbio fault (Fig. 4.17d). Veins are mostly oriented sub-parallel to the Gubbio fault with one peak, which is characterized by both Gubbio fault synthetic and antithetic dips, typically larger than 75º (Fig. 4.17e). On the contrary, fracture orientations are more scattered, with two mayor peaks that are, similarly to L1, 15-20º off the Gubbio fault and are surrounding the peak, observed in the vein orientation (Fig. 4.17f).

4.4.1.2.Quantitative analysis of fracture and vein density in the damage zone

Fracture and vein density were calculated as the number of features counted per meter on a transect, as described in Chapter 1.3.1. Hereafter summarized density (and connectivity in case of 2D and 3D analyses) values of fractures and veins will be referred to as fracture/vein density (and connectivity in case of 2D and 3D analyses).

Summary results of fracture/vein density from both localities are shown in figure 4.18. Figure 4.18a shows all fracture/vein data, regardless of their relative orientation to the Gubbio fault. Fracture/vein density values are gradually decreasing moving away from the fault core-damage zone boundary towards the protolith (Fig. 4.18a). Fracture/vein density values close to the fault core are around 10/m and they decrease to constant background fracturing values of about 5/m. The damage zone has been defined as the portion of the fault zone where fracture and vein density values decay from peak values, measured close to the fault core, to the background values measured in what is considered as the protolith. The width of the damage zone, so defined, can be estimated as at least over 200 m (Fig. 4.18a).

Locally, within the damage zone, some local and narrow peaks of 15-20/m fracture/vein density values are observed (Fig. 4.18a). These zones are interpreted as due to the presence of subsidiary faults damage zones.

Fracture and vein density data have been analysed for selected orientations of the individual features, parallel (Fig. 4.18b) and orthogonal (Fig. 4.18d) to the main trend of the Gubbio fault, respectively. The Gubbio fault parallel data allow the estimation of an over 200 m wide damage zone, similarly to the results obtained when using the whole fracture and vein dataset (Fig. 4.18a). In particular, fracture/vein density values are especially high (>15/m) close to the fault core-damage zone boundary and decrease according to a power-law trend when moving towards the protolith, where background fracture/vein density values are less than 2/m (Fig. 4.18b). The best-fit power law trendline is

$$y=16.947x^{-0.446},\ R^2=0.60.$$

The best-fit trendline obtained for the Gubbio fault parallel fracture and vein density data can be normalized to the background values of the protolith, which are assumed as 1 (Fig. 4.18c). This allows and easier and direct estimation of the relative increase in fracture and vein density from the protolith to the fault core-damage zone boundary. In this case, the normalized trendline obtained shows that fracture/vein density is over 10 times higher at the fault core-damage zone boundary than in the protolith (Fig. 4.18c).

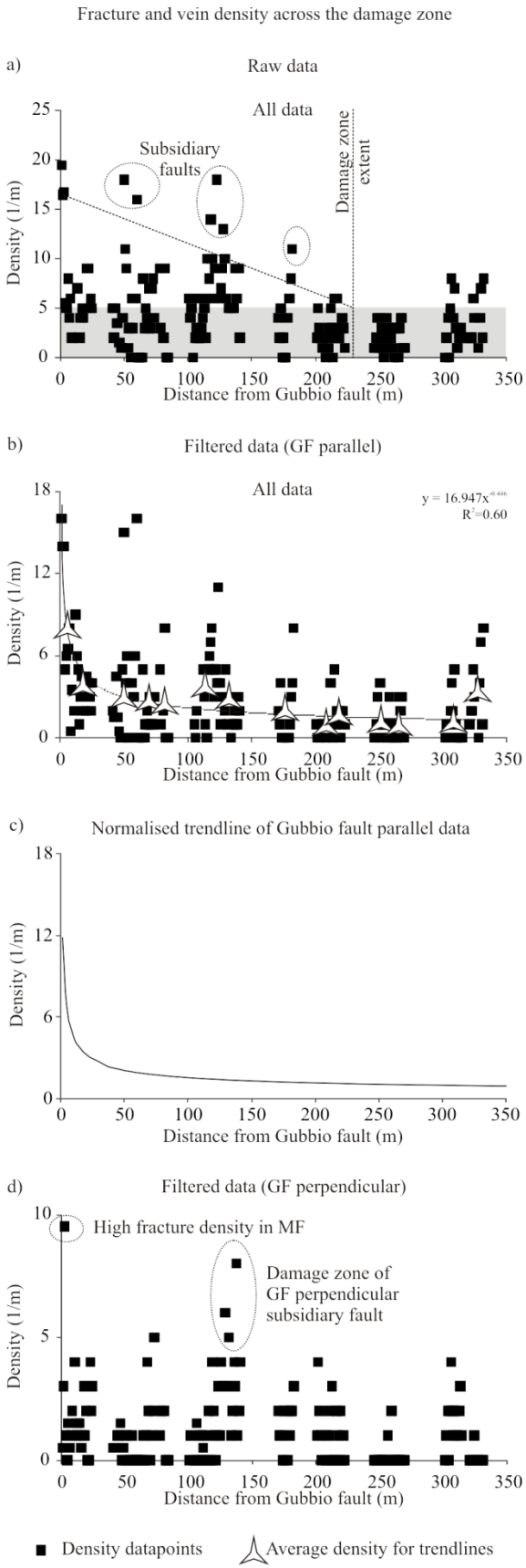

Figure 4.18 - Fracture and vein density across the damage zone
a) Raw data, b) Filtered data (Gubbio fault parallel), c) Normalized best-fit trendline for Gubbio fault parallel data, d) Filtered data (Gubbio fault perpendicular)

Fracture/vein density data, plotted for fault perpendicular features, do not show any direct correlation with increasing distance from the fault core within the damage zone (Fig. 4.18d). Typical fracture/vein density values are lower than 4/m. Only two, isolated peaks of fracture and vein density values have been observed, at 1 m and 120 m, respectively, in correspondence of an intensely fractured outcrop in the Marne a Fucoidi lithology and of a subsidiary fault (Fig. 4.18d). In both cases, fracture and vein density values have reached local maxima of 8-10/m.

Density data of fractures and veins, collected at L1 and L2, can be plotted separately in order to compare the amount of veining and fracturing at the two studied localities (Fig. 4.19). Additionally, power-law trendlines can be fitted to these datasets using the same assumptions as above. This step of processing was only done to Gubbio fault parallel, filtered data, because the data clearly show that only this set of structures have been produced during the extensional phases of deformation producing the Gubbio fault.

Fracture/vein data from L1 shows that their density values are decreasing moving away from the fault core (Fig. 4.19a). The highest values measured are 16/m. A best fit, power-law trendline can be fitted to the data

$$y=11.084x^{-0.265}, (R^2=0.66).$$

Vein density data at L1 show a similar trend than the fracture/vein data (Fig. 4.19b). Density values are gradually decreasing moving away from the fault core. The highest values measured are 16/m. The equation of the best fit, power-law trendline is

$$y=6.3821x^{-0.218} (R^2=0.74).$$

At L1, the measured fracture density values are almost always lower than 4/m (Fig. 4.19c). Only 2 datapoints were measured to be higher than this value, 11/m and 14/m, both

representing outcrop sections less than 5 m away from the fault core. The equation of the best-fit power law trendline is

$$y=2.0036x^{-0.197},$$

with an R^2 value of only 0.07.

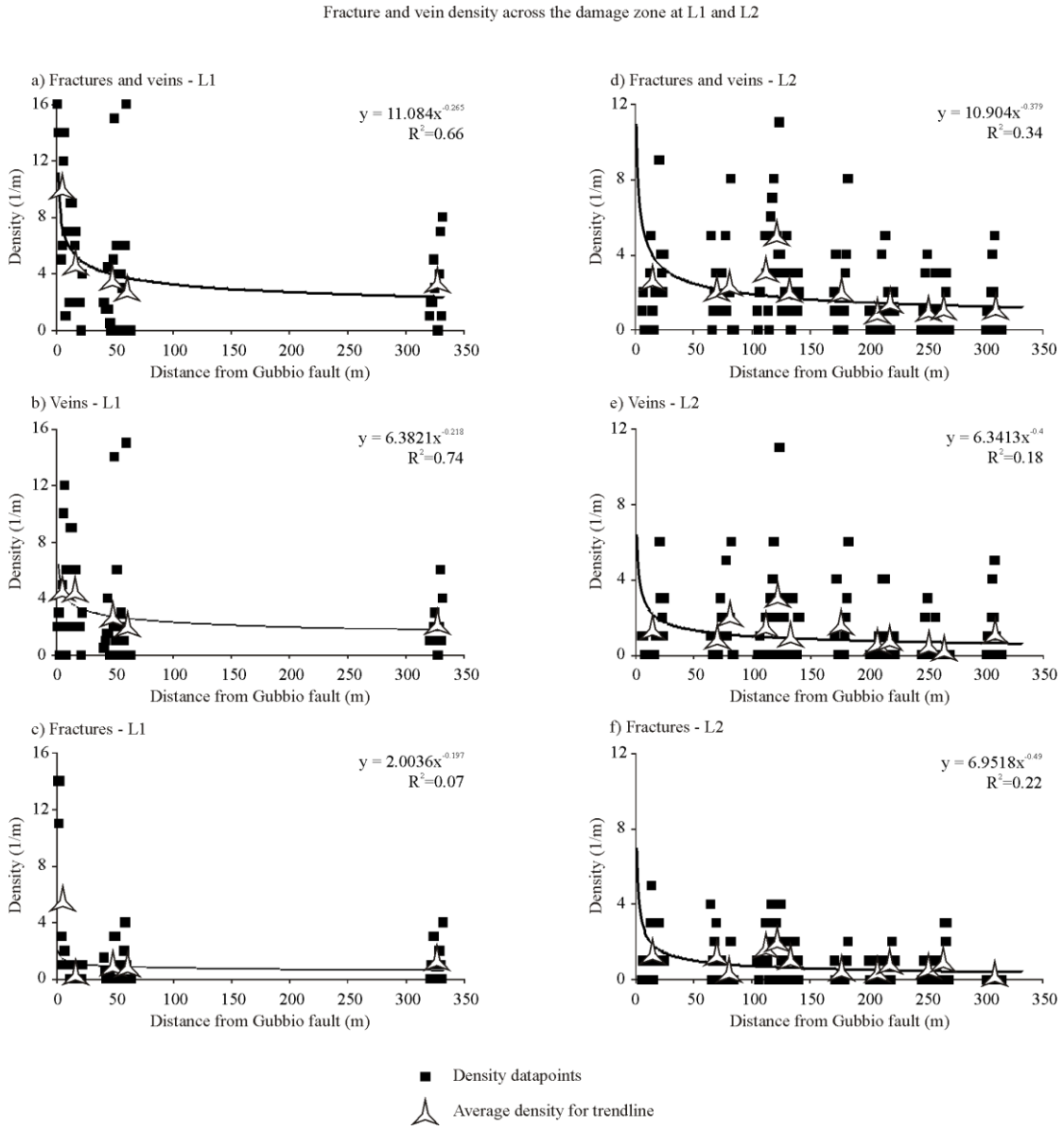

Figure 4.19 - Fracture and vein density across the damage zone at L1 and L2 with best fit power-law trendlines

a) fractures and veins – L1, b) veins – L1, c) fractures – L1, d) fractures and veins – L2, e) veins – L2, f) fractures – L2

Fracture/vein density data at L2 show a generally decreasing trend moving away from the fault core (Fig. 4.19d). However, high fracture/vein density values, comparable to those measured close to the fault core (8-10/m), were measured at other parts of the damage zone. A zone with particularly high fracture/vein density values was found at around 105 m to the fault core, and two smaller peaks at 60 m and 170 m to the fault core (Fig. 4.19d). A best fit power-law trendline was fitted to the data,

$$y=10.904x^{-0.379},$$

with a low R^2 value of 0.34. Vein density values at L2 are showing a similar general trend, with decreasing values when moving away from the fault core (Fig. 4.10e). Vein density values close to the fault core are up to 6/m. An anomalously high peak in the vein density values at 105 m to the fault core was found here as well (with values up to 12/m). Finally, fracture density values at L2 are, again, showing a decreasing trend by moving away from the fault core. Fracture density values close to the fault core are up to 5/m and gradually decrease towards the protolith, where density values are ranging from 0/m to 3/m. The best fit power-law trendline,

$$y=6.9518x^{-0.49}$$

has a low R^2 value (0.22).

4.4.1.3.Lithological control on fracture and vein density in the damage zone

Due to the extent and conditions of exposure of the outcrops at both studied localities, most of the dataset was collected from the Scaglia Rossa and Scaglia Bianca formations (for locations see Fig. 4.3). However, at L1, close to the fault core (up to 3 m), at the bottom of the valley, a relatively small outcrop of Marne a Fucoidi formation was accessible for structural data collection (C1 transect). The same structural measurements could be performed in the Scaglia Bianca formation cropping out in a higher position on the same side

of the valley, representing the same distances from the fault core-damage zone boundary (C2 transect). The comparison of the measured fracture and vein density values in the two lithologies allowed making some considerations on the lithological control on the damage (Fig. 4.20). The cumulative density of fractures and veins in the Marne a Fucoidi formation and in the Scaglia Bianca formation at this section ranges between 14-16/m and 5-12/m, respectively (Fig. 4.20). The data collected from the Marne a Fucoidi formation shows a high density of fractures (10-15/m) and a low density of veins (>3/m, Fig. 4.20). The data collected in the Scaglia Bianca formation at the same distances from the fault core show a higher density of veins (up to 10/m), and significantly lower vein density values (1-3/m) than those measured in the Marne a Fucoidi formation (Fig. 4.20). For comparable values of cumulative fracture and vein density in the damage zone, close to the fault core, the Marne a Fucoidi formation appears to undergo intense fracturing and very minor veining when compared to the Scaglia Bianca formation.

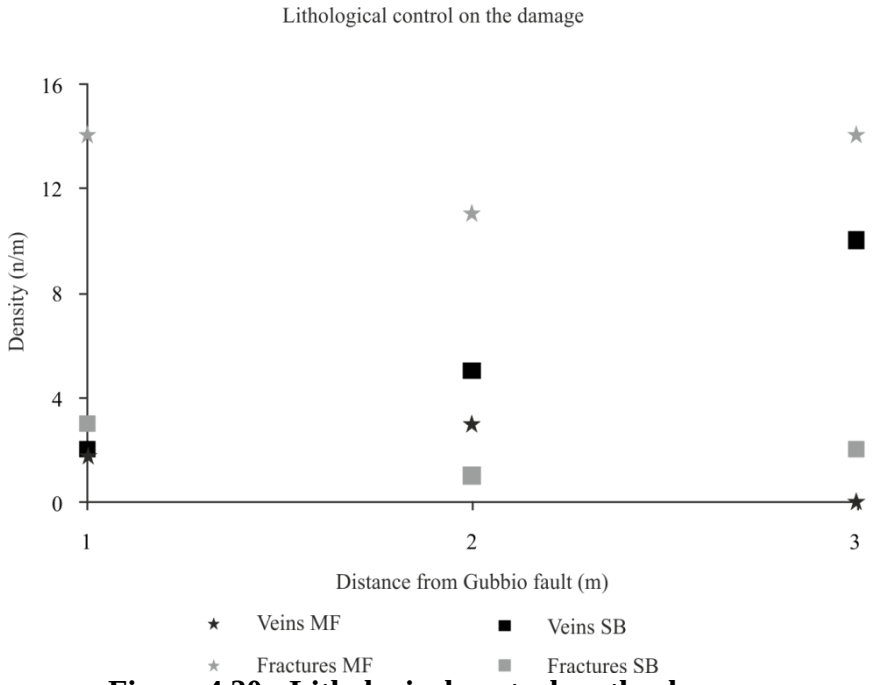

Figure 4.20 - Lithological control on the damage
comparison of fracture and vein density values within the Scaglia Bianca and Marne a Fucoidi formations

4.4.1.4. Subsidiary faults in the damage zone

Subsidiary faults in the damage zone of the Gubbio fault were subdivided based on their relative orientation relative to the Gubbio fault in fault parallel, orthogonal and other orientation ones. Some of these subsidiary faults have a damage zone that can be identified on the 1D transect data, represented by higher fracture and/or vein density values than their surroundings. A few of these subsidiary faults were selected for further analysis, regarding the extent of their damage zones and the orientation distribution of fractures and veins in their damage zones (Fig. 4.21).

Locality 1

At L1 13 subsidiary faults were observed in the damage zone, of which 8 (62%) were parallel to the Gubbio fault, 1 (8%) was perpendicular to it and 4 (30%) displayed different orientations (Fig. 4.9a-d, Fig. 4.21a). Out of these subsidiary faults 4 Gubbio fault parallel ones and 1 other orientation one have damage zones with increased fracture and/or vein density values that can be identified on the transects (Fig. 4.21a). Two of these faults, F1 and F2 located 51 m and 61 m away from the fault core respectively were selected for further analysis (Fig. 4.21b). The fault zone of F1 is approximately 3 m wide and characterized by sharply increasing vein density values (up to 16/m, compared to the surrounding values of 2-3/m) and slightly increasing fracture density values (up to 4/m, compared to the surrounding values of 1-2/m). High fracture and vein density values can be found both in its hanging wall and footwall (Fig. 4.21b). The fault zone of F2 is 1 m wide and also characterized by sharply increasing vein density values (up to 15/m) and slightly increasing fracture density values (up to 2/m). In case of F2 high density values were only found in its hanging wall. In fact, its footwall is characterized by 0/m values of both fracture and vein density (Fig. 4.21b).

F1 subsidiary fault has an orientation of 003/78/E (Fig. 4.21c-d). In the damage zone of F1 fracture orientations are scattered (Fig. 4.21c). Out of the 12 fractures measured in the fault zone, most are striking sub-parallel to the Gubbio fault and only 4 fractures are oriented sub-parallel with F1 (Fig. 4.21c). Veins in the damage zone of F1 are characterized by scattered orientations between the F1 fault and the Gubbio fault (Fig. 4.21d). Again, more veins are sub-parallel to the Gubbio fault than to the F1 fault.

F2 subsidiary fault has an orientation of 171/51/SW, classified as Gubbio fault parallel (Fig. 4.21e-f). In the damage zone of F2 both fractures (Fig. 4.21e) and veins (Fig. 4.21f) are typically sub-parallel to both F2 and the Gubbio fault, but their average orientation is more similar to the orientation of the Gubbio fault.

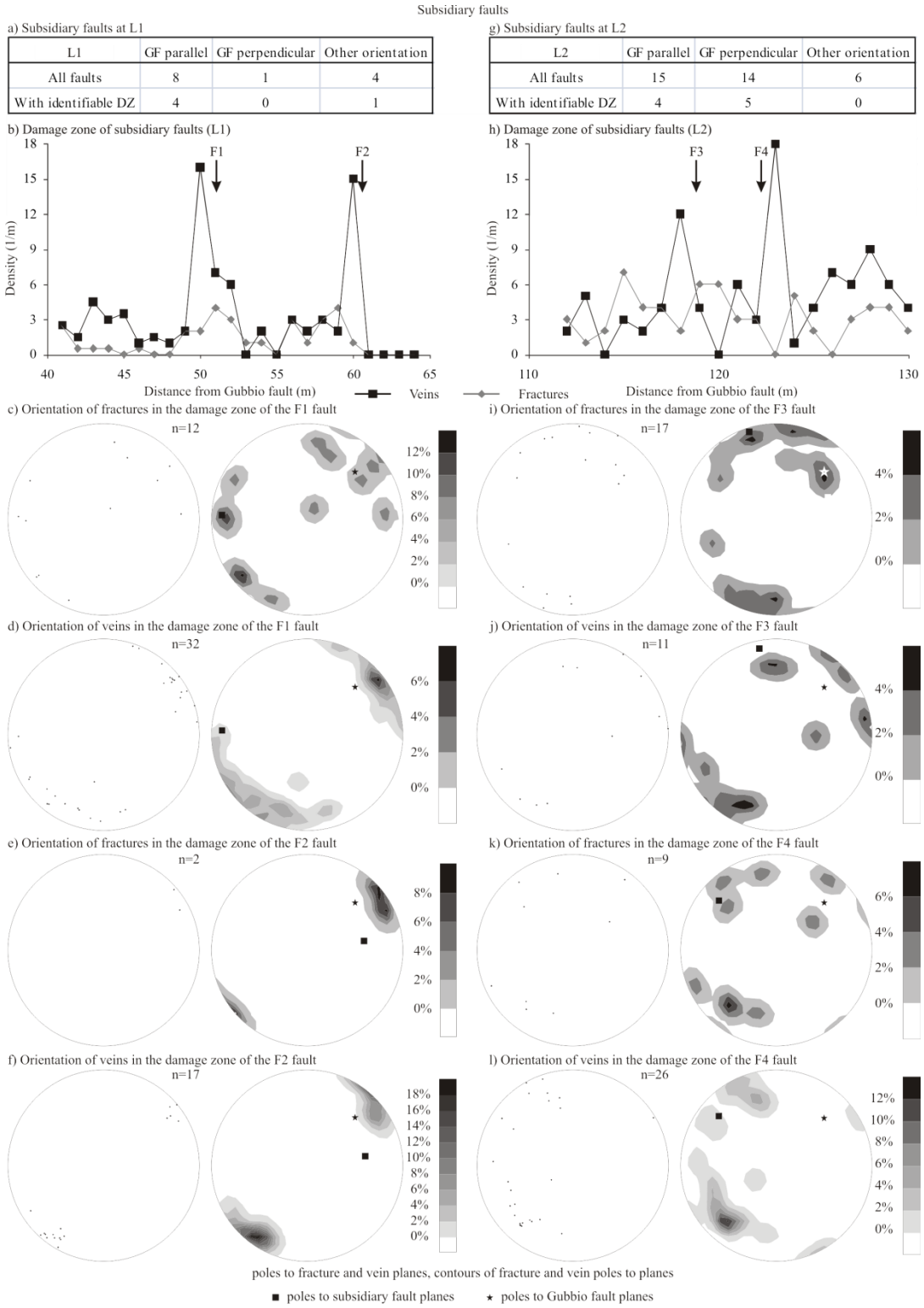

Figure 4.21 - Subsidiary faults

a) Subsidiary faults at L1, b) Damage zone of subsidiary faults (L1), c) Orientation of fractures in the damage zone of F1 fault, d) Orientation of veins in the damage zone of F1 fault, e) Orientation of fractures in the damage zone of F2 fault, f) Orientation of veins in the damage zone of F2 fault, g) Subsidiary faults at L2, h) Damage zone of subsidiary faults (L2), i) Orientation of fractures in the damage zone of F3 fault, j) Orientation of veins in the damage zone of F3 fault, k) Orientation of fractures in the damage zone of F4 fault, l) Orientation of veins in the damage zone of F4 fault

Locality 2

At L2 35 subsidiary faults were observed in the damage zone, of which 15 (43%) were parallel to the Gubbio fault, 14 (40%) was perpendicular to it and 6 (17%) displayed different orientations (Fig. 4.12a-d, Fig. 4.21g). Out of these subsidiary faults 4 Gubbio fault parallel ones and 5 Gubbio fault orthogonal ones had damage zones with increased fracture and/or vein density values that can be identified on the transects (Fig. 4.21h). Two of these faults, F3 and F4, located 128 m and 132 m away from the fault core respectively, were selected for further analysis (Fig. 4.21h). The fault zone of F3 is approximately 2 m wide and is characterized by sharply increasing vein density values (up to 12/m, compared to the surrounding values of 5-6/m) and slightly decreasing fracture density values (down to 3/m, compared to the surrounding values of 4-5/m). The damage zone of this fault is located within the footwall. The fault zone of F4 is 1 m wide and also characterized by sharply increasing vein density values (up to 18/m) and slightly decreasing fracture density values (down to 0/m). In case of F4, high density values were only found in its hanging wall (Fig. 4.21b).

F3 subsidiary fault has an orientation of 079/82/SE, classified as a fault with "other" orientation (Fig. 4.21i-j). Fractures in its damage zone display a scattered orientation distribution, with more than half of them being sub-parallel to the Gubbio fault and approximately a quarter being sub-parallel to F3 (Fig. 4.21i). On the contrary, vein orientations are less scattered, all of them are either striking parallel with the Gubbio fault or with F3 (Fig. 4.21j).

F4 subsidiary fault has an orientation of 041/68/SE, classified as orthogonal to the Gubbio fault (Fig. 4.21k-l). Both fractures (Fig. 4.21k) and veins (Fig. 4.21l) in its damage zone are

either sub-parallel to F4 or to the Gubbio fault, but in case of both fractures and veins more of them are sub-parallel to the Gubbio fault.

4.4.1.5.Orientation data analysis (fault core)

Transects with orientation measurements were also taken in the fault core of the Gubbio fault at L2, at the Cava Filippi outcrop, along the transect CF1 and CF2 (for transect location see Fig. 4.3c). These orientation measurements were completed only on larger, well defined vein and fracture planes in zones where the initial structure of the host rocks were preserved. Zones, close to the slip surfaces, made of highly deformed fault rocks were ignored.

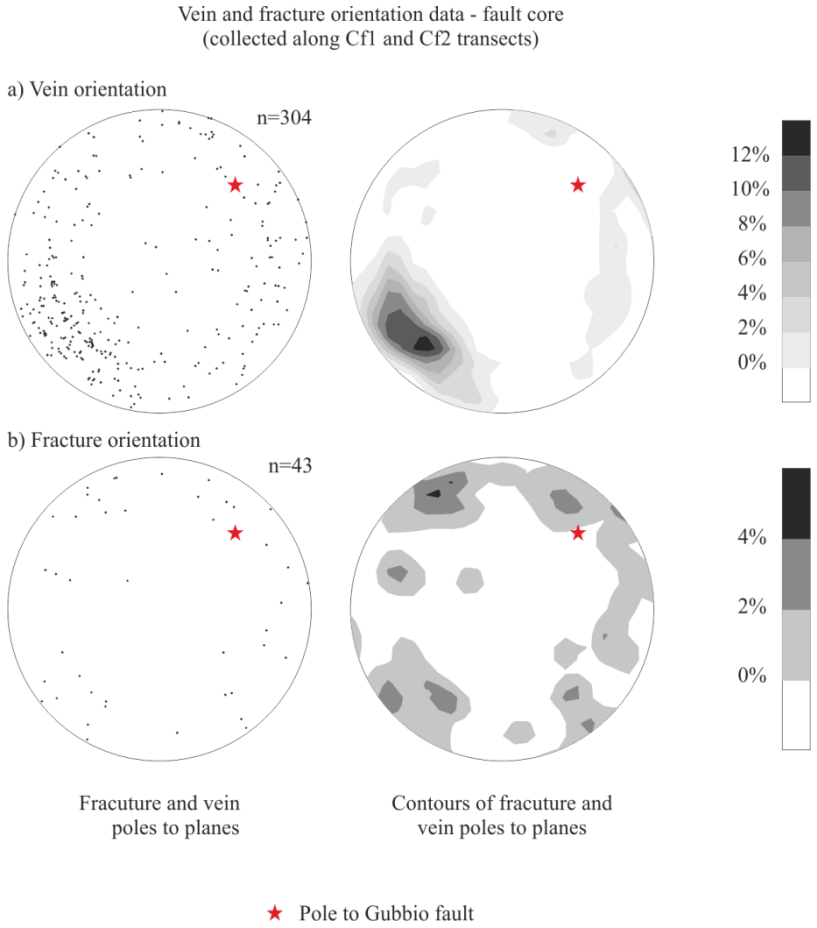

Figure 4.22 - Vein and fracture orientation data – fault core
a) vein orientation, b) fracture orientation

All together 304 (88%) vein and 43 (12%) fracture orientations were measured across transects CF1 and CF2 in the fault core (Fig. 4.22). Veins are typically striking parallel to the fault strike of the Gubbio fault, with over 80% of them characterized by fault antithetic dips, typically >70° (Fig. 4.22a). Compared to veins, fractures are less common and are characterized by very scattered orientations, without any preferred orientations (Fig. 4.22b).

4.4.2. 2D image analysis

4.4.2.1.Outcrop scale image analysis

Outcrop scale image analysis was performed on 39 photos taken from the outcrops of the damage zone of the Gubbio fault, form both localities (L1 and L2), from different distances from the fault core (ranging from 0.1 m to 320 m), from different lithologies (Marne a Fucoidi, Scaglia Bianca, Scaglia Rossa and Scaglia Variegata) and using different outcrop-camera distances (0.5 m, 2 m and 5 m). For a full list of photos used for image analysis see Table 4.1. Image analyses of the photos were done by following the steps introduced in Chapter 1.3.2. Fracture/vein density was quantified as the total length of features/unit area (m/m^2), and fracture/vein connectivity was defined as the number of intersection points, n, per unit area (n/m^2). Since it was difficult to distinguish between fractures and veins using this method, density and connectivity results have been referred to fractures and veins together (fractures/veins).

Locality	Distance from Gubbio fault	Outcrop-camera distance	Lithology	Photo #
L1	0.1	0.5	SB	3122
L1	0.1	2	SB	766
L1	0.1	5	SB	3123
L1	0.2	2	MF	556
L1	2	0.5	SB	816
L1	2	2	SB	817
L1	2	5	SB	815
L1	2.5	5	MF	560
L1	45	0.5	SB	499
L1	45	5	SB	497
L1	47	0.5	SB	507
L1	47	2	SB	790
L1	47	5	SB	791
L1	62	0.5	SB	518
L1	62	2	SB	3117
L1	62	5	SB	3118
L1	103	0.5	SB	521
L1	103	2	SB	520
L1	103	5	SB	519
L1	320	2	SB	3108
L1	320	5	SB	533
L1	320	5	SB	3109
L2	0.5	5	SR	678
L2	10	0.5	SR	3104
L2	10	2	SR	3106
L2	10	5	SR	3107
L2	71	2	SR	839
L2	71	5	SR	840
L2	134	0.5	SR	593
L2	134	2	SR	594
L2	134	5	SR	601
L2	135	5	SR	592
L2	141	2	SR	590
L2	171	2	SR	588
L2	172	2	SR	587
L2	182	2	SR	584
L2	308	5	SV	551
L2	310	2	SV	542
L2	310	5	SV	545

Table 4.1 - List and attributes of photos used for outcrop scale image analysis

Density and connectivity across the damage zone

The results of the outcrop scale image analysis are summarized in Fig 4.23. Fracture/vein density across the damage zone decreases from high values close to the fault core (>2 m/m^2) to relatively lower values (<0.4 m/m^2) further away from it (Fig. 4.23a). Locally, fracture/vein density values can be as high as 4.7 m/m^2 within the damage zone, but most fracture/vein density values range from 0.8 m/m^2 to 1.2 m/m^2 relatively close to the fault core (between 10-110 m distance), and between 0.4 m/m^2 and 0.8 m/m^2 further away from the fault core (Fig. 4.23a-b). Fracture/vein density values do not show any significant variation beyond approximately 200 m away from the fault core, suggesting that these are background values defining the extent of the damage zone.

Fracture/vein connectivity values show a similar trend to fracture/vein density, as they decrease from high values (0.2 n/m^2) close to the fault core, to low background values typical of the protolith (<0.1 n/m^2, Fig. 4.23b). In the damage zone, the high fracture/vein connectivity domains in the damage zone appear to be narrower, approximately 100 m, than the high fracture/vein density ones, which are about 200 m (Fig. 4.23c-d).

The fracture/vein density-connectivity crossplot shows a power law relation between the two variables

$y=1.8267x^{0.4781}$, $R^2=0.95$, (Fig. 4.23e-f).

At lower values (e.g. further away from the fault core), fracture/vein density values increase quicker than connectivity ones, but at higher values (e.g. closer to the fault core) connectivity values increase quicker.

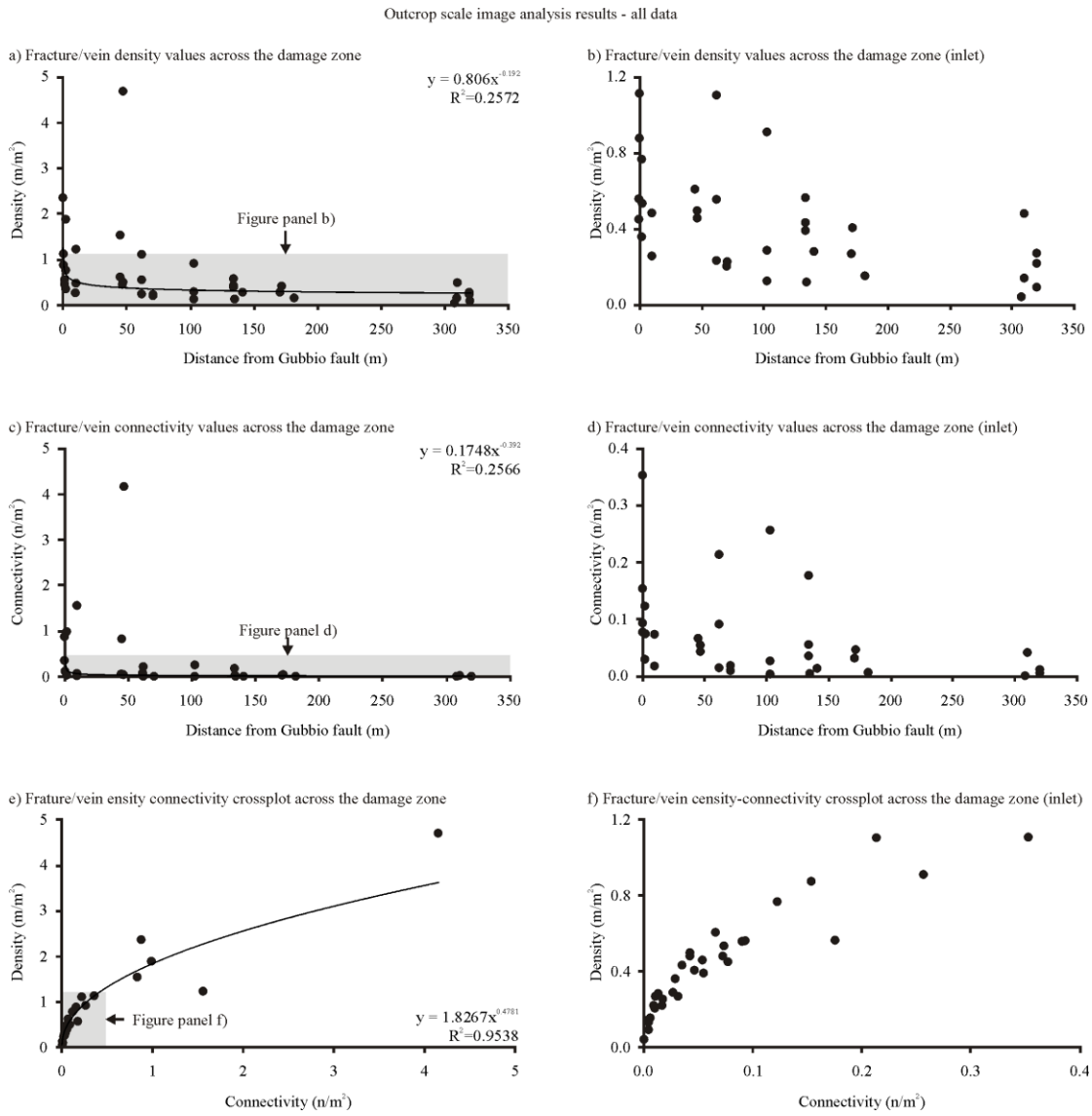

Figure 4.23 - Outcrop scale image analysis results – all data

a) Fracture/vein density values across the damage zone, b) Fracture/vein density values across the damage zone (inlet), c) Fracture/vein connectivity values across the damage zone, d) Fracture/vein connectivity values across the damage zone (inlet), e) Fracture/vein density connectivity crossplot across the damage zone, f) Fracture/vein density connectivity crossplot across the damage zone (inlet)

The effects of using different outcrop-camera distance for image analysis

The photos used for 2D quantitative analysis were taken from different distances to the outcrop, 0.5 m, 2 m and 5 m respectively. Therefore, their resolutions (e.g. the smallest fractures and veins possible to identify) are different. In order to assess whether or not this can affect the results of the analyses, fracture/vein density and connectivity data from pictures, taken at different distances from the outcrop have been plotted separately on the

same graphs (Fig. 4.24). Overall the three datasets (three different outcrop-camera distances) show similar trends. Fracture/vein density (4.24a) and connectivity (4.24b) values are both higher close to the fault core (e.g. distances <100 m: up to 1.2 m/m^2, and 0.35 n/m^2, respectively), and lower (0.4 m/m^2, and >0.1 n/m^2 respectively) further away (e.g. distances>100 m) from it. The density-connectivity crossplot shows that all three datasets are similar to each other, but datapoints, typically gained from smaller outcrop-camera distances, can be plotted at larger distances from the origin of the graph. However the datapoint, plotted the furthest distance from the origin is one from the 2 m outcrop camera distance data (Fig. 4.24c).

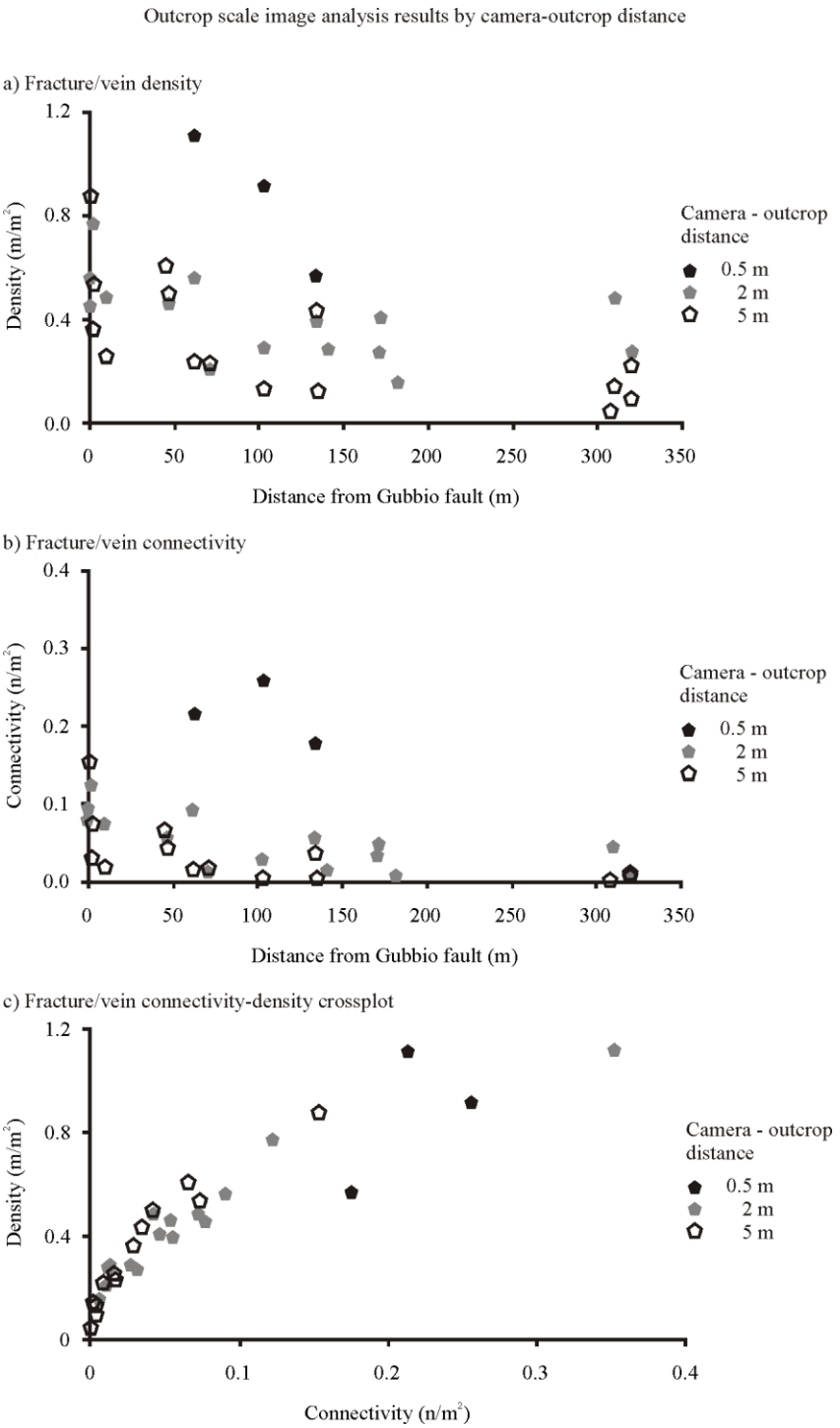

Figure 4.24 - Outcrop scale image analysis results by different camera-outcrop distance
a) Fracture/vein density across the damage zone; b) Fracture/vein connectivity across the damage zone; c) Fracture/vein connectivity density crossplot across the damage zone

The effect that the camera-outcrop distance has on the results has been investigated in more details for a few locations, where data from all three outcrop-camera distances were available. In total, seven locations were studied at both localities, L1 and L2, for a range of

distances from the fault core-damage zone boundary (from 0.1 m to 134 m). Figure 4.25a-c shows three photos taken from the same outcrop from different distances, at 47 m away from the Gubbio fault at L1, from the Scaglia Bianca formation. The extent of the sampling area was marked on each photo. The 5 m outcrop-camera distance photo (Fig. 4.25a) shows an overall view of the outcrop and the larger fractures and veins are visible. The 2 m outcrop-camera distance photo (Fig. 4.25b) is more detailed and most fractures and veins that are displaying irregularities on the outcrop surface can be seen. The 0.5 m outcrop-camera distance photo (Fig. 4.25c) is the most detailed. Even small veins can be seen on it that are not displaying surface irregularities.

Fracture/vein density and connectivity results from the seven different locations are summarized in Figures 4.25d-e. The colour code on both figures, 4.25d and 4.25e, are darker colours for photos taken closer to the fault core and lighter colours for those taken further away from it. For each camera-outcrop distance, the datasets show the same general trend, with higher fracture/vein density and connectivity values close to the fault core and lower values further away from it. In case of the 0.5 m outcrop-camera distance fracture/vein density results range between 0.5 n/m^2 and 4.5 n/m^2 that is a difference of 1 magnitude between the smallest and largest values (Fig. 4.25d). For the other two outcrop-camera distances, 2 m and 5 m the smallest and largest values are 0.2 n/m^2 and 0.8 n/m^2; and 0.1 n/m^2 and 0.5 n/m^2 respectively. The differences between the smallest and largest fracture/vein density values in case of both the 2 m and 5 m outcrop-camera distances are approximately half an order of a magnitude (4.25d).

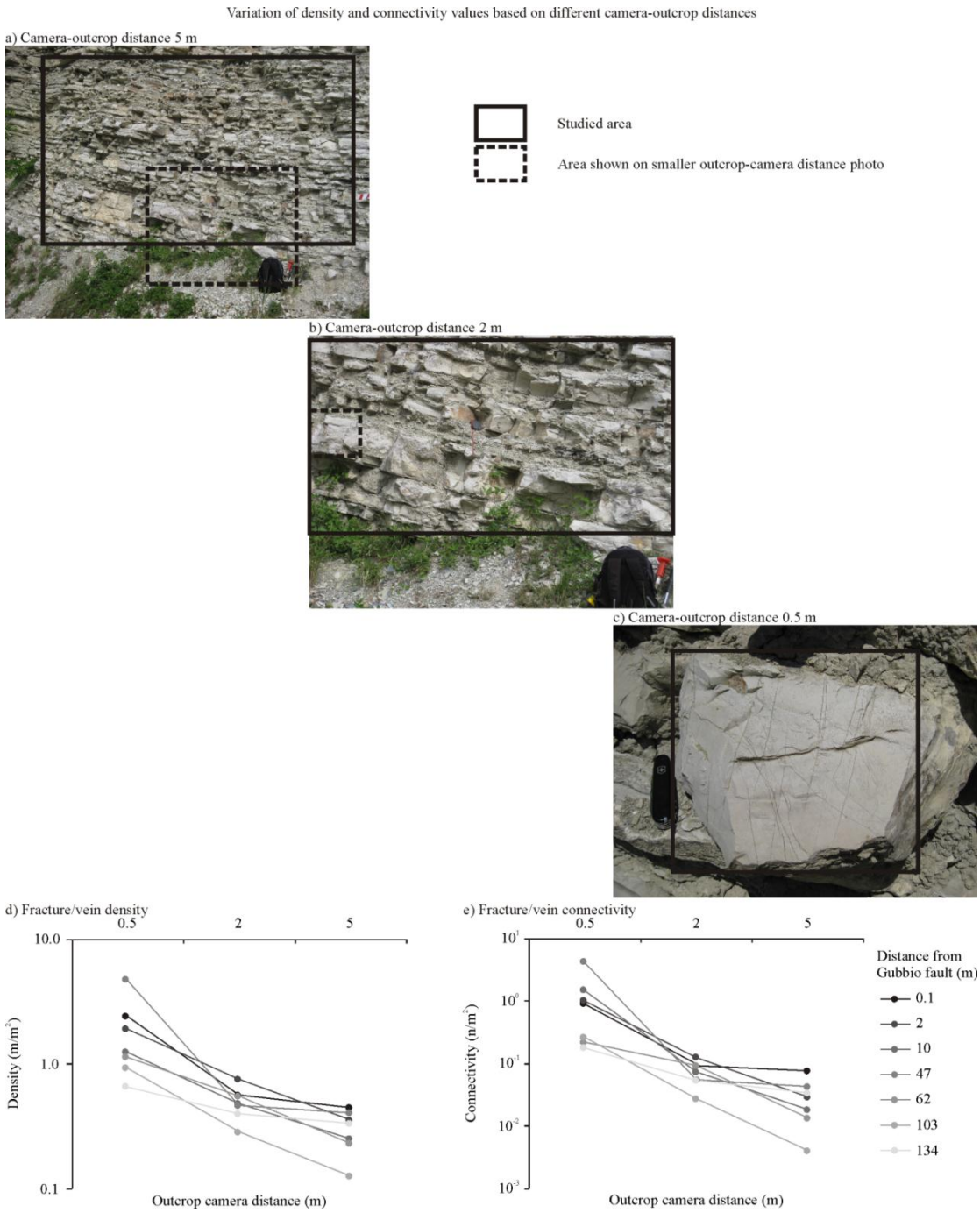

Figure 4.25 - Variation of density and connectivity values based on different camera-outcrop distances

a) Example photo 1 (5 m camera-outcrop distance), b) examples photo 2 (2 m camera-outcrop distance), c) Example photo 3 (0.5 m outcrop-camera distance), d) Fracture/vein density results for given distance from the fault core calculated using different outcrop-camera distance photos, e) Fracture/vein connectivity results for given distance from the fault core calculated using different outcrop-camera distance photos

Fracture/vein density results, gained from the same distance to the fault core, but using different outcrop-camera distances, range over wide intervals. In case of photos, taken

relatively close to the fault core (up to 10 m) the difference between the smallest (5 m outcrop-camera distance) and largest (0.5 m outcrop-camera distance) fracture/vein density values gained range over half a magnitude (4.25d). For example the fracture/vein density values gained at 0.1 m to the fault core are 2.3 m/m^2, 0.56 m/m^2 and 0.45 m/m^2 for the 0.5 m, 2 m and 5 m outcrop-camera distances, respectively. Values gained from 2 m outcrop-camera distances are usually more similar to the 5 m ones than the 0.5 m ones. In case of the photos taken 47 m away from the fault core, the difference between the smallest (0.5 m/m^2, 5 m outcrop-camera distance) and largest (4.75 m/m^2, 0.5 m outcrop-camera distance) fracture/vein density values is close to one magnitude (9.5 times difference). Fracture/vein density values, obtained from photos taken at larger distances from the fault core (62 m and 103 m), similarly to the ones taken close to the core, range across approximately half an order of a magnitude, depending on the different outcrop-camera distances used. Finally, in case of the photos taken from the largest distance from the fault core (134 m), the difference between the smallest (0.43 m/m^2, 5 m outcrop-camera distance) and largest (0.56 m/m^2, 0.5 m outcrop-camera distance) fracture/vein density values is only 1.3 times (4.25d).

Fracture/vein connectivity results, in case of the 0.5 m outcrop-camera distance results range between 0.15 n/m^2 and 10 n/m^2, that is almost an order of a magnitude of a difference between the smallest and largest values (Fig. 4.25e). For the other two outcrop-camera distances, 2 m and 5 m, the smallest and largest values are 0.03 n/m^2 and 0.12 n/m^2; and 0.004 n/m^2 and 0.8 n/m^2 respectively. The differences between the smallest and largest fracture/vein connectivity values in case of the 2 m and 5 m outcrop-camera distances are approximately one order of a magnitude and over 2 orders of magnitudes, respectively (4.25e).

Fracture/vein connectivity results, similarly to fracture/vein density results, gained from the same distance from the fault core, but using different outcrop-camera distances, range over wide intervals. Except for the photos taken from the largest distance from the fault core (134 m) all other given distances from the fault core show at least one order of a magnitude of a difference between the largest and smallest fracture/vein connectivity values. In case of the photos taken 47 m away from the core, the difference between the smallest (0.017 n/m^2, 0.5 m outcrop-camera distance) and largest (1.553 n/m^2) fracture/vein connectivity values is nearly 2 orders of magnitudes (91 times difference). Finally, in case of the photo taken from the largest distance from the fault core (134 m), the difference between the smallest (0.035 n/m^2, 5 outcrop-camera distance) and largest (0.176 n/m^2, 0.5 m outcrop-camera distance) fracture/vein connectivity values are only 5 times, half an order of a magnitude (4.25e).

Similarly to what done for 1D fracture/vein density data, the best fit trendlines obtained for the 2D fracture and vein density and connectivity data can also be normalized to the values of the protolith, which is so fixed to 1 (Fig. 4.26). The best fit normalized trendlines for the density data are

$$y=2.001x^{-0.114}\ (R^2=0.19),$$

$$y=0.6401x^{-0.14}\ (R^2=0.50),$$

$$y=0.520x^{-0.216}\ (R^2=0.44)$$

for the 0.5 m, 2 m and 5 m outcrop-camera distances respectively. The best fit normalized trendlines for the connectivity data are

$$y=1.034x^{-0.154}\ (R^2=0.12),$$

$$y=0.115x^{-0.298}\ (R^2=0.51),$$

$$y=0.070x^{-0.497}\ (R^2=0.54)$$

for the 0.5 m, 2 m and 5 m outcrop-camera distances respectively. The best fit normalized trendlines show that, regardless of the outcrop-camera distance, the relative increase in fracture/vein connectivity values are always higher than the relative increase in fracture/vein density values by the fault core-damage zone boundary.

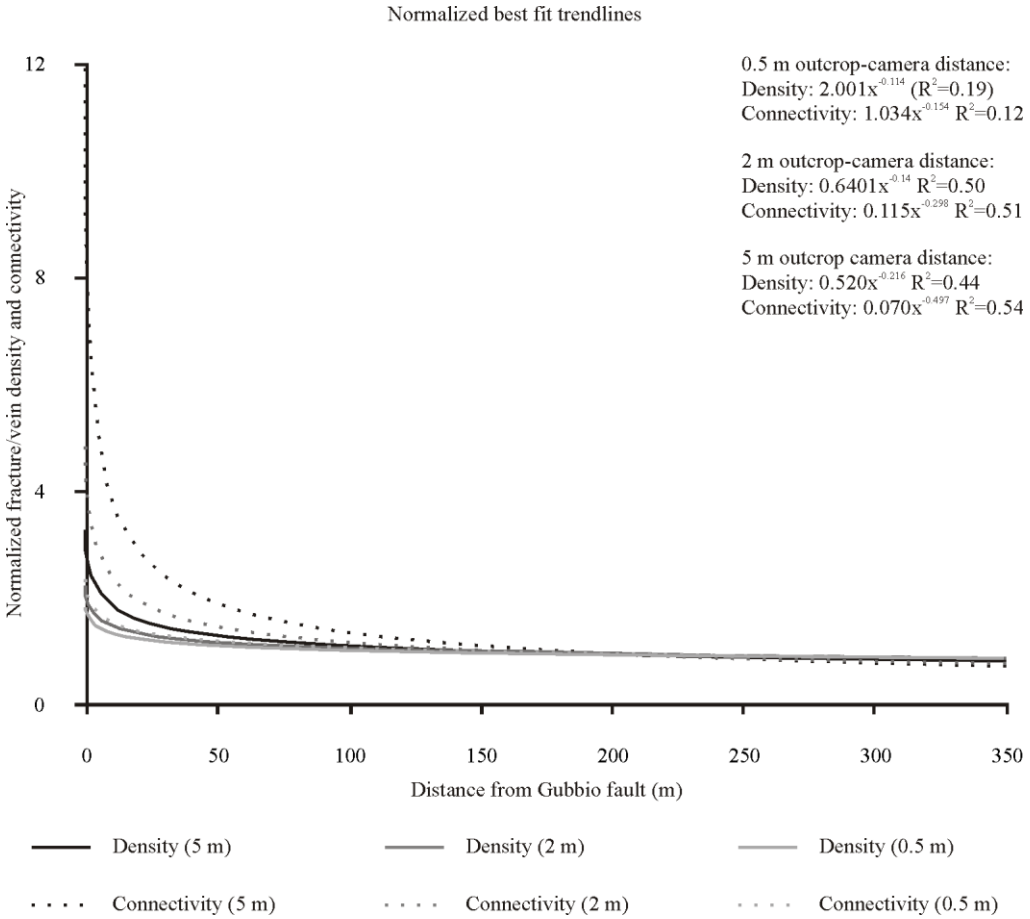

Figure 4.26 - Normalized best fit trendlines for fracture/vein density and connectivity values
gained from different outcrop-camera distance datasets

Lithological control on fracture/vein density and connectivity values

The 2D image analysis results can be subdivided based on the different lithologies these were collected from (Fig. 4.27). 2D fracture/vein density and connectivity data were collected from all four studied lithologies: the Marne a Fucoidi, the Scalgia Bianca, the Scaglia Rossa and the Scaglia Variegata formations. Fracture/vein density values, gained from 5 m outcrop-

camera distance, show similar fracture/vein density values at similar distances to the fault core, regardless of the host lithology. The measured fracture/vein density values are only a function of the distance to the fault core and are independent of the lithology (4.27a). The equation of the best fit, power-law trendline fitted to this dataset is

$$y=0.5201x^{-0.216},$$

with a relatively low R^2 value of 0.44. Fracture/vein connectivity values show similar trends to density values (4.27b). The measured fracture/vein connectivity is not a function of the given lithology, only depends on the distance from the fault core. The equation of the best fit, power-law trendline fitted to the dataset is

$$y=0.0704x^{-0.457} (R^2=0.54).$$

The equation of the best fit, power law trendline, fitted to the fracture/vein density-connectivity crossplot is

$$y=2.1141x^{0.5079},$$

with a very high R^2 value of 0.95 (Fig. 4.27c).

Fracture/vein density values, gained from 2 m outcrop-camera distance somewhat differ from the values gained from 5 m camera distance. In case of the 2 m outcrop-camera distance, fracture/vein density values gained from the Marne a Fucoidi formation (2.5 m away from the fault core-damage zone boundary) are higher (1.1 m/m^2) than fracture/vein density values gained from other lithologies, such as the Scaglia Bianca and the Scaglia Rossa formations and at similar distances (0.1 m, 2 m and 10 m) to the fault core (Fig. 4.27d). At these distances, the measured fracture/vein densities were 0.55 m/m^2 (Scaglia Bianca formation), 0.75 m/m^2 (Scalgia Bianca formation) and 0.5 m/m^2 (Scaglia Rossa formation) respectively (Fig. 4.27d). Fracture/vein density values in the Marne a Fucoidi formation was found to be almost twice as high as fracture/vein density values in other host lithologies, at similar distances to the fault core.

Outcrop scale image analysis results - fracture/vein density and connecitivty

a) density across the damage zone (outcrop camera distance: 5 m)

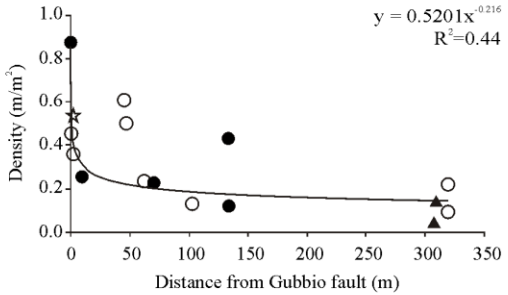

b) connectivity across the damage zone (outcrop camera distance: 5 m)

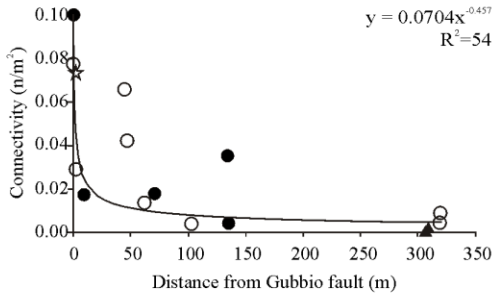

c) density connectivity crossplot (outcrop camera distance: 5 m)

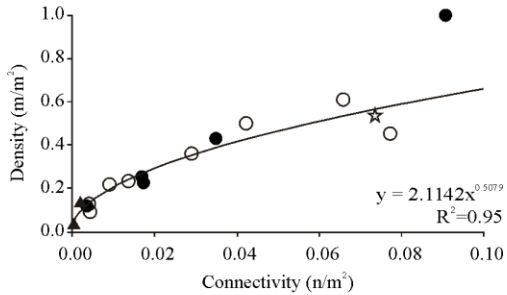

d) density across the damage zone (outcrop camera distance: 2 m)

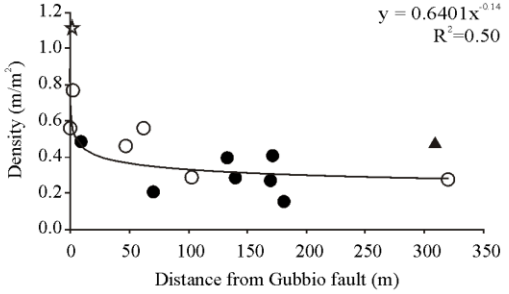

e) connectivity across the damage zone (outcrop camera distance: 2 m)

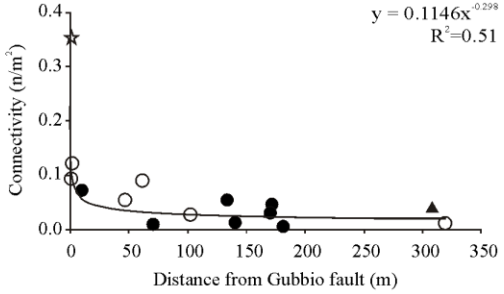

f) density connectivity crossplot (outcrop camera distance: 2 m)

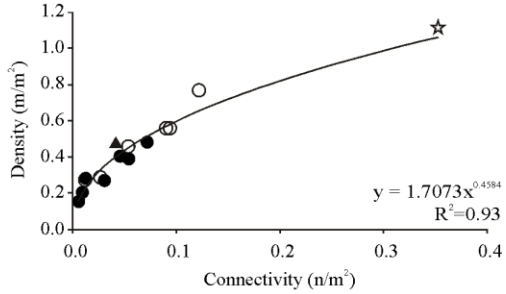

g) density across the damage zone (outcrop camera distance: 0.5 m)

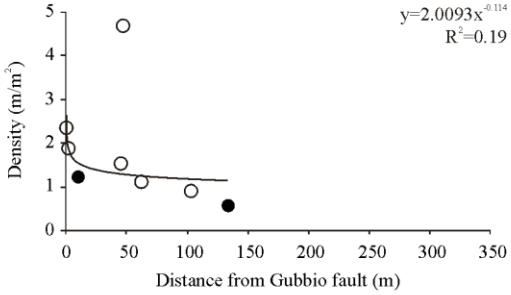

h) connectivity across the damage zone (outcrop camera distance: 0.5 m)

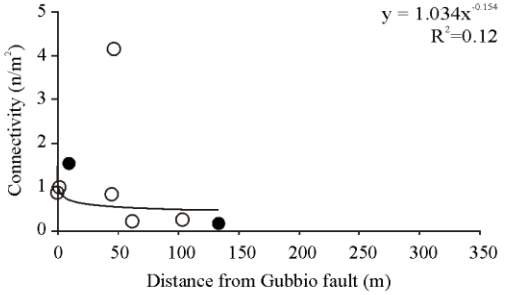

i) density connectivity crossplot (outcrop camera distance: 0.5 m)

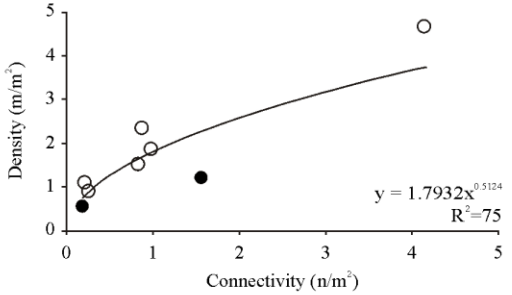

Figure 4.27 - Outcrop scale image analysis results – fracture/vein density and connectivity

a) Density across the damage zone (outcrop-camera distance: 5 m), b) Connectivity across the damage zone (outcrop-camera distance: 5 m), c) Density connectivity crossplot (outcrop-camera distance 5 m), d) Density across the damage zone (outcrop-camera distance: 2 m), e) Connectivity across the damage zone (outcrop-camera distance: 2 m), f) Density connectivity crossplot (outcrop-camera distance 2 m), g) Density across the damage zone (outcrop-camera distance: 0.5 m), h) Connectivity across the damage zone (outcrop-camera distance: 0.5 m), i) Density connectivity crossplot (outcrop-camera distance 0.5 m)

Over 300 m away from the fault core, in what is considered as the protolith, fracture/vein density results gained from the Scaglia Variegata formation are 1.5 times higher (0.6 m/m^2) than fracture/vein density results from the Scaglia Bianca formation (0.4 m/m^2, Fig. 4.27d). The equation of the best fit, power-law trendline fitted to this dataset is

$$y=0.6401x^{-0.14},$$

with an R^2 value of 0.50.

Fracture/vein connectivity values from the 2 m outcrop-camera distance dataset shows similar trends than the fracture/vein density values gained from the same outcrop-camera distance. Fracture/vein connectivity values gained from the Marne a Fucoidi formation (2.5 m away from the fault core-damage zone boundary) are significantly higher (0.35 n/m^2) than fracture/vein connectivity values gained from other lithologies, at similar distances (0.1 m, 2 m and 10 m) to the fault core. At these distances the measured fracture/vein connectivity values were 0.1 n/m^2 (Scaglia Bianca formation), 0.12 n/m^2 (Scalgia Bianca formation) and 0.8 n/m^2 (Scaglia Rossa formation), respectively (Fig. 4.27e). Fracture/vein connectivity in the Marne a Fucoidi formation was found to be more than three times higher than fracture/vein connectivity in other lithologies at similar distances to the fault core. The equation of the best fit, power-law trendline fitted to this dataset is

$$y=0.1146x^{-0.298},$$

with an R^2 value of 0.51 (4.27e). The equation of the best fit, power-law trendline, fitted to the fracture/vein density-connectivity crossplot is

$$y=1.7073x^{0.4584},$$

with a very high R^2 value of 0.93 (Fig. 4.27f).

The results, representing 0.5 outcrop-camera distances are smaller in numbers than the other two-outcrop camera distances; this dataset only covers the inner parts of the damage zone (up to 134 m from the fault core-damage zone boundary) and gained from only two types of lithologies, the Scaglia Bianca and the Scaglia Rossa formations (Fig. 4.27g-i). In case of both fracture/vein density (Fig. 4.26.g) and fracture/vein connectivity (Fig. 4.27h) the measured values are not functions of the lithology, but only depending on the distance from the fault core-damage zone boundary. The only exceptional datapoints (in case of both fracture/vein density and connectivity) are located 47 m from the fault core in the Scaglia Rossa formation and are characterized by 4.8 m/m^2 values of fracture/vein density and 4.2 n/m^2 values of fracture/vein connectivity. These values are approximately twice as high as the second largest values, located close to the fault core (up to 10 m). The equations of the best fit power-law trendlines are

$$y=2.0093x^{-0.114} \ (R^2=0.19, \text{Fig. 4.27g})$$

for the fracture/vein density data,

$$y=1.034x^{-0.154} \ (R^2=0.12, \text{Fig. 4.27h})$$

for the fracture/vein connectivity data and

$$1.7932x^{0.5124} \ (R^2=0.75, \text{Fig. 4.27i})$$

for the fracture/vein density connectivity crossplot.

Based on the three different datasets representing different outcrop-camera distances it is not straightforward to decide if the lithology has an effect on the developed fracture/vein density and connectivity. At given distances to the fault core-damage zone boundary, fracture/vein density and connectivity values gained from the Scaglia Bianca and Scaglia Rossa formations do not show significant differences. The 5 m outcrop-camera distance dataset do not show any significant differences with other lithologies (the Marne a Fucoidi and the Scaglia Bianca formations) either. However, the 2 m outcrop-camera distance dataset suggests that fracture/vein density and connectivity in the Marne a Fucoidi and the Scaglia Variegata formations is significantly higher than in the Scaglia Bianca and Scaglia Rossa formations, at given distances to the fault core.

Along strike variation of fracture/vein density and connectivity values

Apart from studying the lithological control on fracture/vein density and connectivity, Fig. 4.27 can also be used to study the differences between the fracture/vein density and connectivity patterns, developed at the two different localities, L1 (white marks on the graphs) and L2 (black marks on the graphs) at given distances to the fault core-damage zone boundary. However, almost no significant differences were found between the fracture/vein density and connectivity values gained from L1 and L2. The 2 m outcrop-camera distance dataset suggest that close to the fault core-damage zone boundary, fracture/vein density and connectivity values are higher at L1 than at L2 (Fig. 4.27d-f). However, these differences have been explained previously by the lithological control as the high values are gained from photos taken of the Marne a Fucoidi formation (at L1), while the relatively low values are taken of the Scalgia Bianca formation (also at L1) and the Scaglia Rossa formations (at L2).

4.4.2.2.Microscale image analysis

Microscale image analyses were performed on scans of 22 thin sections, cut from representative rock samples, collected at both localites, L1 and L2, at different distances to the fault core-damage zone boundary and from different lithologies (Table 4.2). Since open fractures are not cohesive, the density and connectivity of these features have not been measured. The density and connectivity of veins were measured for each of the thin sections, following the procedures explained in details in Chapter 1.3.2. Vein density was quantified as the total length of features/unit area (mm/mm^2), and vein connectivity was defined as the number of intersection points (n) per unit area (n/mm^2). Additionally, several stylolitic surfaces were identified on the thin sections (see also Chapter 4.3.4, Fig. 4.15), therefore the density of these features were also measured using the same method as for veins and these results of stylolite densities were cross-correlated with vein density and connectivity.

Eight thin sections from locality L1 were analysed (Table 4.2). One of these thin sections is from the fault core (where it is in contact with the Marne a Fucoidi, CEM18 sample) and was collected along transect C1 (for transect locations at L1 see Fig. 4.3b). A further 5 thin sections were cut from rock samples, collected close to the fault core-damage zone boundary (up to 4 m distances), out of which 3 are from the Marne a Fucoidi formation along the C1 transect (20 cm, 1 m and 4 m distances to the fault core, CEM12, CEM13, CEM14 samples, respectively), and two are from the Scaglia Bianca formation along the C2 transect (5 cm and 20 cm distances, CEM 16, CEM15 samples, respectively). At L1, a further 2 thin sections were analysed that were cut from rock samples, collected from the damage zone located in the Scaglia Bianca formation at 42 m (CEM05 sample) and 110 m (CEM09 sample) away from the fault core-damage zone boundary (along transects C3 and C4).

Locality	Distance from Gubbio fault	Lithology	Thin section
L1	-0.1	FC	CEM18
L1	0.05	SB	CEM16
L1	0.2	MF	CEM12
L1	0.2	SB	CEM15
L1	1	MF	CEM13
L1	4	MF	CEM14
L1	42	SB	CEM05
L1	110	SB	CEM09
L2	-2.2	FC	CF01
L2	-2.1	FC	CF02
L2	-1.9	FC	CF05
L2	-1	FC	CF13
L2	-1	FC	CF10
L2	-0.8	FC	CF27
L2	-0.7	FC	CF26
L2	-0.6	FC	CF25
L2	-0.2	FC	CF15
L2	0.05	SR	CF18
L2	0.2	SR	CF19
L2	0.4	SR	CF20
L2	2	SR	CF16
L2	3	SR	CF17

Table 4.2 - List and attributes of thin sections used for microscale image analysis

Fourteen thin sections from locality L2 were analysed, all from the Cava Filippi outcrop, 5 are from the damage zone (CF16, CF17, CF18, CF19 and CF20 samples) and 11 are from the fault core (CF01-CF02, CF05, CF10, CF13, CF15, CF25-CF27 samples, Table 4.2). All thin sections were cut from rock samples collected along transects CF1 and CF2 (for transect locations at L2 see Fig. 4.3c). Thin sections of the damage zone are from samples collected from up to 3 m away from the fault core-damage zone boundary, from the Scaglia Rossa formation. Thin sections from the fault core are cut from samples collected up to 2.2 m away from the fault core-damage zone boundary, representing domain1 and domain2 (for fault rock descriptions of the domains see Chapter 4.3.3).

Vein and stylolite density and vein connectivity across the fault zone

Vein density values in the fault core and in the damage zone up to 4 m away from the fault core range on a wide interval between 0.05 mm/mm^2 and 0.9 mm/mm^2 (Fig. 4.28a). The vein density value, measured on the thin section that was cut from a rock sample collected 40 m away from the fault core, is 0.6 mm/mm^2 (Fig. 4.28a), which is similar to higher vein density values of the fault core. In comparison, the vein density value, measured on the thin section that was cut from a rock sample collected 110 m away from the fault core, is 0.05 mm/mm^2 that is similar to low vein density values of the fault core. The fault core is characterized by vein density values ranging between 0.05 mm/mm^2 and 0.9 mm/mm^2, while within the damage zone the relatively small amount of studied thin sections suggest that vein density gradually decreases as one moves away from the fault core.

In case of vein connectivity, similarly to vein density, the values measured in the fault core range on a wide interval, between 0.01 n/mm^2 and 0.5 n/mm^2 (Fig. 4.28b). Most vein connectivity values, measured in the damage zone, close to the fault core (up to 4 m) range along similar intervals. However, the vein connectivity values measured from thin sections, cut from rock samples collected further away from the fault core (40 m and 110 m), are low compared to these values, < 0.05 n/mm^2. Within the damage zone, vein connectivity values were found to be relatively high close to the fault core (up to 4 m distance), but low in the outer parts of the damage zone.

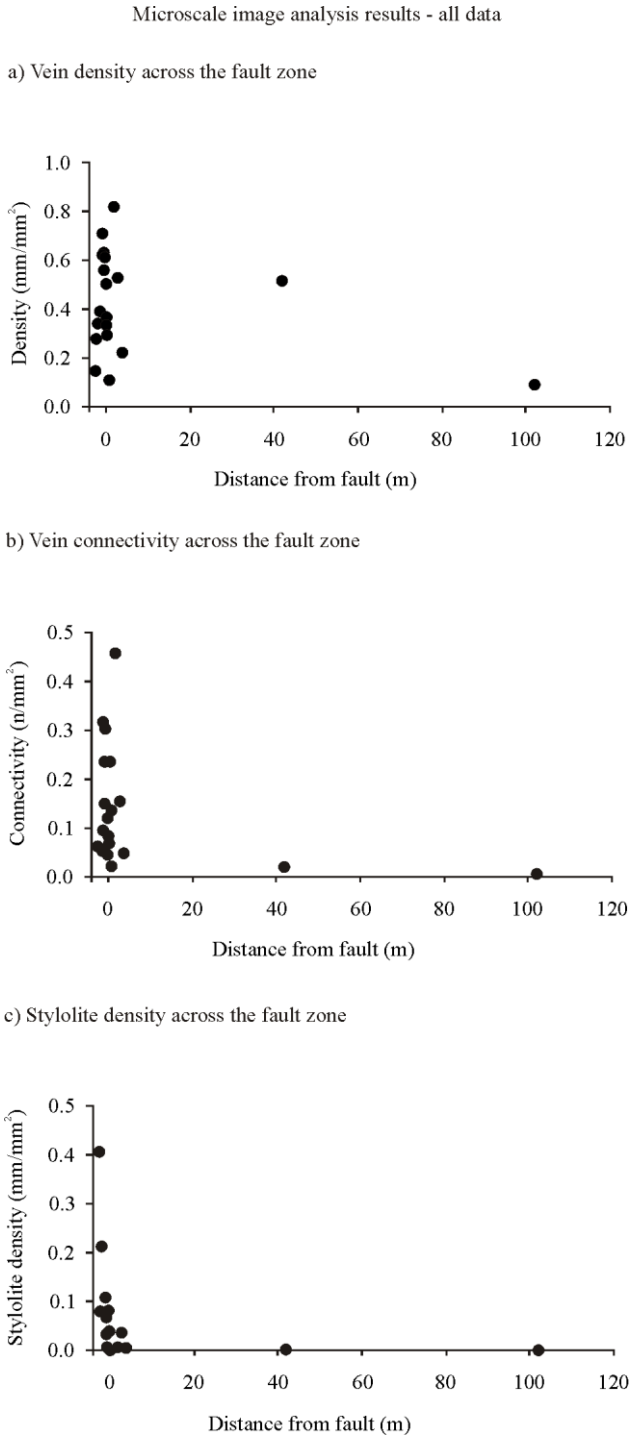

Figure 4.28 - Microscale image analysis results – all data
a) Vein density across the fault zone, b) Vein connectivity across the fault zone, c) Stylolite density across the fault zone

Stylolite density values, gained from thin sections representing the fault core, range between 0 mm/mm^2 and 0.4 mm/mm^2 (Fig. 4.28c). The highest values are found closer to the fault

core. Within the samples, representing the outer parts of the damage zone (collected 42 m and 110 m away from the fault core) stylolite density was found to be 0 mm/mm^2.

Lithological control and along strike variation in vein and styolite density and vein connectivity

A more detailed study of vein and stylolite density and connectivity values were accomplished in the zone close to the fault core-damage zone boundary from 3 m into the fault core and to 4 m into the damage zone, from where most of the studied samples were collected from (Fig. 4.29). In this case, it was also considered which study areas the given samples were collected from (L1 or L2) and from what type of lithology (Scaglia Bianca/Scaglia Rossa formations, Marne a Fucoidi formation, fault core material from domain1, fault core material from domain2).

Vein density in domain2 of the fault core ranges between 0.2 mm/mm^2 and 4 mm/mm^2. These values are all calculated from samples collected at Cava Filippi, at L2 (Fig. 4.29a). In domain1 of the fault core vein density values are higher on average (0.6 mm/mm^2) and range between 0.4 mm/mm^2 and 0.8 mm/mm^2). One of these samples is from L1, in which the measured density value is 0.4 mm/mm^2, the lowest value measured for this domain, however this value is not significantly lower than the values measured in other samples of domain1, collected at L2. In the damage zone the measured vein density values do not follow a trend, when compared to distance to the fault core. Regardless of the locality these were collected from (L1 or L2), samples representing the Scaglia Bianca and Scaglia Rossa formations range between 0.3 mm/mm^2 and 0.8 mm/mm^2. For the Scaglia Rossa and Scaglia Bianca formations, average vein density values at L1 (0.6 mm/mm^2) are higher than the same values

at L2 (0.4 mm/mm^2). Vein density values from the Marne a Fucoidi formation (all collected at L1) are significantly lower, only 0.2 mm/mm^2 (Fig. 4.29a).

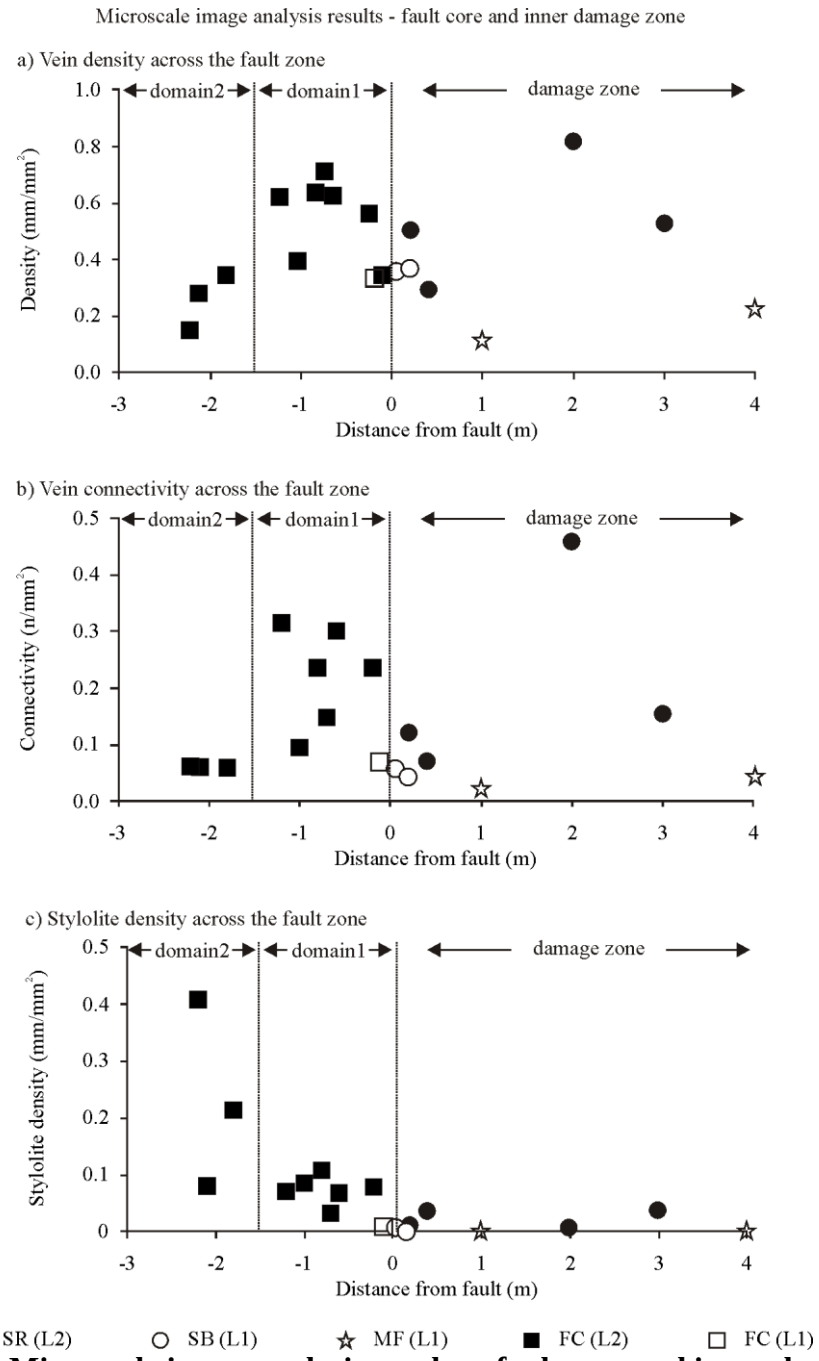

Figure 4.29 - Microscale image analysis results – fault core and inner damage zone
a) Vein density across the fault zone, b) Vein connectivity across the fault zone, c) Stylolite density across the fault zone

In general terms, vein connectivity values follow the same trend as vein density values (Fig. 4.29b). Vein connectivity values in domain2 of the fault core (from samples at L2) all

range around 0.08 n/mm^2. In domain1 connectivity values, measured on samples from L2, range between 0.1 n/mm^2 and 0.3 n/mm^2. These values are over 3 times higher than the same values measured for domain2. The smallest measured vein connectivity value is in domain1 and is from L1, where it was found to be less than 0.1 n/mm^2. Within the damage zone, vein connectivity values range between 0.01 n/mm^2 and 0.5 n/mm^2. There was no systematic variation found between vein connectivity values and distance from the fault core. Vein connectivity values representing the Scaglia Rossa formation at L2 are higher on average (0.25 n/mm^2) than vein connectivity results from L1, representing the Scaglia Bianca formation (0.07 n/mm^2) and the Marne a Fucoidi formation (0.02 n/mm^2).

The measured stylolite densities within domain2 of the fault core are relatively high, ranging from 0.1 mm/mm^2 to 0.4 mm/mm^2 (Fig. 4.29c). In comparison, stylolite density values on domain1 are lower (0.08 mm/mm^2 average) and range on a narrower scale. Within domain1 the smallest measured stylolite density value is from the only sample collected at L1 (0.02 mm/mm^2). Finally, regardless of the along strike position and studied formations, stylolite density was found to be the lowest in the damage zone (up to 0.03 mm/mm^2, Fig. 4.29c).

Crossplots between vein density, vein connectivity and stylolite density were made for the entire 2D microscale dataset, including samples from the outer parts of the damage zone (Fig. 4.30.) The vein density-vein connectivity crosplot shows that a best fit power-law trendline can be fitted to the dataset with a relatively high R^2 value of 0.73, and with an equation of

$$y=1.2401x^{0.5047}$$ (Fig. 4.30a).

Datapoints representing the fault core are spread out along the trendline and are present at both lower and higher values. Datapoints representing the Scaglia Rossa formation at L2 are typically found around high vein density and connectivity values, the datapoints of the Scaglia Bianca formation from L1 are at lower vein density and connectivity values and, finally, datapoints of the Marne a Fucoidi formation, also from L1, are the closest to zero values (Fig. 4.30a).

The vein density-stylolite density crossplot (Fig. 4.30b) and the vein connectivity-styolite density crossplot (Fig. 4.30c) follow a similar trend to each other. Datapoints representing L1, regardless of the lithology, are scattered around low stylolite density values and low to medium vein density and connectivity values. Datapoints representing the damage zone at L2 are scattered around low stylolite density values and medium to high vein density and connectivity values. Datapoints from the fault core at L2, from where most of the samples were taken from, show a correlation between stylolite density and vein density

$$(y=0.0375x^{-1.124}, R^2=0.66, \text{Fig, 4.30b})$$

and between stylolite density and vein connectivity

$$(y=0.0318x^{-0.559}, R^2=0.30, \text{Fig. 4.30c}).$$

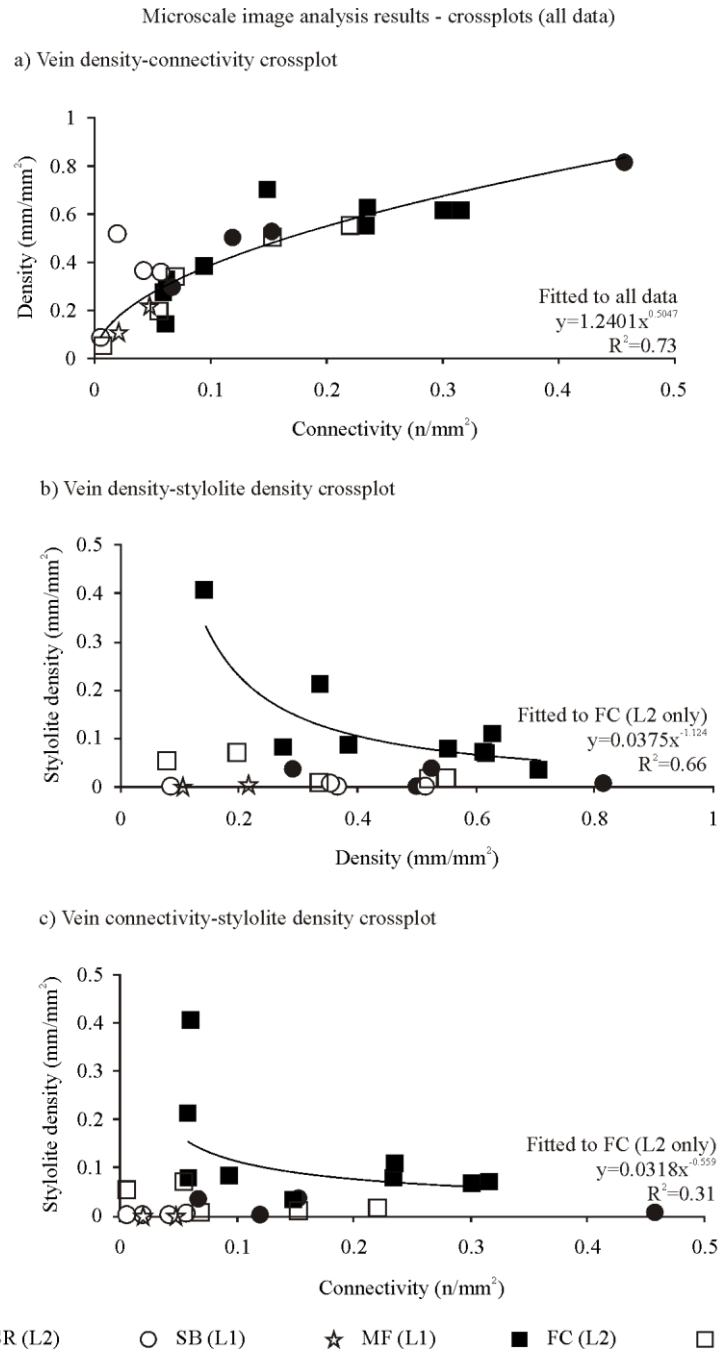

Figure 4.30 - Microscale image analysis results – crossplots (all data)
a) Vein density-connectivity crossplot, b) Vein density-styolite density crossplot c) Vein connectivity -stylolite density across the fault zone

4.4.3. 3D analysis and modelling

4.4.3.1.Locality 1

At L1, LiDAR data was collected at two Gubbio fault perpendicular outcrops in the damage zone, CS1 and CS2, along the SE side of the valley behind the cemetery (for location of the outcrops see Fig. 4.3b). At a stratigraphically lower position, CS1 contains outcrops of the Marne a Fucoidi formation. It is approximately 60 m long and bounded by the fault core-damage zone boundary to the SW (Fig. 4.31a). Due to the large distance (>20 m) between the scan positions and the outcrop, only the most prominent subsidiary faults were identified from these scans (4.31b). Higher up, on the plateau above CS1, CS2 contains outcrops of the Scaglia Bianca formation. CS2 is approximately 120 m long and is also bounded by the fault core-damage zone boundary to the SW (Fig. 4.32a). Due to the distance (>10 m) between the different scan positions and the outcrop, only the subsidiary faults and largest fractures were identified from this pointcloud that are at least approximately 2 cm wide (Fig. 4.32b). Hereafter, when discussing the 3D results, these will be referred to as subsidiary fault density and connectivity.

The scanned data was used to model and quantify the variation of subsidiary fault density and connectivity across the damage zone in the two studied lithologies; the Marne a Fucoidi formation at CS1 and the Scaglia Bianca formation at CS2. Five different aspect ratios, 1/1, 1/2, 1/3, 1/5 and 1/8, respectively, and an additional model, referred to as 1/- (in which case the horizontal extent of the fractures were not limited, see Chapter 1.3.4, but were let to run across the entire geocellular model) were used to model the acquired 3D scan data.

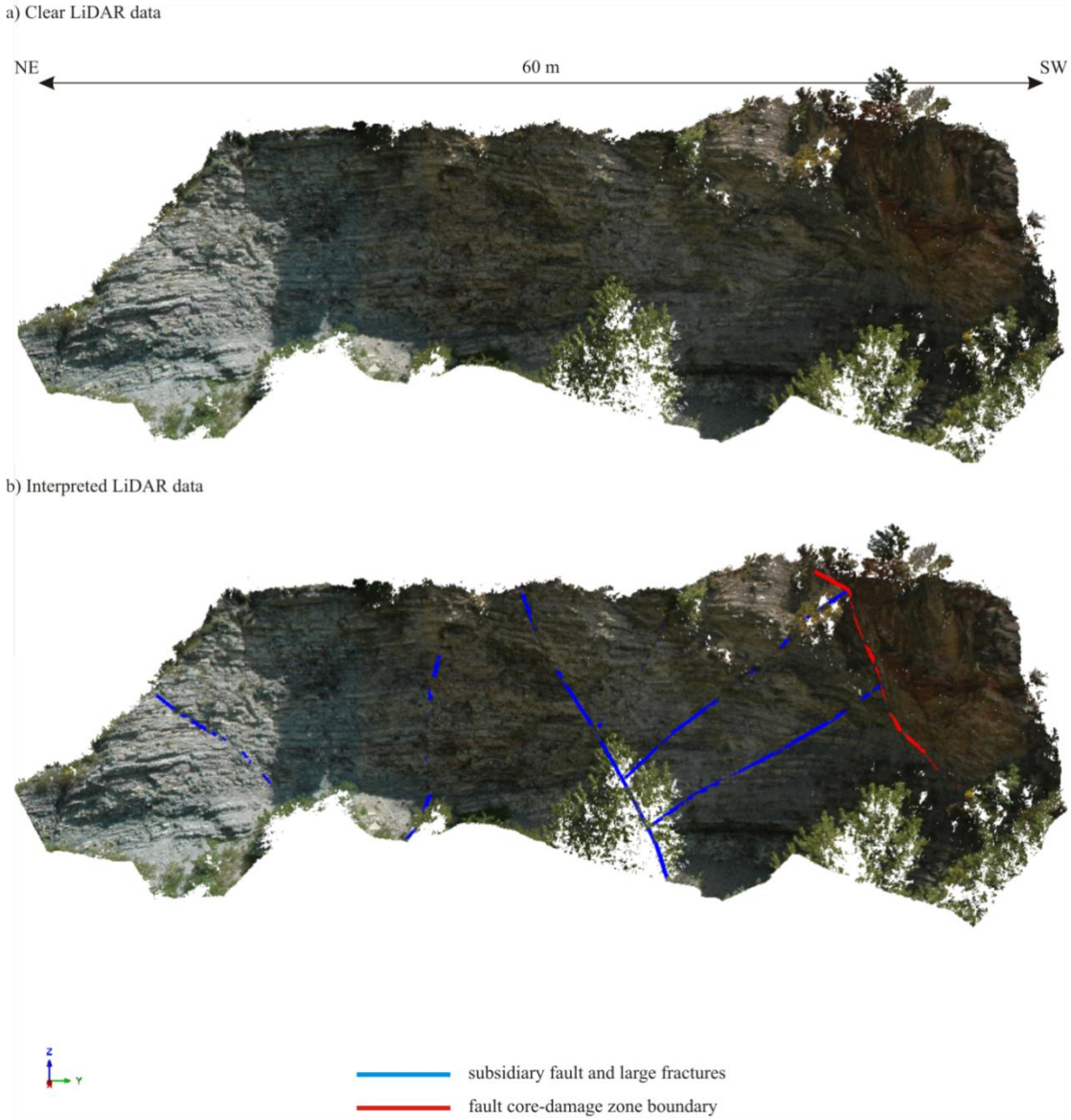

Figure 4.31 - LiDAR data and interpreted subsidiary faults and large fractures – L1, Marne a Fucoidi formation

a) Clear LiDARdata, b) Interpreted LiDAR data

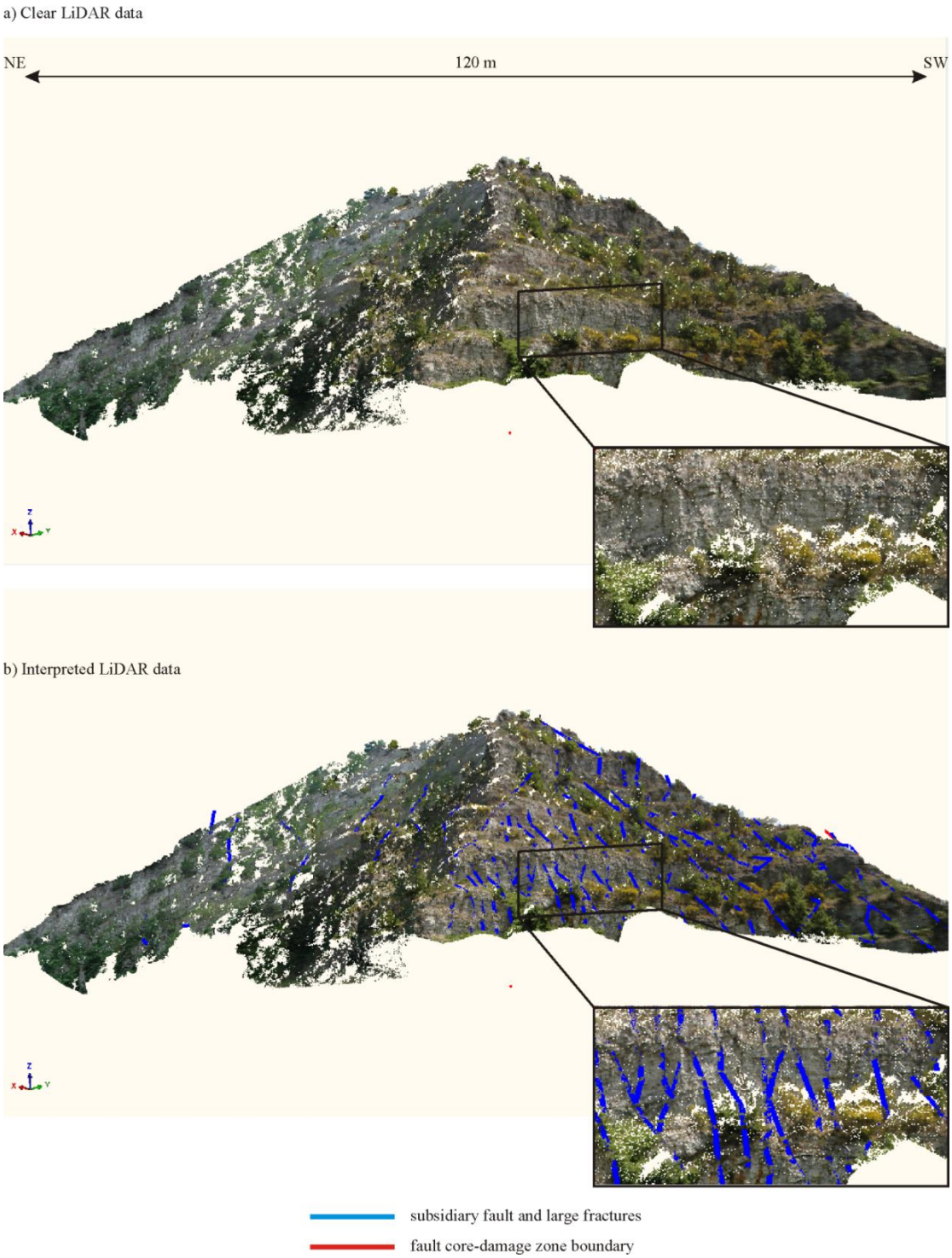

Figure 4.32 - LiDAR data and interpreted subsidiary faults and large fractures – L1, Scaglia Bianca formation

a) Clear LiDARdata, b) Interpreted LiDAR data

CS1 – Marne a Fucoidi

Subsidiary fault density in 3D, across the damage zone, in the Marne a Fucoidi formation, was calculated using all 6 different aspect ratio models (Fig. 4.33a). In all cases, subsidiary fault density decreases from the fault core-damage zone towards the protolith. In case of the 1/1 aspect ratio model, subsidiary fault density is 0.002 m^2/m^3, close to the fault core, and 0 m^2/m^3 in the protolith. In case of the 1/- aspect ratio model, fracture density is 0.034 m^2/m^3, close to the fault core, and 0.03 m^2/mm^3 in the protolith. The intermediate aspect ratio models are characterized by intermediate values. In case of models containing more elongated subsidiary faults (e.g. aspect ratio < 1/3), subsidiary fault density values decrease rapidly within the first 20 m section, next to the fault core and then decrease slower further away from it (Fig. 4.33a).

Best fit, power-law trendlines were fitted to the subsidiary fault density values gained from the different 3D models (Fig. 4.33a). These are

$y=3*10^{-5}x^{-2.371}$ ($R^2=0.61$) for the 1/1 aspect ratio model,

$y=5.457x^{-4.313}$ ($R^2=0.53$) for the 1/2 aspect ratio model,

$y=3.3868x^{-3.497}$ ($R^2=0.41$) for the 1/3 aspect ratio model,

$y=0.0496x^{-0.852}$ ($R^2=0.80$) for the 1/5 aspect ratio model,

$y=0.0481x^{-0.739}$ ($R^2=0.91$) for the 1/8 aspect ratio model and

$y=0.0622x^{-0.714}$ ($R^2=0.84$) for the 1/- aspect ratio model.

The R^2 values are relatively low for the higher aspect ratio models (0.41-0.61), but significantly higher for the lower aspect ratio models (0.80-0.91).

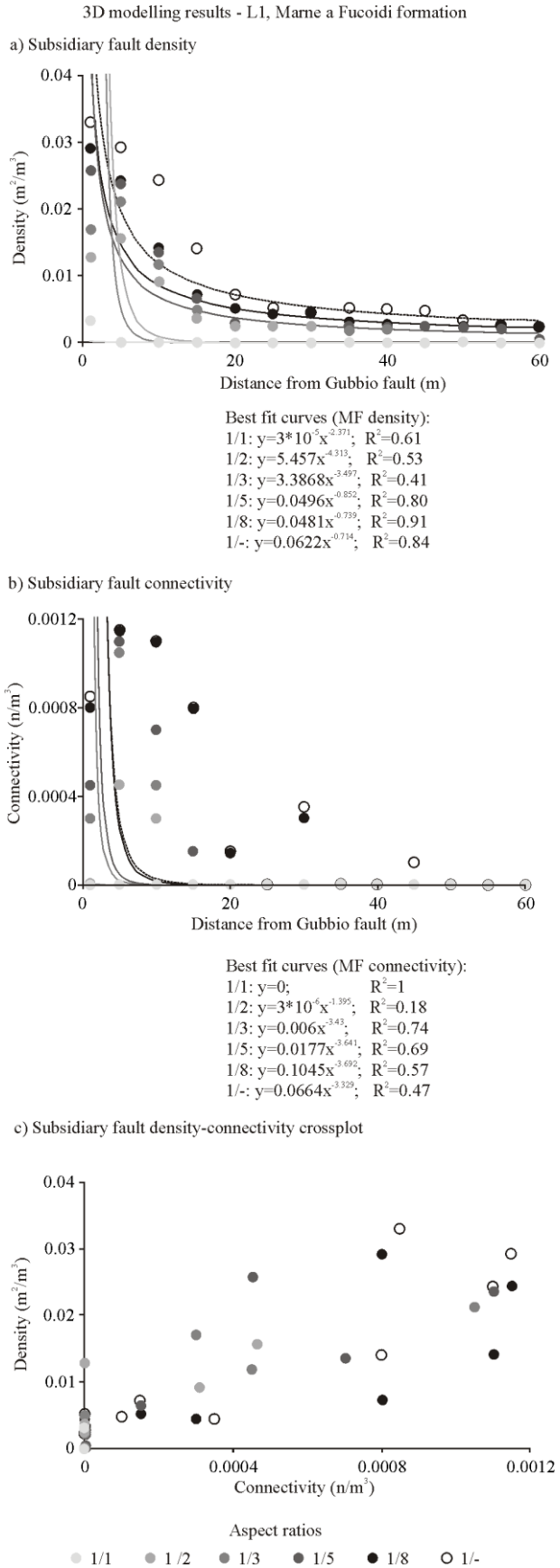

Figure 4.33 - 3D modelling results – L1, Marne a Fucoidi formation
a) Subsidiary fault density, b) Subsidiary fault connectivity, c) Subsidiary fault density-connectivity crossplot

Subsidiary fault connectivity values were also calculated along the same outcrop, at the same distances from the fault as within the Marne a Fucoidi formation (Fig. 4.33b). Subsidiary fault connectivity values show a decreasing pattern from the fault core-damage zone boundary towards the protolith, except for the 1/1 aspect ratio model, in which case no subsidiary fault intersections and, therefore, no subsidiary fault connectivity was found across the entire outcrop. Additionally, for the higher aspect ratio models (1/1, 1/2, 1/3), the subsidiary fault connectivity values closest to the fault core are usually lower than the same values approximately 5-15 m away from the fault core. Subsidiary fault connectivity values are 0.0012 m/m^3 close to the fault core in case of the 1/- aspect ratio model, but when moving away from the fault core, values are decreasing quickly and reach 0 m/m^3 values at 50 m distance from it (Fig. 4.33b).

Best fit, power-law trendlines were fitted to the subsidiary fault connectivity values gained from the different 3D models (Fig. 4.33b). These are

$y=0$ ($R^2=1$) for the 1/1 aspect ratio model (as all values were 0 m/m^3),

$y=3*10^{-6}x^{-1.395}$ ($R^2=0.18$) for the 1/2 aspect ratio model,

$y=0.006x^{-3.43}$ ($R^2=0.74$) for the 1/3 aspect ratio model,

$y=0.0177x^{-3.641}$ ($R^2=0.69$) for the 1/5 aspect ratio model,

$y=0.1045x^{-3.692}$ ($R^2=0.57$) for the 1/8 aspect ratio model and

$y=0.0644x^{-3.329}$ ($R^2=0.47$) for the 1/- aspect ratio model.

R^2 values of the fitted trendlines are relatively high in case of the 1/3, 1/5 and 1/8 aspect ratio models, and lower for the other ones (Fig. 4.33b).

Based on the measured subsidiary fault density and connectivity values, crossplots between the two variables were plotted for the different aspect ratio models (Fig. 4.33c). Since a

relative majority of the subsidiary fault connectivity values were 0 m/m^3, no power-law best fit trendlines could have been fitted to this data. A general trend however, can be seen on the plot. Lower subsidiary fault density values are associated with lower subsidiary fault connectivity values and higher subsidiary fault density values are associated with higher subsidiary fault connectivity values.

CS2 – Scaglia Bianca

3D subsidiary fault density results from Scaglia Bianca show a generally decreasing pattern moving away from the fault core towards the protolith (Fig. 4.34a). For the three smallest aspect ratio models (1/1, 1/2, 1/3) an "edge-effect" was observed: an increase in the subsidiary fault density values in the first 20-30 m of the transect was followed by a decrease when moving further away from the fault core. In case of the other three, lower aspect ratio 3D models (1/5, 1/8, 1/-) subsidiary fault density values are fairly uniform in the first 40 m (average 0.09 m^2/m^3, 0.12 m^2/m^3 and 0.13 m^2/m^3, respectively), steeply decrease up to 70 m (to 0.07 m^2/m^3, 0.06 m^2/m^3 and 0.05 m^2/m^3, respectively), and finally, slowly decrease further away from the fault core towards the protolith (to 0.03 m^2/m^3 regardless the aspect ratio).

The best fit, power-law trendlines that were fitted to the different aspect ratio subsidiary fault density datasets, gained from the Scaglia Bianca formation, are showing different damage zone characteristics. (Fig. 34a). The trendlines were fitted ignoring datapoints between 25-40 m, due to anomalously high connectivity values (see notes below). The equations of the best fit trendlines are

$y=201.33x^{-3.083}$ ($R^2=0.33$) for the 1/1 aspect ratio model,

$y=1.0884x^{-1.413}$ ($R^2=0.15$) for the 1/2 aspect ratio model,

$y=0.2039x^{-0.541}$ ($R^2=0.28$) for the 1/3 aspect ratio model,

$y=0.216x^{-0.406}$ ($R^2=0.51$) for the 1/5 aspect ratio model,

$y=0.2584x^{-0.401}$ ($R^2=0.54$) for the 1/8 aspect ratio model and

$y=0.2679x^{-386}$ ($R^2=0.59$) for the 1/- aspect ratio model.

The higher aspect ratio models (1/1, 1/2, 1/3) are characterized by very low R^2 values (0.15-0.33), due to the edge-effect close to the fault core. The lower aspect ratio models (1/5, 1/8, 1/-) are characterized by higher R^2 values (0.51-0.59).

Subsidiary fault connectivity data, from the same location and lithology, show a similar trend as the density data, with generally decreasing values towards the protolith (Fig. 34.b). In case of the higher aspect ratio models (1/1, 1/2, 1/3) the same edge-effect can be seen as for the subsidiary fault density values up to 20 m away from the fault core. At the same distances subsidiary fault connectivity values are 0.005-0.009 m/m^3, 0.005-0.008 m/m^3 and 0.006-0.004 m/m^3 for the 1/-, 1/8 an 1/5 aspect ratio models, respectively. Regardless of the particular aspect ratios, subsidiary fault connectivity values are anomalously high between 20 m and 40 m to the fault core, possibly due to the presence of a large fracture corridor, containing several subsidiary faults. Within this zone subsidiary fault connectivity values can be up to twice as high (0.012 m/m^3) as values measured closer to the fault core. Beyond this zone, characterized by high values, subsidiary fault connectivity sharply decreases in case of all 3D models and become fairly uniform after 70 m. The measured subsidiary fault connectivity values are 0 m/m^3 for the 1/1 aspect ratio model, and gradually increases for lower aspect ratio models, with the 1/- model being characterized by 0.002 m/m^2 fracture connectivity values (Fig. 4.34b).

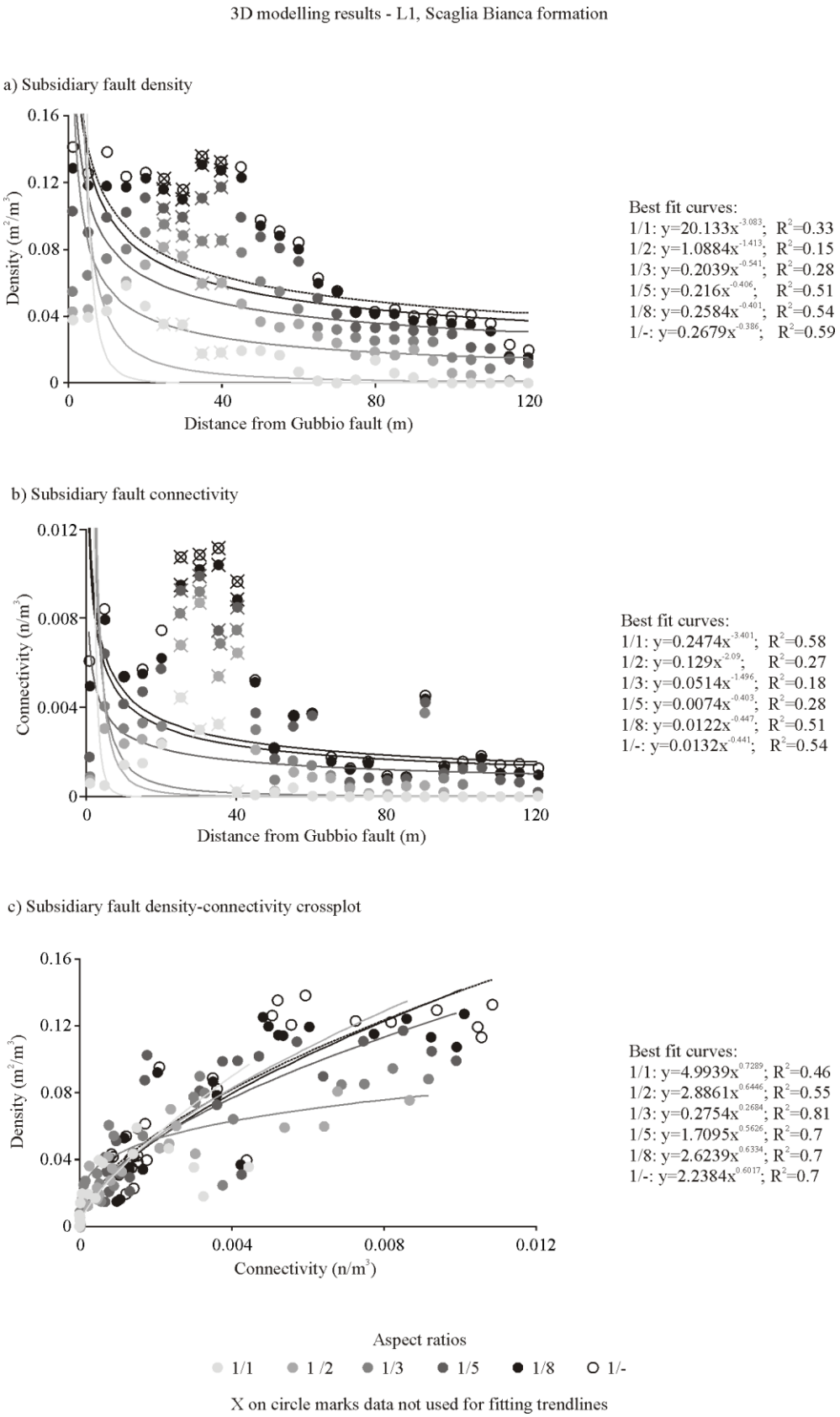

Figure 4.34 - 3D modelling results – L1, Scaglia Bianca formation
a) Subsidiary fault density, b) Subsidiary fault connectivity, c) Subsidiary fault density-connectivity crossplot

Best fit, power-law trendlines were fitted to the different aspect ratio subsidiary fault connectivity datasets gained from the Scaglia Bianca formation (Fig. 4.34b). The anomalously high value datapoints between 20 m and 40 m to the fault core were not used for these fits. The equations of the trendlines are

$y=0.2474x^{-3.401}$ ($R^2=0.58$) for the 1/1 aspect ratio model,

$y=0.129x^{-2.09}$ ($R^2=0.27$) for the 1/2 aspect ratio model,

$y=0.0514x^{-1.496}$ ($R^2=0.18$) for the 1/3 aspect ratio model,

$y=0.0074x^{-0.403}$ ($R^2=0.28$) for the 1/5 aspect ratio model,

$y=0.0122x^{-0.447}$ ($R^2=0.51$) for the 1/8 aspect ratio model and

$y=0.0132x^{-0.441}$ ($R^2=0.54$) for the 1/- aspect ratio model.

The R^2 values are all relatively low (all of them under 0.6). The best correlations were found for the 1/1, 1/8 and 1/- aspect ratio models, where the R^2 value ranges between 0.51 and 0.58 (Fig. 4.34b).

Crossplots, plotted for subsidiary fault density and connectivity results is the Scaglia Bianca formation (Fig. 4.34b) show similar power-law trends between the two variables as it was shown from 2D results (Fig. 4.27c, f, i). Models containing more elongated fractures reach the top right corner of the graph with high subsidiary fault density and connectivity values (up to 0.15 m^2/m^3 and 0.012 m/m^3, respectively), while data gained from models containing less elongated fractures are clustered towards the bottom left corner of the graph at low subsidiary fault density and connectivity values. The equations of the best fit, power-law trendlines are

$y=4.9939x^{0.7289}$ ($R^2=0.46$) for the 1/1 aspect ratio model,

$y=2.8861x^{0.6446}$ ($R^2=0.55$) for the 1/2 aspect ratio model,

$y=0.2754x^{0.2684}$ ($R^2=0.81$) for the 1/3 aspect ratio model,

$y=1.7095x^{0.5626}$ ($R^2=0.7$) for the 1/5 aspect ratio model,

$y=2.6239x^{0.6334}$ ($R^2=0.7$) for the 1/8 aspect ratio model and

$y=2.2384x^{06017}$ ($R^2=0.7$) for the 1/- aspect ratio model.

The R^2 values are all relatively high (over 0.46), and for all the models with aspect ratios lower than 1/3 the correlation between the two variables can be considered strong.

The best fit, power-law trendlines of subsidiary fault density and connectivity, gained from the different aspect ratio 3D models, similarly to the 1D and 2D data, were normalized to 1 in the protolith to study the relative increase of these variable throughout the damage zone and to, later, estimate the mean aspect ratio of fractures and veins (Fig. 4.35). Although, the length of the outcrop was only 120 m, the protolith value was chosen to be at 300 m from the fault core-damage zone boundary as it was done in case of the 1D (Fig. 4.18c) and 2D (Fig. 4.26) data in order to make these normalized curves comparable with each other.

Normalized trendlines of subsidiary fault density values are strongly dependent on the aspect ratio of the given 3D model these were normalized from (Fig. 4.35a-b). The highest aspect ratio models (1/1 and 1/2) are showing an increase in subsidiary fault density from the protolith to the fault core over 8 and 3 orders of magnitudes, respectively (Fig. 4.35a). In comparison, higher aspect ratio models (1/3, 1/5, 1/8 and 1/-) are showing considerably smaller increases, between 9 and 11 times (Fig. 4.35b).

Normalized trendlines of subsidiary fault connectivity values are also dependent on the aspect ratio of the given 3D models these were normalized from (Fig. 4.35c-d). The high aspect ratio models (1/1, 1/2 and 1/3) are showing an unrealistic increase in subsidiary fault connectivity from the protolith to the fault core over 8, 5 and 4 orders of magnitudes, respectively

(Fig. 4.35c). In comparison, low aspect ratio models (1/5, 1/8, 1/-) are showing considerably smaller increases, between 12 and 14 times (Fig. 4.35b).

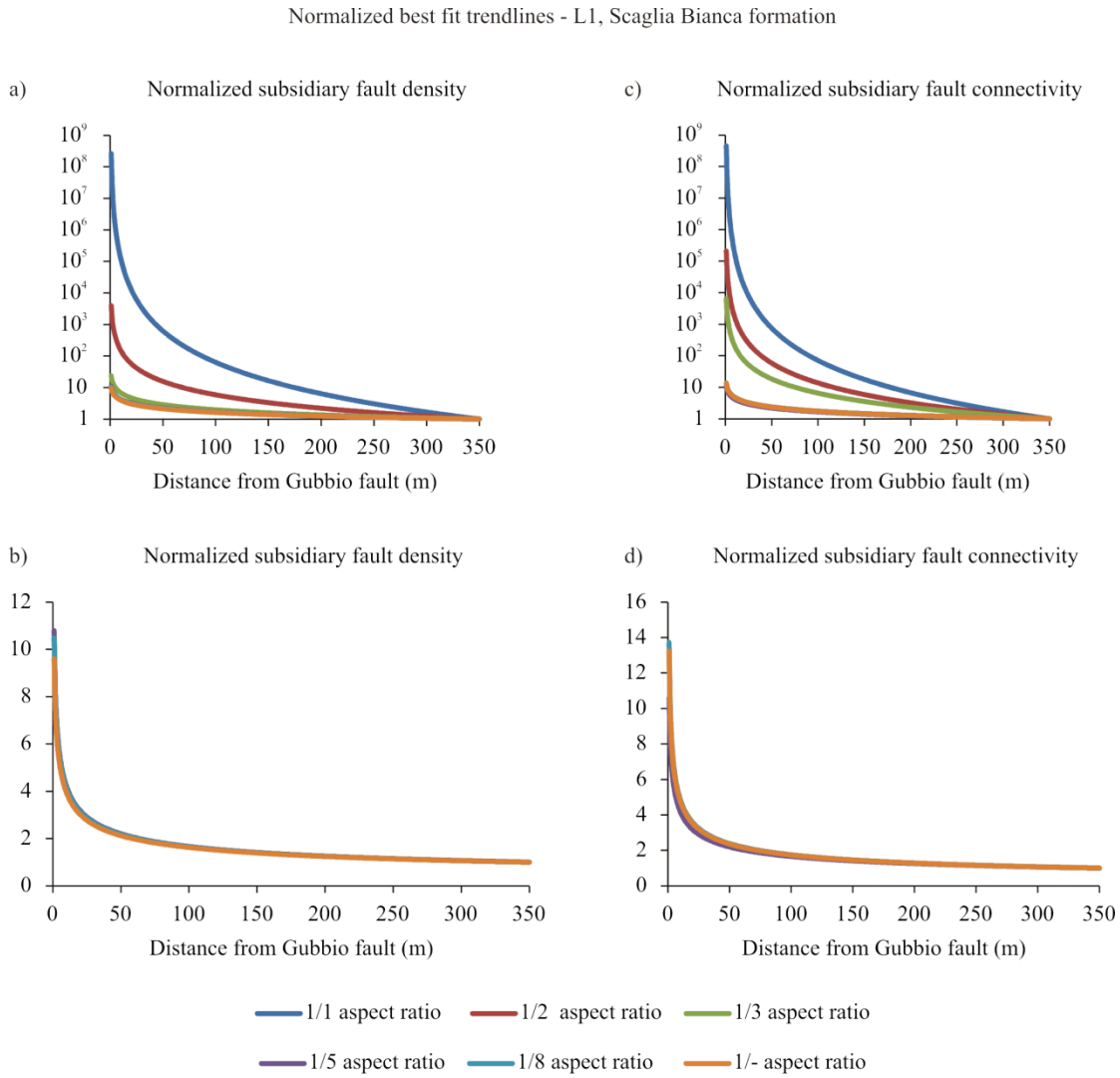

Figure 4.35 - Normalized best fit trendlines – L1, Scaglia Bianca formation
a) Normalized subsidiary fault density (all aspect ratio models), b) Normalized subsidiary fault connectivity (all aspect models), c) Normalized subsidiary fault density (1/5 – 1/- aspect ratio models), d) Normalized subsidiary fault connectivity (1/5 – 1/- aspect models)

4.4.3.2.Locality 2

At L2, 3D LiDAR data have been collected along transect CF1 at the Cava Filippi outcrop (for transect location see Fig. 4.3c). The scanned section contains 3 fault core domains (domain1-domain3) and the most fractured parts of the damage zone (up to 5 m away from the fault core-damage zone boundary, Fig. 4.36a). From the scan of the fault core-damage zone boundary, three principal slip surfaces were picked as primary features (Fig. 4.36b) that were later used as frames for the geocellular model (for methodology see Chapter 1.3.4). The fractures and veins, visible on the scan (with widths over approximately 5 mm) were also picked to calculate fracture/vein density and connectivity in domains1, 2 and 3 of the fault core and in the most intensively fractured parts of the damage zone (up to 5 m away from the fault core-damage zone boundary, Fig. 4.36b). 31 fractures/veins from the damage zone, 20 from domain1, 12 from domain2, and 9 from domain 3 were picked. The picked polylines, representing the fractures/veins, were interpolated to surfaces and were terminated against the slip surfaces. Due to the ratio between the average height of the picked fractures/veins (>0.5 m) and the typical thickness of the domains (2-3 m) different aspect ratios were not studied at this locations. After terminating most fractures/veins against slip surfaces, their aspect ratio was between 1/2 to 1/3. Additionally, the picked fractures and veins were used to plot their orientation distribution in stereonets and qualitatively compare them to field-based orientation measurement.

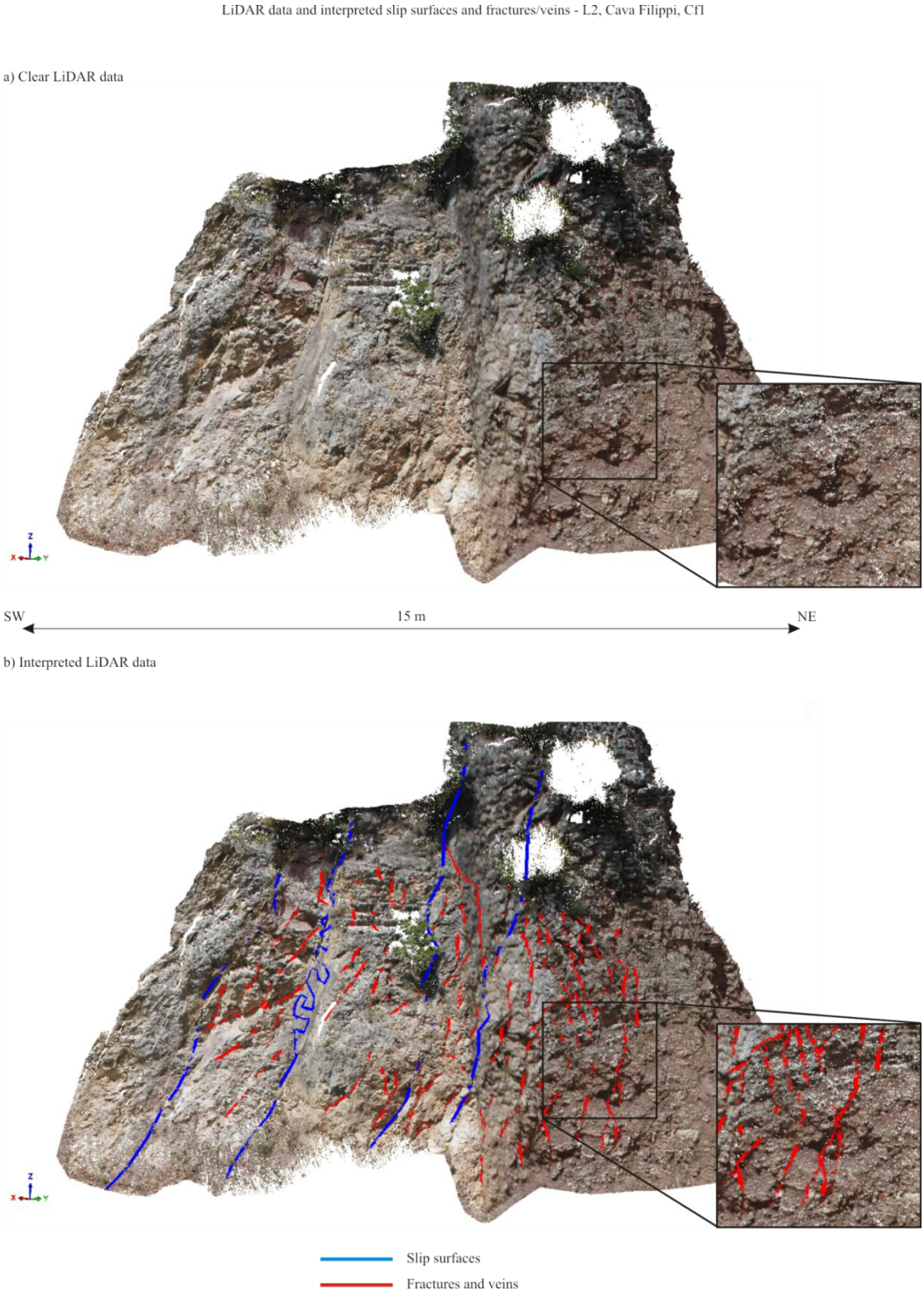

Figure 4.36 - LiDAR data and interpreted slip surfaces and fractures/veins – L2, Cava Filippi, CF1

a) clear LiDARdata, b) interpreted LiDAR data

Orientation of slip surfaces and fractures/veins in the fault core

The orientation of fractures and veins determined from the LiDAR data shows one mayor peak of E-W striking fractures/veins (Fig. 4.37a). This peak has an approximately 45° acute angle to the strike of the slip surfaces, determined by the same method (Fig. 4.37a), and also by the field-based orientation measurement along the same outcrop (Fig. 4.37b). The different fault core domains and the damage zone do not cluster separately; the distribution of the orientation data from the different sections is similar.

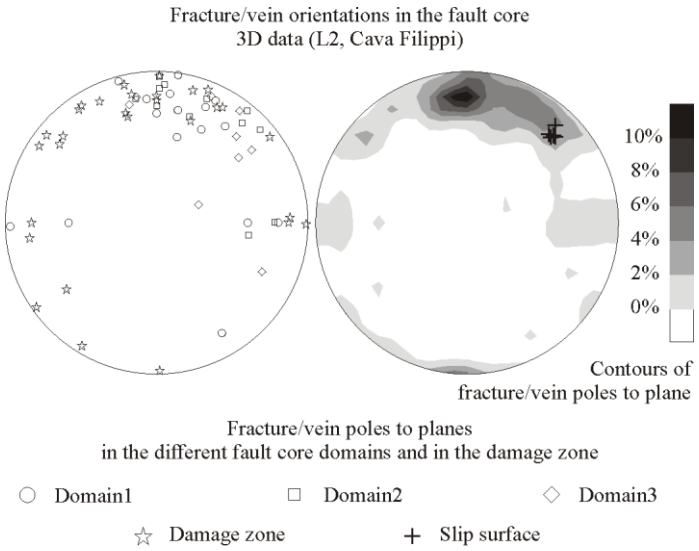

Figure 4.37 - Fracture/vein orientation in the fault core, 3D data (L2, Cava Filippi)

Fracture/vein density in the fault core

Fracture/vein density data, gained from the LiDAR data collected at Cava Filippi, shows that the values are up to 2 times higher (up to 0.6 m^2/m^3) in the damage zone close to the fault core, than in the fault core itself. Within the fault core, the different domains are characterized by fracture/vein density values ranging from 0.2 to 0.4 m^2/m^3 (Fig. 4.38a). In case of domain2 and domain3, fracture/vein density values are approximately two times higher in the centre of the domains (approximately 0.4 m^2/m^3) than close to the slip surfaces (approximately 0.2 m^2/m^3). In comparison, in domain1 the fracture/vein density values are

constant throughout the section, around 0.2 m^2/m^3, similar to those, obtained for the other two domains close to the slip surfaces, and half as large as the maximum fracture/vein density values obtained within the fault core (Fig. 4.38a).

In domain3 and domain2 parabolic best-fit trendlines were fitted to the fracture/vein density data (Fig. 4.38a), whilst in domain1 the fracture/vein density data could be fitted by a linear trendline (Fig. 4.38a). In the damage zone, fracture/vein density values are decreasing when moving away from the fault core and were fitted by a power-law trendline (Fig. 4.38a).

Fracture/vein connectivity data shows that the values are higher (up to 0.045 m/m^3) in the damage zone close to the fault core, than in the fault core itself (Fig. 4.38b). Within the fault core the different domains are characterized by fracture/vein connectivity values ranging from 0.0 m/m^3 to 0.03 m/m^3 with average values around 0.005 m/m^3 (Fig. 4.38b). Fracture/vein connectivity values are several times (orders of magnitudes) higher in the centre of the domains (approximately 0.03 m/m^3, 0.015 m/m^3 and 0.02 m/m^3 for domains 1, 2 and 3, respectively) than close to the slip surfaces (down to 0 m/m^3, Fig. 4.38b).

In the individual fault core domains parabolic best-fit trendlines were fitted to the fracture/vein connectivity data (Fig. 4.38b), whilst in the damage zone, fracture/vein connectivity values are decreasing when moving away from the fault core and were fitted by a power-law trendline (Fig. 4.38b).

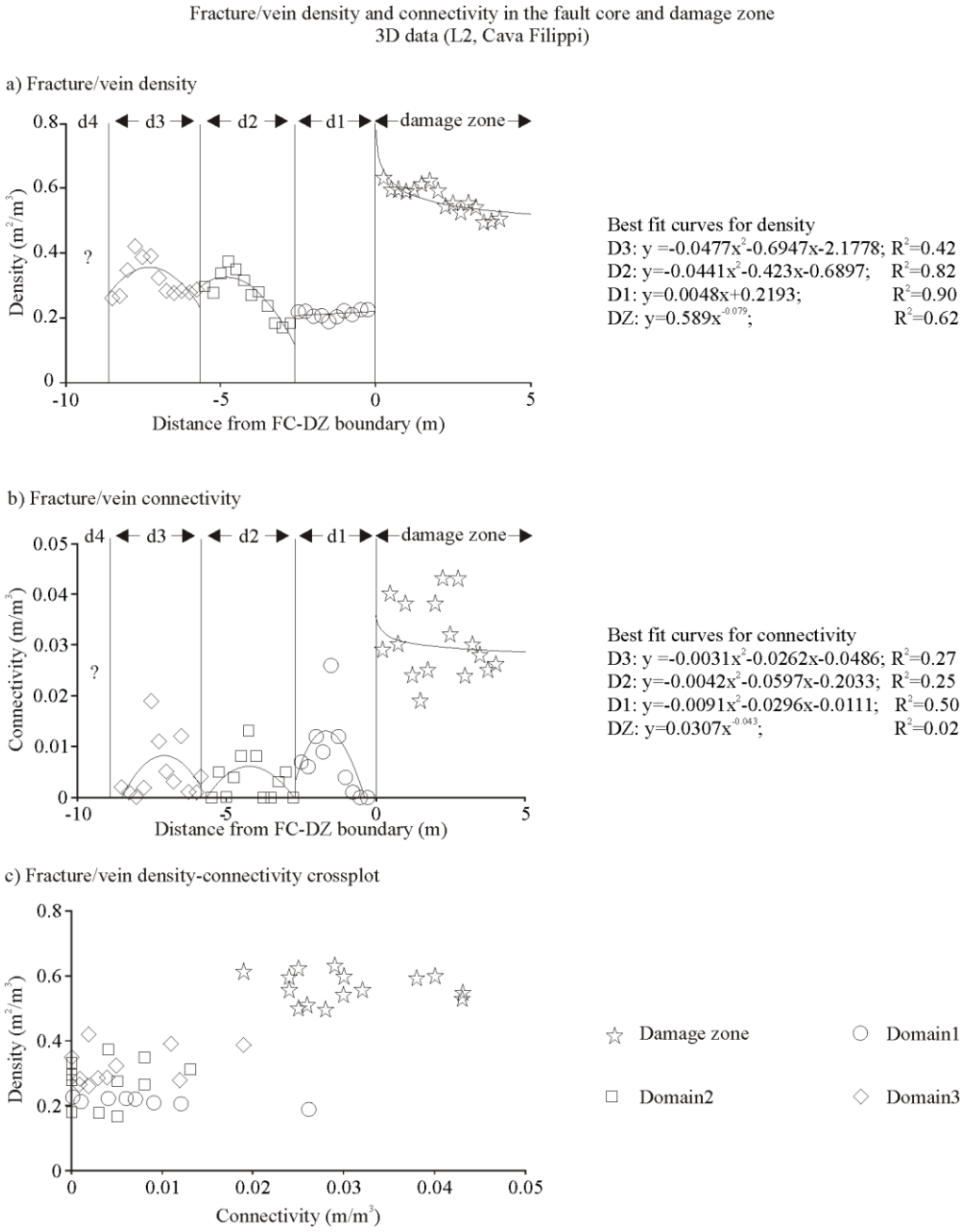

Figure 4.38 - Fracture/vein density and connectivity in the fault core and damage zone, 3D data (L2, Cava Filippi)

a) Fracture/vein density, b) Fracture/vein connectivity, c) Fracture/vein density-connectivity crossplot

Fracture/vein density-connectivity crossplots show a clustered distribution of the data (Fig. 4.38c). One cluster, representative of datapoints of the fault core, clusters close to the origin of the graph, around 0.2-0.4 m^2/m^3 fracture/vein density and 0-0.015 m/m^3 fracture/vein connectivity values. The other cluster, representative of datapoints of the

damage zone, clusters further away from the origin of the graph, around 0.5-0.6 m^2/m^3 fracture/vein density and 0.02-0.045 m/m^3 fracture/vein connectivity values (Fig. 4.38c).

4.5. Discussion

4.5.1. Fault zone architecture

The Gubbio fault zone was studied at two localities, L1 and L2, respectively, along the strike of the fault. At both localities the fault zone comprises of a damage zone, over 200 m wide and a fault core, built up of several fault core domains that are bounded and separated by well-defined slip surfaces. The fault core and the damage zone are also clearly separated by a well-defined slip surface, as predicted by classical fault zone models (Caine et al., 1993, Sibson, 1977).

4.5.1.1.The damage zone

Locality 1

The damage zone of the Gubbio fault at L1, in the Scaglia Bianca formation, is characterized by intense fracturing and veining. Both fracturing and veining increase when moving from the protolith towards the fault core (Fig. 4.8b-c). Most of the fractures and veins in the damage zone are striking parallel to the Gubbio fault itself (Fig. 4.8a), and are characterized by both Gubbio fault synthetic and antithetic dips (Fig. 4.8c). Throughout the damage zone, regardless of the distance from the fault core, fractures and veins appear similarly distributed to each other.

Subsidiary faults studied at L1, in the Scaglia Bianca formation are mostly sub-parallel to the Gubbio fault, but Gubbio fault orthogonal subsidiary faults are also present in the damage zone (Fig. 4.9a-d). Gubbio fault parallel subsidiary faults are always dip-slip normal faults,

Gubbio fault perpendicular subsidiary faults are always strike-slip faults and subsidiary faults with different orientations show a range of kinematics from dip-slip to oblique-slip (Fig. 4.9a-d). Based on their relative orientations to the Gubbio fault and the kinematic indicators present on their slip surfaces, the Gubbio fault parallel subsidiary faults are likely to be formed by one of the extensional phases of deformation affecting the Gubbio area, while the Gubbio fault orthogonal subsidiary faults were likely to be formed during the compressional phase of deformation affecting the Gubbio area (De Paola et al. 2006, Fig. 4.2b). However, due to the lack of intersecting subsidiary faults on the cliffs, crosscutting relationships between the subsidiary faults, characterized by Gubbio fault parallel and perpendicular directions, were not observed.

The displacements of the Gubbio fault parallel subsidiary faults ranges from 0.2-5 m and are usually characterized by a well-developed fault zone with a fault core and damage zone. These fault zones are superimposed on the damage zone of the Gubio fault. Their fault cores are typically 10-50 cm wide and are surrounded by damage zones, up to 1-5 m thickness (Fig. 4.9e-f). The damage zone of the subsidiary faults are usually characterized by anomalously high fracturing and/or veining as they are overlapping with the damage zone of the Gubbio fault, forming localised fracture corridors.

Microscale structural observations revealed the internal structure of veins and the role of stylolites in the damage zone. Observed on thin sections, veins at L1 usually displayed an anastomosing pattern (Fig. 4.15b). This geometry is similar to the “zebra-rocks” described by Holland and Urai (2010), who interpreted this geometry as the result of several reactivation events. Many of the observed veins are terminating against styolite surfaces (Fig. 4.15d) and some of the observed stylolites are (partially) reactivated as veins.

At L1, the damage zone of the Gubbio fault was also observed within the Marne a Fucoidi formation along an approximately 60 m long transect, CS1 from the distance and along a shorter transect, C1, from closer distance (for transect locations see Fig. 4.3b). The damage zone within the Marne a Fucoidi formation is characterized by intense fracturing (Fig. 4.10b). Fracture density appears to be several times higher in this formation than in the Scaglia Bianca formation, at similar distances from the fault core. However, veins and other fluid assisted deformation features are almost absent in the Marne a Fucoidi formation. Only a few narrow and short veins were observed, randomly dispersed within the studied sections.

Subsidiary faults are also present in the Marne a Fucoidi formation. Due to the limited access to the outcrops, these were only observed from the distance, along the CS1 outcrop, from the NW side of the valley. These faults are characterized by continuous slip surfaces that cut through the entire, approximately 20 m, height of the outcrop (Fig. 4.10a). Since the total thickness of the Marne a Fucoidi formation varies between 45-90 m (Alvarez et al., 1977, Alvarez and Montanara, 1988), it is possible that some of the subsidiary faults are cutting through the entire formation, connecting the under- and overlying low marl content carbonates.

Locality2

The damage zone at L2 was observed in the Scaglia Rossa formation, along an almost continuous outcrop at a road section, above Moccaiana village, marked as transects M1-M6 (for transect location see Fig. 4.3c). The damage zone at this locality is characterized by intense fracturing and veining, both increasing from the protolith towards the fault core (Fig. 4.11b-e). Throughout most of the damage zone, especially in the inner parts of it,

fractures and veins are forming a fully connected network, with almost all of them being intersected by at least one other vein (Fig. 4.11c).

At L2 there are two sets of fractures and veins present, one striking parallel with the Gubbio fault (with mostly fault antithetic dips) and another one with Gubbio fault orthogonal strikes and south-eastwards dips (Fig. 4.11a). The Gubbio fault parallel fractures and veins are likely to be formed during one of the extensional phases of deformation affecting the Gubbio area, while the orthogonal ones during the compressional phase (De Paola et al., 2006, Fig. 4.2b). Crosscutting relationships show that some of the Gubio fault orthogonal fractures are crosscutting and some others are crosscut by Gubbio fault parallel fractures and veins, suggesting that fracturing and veining occurred during all three deformation phases.

Subsidiary faults, studied at L2, in the Scaglia Rossa formation are characterised by more scattered orientations than the subsidiary faults at L1. There were as many Gubbio fault orthogonal faults found as Gubbio fault parallel ones (Fig. 4.12a). On the other hand, kinematic indicators are showing that Gubbio fault parallel subsidiary faults are always dip-slip normal faults, Gubbio fault perpendicular subsidiary faults are always strike-slip faults and subsidiary faults with different orientations show a range of kinematics from dip-slip to oblique-slip (Fig. 4.12a-d). Interpreted similarly as the subsidiary faults at L1, based on their relative orientations to the Gubbio fault and the kinematic indicators present on their slip surfaces, the Gubbio fault parallel subsidiary faults are likely to be formed by one of the extensional phases of deformation affecting the Gubbio area, while the Gubbio fault orthogonal subsidiary faults were likely to be during by the compressional phase of deformation affecting the Gubbio area (De Paola et al. 2006, Fig. 4.2b).

Microscale structural observations showed that the veins, present in the damage zone have gone through several reactivation events (Fig. 4.15d). Many of the veins are terminating against bedding surfaces and stylolites, and some of the stylolites were reactivated as veins and were filled with calcite (Fig. 4.15e).

4.5.1.2.The fault core

The fault core and its boundary with the damage zone were studied at both localities L1 and L2 (Fig. 4.13, 4.14). Structural observations showed that no fractures, veins, or any other deformation features are crosscutting the primary slip surfaces. At L2, the different fault core domains are all characterized by their own suite of fault rocks (Fig. 4.14a). Moving through the domains from the footwall, there are less and less preserved bedding surfaces, and after domain3 these features are absent. At the same time, the amount of brecciation increases. Within domain4 breccias become absent as well, and foliated cataclasites are present possibly due to the initial host rock lithology, that appears to be more clay-rich in this section.

4.5.2. Quantitative fault zone attributes: 1D and 2D analysis

Fracture and vein density and connectivity

Fracture and vein density was quantified in the damage zone of the Gubbio fault, at both studied localities, L1 and L2, using 1D and 2D methods described in Chapter 1.3.1 and 1.3.2, respectively. Within the damage zone, at both localities fracture/vein density decreases with distance from the fault core (Fig. 4.18, 4.19, 4.23), as predicted by classical fault zone models (Chester et al., 1993; Sibson, 1977; Wallace and Moris, 1986).

Using the variations of fracture/vein density along Gubbio fault orthogonal 1D transects allowed the quantification of the width of the damage zone, which was estimated to be approximately 220 m in the footwall damage zone (Fig. 4.18a), at both localities (Fig. 4.a, d). This width is similar to the damage zone width of other faults with the same maximum displacement (3 km, see Fig. 2.8 and 2.9, Torabi and Berg, 2011, Faulkner et al., 2011). The average density of fractures/vein at the two localities was approximated with a best fit, power law trendline (Fig. 4.18b). The trendline suggest that fracture/vein density close to the fault core is approximately 17/m and in the protolith it is between 2/m and 3/m.

1D results show that Gubbio fault parallel fracture/vein density has a similar variation across the damage zone at both localities (Fig. 4.19a, d). Best fit, power-law trendlines suggest that, at both localities, fracture/vein density is approximately an order of a magnitude higher at the fault core-damage zone boundary than in the protolith. However, at L1, close to the fault core, anomalously high fracture/vein density values were measured (Fig. 4.19a). When only vein densities are compared from the two localities, the general trends are the same (Fig. 4.19b, e). Vein density is 2-3 times higher close to the fault core than in the protolith. On the contrary, fractures show different density patterns across the damage zone at the two localities (Fig. 4.19c, f). At L1, fracture density is almost constant (around 1/m) throughout the damage zone, except for a few meter section, close to the fault core, but this data was collected in the Marne a Fucoidi formation (Fig. 4.19c). In comparison, fracture density at L2 varies in a similar manner than vein density (Fig. 4.19f). Fracture density is approximately 7 times higher close to the fault core than in the protolith.

1D data, gained from transects C1 (from the Marne a Fucoidi formation) and C2 (from the Scaglia Bianca formation, for transect locations see Fig. 4.3b) at approximately the same

along-strike position (locality L1) and at the same distance to the fault core-damage zone boundary (0-3 m) allowed to comment on the lithological control on the damage (Fig. 4.20). Cumulative fracture and vein density was measured to be higher within the Marne a Fucoidi formation (average 15/m) than in the Scaglia Bianca formation (average 6/m), but these higher values in the Marne a Fucoidi formation are gained from high fracture density values (average 13/m), as veins are rare features. In comparison, within this formation average vein density in the Scaglia Bianca formation (6/m) is higher than average fracture density (2/m). These fracture and vein density values are similar to the fracture and vein density values, estimated by the best fit power-law trendlines at L1 (Fig. 4.19a-c). The high cumulative fracture and vein density in the Marne a Fucoidi formation can be explained by the thinner beds present within the unit. The low number/absence of veins can be explained by the high marl content of the unit.

Gubbio fault orthogonal fractures/veins were also studied separately from fractures/veins with fault parallel directions (Fig. 18d). The density of these features is uniform throughout the damage zone; approximately, on average 3/m. This suggests that these features formed independently from the Gubbio fault and are only part of the background fracturing. Higher (up to 10/m) densities of Gubbio fault orthogonal fractures/veins were only observed within a) the Marne a Fucoidi formation, which is generally characterized by higher fracture/vein densities than the Scaglia group and b) in the damage zone of subsidiary faults that are oriented orthogonal to the Gubbio fault itself, which are characterized by fractures that are oriented sub-parallel to the subsidiary faults themselves.

The power-law trendline fitted to the Gubbio fault parallel fracture/vein density data (Fig. 4.18b) was normalized in a way that the protolith is characterized by a value of 1

(Fig. 4.18c). This was done in order to see the relative changes in the variation of fracture/vein density across the damage zone and to, later, compare these variations with 2D and 3D quantitative results (see Chapter 1.3.5). The normalized trendline shows that fracture/vein density at the fault core-damage zone boundary is almost 10 times, nearly an order of a magnitude, higher than in the protolith (Fig. 4.18c). This increase is very similar to the increase found by Mitchell and Faulkner (2009), who studied fault zones of strike-slip faults with displacements ranging from 30 m to 5000 m (for a detailed comparison see Chapter 5.2).

In case of 2D analysis, in addition to fracture/vein density data, fracture/vein connectivity data were also gathered. Outcrop scale fracture/vein density and connectivity data were collected using 3 different outcrop-camera distances: 5 m, 2 m and 0.5 m. In general terms, regardless of the particular outcrop-camera distance, outcrop scale 2D image analysis results show that fracture/vein density and connectivity values are decreasing when moving away from the fault core towards the protolith (Fig. 4.27). In case of all three different datasets there were no differences found between the variation of fracture/vein density and connectivity values at L1 and L2. Results from the Marne a Fucoidi formation, similarly to the 1D results, are showing higher fracture/vein density and connectivity results than results from the Scaglia Bianca formation, collected at the same along strike position and distance to the fault core in case of the 2 m outcrop-camera distance dataset (Fig. 4.27d-e). However, in case of the 5 m outcrop-camera distance dataset, fracture/vein density and connectivity values gained from the Marne a Fucoidi formation are not higher than the same values gained from the Scaglia Bianca formation (Fig. 4.27a-b).

The variation of fracture/vein density values within any given 2D outcrop scale dataset is approximately one order of a magnitude, and density values decrease gradually throughout the damage zone (Fig. 4.27a, d, g). In comparison, the variations of fracture/vein connectivity values are over two orders of magnitudes, and high connectivity values seem to concentrate in the inner parts of the damage zone (up to approximately 50 m away from the fault core). In the outer parts of the damage zone fracture/vein connectivity values are more similar to the values representative of the protolith (Fig. 4.27b, e, h). This dissimilarity between the two variables can be seen on the density connectivity crossplots as well (Fig. 4.27c, f, i). Datapoints plotted on these graphs were also approximated by power-law trendlines. In general, the closer a datapoint is to the origin of the graph (low fracture/vein density and connectivity values) the further the corresponding photo was taken from the fault core-damage zone boundary. As these distributions are approximated with power-law trendlines, the variation of fracture/vein density throughout the damage zone is as follows: a) the protolith is characterized by low fracture/vein density and connectivity values, b) within an outer damage zone fracture/vein density values start to increase, but fracture/vein connectivity values remain low, c) in an inner damage zone fracture/vein connectivity values start to increase rapidly overtaking the relative increase in fracture/vein density.

The power-law trendlines, fitted to the datasets were normalized in a way that their protolith value became 1 (Fig. 4.26). With this normalization the relative increase in fracture/vein density and connectivity can be seen and can be compared to 1D data. Compared to the protolith values, fracture/vein density and connectivity data are 2 and 2.5; 2.3 and 6; 3.5 and 14 times higher for the 0.5 m, 2 m and 5 m outcrop-camera distance datasets, respectively (Fig 4.26). When this increase in density is compared to the increase found in case of the 1D datasets there is a relatively large mismatch. In case of the 1D data the increase in

fracture/vein density was 12 times, while the largest increase in case of the different outcrop scale, 2D datasets are 4 times (5 m outcrop-camera distance). The difference between the increase in fracture/vein density and connectivity values increases with increasing outcrop-camera distances (0.5, 2.7 and 11 for the 0.5 m, 2 m and 5 m outcrop-camera distances, respectively).

Subsidiary faults

Subsidiary faults are present at both studied localities, L1 and L2. They can be classified based on their relative orientation to the Gubbio fault (Fig. 4.9a-d, 4.12a-d, 4.21a, g). At both localities Gubbio fault parallel subsidiary faults are always normal fault (Fig. 4.9b, 4.12b), and Gubbio fault orthogonal subsidiary faults are always strike-slip faults (Fig. 4.9d, Fig. 4.12d). Gubbio fault parallel subsidiary faults are likely to have formed during the extensional phases of deformation, when the Gubbio normal fault was active, during extensional phases of deformation in the Lower Miocene and the Quaternary (De Paola et al., 2006), while fault orthogonal faults are likely to have formed during the compressional phase of deformation in the Upper Miocene when the Gubbio thrust and anticline were forming (De Paola et al., 2006). At L1 2/3 of the subsidiary fault present are Gubbio fault parallel, while at L2 this amount is less than 50% (Fig. 4.21a, g). At L1, close to the tip of the Gubbio fault there are more fault orthogonal subsidiary faults present than fault parallel ones.

Many subsidiary faults have a damage zone with increased fracture and/or vein density that can be identified on the 1D transects (Fig. 4.21b, h) and on the 2D image analysis results (Fig. 4.23-4.24). These zones of intense fracturing/veining are usually 1-2 m wide and within them the anomalously high fracture/vein density values are caused by the overlapping position of the damage zones of the Gubbio fault and the subsidiary faults. Since two sets of

fractures/veins with slightly different peak orientations are crosscutting each other, fractures/vein connectivity is also anomalously high in these zones. These highly fractured damage zones can be interpreted as fracture corridors that have an important role in fluid flow (see Chapter 4.5.5.).

Scaling issues

2D image analyses were performed on thin sections and outcrop photos, taken with different outcrop camera distances. Maximum fracture/vein density values are 0.9 m/m^2, 1.1 m/m^2, 5 m/m^2 and 800 m/m^2 in case of the 5 m, 2 m, 0.5 m outcrop camera distance outcrop scale, and the microscale image analysis data, respectively (Fig. 4.27a, d, g, 4.28a, 4.29a). (Microscale fracture/vein density results were converted to standard SI units using the following equation: 1 mm/mm^2 = 1000 m/m^2.) In case of fracture/vein connectivity, maximum values are 0.1 n/m^2, 0.35 n/m^2, 4.2 n/m^2 and 500 000 n/m^2, respectively (Fig. 4.27b, e, h, 4.28b, 4.29b). (Microscale fracture/vein connectivity results were converted to SI units: 1 n/mm^2 = 1 000 000 n/m^2.) It is apparent that the closer the camera is to the outcrop/thin section, the higher fracture/vein density and connectivity values are measured, regardless of the samples relative position to the fault. These differences in fracture/vein density and connectivity values are largely due to the resolution of the different datasets. When the camera is placed closer to the outcrop/thin section, than the smaller features are also becoming visible, therefore higher fracture/vein density and connectivity values are measured.

To analyse how different outcrop-camera distances can affect the measured fracture/vein density and connectivity values, the maximum values listed above were plotted against their acquisition distance (Fig. 4.39). In case of the microscale results a 1 mm distance was

assumed, which refers to the thickness of the glass in the scanner. In case of both fracture/vein density and connectivity, power-law relations, with high R^2 values were found (density: $y=2.6665x^{-0.823}$; $R^2=0.995$, connectivity: $y=1.4472x^{-1.836}$, $R^2=0.999$, Fig. 4.39). This shows that the fracture/vein density and connectivity results, gained form 2D analysis, are strongly dependent on the particular outcrop-camera distance used, and different outcrop-camera distances can be compared with each other using power-law scaling relationships.

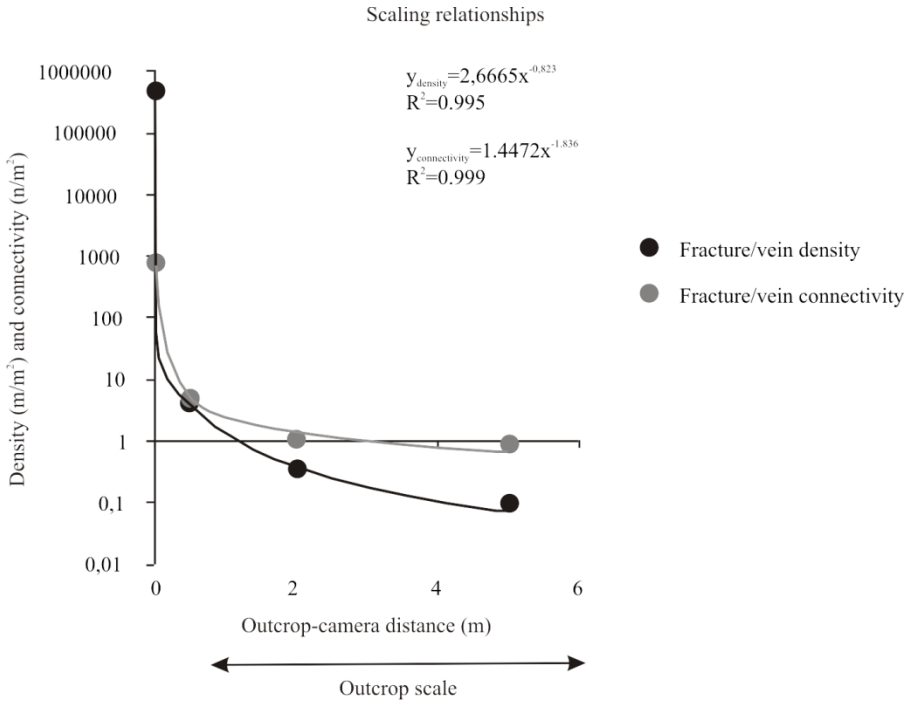

Figure 4.39 - Scaling relationship between the different outcrop-camera distance 2D datasets

4.5.3. Modelling fractured reservoirs in 3D

3D fracture/vein and subsidiary fault models were made based on data collected at the Cemetery outcrop, L1 (representative of the damage zone of the Gubbio fault), and at Cava Filippi, L2 (representative of the fault core). At L1, the variation of subsidiary fault density and connectivity, and at L2, the variation of fracture/vein density and connectivity were measured in the fault orthogonal direction.

L1, Cemetery outcrop

3D subsidiary fault models of the Cemetery outcrop were modelled using 6 different fracture aspect ratios, 1/1, 1/2, 1/3, 1/5, 1/8 and 1/- along two outcrops: the 60 m long CS1, representative of the Marne a Fucoidi formation and the 120 m CS2, representative of the Scaglia Bianca formation (for transect locations see Fig. 4.3b).

Within the Marne a Fucoidi formation, result of the 3D analysis showed that, regardless of the particular aspect ratio, subsidiary fault density and connectivity results are sharply decreasing in the first 20 m from the fault core, while further away from it subsidiary fault density and connectivity values are decreasing much less sharp (Fig. 4.33a-b). In case of the 1/5, 1/8 and 1/- aspect ratio models R^2 values for the best fit, power-law trendlines are relatively high, and suggesting a good correlation between subsidiary fault density and distance from the fault core (Fig. 4.33a). In case of subsidiary fault connectivity against distance from the fault core, R^2 values are high, suggesting a good correlation in case of the 1/3, 1/5 and 1/8 aspect ratio models (Fig. 4.33b). Subsidiary fault density and connectivity results suggest that the highest aspect ratio models (1/1, 1/2) are not realistic and should not be considered when modelling fractured subsurface reservoirs. The 3D models with high R^2 values for both subsidiary fault density and connectivity are the 1/5 and 1/8 aspect ratio models, suggesting that these aspect ratio models are more realistic and can be considered when modelling fractured subsurface reservoirs.

Within the Scaglia Bianca formation, results of the 3D analysis showed that for lower aspect ratio models (1/5, 1/8, 1/-) subsidiary fault density values are fairly uniform in the first 50 m of the damage zone, sharply decreasing between 50 and 70 m and slowly decreasing further away (Fig. 4.34a). In comparison, in case of high aspect ratio models (1/1, 1/2, 1/3) an edge

effect can be observed close to the fault core (up to 20 m distance) where the subsidiary fault density values are increasing as one moves away from the fault core. Such variation in fracture/vein density was not observed in case of 1D and 2D analysis. Additionally, the R^2 values of the best fit, power-law trendlines, fitted to the results of the different 3D models are low in case of the high aspect ratio models that are characterized by an edge effect. The lower aspect ratio models, 1/5, 1/8, 1/-, are characterized by higher R^2 values, 0.51, 0.54, 0.59, respectively, showing a better correlation between subsidiary fault density and distance from the fault core (Fig. 4.34a).

Subsidiary fault connectivity across the damage zone in the Scaglia Bianca formation are showing a somewhat different trend (Fig. 4.34b). Although there is a generally decreasing trend in the values as one moves away from the fault core, regardless the particular aspect ratio, there are anomalously high values between 20 m to 40 m from the fault core. These high values are interpreted to be caused by a fracture corridor, with several subsidiary faults and associated fractures crosscutting each other. The best fit, power law trendlines were fitted to the different aspect ratio datasets by ignoring this zone of high values, but the R^2 values were still calculated to be relatively low. Only the 1/1, 1/8 and 1/- aspect ratio models are characterized with relatively higher (0.51-0.58) R^2 values.

L2, Cava Filippi

LiDAR based 3D modelling of Cava Filippi allowed to characterize fracture patterns in domain1-3 of the fault core, and in the most intensely fractured parts of the damage zone (Fig. 4.36-4.37). Results showed that fracture/vein density and connectivity values are 2 times and one order of a magnitude higher, respectively in the damage zone than in the fault core. Within the fault core, in domain2 and domain3, both fracture/vein density and

connectivity values increase moving away from the principal slip surfaces, towards the middle of the domains. In domain1 only the fracture/vein connectivity values behave in a similar way, while density values are constant throughout the domain.

4.5.4. 1D/2D versus 3D quantitative analysis, validating 3D models, estimating mean aspect ratios of fractures

To estimate the mean aspect ratio of the fractures in the damage zone, normalized trendlines, fitted to subsidiary fault density and connectivity results, of different aspect ratio 3D models were qualitatively compared with normalized trendlines gained from 1D and 2D analyses, using misfit calculations following the steps described in Chapter 1.3.5. Misfit values were calculated between the different aspect ratio models versus 1D density, 2D density (5 m outcrop-camera distance), 2D connectivity (5 m outcrop-camera distance), and a sum of the three methods combined (Fig. 4.40). The 5 m outcrop-camera distance was chosen for comparison because, compared to the other outcrop-camera distance datasets, this one gave the overall best R^2 values for the best fit trendlines, it was the largest dataset in terms of number of datapoints and because its resolution is the most similar to the resolution of the LiDAR data.

The subsidiary fault density and connectivity values, gained from the 1/1, 1/2, 1/3 aspect ratio models differ greatly from the 1D and 2D datasets, and can be interpreted as non-realistic models (Fig. 4.35a, c). The other three models (1/5, 1/8, 1/- aspect ratios) give more realistic results. The best match with the 1D density values were given by the 1/5 aspect ratio model (52 misfit value), while the 1/8 and 1/- models gave misfits values of 56 and 59, respectively. The best match with the 2D density values were given by the 1/- aspect ratio model (129 misfit value), while the 1/5 and 1/8 models gave misfits of 146 and 141, respectively. Finally, the best match with the 2D connectivity values were given by the 1/5 aspect ratio model

(10 misfit value), while the 1/8 and 1/- models gave misfits of 51 and 45, respectively. Considering the summarized values of the misfits, the 2D density results have the worst results compared to different aspect ratio models (ranging from 129 to 146), 1D density misfits are ranging from 52 to 59 and the lowest misfits were calculated for the 2D connectivity data, ranging from 10 to 51.

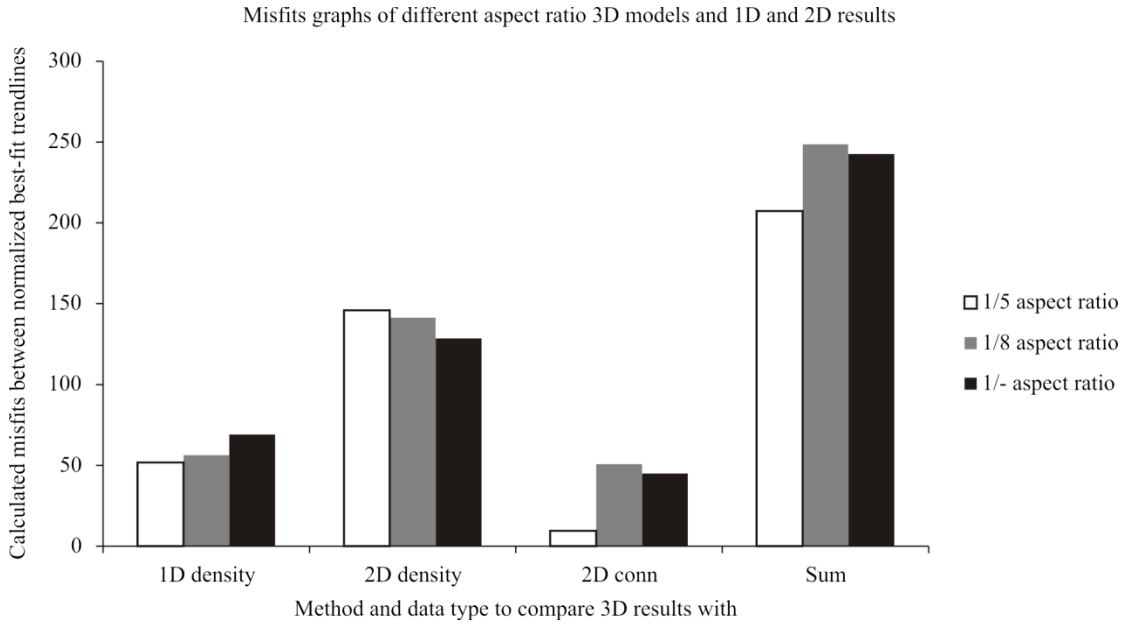

Figure 4.40 - Misfit graphs of different aspect ratio 3D models and 1D and 2D results

If the misfits from different models are summarized for each aspect ratio models, than the 1/5 aspect ratio models is characterized by the smallest misfit (207), while the 1/8, and 1/- aspect ratio models are characterized by total misfits of 249 and 243, respectively (Fig. 4.40). This suggests that, according to the method used, the most realistic 3D model is the one with the 1/5 aspect ratio, meaning that the estimated mean aspect ratio of the fractures/veins in the damage zone is 1/5. This estimated mean value of fracture aspect ratios is in the middle of the range, predicted by Schultz and Fossen (2002), who estimated the fracture aspect ratios to be between 1/1 and 1/10 based on 3D exposures of fracture patterns.

4.5.5. A conceptual fluid flow model

Based on the results gained from structural observations and 1D, 2D, 3D quantitative analyses a conceptual fluid flow model is proposed for the fault zone of the Gubbio fault (Fig. 4.41). The fluid flow model describes the variation of fluid transmissibility in different directions relative to the fault (fault orthogonal, dip parallel and strike parallel) in the different domains and host lithologies of the fault zone. Based on the different domains and lithologies the fluid flow model is divided into 3 sections: 1) the fault core, 2) the damage zone hosted in the Scalia group and 3) the damage zone hosted in the Marne a Fucoidi formation.

Fluid flow in the damage zone hosted in the Scaglia group

Fault parallel fluid transmissibility in the 220 m wide damage zone of the Gubbio fault, within the Scaglia Bianca and Scaglia Rossa formations, varies from the protolith towards the fault core and from the tips towards the centre of the fault. Moving in the fault orthogonal direction from the protolith, fault parallel fluid transmissibility increases gradually in the outer damage zone (more than 40-60 m away from the fault core) and steeply in the inner parts of the damage zone (less than 40-60 m away from it). Moving in the strike parallel direction, fluid transmissibility slightly increases from the tips to the centre of the fault, but this variation is likely to be smaller than the variation in fault orthogonal directions. Due to the main orientation of fractures and veins, in most of the damage zone fault orthogonal fluid transmissibility is not favoured.

Subsidiary faults and fracture corridors play an important role in the fluid flow around the Gubbio fault. Based on their relative orientation to the Gubbio fault, these subsidiary faults can be divided into Gubbio fault parallel and orthogonal faults. Within the damage zones of

subsidiary faults, oriented parallel with the Gubbio fault, fractures can strongly enhance fluid transmissibility in directions, parallel with them, by providing migration paths. On the contrary, Gubbio fault perpendicular subsidiary faults, likely to be developed during the compressional phase of deformation, can behave in two different ways. Collettini (2002) found evidences that some of these Gubbio fault orthogonal subsidiary faults reactivated during the current extensional event. When this occurs, the conductive fractures in their damage zone can provide migration paths for fluids migrating in the fault orthogonal direction, enhancing fluid flow between the inner and outer parts of the damage zone of the Gubbio fault. However, most of the Gubbio fault perpendicular subsidiary faults probably did not reactivate during extension. In this latter case, the previously precipitated calcite in the fractures of the damage zones would have healed them and they could behave as local barrier for fluids migrating in directions parallel with the Gubbio fault, unless the Gubbio fault parallel fractures and faults, formed during the extensional phase, cut through them (Fig. 4.41). This can result in local compartmentalization of the damage zone within a fractured carbonate reservoir.

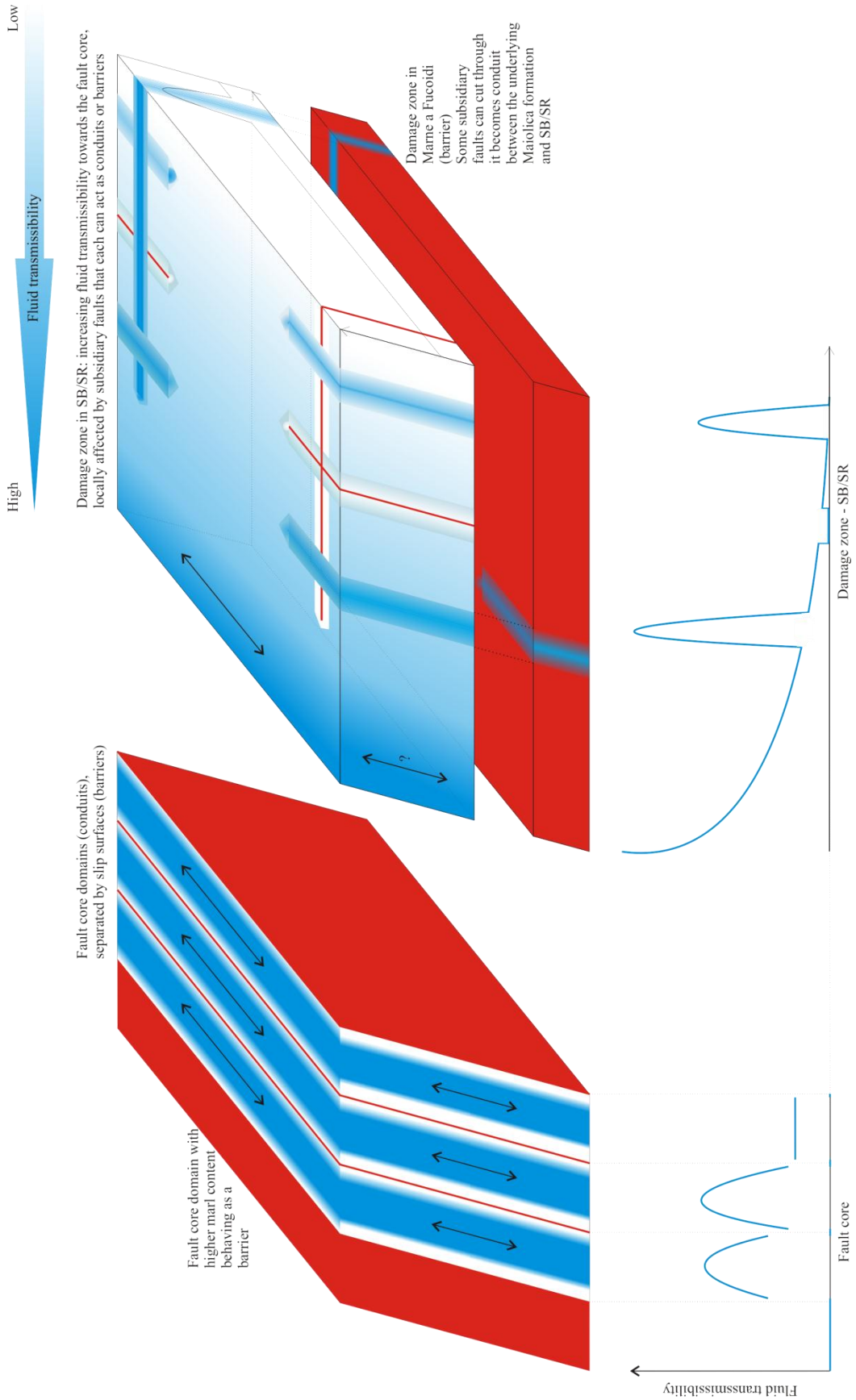

Figure 4.41 - Conceptual fluid flow model of the Gubbio fault zone

Fluid flow in the damage zone hosted in the Marne a Fucoidi formation

Within the Marne a Fucoidi formation, although it is heavily fractured, fluid assisted deformation features were minor or absent. This could be due to the high marl content of the formation that acts as a barrier for fluid in every directions (Fig. 4.41). Since the Marne a Fucoidi formation can be classified as a barrier, the lower parts of the directly overlying Scaglia group might lack dip parallel fluid flow.

Subsidiary faults of the Gubbio fault are also present within the Marne a Fucodi formation. Structural observations showed that in the vertical direction these subsidiary faults can cut through the Marne a Fuciodi formation, connecting the under and overlying low marl content carbonates, enhancing dip parallel fluid flow within the damage zone of the Gubbio fault in the otherwise low permeability formation (Fig. 4.41).

Fluid flow in the fault core

The fault core-damage zone boundary and the principal slip surfaces within the fault core, which bound the fault core domains, behave as strong, effective barriers for fluids flowing in across-fault directions. Within some fault core domains, especially in those closer to the damage zone (especially domain1-3), fluid flow may occurr in fault parallel (strike or dip) directions, while in other fault core domains (especially domain4-5) only limited evidences for fluid flow were found (Fig. 4.41). Fluid flow within the more conductive fault core domains occurs mainly in the centre of them, while fluid transmissibility decreases moving towards the slip surfaces. The low number/absence of fluid assisted deformation features in domains4-5 can be either due to the fact that these entire domains are behaving as barriers, or due to the bordering principal slip surfaces behaving as barriers restricting fluids flowing into these domains.

4.6. Conclusions

Based on structural observations and 1D, 2D and 3D quantitative analyses of the fracture patterns of the Gubbio fault zone the following conclusions can be made:

(a) The fault zone architecture of the Gubbio fault is similar to the models predicted by classical fault zone models (e.g. Caine et al. 1993, Sibson 1977). The fault core is built up of different fault rocks and within the approximately 220 m wide damage zone both fracture and vein density and connectivity decreases when moving away from the fault core.

(b) Quantitative analysis showed that both fracture/vein density and connectivity is several times higher close to the fault core than in the protolith. Fracture/vein density values are typically 4-8 times higher close to the fault core than in the protolith, while fracture/vein connectivity values are approximately one order of a magnitude higher close to the fault core than in the protolith.

(c) The lithological control on damage was studied by comparing fracture and vein patterns in the Scaglia Bianca and in the Marne a Fucoidi formation. Within the marl rich, thin bedded Marne a Fucoidi formation fracture density is high and veins are absent. Within the less marly Scaglia Bianca formation both fractures and veins are present but their overall density is lower than in the Marne a Fucoidi formation. Although, the Marne a Fucoidi formation is more densely fractured, the Scaglia Bianca formation has higher fluid transmissibility due to the lower marl content.

(d) The along strike variation of damage was studied by comparing fracture and vein patterns at the two studied localities, L1 and L2, at the centre and tip of the fault respectively.

Cumulative density and connectivity of fractures and veins are varying similarly across the damage zone at the two locations; however, closer to the fault core, vein density and connectivity is higher at L1 suggesting a higher fluid transmissibility at the centre of the fault than at the tip.

(e) Subsidiary faults in the damage zone can locally increase fracture and vein density and connectivity. These features can act as fracture corridors, enhancing fluid transmissibility in directions, parallel with them.

(f) Based on the orientation distribution of veins, fluid flow, when occurs, is enhanced in fault parallel directions. On the contrary, fluid flow is retarded in across-fault directions due to the presence of low permeability fault rocks, surrounding the slip surfaces of the fault core.

(g) The comparison of different resolution 2D datasets showed that there is a power-law scaling relationship between the calculated fracture/vein density and connectivity values and the distance between the camera and the outcrop.

(h) The validation of the different aspect ratio 3D models showed that the 3D model with the smallest misfit, therefore the most realistic one is the 1/5 aspect ratio model.

5. Discussion and conclusions

Detailed structural observations, complemented with micro- and outcrop scale 1D, 2D quantitative analyses and 3D modelling of a regional scale (> 1 km displacement), active normal fault (e.g. the Gubbio fault) and of smaller scale (displacement up to 25 m) normal faults at Flamborough Head (Selwick Bay and Dykes End) enabled a) to define the main characteristics of the fault zone architectures, b) to quantify the 1D and 2D distribution of fracture and vein density and connectivity of the fault zones in across-fault directions, c) to use a new method, developed during this project, to quantify fracture density and connectivity across fault zones in 3D using LiDAR data and modelling in GoCAD software, d) to estimate the mean aspect ratio of fractures in the damage zone of faults, e) to create conceptual fault zone sarchitecture models based on qualitative observations and quantitative analyses and f) to build conceptual fluid flow models applicable to fractured carbonate reservoirs.

5.1. Fault zone architecture

All of the studied faults, at Dykes End, Selwick Bay and Gubbio, show a fault zone architecture characterized by well-defined fault cores, surrounded by damage zones, where the intensity of fracturing progressively decrease when moving towards the protolith. These observations are in accord with the type of structure predicted by classical fault zone models (e.g. Sibson, 1977, Chester et al., 1993).

Damage zones

At all study areas the most prominent mesoscale deformation features of the damage zones are fractures and veins. The damage zones, regardless of their width and fault displacement, are characterized by increasing fracturing and veining when moving from the protolith

towards the fault core, where most of the displacement is localised. Fractures and veins are mainly pure tensional features, with no displacement observed along their plane. Their strike is sub-parallel to the main fault and display both synthetic and antithetic dips.

At both study areas, Flamborough Head and Gubbio, host lithologies with different marl content were studied. At Flamborough Head, faults hosted in a marl free host rock were found at Selwick Bay, whilst faults hosted in a marl rich host rock were found at Dykes End. In comparison, the Gubbio fault cuts through the Marne a Fucoidi formation, which is characterized by high marl and clay content, and also cuts through the overlying Scaglia Group, which is characterized by marl free carbonates, except for the lowermost members of the Scaglia Bianca formation, which represents a gradual transition from the Marne a Fucoidi formation. The distribution of marls within the Marne a Fucoidi formation is fairly uniform, while at Dykes End it is not, as marls localise along interlayered horizons. At both study areas, within the marl rich units, regardless of the distribution of the marls, veining is rare or absent, mostly only fracturing occurs. In comparison, all the studied marl free units are characterized by widespread fracturing and veining. This difference between the different marl content units has important effects on fluid flow and its implications are discussed in details in Chapter 5.5.

Fault cores

The fault cores and intensively brecciated zones observed at the different study areas are displaying very different architectures to each other. The fault core of the large displacement normal fault at Dykes End (displacement ≈ 1 m) is narrow (approximately 10 cm) and it is made of fault gouges and clay from the marl horizons interlayered within the chalk, which has been smeared out on the slip surface. Within the small grain size matrix, mm-scale chalk

fragments are still visible. In the middle of the core there is a dicrete slip surface with slickenlines indicating pure dip-slip normal displacement. Outcrop scale and microscale observations showed no fractures within this fault core. The fault core of the normal fault, observed at Dykes End displays an architecture that is very similar to that predicted by classical fault zone models.

The large displacement normal fault at Selwick Bay (displacement ≈ 20 m) contains two heavily damaged units that were referred to as fault core (FC) and intensely brecciated zones (IBZ), respectively. The FC comprises of a narrow (cm scale) gouge unit with a slip surface embedded within it, and a wider (m scale) zone, towards the footwall, made of breccias and some cataclasites. Both outcrop scale and microscale observations showed the presence of calcite filled fractures and cavities within this breccia zone. In comparison, the IBZ lacks gouges, cataclasites and a slip surface; this meter thick unit is entirely made of breccias. The cavities and fractures in-between breccias are filled with calcite. Borders between the IBZ/FC and the surrounding damage zones are not sharp, but they gradually pass into to the damage zone.

The third fault core studied was the one of the Gubbio fault`s. It is made of several fault core domains, with all the domains characterized by different fault rocks and all bounded by well-defined principal slip surfaces. The fault rocks in the centre of the individual domains are breccias and cataclasites, while towards the principal slip surfaces it is richer in gouges. LiDAR based 3D studies, quantifying the variation of fracture/vein density and connectivity within the core showed that both fracture/vein density and connectivity values are higher in the breccia and cataclasite bearing centre of the domains and lower towards the more gouge rich areas close to principal slip surfaces.

The fault core of the large displacement normal fault at Dykes End showed a relatively simple structure when compared to the fault cores of the other two studied faults, which were characterized by sub-domains and associated suites of fault rocks (e.g. breccias, cataclasites and fault gouges), bounded by principal slip surfaces that separate the domains from each other.

The fault core-damage zone boundaries are different in case of all studied faults. At Selwick Bay the fault core-damage zone boundary is a sharp line towards the hanging wall, represented by a well-defined slip surface, but it is distributed towards the footwall, where the amount of brecciation gradually decreases through an over 1 m wide section. This architecture is similar to the one observed by Billi et al. (2003) in carbonates. At Dykes End, the fault core-damage zone boundary is a sharp line represented by the disappearance of bedding planes and appearance of fault gouges when moving towards the centre of the fault. Finally, the fault core-damage zone boundary at the Gubbio fault, both at L1 and L2, is a sharp boundary with a well-defined slip surface with up to 30 m displacement on it (Bussolotto et al. 2007). This section of the fault zone can also interpreted to be similar to the one describe by Billi et al. (2003), however, since the hanging wall damage zone is eroded, the nature of the fault core-damage zone boundary on the hanging wall side is unknown. The width of the fault core of the studied faults appears to be proportional with the displacement on the fault as also shown by Torabi and Berg (2011) and references within (for quantitative comparison see text below).

5.2. Quantitative fault zone attributes: 1D and 2D quantitative analysis

Fault zone scaling relationship with displacement

Based upon the results of 1D analyses, the width of the damage zone of the Gubbio fault is approximately 220 m and the width of the damage zone of the Selwick Bay and Dykes End large displacement normal faults are approximately 4 m and 2 m, respectively. The displacements of these faults are approximately 3000 m (Mirabella et al., 2004), 20 m (Lamplugh, 1895) and 1 m (from field observations), respectively. For each individual fault studied, the scaling relationships between the width of the damage zone and the displacement along the fault plane can be compared with results from other authors working on different faults (Fig. 5.1). Both Faulkner et al. (2011 and references therein, Fig. 5.1a) and Torabi and Berg (2011 and references therein, Fig. 5.1b) studied the scaling relationships between the displacements on faults against the width of their damage zones. The faults studied in this Thesis can be plotted on the displacement-damage zone width graphs published by these authors. The studied faults all plot close to the estimated values, calculated by Faulkner et al. (2011) and by Torabi and Berg (2011), suggesting that they are regular faults in terms of these fault zone attributes (Fig. 5.1a-b).

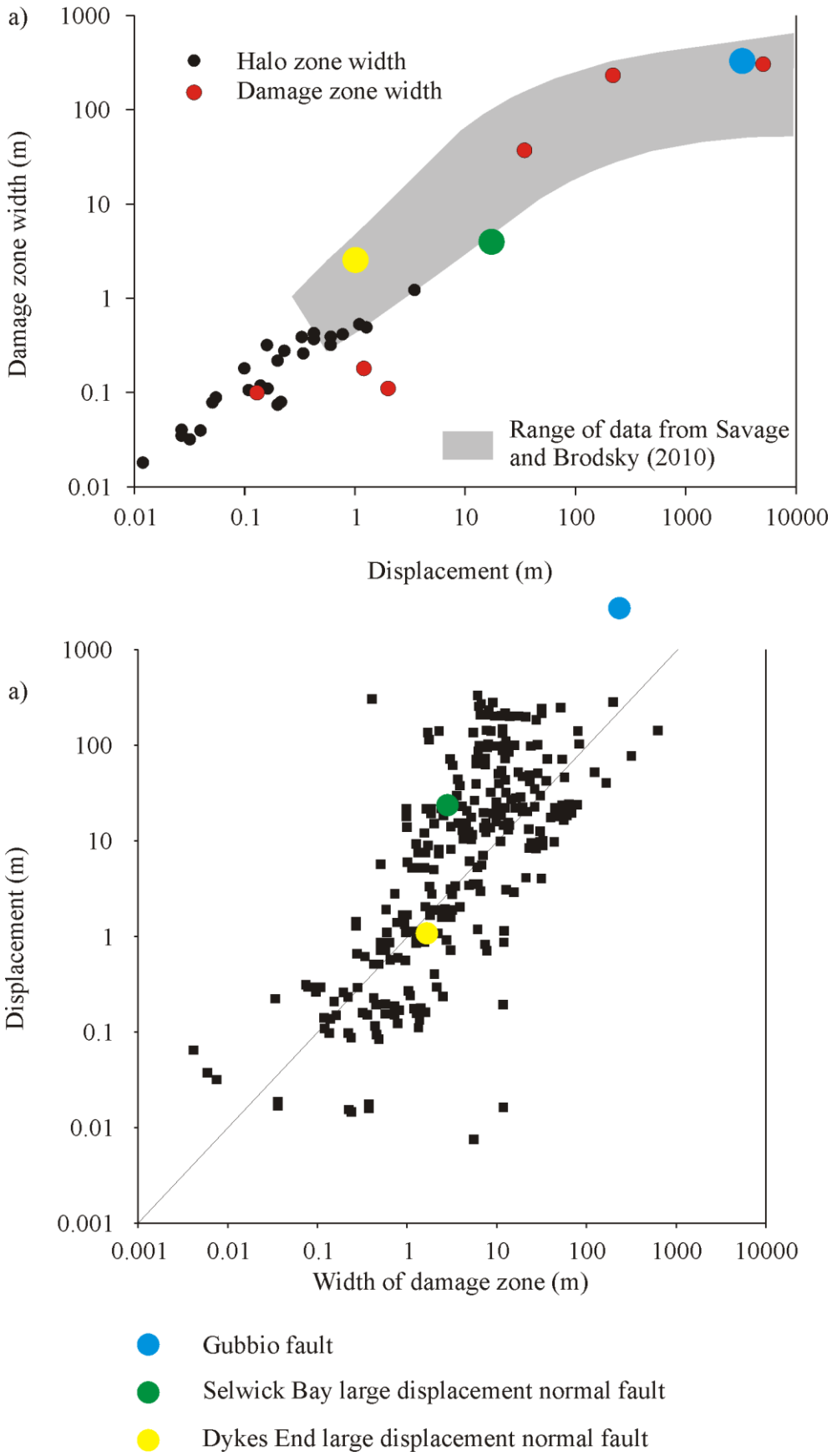

Figure 5.1 - Comparison of scaling relations (displacement-width) of the studied faults with previous studies

a) from Faulkner et al., (2011) and references therein, b) from Torabi and Berg (2011)

Variation of fracture and vein density and connectivity in the damage zones

Using 1D and 2D quantitative analyses enabled to study how fracture and vein density and connectivity vary across the damage zones. Classical fault zone models (Chester et al., 1993; Sibson, 1977; Wallace and Morris, 1986) predict a decreasing intensity of fracturing/veining as moving away from the fault core-damage zone boundary towards the protolith. Mitchell and Faulkner (2009) predicted the decrease in fracture density to be exponential. However, trying different best-fit trendlines in case of the studied faults showed that the decrease can be better approximated with a power-law relationship.

By the normalization of the best fit power-law trendlines of fracture/vein density and connectivity data to the background values of the protolith it was possible to quantify the relative increase of these variables throughout the damage zones of the different faults, studied (Fig. 5.2). For the Dykes End large displacement normal fault, the Selwick Bay large displacement normal fault and the Gubbio fault the relative increase in fracture/vein density is approximately 4, 8 and 12 times, respectively, to the protolith background values using 1D method. The relative increases in fracture/vein density, in case of the 2D results, are 3.4, 3.5 and 3.3, respectively (Fig. 5.2). These values are all gained from 5 m outcrop-camera distance photos. In case of the Gubbio fault dataset 2 m and 0.5 m outcrop-camera distances were also used. These analyses show the increases of density by 2.2 and 1.9 times, respectively. While 1D results suggest that the relative increase of fracture/vein density scales with the displacement of the fault (the larger the displacement the larger the relative increase in fracture/vein density), 2D results suggest that these variables are independent (e.g. the relative increase in fracture/vein density is constant for all faults). In comparison, results from Mitchell and Faulkner (2009) suggest that the relative changes in the increase of fracture/vein

density do not scale with displacement and ranges between 3 and 5. The results of Mitchell and Faulkner (2009) are the same as gained during this project for the 2D method.

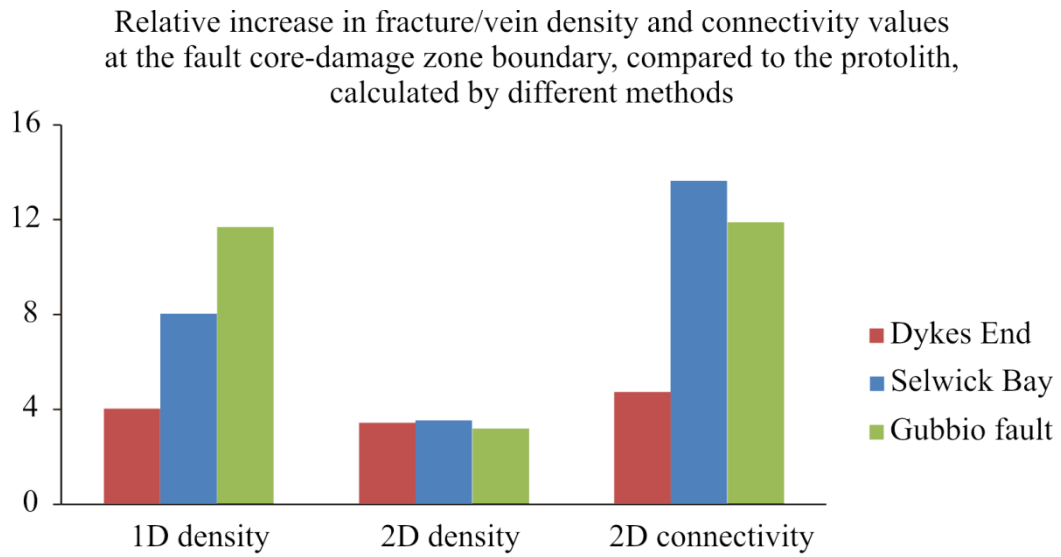

Figure 5.2 - Relative increase in density and connectivity values from the protolith to the fault core-damage zone boundary at Selwick Bay, Dykes End large displacement normal faults and at the Gubbio fault based on different quantitative methods

Normalized trendlines of 2D fracture/vein connectivity across the damage zones have also been plotted, and the relative increase of fracture/vein connectivity from the protolith to the fault core-damage zone boundary have been quantified (Fig. 5.2). 2D analyses, all using 5 m outcrop-camera distances, showed that the relative increase in fracture/vein connectivity from the protolith to the fault core-damage zone boundary is 4.7 times for the Dykes End large displacement normal fault, 13.6 times for the Selwick Bay large displacement normal fault and 12.5 times for the Gubbio fault (Fig. 5.2). (In case of the Gubbio fault dataset 2 m and 0.5 m outcrop-camera distances were also used. These analyses showed that the relative increases of fracture/vein connectivity are 5.2 and 2.3 times, respectively.) These results may suggest that the relative increase in fracture/vein connectivity throughout the damage zone does not scale with the displacement, nor has a constant value.

Regardless of the given study area and particular outcrop-camera distance, the comparison of 2D fracture/vein density and connectivity values show that in the outer parts of the damage zones the relative increase in fracture/vein connectivity from its background value of the protolith is low, close to zero (Fig. 5.3). As a result, quantifying the width of the damage zone based on fracture/vein connectivity values and not fracture/vein density values would result in the estimation of narrower damage zone widths. However, in the inner parts of the damage zone fracture/vein connectivity values are increasing quicker than fracture/vein density values (Fig. 5.3). The relative increase in fracture/vein connectivity from its protolith values is always higher at the fault core-damage zone boundary than the relative increase in fracture/vein density. Normalized fracture/vein connectivity values are calculated to be 1.3-3.9 times higher at the fault core-damage zone boundary than normalized fracture/vein density values, depending on the particular study area and outcrop-camera distance. These differences in the variation of fracture/vein density and connectivity values throughout the damage zone can also be seen on the equations of the best-fit power law trendlines, as, in general, trendlines of fracture/vein connectivity data are characterized by larger coefficients.

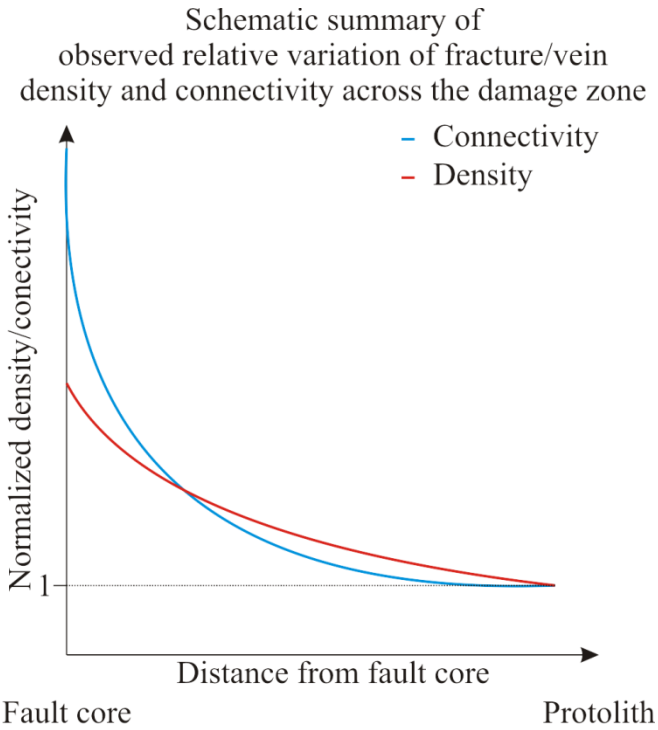

Figure 5.3 - Observed differences in the relative variation of density and connectivity across the fault zones

The observed variations in 2D fracture/vein density and connectivity can be explained by a simple conceptual model shown in Figure 5.4. This model considers an idealised fault zone, developed in protolith rocks, made of non-fractured rocks and rocks displaying background fracturing (Fig. 5.4a-b). The damage zone of the fault zone itself is made of three different domains: an outer damage zone (Fig. 5.4c), a middle damage zone (Fig. 5.4d) and finally, an inner damage zone (Fig. 5.4e). Following observations and quantitative analyses of the fracture/vein orientations in the field, it is assumed that in the different damage zone domains fractures/vein strike sub-parallel to the main fault and always dip at 60°, with both synthetic and antithetic dips relative to the main fault. Within the model, the different fault damage zone domains have been populated with fractures/veins according to the values of fracture density obtained from field-based 2D quantitative analyses (Fig. 5.4c-e). The mean values of fracture density are displayed and measured through a 1 m x 1 m frame (Fig. 5.4a-e). Fracture/vein connectivity can be calculated from the assumed fracture density in the model for each sub-domain looking through the 1 m x 1 m frame (Fig. 5.4a-e).

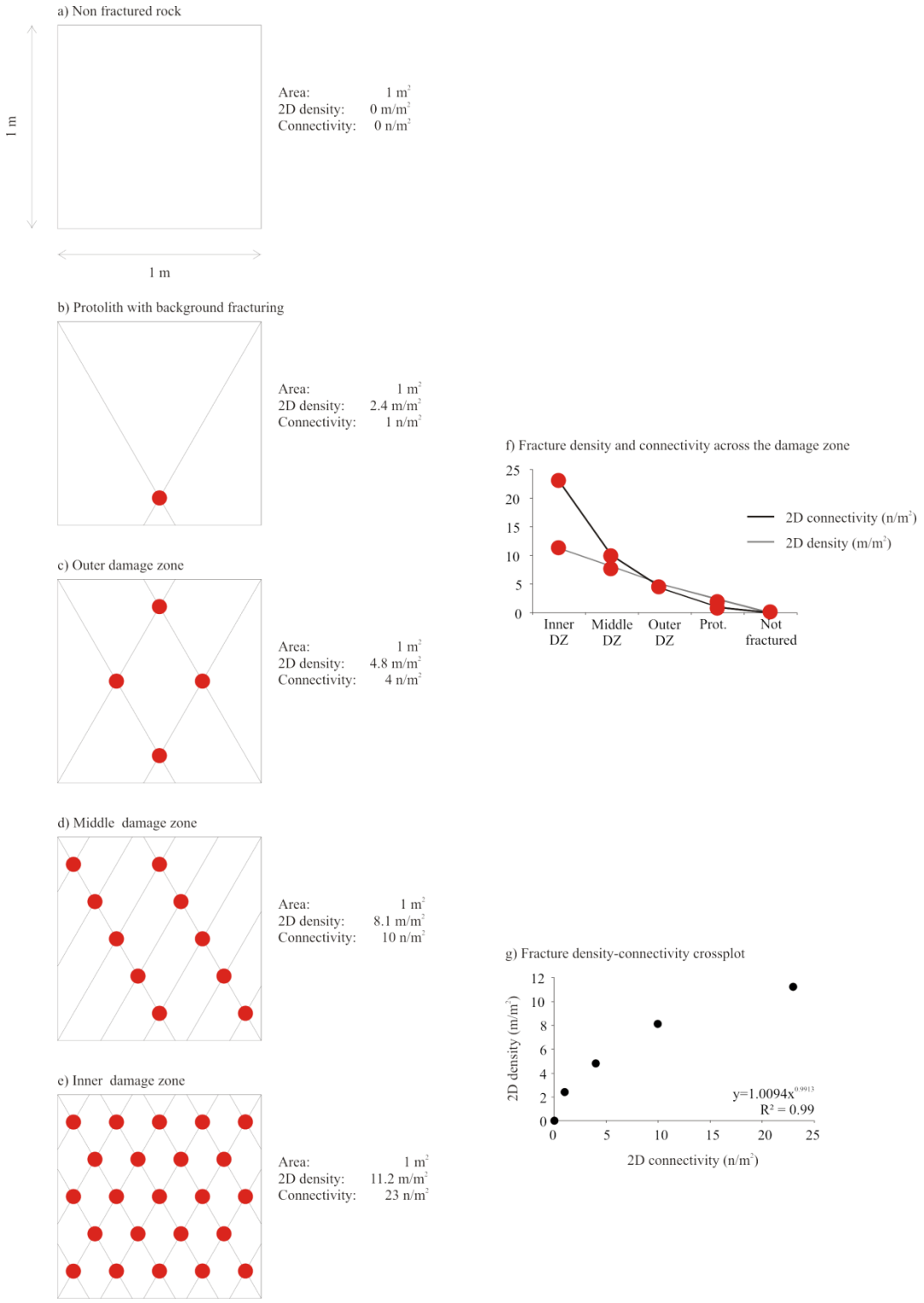

Figure 5.4 - Model explaining how density and connectivity varies across a damage zone a) fracture density and connectivity of an unfractured section, b) fracture density and connectivity of the protolith with background fracturing, c) fracture density and connectivity of the "outer damage zone", d) fracture density and connectivity of the "middle damage zone", e) fracture density and connectivity of the inner damage zone, f) results of a)-e) plotted on a summarized graph, g) density-connectivity crossplot of the results

The results from this simple conceptual model have been plotted on a graph, where the y-axis represents density and connectivity values and the x-axis represents points of the different sub-domains of the model (Fig. 5.4f). The relative variations in both fracture/vein density and connectivity are similar to those obtained from field-based measurements. It shows that fracture/vein density gradually increases as one moves from the protolith towards the fault core through the damage zone, while fracture/vein connectivity values are showing a slow relative increase in the outer parts of the damage zone, but increasing quickly in the inner parts (Fig. 5.4f).

The results from the model have also been plotted on a fracture/vein density vs. connectivity crossplot as well (Fig. 5.4g). When the data is view this way, they show that the modelled connectivity values are closely comparable to those, obtained by field measurements and analyses. These results show that it is possible to obtain realistic values of fracture/vein connectivity distribution across a damage zone, once the fracture density variation across naturally developed damage zones is known. Similarly to the real data presented in Chapters 3 and 4, a power-law relation was found between the two variables. The equation of the best-fit trendline is $y=1.0094x^{0.9913}$, with an R^2 value of 0.99 (Fig. 5.4g).

5.3. Modelling fractured reservoirs in 3D

LiDAR technology is a new methodology used in Earth Sciences, which has been previously used to create virtual outcrops (e.g. McCaffrey et al., 2008; Trinks et al., 2005; Xu et al., 2000; Xu et al., 1999) and to determine the orientation and orientation distribution of different geological features, such as bedding, faults and fractures (McCaffrey et al., 2008). During this project, a new method was developed to quantify the 3D density and connectivity of fractures/veins across fault zones as analogues of fractured, subsurface reservoirs.

Additionally, results from the 3D modelling method were used to estimate the mean aspect ratio of fractures in fault damage zones.

The method included the constraining of fault core-damage zone boundaries, the definition of the principal slip surfaces within the fault core, and the picking of subsidiary faults, fractures and veins in the fault damage zones as polylines from the LiDAR pointclouds. The polylines were exported to GoCAD software where planes were fitted to them according to different aspect ratio fractures: 1/1, 1/2, 1/3, 1/5 and 1/8, respectively. By placing a geocellular model (SGrid) around the fractures, that was oriented parallel with the fault zone, it was possible to quantify fracture/vein or subsidiary fault density and connectivity across the fault zones by counting the number of cells in each fault zone parallel slice of the geocellular model. The cells can be intersected by modelled planes or intersection line of planes (for a more detailed description of the data processing see Chapter 1.3.4). Finally, the mean aspect ratio of fractures/veins or subsidiary faults were estimated by comparing the different 3D models obtained, for each fracture aspect ratio, with the results of the 1D and 2D quantitative analyses. Normalization of the results obtained by the application of the different methods was performed in order to compare the results (for a more detailed description of the comparison see misfit graphs in Chapter 1.3.5).

The method was used in three instences, where fracture/vein or subsidiary fault density and connectivity were quantified: 1) the large displacement normal fault at Selwick Bay, Flamborough Head, 2) the damage zone of the Gubbio fault (data collected at L1, at the Cemetery outcrop) and 3) the fault core of the Gubbio fault (data collected at L2, at Cava Filippi). In case of Selwick Bay and L1, different fracture aspect ratio models were built for the damage zone datasets (see Chapter 3 and 4, respectively).

Fracture/vein density and connectivity values, obtained from modelling of 3D data according to the 1/1 and 1/2 fracture aspect ratios, did not show any significant variation across the damage zones, with progressive distance from the fault core, as it was reviled by the 1D and 2D datasets. In fact, data gained from these models are noisy due to the small total area of modelled planes compared to the studied volumes and due to the lack of and/or very short length of intersection lines. On the other hand, fracture/vein density and connectivity values obtained from modelling of 3D data according to the 1/3, 1/5, 1/8 and 1/- fracture aspect ratios are able to capture the overall evolution of these parameters across the damage zones, for increasing distances from the fault cores, in a similar way to 1D and 2D datasets. In particular, these models are characterized by a generally decreasing trend of fracture/vein or subsidiary fault density and connectivity values, according to a power-law variation. Moreover, secondary anomalies in fracture/vein density and connectivity values in the damage zone, due to the overlapping position of damage zones and due to the presence of subsidiary faults, shown by 1D and 2D quantitative analyses, can also be recognised on the 3D models obtained, using 1/3, 1/5, 1/8 and 1/- fracture aspect ratios (See details discussed in Chapter 5.4).

Fracture/vein density and connectivity values were also calculated within the fault core, by modelling data collected from the Gubbio fault, at locality L2 (Cava Filippi). The variation of these values within the different fault core domains shows that within the individual fault core domains fracture/vein density and connectivity increases moving away from the slip surfaces towards the centre of the domains. The values of fracture/vein density obtained in the fault core are lower than those in the damage zone of the same fault, directly next to the

fault core-damage zone boundary. These results have relevant implications on the transport properties of the fault core, which are discussed in details in Chapter 5.5.

Overall, these results show that, if the right choice of the fracture aspect ratio is made, then 3D modelling of fault zones is a powerful tool to: 1) visualize fractured, subsurface reservoirs, as it can reveal the complex internal architecture of fault zones, 2) calculate and predict fault zone parameters such as the variation fracture/vein or subsidiary fault density and connectivity across the damage zone.

1D/2D versus 3D quantitative analysis, validating 3D models and estimating mean aspect ratios of fractures

The validation of 3D models and estimation of the mean aspect ratio of fractures/veins in the damage zone was performed by using misfit graphs for data collected at both study areas. Overall, it showed that results from 3D models contain less elongated fractures (e.g. 1/1, 1/2, 1/3 aspect ratios, respectively) do not deliver similar results as those obtained by 1D and 2D methods. These models are overestimating the relative growth of fracture/vein density and connectivity towards the fault core damage zone-boundary; in case of the Cemetery outcrop, the dataset shows misfit values several orders of magnitudes higher than for low aspect ratio models. Therefore these models are not realistic. Moreover, these models do not posses the same resolution as the 1D and 2D ones, as they are able to image the local anomalies of fracture/vein or subsidiary fault density and connectivity as imaged by 1D and 2D methods.

Results from 3D models obtained for lower aspect ratios (e.g. 1/5, 1/8, 1/-, more elongated fractures) are characterized by lower misfit values, within the same order of magnitude, when compared to 1D and 2D results. The best fitting model, for both cases modelled (i.e. Selwick

Bay large displacement normal fault and the Gubbio fault), was the 1/5 aspect ratio one, suggesting that the most realistic mean aspect ratio of fractures within the damage zone of these faults is 1/5. This value is in the middle of the range of the aspect ratios of fractures predicted by (Schultz and Fossen, 2002), based on field observations.

5.4. Complex fault zone architectures

Classical fault zone models suggest that fault zones are symmetrical to the fault core, where most of the displacement is localised, with damage zones being developed on both sides of the fault cores (Chester et al., 1993; SIBSON, 1977; Wallace and Morris, 1986). The intensity of fracturing/veining in the damage zone monotonically decreases from the fault core-damage zone boundary towards the protolith. Structural observations and quantitative analyses both at Flamborough Head and at the Gubbio fault showed that, although the individual fault zones show similar gross architectures as predicted by classical models, still faults are characterized by internal complexities, which may control their transport properties. The following internal fault zone complexities were observed, quantified and discussed: a) overlapping damage zones and b) the role of subsidiary faults as fracture corridors in the damage zones.

Overlapping damage zones

Quantitative 2D analyses at the Selwick Bay large displacement normal fault and showed that the inner part of the footwall damage zone is characterized by gradually increasing vein density values, while vein connectivity values are high only in the inner parts of the damage zone and close to zero in the outer parts. The boundary between these two zones is sharp. As a result, the damage zone was divided into a weakly and an intensively connected damage zone (WCDZ and ICDZ), based on the damage zone subdivision of Micarelli et al. (2003, 2006b), who divided damage zones into outer and inner ones (WDDZ and IDDZ), based on

the intensity of damage. The development of these subdomains is interpreted as the overlapping position of the damage zones of two individual faults. In case of the large displacement normal fault at Selwick Bay these faults strike almost parallel with each other forming a 2D, sheet-like high connectivity zone (Fig. 5.5a).

It is also possible that other faults in subsurface reservoirs or other reservoir outcrop analogues crosscut each other with perpendicular strikes; in that case a 1D, pipe-like high connectivity, overlapping damage zone would form (Fig. 5.5b). In this latter case the 3D connectivity of fractures within the overlapping zone can be exceptionally high, since, given this geometry, two, perpendicular sets of fractures would mutually crosscut each other.

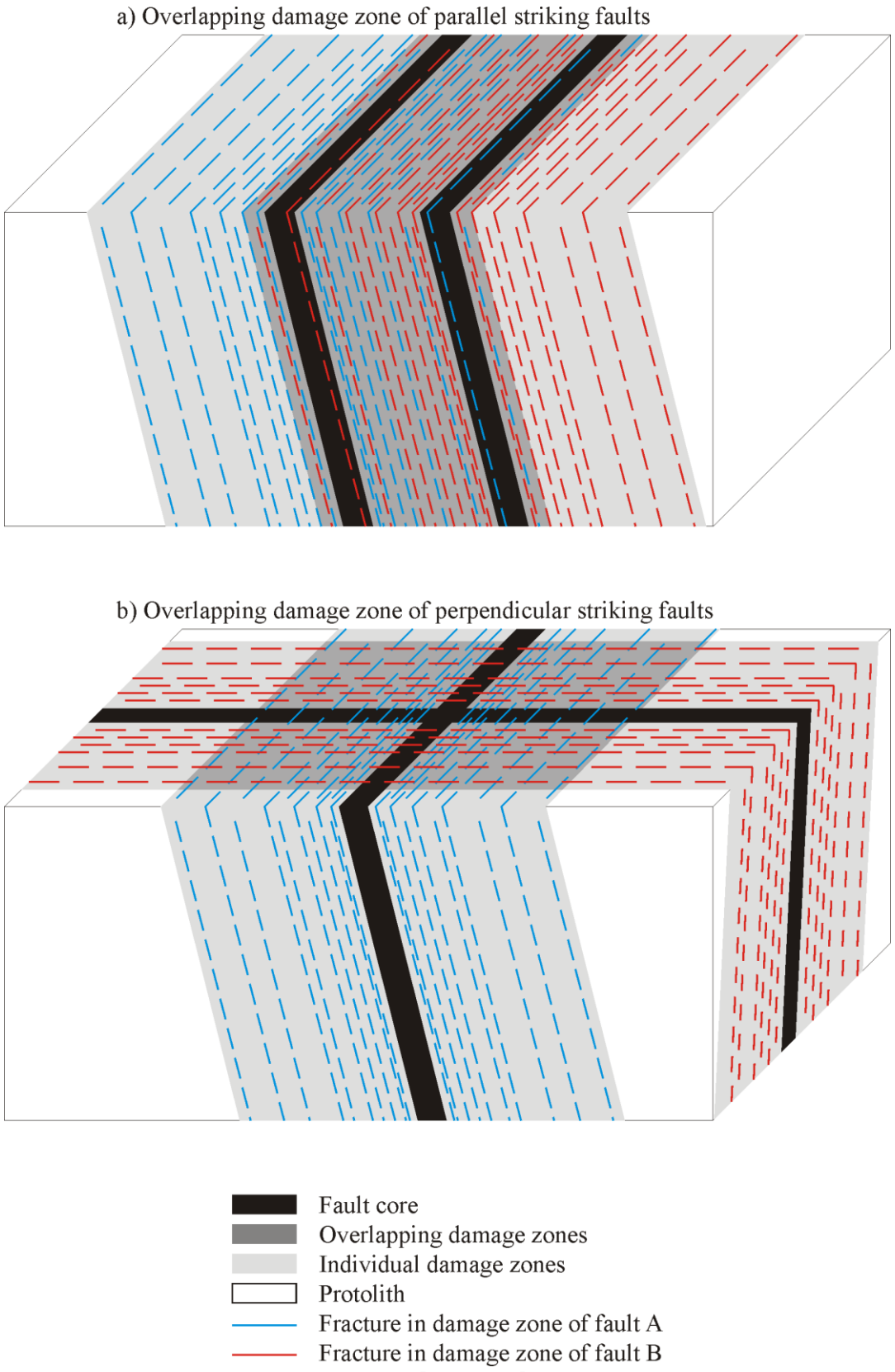

Figure 5.5 - Overlapping damage zones

a) two parallel fault zones forming a sheet-like overlapping damage zone, b) two perpendicular fault zones forming a pipe-like overlapping damage zone

Subsidiary faults, fracture corridors

High connectivity sections in the damage zones have not only been associated with overlapping damage zones. At the Gubbio fault, high fracture/vein density and connectivity zones were also found further away from the fault core, usually associated with subsidiary faults, developed in the damage zone (Fig. 5.6). These zones can form fracture corridors, characterized by high fracture and/or vein density and connectivity values, but not all the subsidiary faults have well developed fault cores with fault rocks within them. These have important implications for the transport properties of the fault zone, which are discussed in details in Chapter 5.5.

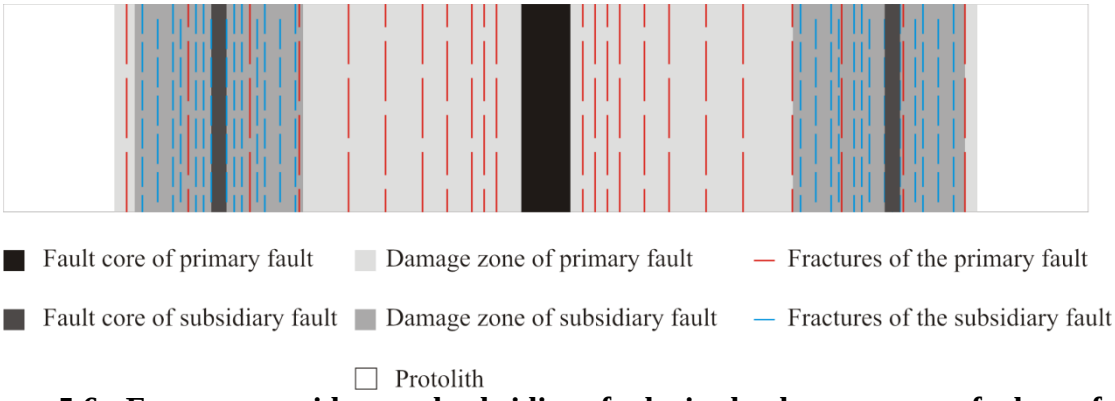

Figure 5.6 - Fracture corridors and subsidiary faults in the damage zone of a large fault

5.5. Conceptual fluid flow models

Results of the detailed structural observations and quantitative fault attribute analyses reviled the importance of different lithological units and deformation features present in the fault zones, which can enhance or, conversely, reduce fluid transmissibility. These features can also cause the anisotropy of fluid transmissibility within the fault zone.

At Flamborough Head no fluid assisted deformation features were found around the Dykes End study area. The absence of these features suggests that no fluid flow occurred along the

fault. Conversely, at Selwick Bay fluid assisted deformation features (e.g. veins) are widespread, suggesting the occurrence of fluid circulation. These observations hold for both small and large displacement normal faults, respectively. Since interlayered marl horizons are only present at Dykes End, but absent at Selwick Bay, these features may be responsible for the lack of fluid flow. During different deformations phases, parts of the interlayered marl horizons were smeared out and injected into faults and fracture planes, enhancing the barrier-like behaviour. At the same time at Selwick Bay, faults and fractures developed within the marl free units were able to enhance fluid flow. Within the fault zone of the large displacement normal fault at Selwick Bay, fluid flow was significantly enhanced, especially along fault parallel directions, due to the anomalously high vein connectivity, produced by the overlapping damage zones of the two main faults. Based on outcrop scale structural observation and quantitative data, fluid flow was exceptionally high in the ICDZ and relatively low in the WCDZ. Microscale data showed that fluid flow also occurred in the IBZ and FC, but within smaller scale fractures and cavities. On the other hand, the fine grained fault gouge layer, present around the slip surface of the FC and the abundance of stylolites may have acted as barriers, reducing flow, as suggested by the absence of veins on the hanging wall damage zone.

In the damage zone of the Gubbio fault, fluid assisted deformation features are common in the marl free units (Scaglia Group) and absent in the marl rich units (Marne a Fucoidi). Within the marl free units fluid assisted deformation features, such as fault parallel veins, are widespread and particularly abundant close to the fault core-damage zone boundary. Throughout the damage zone, fracture corridors, represented by damage zones of subsidiary faults can act as localised migration paths; whilst high marl content units (Marne a Fucoidi), gouge rich fault cores of subsidiary faults and small scale stylolites can behave as barriers for

fluids. Within the fault core of the Gubbio fault, breccias can enhance fluid flow, whilst gouges and catacalsites, associated with principal slip zones can behave as barriers, especially along across-fault directions.

Conductive and sealing host rocks

Both at Flamborough Head and the Gubbio fault, fracturing and faulting within lithological units with different marl content were studied. The marls, where present, were either organised in interlayered horizons or homogenously distributed throughout the entire formation. Regardless of the geometry, marl-rich units were always observed to behave as seals, apparently inhibiting fluid flow.

At the study areas a range of deformation features were found that can enhance fluid flow, such as fractured damage zones (see also: Caine et al., 1996), overlapping damage zones, fracture corridors (see also: Agosta et al., 2007; Micarelli et al., 2003) associated with the damage zones of subsidiary faults (see also: Questiaux et al., 2010) and fault breccias (see also: Evans et al., 1997). Conversely, fault cores of subsidiary faults and principal slip surfaces, due to the development of fine-grained gouges and cataclasites behave as barriers, retarding fluid migration (Byerlee, 1993; Caine et al., 1996; Evans et al., 1997; Sibson, 1977; Sibson, 2000).

Anisotropy of fluid flow

Based on the presence and orientation of the features influencing fluid flow, fault zones can show a high degree of anisotropy in fluid transmissibility (Fig. 5.7, also in e.g. De Paola et al., 2009; Evans et al., 1997; Rowland and Sibson, 2004). Along strike parallel directions fluid transmissibility is a function of fracture density, connectivity, aspect ratios and

orientation (distribution) as found also by McQuillan (1973), Ghosh and Mitra (2009), Odling (1992), Schultz and Fossen (2002) and (Sleight, 2001), respectively. Strike parallel fluid flow can be locally enhanced by the presence of fault parallel fracture corridors in subsidiary faults (see also: Agosta et al., 2007; Micarelli et al., 2003; Questiaux et al., 2010), overlapping damage zones and fault breccias (see also: Evans et al., 1997); whilst it is reduced by fault perpendicular subsidiary faults and damage zone tips (Fig. 5.7). Along dip parallel directions fluid transmissibility is controlled by similar fault zone attributes as the strike parallel flow ones. Additionally, dip parallel transmissibility may also be controlled by the lithology, as the initial permeability of the host rock (see also: Mallon, 2008; Mallon et al., 2005), when the major faults are not able to propagate through the sealing unit. High marl content rocks and interlayered marl horizons can behave as barriers, strongly reducing fluid transmissibility, while marl free carbonates can behave as conduits (Fig. 5.7). Finally, across-fault fluid transmissibility can be enhanced by the presence of fault perpendicular subsidiary faults, overlapping damage zones and breccias, while it is reduced by fault parallel fracture corridors associated with subsidiary faults and principal slip surfaces, due to the presence of fault rocks, such as gouges and cataclasites. Some deformation features, such as fault parallel fractures, fracture corridors, associated with subsidiary faults can enhance fluid transmissibility in one direction, but reduce it in the perpendicular direction (Fig. 5.7).

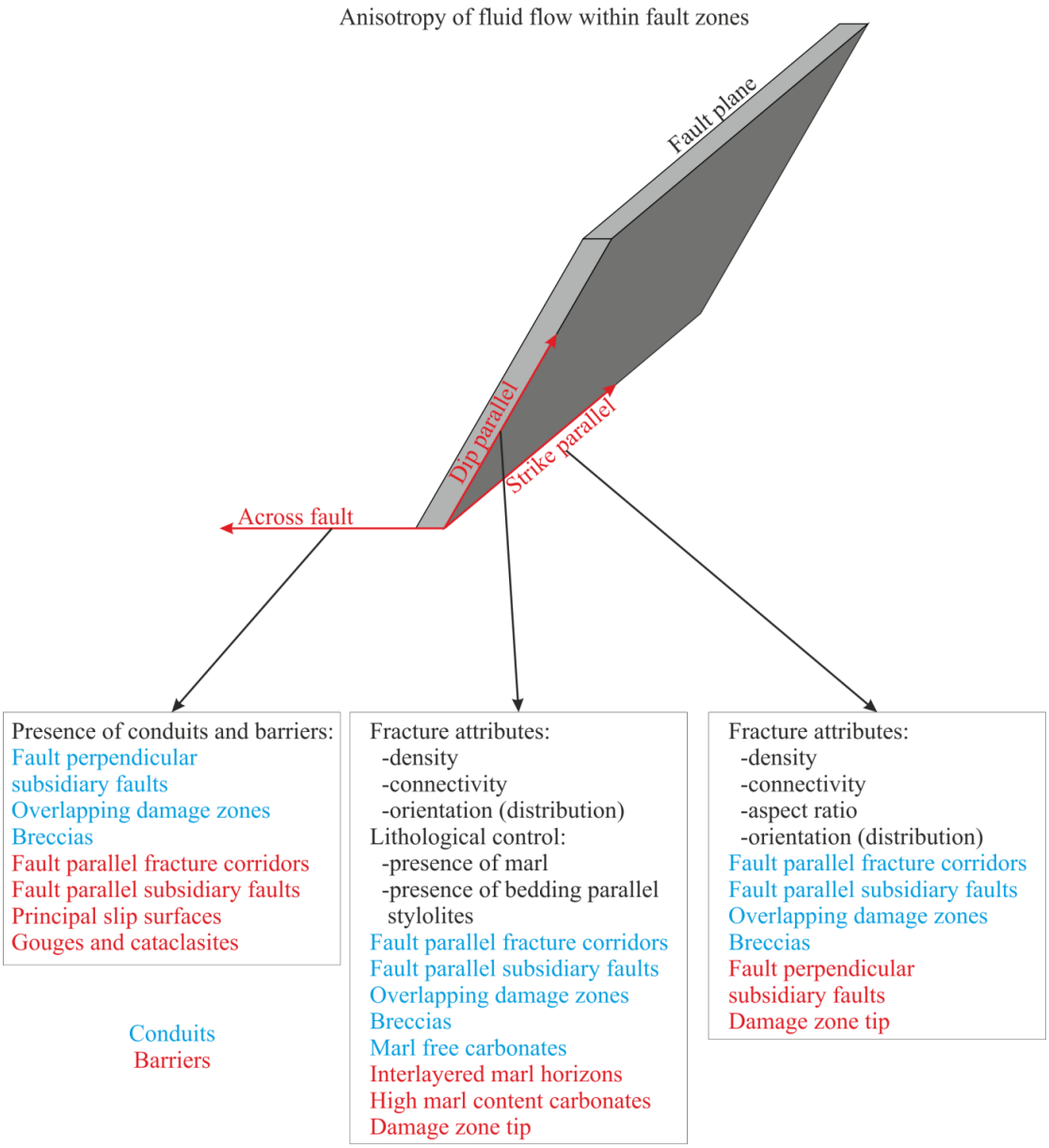

Figure 5.7 - Features influencing fluid flow within a fault zone and the observed anisotropy

As some of the features described above are more common than others, fluid migration was favoured in certain directions within the fault zones. Within marl free units, the fault seals limit across-fault flow, while it is favoured in both fault parallel directions (strike and dip parallel). However, the under- or overlying marl rich, sealing units can reduce widespread dip parallel flow, unless these units are fully crosscut by subsidiary faults with well-developed conductive damage zones. As a result, when fluid flow occurs, it is mostly favoured in the

strike-parallel direction, secondarily in the dip-parallel direction, while it is usually retarded in the across-fault direction.

Distribution of fault parallel flow

It has been shown that the directions with the largest volumes of migrating fluids are strike and dip parallel (Byerlee, 1993; Caine et al., 1996). Along the fault parallel direction fluid flow may not be homogenously distributed across the damage zone from the protolith to the fault core. Structural observations suggested that more veins are present closer to the fault core than further away from it. Quantitative analyses (1D, 2D, 3D, outcrop and microscale) proved that vein density and connectivity increases as one move towards the fault core. Both vein density and connectivity can be used as a proxy to estimate flow rates; however, high vein density without vein connectivity does not significantly enhance fluid transmissibility. As a result, the variations in vein connectivity represent a better estimate of fault-parallel flow across the damage zones of the faults than vein density. As vein connectivity remains low on the outer parts of damage zones, but rises sharply in the inner parts, fault parallel fluid flow is expected to be particularly intense in the inner parts of the damage zones, but almost as low as the protolith values in the outer parts of it (Fig. 5.8).

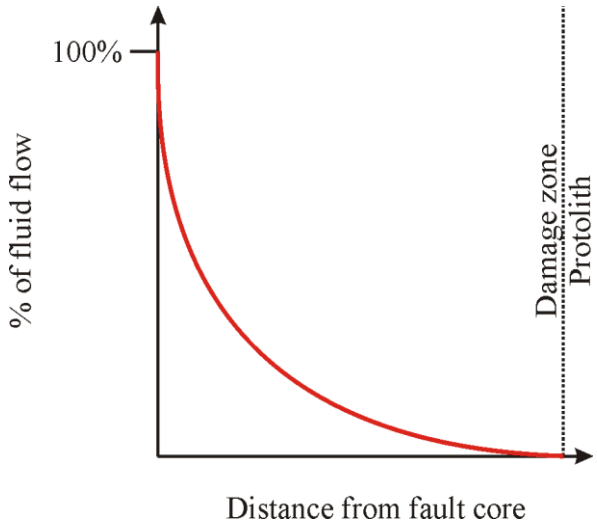

Figure 5.8 - Distribution of fault parallel flow across the damage zone

5.6. Applications for reservoir engineers

When creating/updating field development plans for the hydrocarbon industry, reservoir engineers usually use simplified fault geometries, where the fault itself is considered as a single plane. This simplified is based on the imaging of faults from seismic profiles, which usually have a relatively low resolution (a few 10 m), therefore displaying faults as single planes. In many cases modelling faults as single planes can be satisfactory; however, for more detailed studies the understating of the 3D architecture of fault zones is essential for effective planning. This is especially true for fractured reservoirs, hosted in low porosity and low permeability host rocks, where both the reservoir volume and the migration paths are represented by fractures.

It should also be noted that the host lithology can have a great impact on the fluid transmissibility of the fractures developed in fault zones or as background fracturing. Results of this study showed that only a few per cent of marl content in the host rock can significantly reduce fluid transmissibility in every direction. This observation is valid regardless of the spatial distribution of the marls. At Dykes End, Flamborough Head marl was initially enriched in horizons interlaying the chalk. The interlayered marl horizons may have prevented fluid flow in the vertical direction. Upon faulting the marls got smeared out onto and injected into the fracture planes, reducing fluid transmissibility in the horizontal directions. On the contrary, within the Marne a Fucoidi formation of the Gubbio fault, marls were more evenly distributed. Hence, within the marly units of the Gubbio fault, fluid flow was retarded in all directions.

In case of detailed field development plans, reservoir engineers should consider which parts of the different fault zone domains are potentially characterized by high structural

permeability values. According to the results of this study high permeability fault zone domains, zones that are characterized by both high fracture density and connectivity, are usually located in the damage zone, hosted in low marl content lithologies, close to the fault core, where fracture density and connectivity values are both high. These damage zone domains are referred to as intensely connected damage zones. When developed, brecciated fault cores and fracture corridors, further away from the fault core can also behave as fluid conduits.

This study also showed that the variation of fracture attributes, such as the height/length aspect ratio can greatly affect fluid transmissibility. Results of the 3D modelling showed that the mean aspect ratio of fractures in damage zones is 1/5 in case of both studied faults, the Gubbio fault and the large displacement normal fault at Selwick Bay. When reservoir engineers model hydrocarbon fields they should consider that the shape of the fractures (i.e. how elongated are they?) can have a great effect on the connectivity attributes and therefore on the distribution and anisotropy of fluid transmissibility in the damage zone.

5.7. Conclusions

Based on detailed multiscale structural observations, 1D and 2D quantitative analyses and LiDAR based 3D modelling of density and connectivity attributes of fracture and vein systems in carbonate reservoir analogues at Flamborough Head and the Gubbio fault, the following findings can be summarized:

Fault zone architecture

(1) Fault zones are characterized by an increasing trend in fracture and vein density and connectivity values when moving towards the fault core from the protolith. However, the

relative increases of the two variables do not occur with the same gradient throughout the damage zone. Fracture/vein density increases gradually throughout the outer damage zone, while connectivity increases slower in the outer parts and quicker in the inner parts of it. Overall, when the values close to the fault core are compared with values of the protolith, the relative increase in fracture/vein connectivity is higher than the relative increase in fracture/vein connectivity.

(2) LiDAR based 3D modelling of fault zones was found to be a powerful tool to analyse the fracture/vein and subsidiary fault density and connectivity attributes of fault zones, both in the damage zone and in the fault core. 3D modelling results obtained for up to 1/3 aspect ratios, reveal many characteristics related to the internal architecture of the fault zones, by showing the variation of fracture/vein or subsidiary fault density and connectivity in across-fault directions. These variations appear to be highly similar to the variations observed using 1D and 2D methods.

(3) Based on the quantitative comparison between different aspect ratio 3D models and 1D/2D analyses, it was shown that 3D models, containing less elongated fractures (1/1, 1/2, 1/3 aspect ratios) deliver non-realistic results. On the contrary, 3D models, obtained for more elongated fractures/veins or subsidiary faults (1/5, 1/8, 1/- aspect ratios) deliver more realistic results. In case of both studied damage zones, the 3D model with the smallest misfit values is the 1/5 aspect ratio one, suggesting that the mean aspect ratios of fractures/veins and subsidiary faults in the damage zones are 1/5.

(4) Although there was a generally increasing trend in fracture/vein density and connectivity values towards the fault core, all quantitative datasets showed that this trend can be locally

disturbed by the presence of fracture corridors, associated with subsidiary faults, and overlapping damage zones. Within these areas both fracture/vein density and connectivity values can be exceptionally high.

Applications to fluid flow

(5) The occurrence of fluid flow is primary controlled by the lithology. Units with high marl content lack the presence of fluid assisted deformation features; therefore can be interpreted as barriers. The marl can either be localised within interlayered horizons or distributed homogenously within carbonates. Within high marl content units, fluid flow can only occur in fracture corridors associated with damage zones of subsidiary faults. If these are fully crosscutting the marl rich unit, they can provide migration paths between under and overlying marl-free units. On the contrary, fluid flow within marl-free units can be widespread.

(6) It has been known that the transport properties of fault zones are heavily dependent on the fracture connectivity within them. In this project it was shown that high fracture connectivity domains are dominantly present only in the inner parts of damage zones. As a result of this, the inner parts of damage zones are characterized by higher fluid transmissibility and the majority of fluid flow occurs in these parts of the fault zones, while the outer parts of fault damage zone contribute much less to the total volume of flow.

(7) As a function of the presence and orientation of different deformation features, fluid transmissibility within a fault zone can show a high level of anisotropy. In fault damage zones subsidiary faults and fracture corridors, which can be oriented in either fault parallel or perpendicular directions, can strongly enhance fluid flow in directions parallel with them. Other, smaller scale deformation features of the damage zones that can retard flow are

stylolites (usually bedding parallel orientation, retarding dip parallel flow). Within the fault cores fluid flow can be enhanced in fault parallel directions in fault breccias, but strongly retarded in across-fault directions by catalclasites and gouges, usually present in the near vicinity of principal slip surfaces.

5.8. Future Work

Based on the results obtained during project, a list of potential further research topics can be suggested. These are studies to achieve a better understanding of the a) 3D architecture of fault zones, b) scaling relationships between fault displacement and fault zone attributes such as damage zone width, c) quantitative fluid flow properties of the different fault zone domains and, finally, d) how different rock mechanical properties of the host rock influence the development of fault zone architectures.

The conceptual fault zone architecture models presented and discussed in this study (e.g. Figs 3.19 and 4.41) can be made more detailed and realistic in all three directions. To achieve this, several fault perpendicular transects needs to be completed for the same fault in the along strike and dip directions. Fracture and vein density can be defined in smaller windows (e.g. 0.5 m) in order to achieve higher resolution and to more accurately highlight zones of anomalously low/high values or fracture and/or vein density. Completing several fault perpendicular transects along strike can show how does the damage zone width and the intensity of fracturing vary in this direction, possibly related to the varying displacement along the fault. Completing several transects along dip can highlight the importance of the lithological control on the fault zone architecture and show how damage zone width and fracturing intensity varies in different types of host rocks.

Although the width and displacement of several faults have been studied previously (e.g. Fig 5.1) these studies were dominantly focusing on faults with displacement less than a few hundred meters. Only a few faults with displacements more than 500 m have been studied previously in terms of quantitatively comparing their displacement and damage zone extent. By studying the Gubbio fault, it was possible to slightly fill the gaps on the graph at large displacement faults; however, more work needs to be done on large (i.e. km scale) displacement faults to accurately understand the relationship between fault displacement and damage zone width.

The fault zone architecture models were built using qualitative and quantitative data in order to create conceptual fluid flow models of the fault zones. However, the collected data could be used to produce quantitative fluid flow predictions. Several industry-standard and academic software (e.g. GoCAD Move 2D and 3D, Petrel) have built-in modules for fluid flow predictions. The quantitative 1D and 2D data and the different aspect ratio of 3D fracture models could be integrated in these software to complete fluid flow predictions.

Finally, the fault zone architecture model could be complemented with rock mechanics data. These data can be collected for all the different host lithologies of the fault zone and could be done using the new triaxial loading apparatus built in the Department of Earth Sciences at Durham University.

References

A.J. Mallon, R. E. S., 2008, How should permeability be measured in fine-grained lithologies? Evidence from the chalk: Geofluids, v. 8, no. 1, p. 35-45.

Aarland, R. K., and Skjerven, J., 1998, Fault and fracture characteristics of major fault zone in the North Sea: analyses of 3D seismic and oriented cores in the Brage Field (Block 31/4). In: Coward, M.P., Databan, T.S., Johnson, H. (Eds.): Structural Geology in Reservoir Characterization, v. 127, p. 209-229.

Agosta, F., Alessandroni, M., Tondi, E., and Aydin, A., 2009, Oblique normal faulting along the northern edge of the Majella Anticline, central Italy: Inferences on hydrocarbon migration and accumulation: Journal of Structural Geology, v. 31, no. 7, p. 674-690.

Agosta, F., and Aydin, A., 2006, Architecture and deformation mechanism of a basin-bounding normal fault in Mesozoic platform carbonates, central Italy: Journal of Structural Geology, v. 28, no. 8, p. 1445-1467.

Agosta, F., and Kirschner, D. L., 2003, Fluid conduits in carbonate-hosted seismogenic normal faults of central Italy: Journal of Geophysical Research-Solid Earth, v. 108, no. B4, p. 13.

Agosta, F., Prasad, M., and Aydin, A., 2007, Physical properties of carbonate fault rocks, fucino basin (Central Italy): implications for fault seal in platform carbonates: Geofluids, v. 7, no. 1, p. 19-32.

Allan, U. S., 1989, Model for hydrocarbon migration and entrapment within faulted structures: Aapg Bulletin, v. 73, no. 7, p. 803-811.

Alvarez, W., Arthur, M. A., Fischer, A. G., Lowrie, W., Napoleone, G., Silva, I. P., and Roggenthen, W. M., 1977, Upper Cretaceous–Paleocene magnetic stratigraphy at Gubbio, Italy V. Type section for the Late Cretaceous-Paleocene geomagnetic reversal time scale: Geological Society of America Bulletin, v. 88, no. 3, p. 383-389.

Alvarez, W., Engelder, T., and Geiser, P. A., 1978, Classification of solution cleavage in pelagic limestones: Geology, v. 6, no. 5, p. 263-266.

Alvarez, W., and Montanari, A., 1988, The Scaglia limestones (Late Cretaceous-Oligocene) in the northeastern Apennines carbonate sequence: stratigraphic context and geological significance, *in* Premori Silva, I., Coccioni, R., and Montanari, A., eds., The Eocene-Oligocene boundary in the Marche-Umbria Basin (Italy): Ancona, International Union of Geological Sciences, p. 13-30.

Anderson, E., 1951, The Dynamics of Faulting, Edinburgh, Oliver and Boyd.

Anderson, E. M., 1942, The Dynamics of Faulting and Dyke Formation with Applications to Britain, Edinburgh, Oliver and Boyd.

Anelli, L., Gorza, M., Pieri, M., and Riva, M., 1994, Subsurface well data in the Northern Apennines (Italy): Mem. Soc. Geol. It., v. 48, p. 461-474.

Antonellini, M., and Aydin, A., 1994, Effect of faulting on fluid-flow in porous sandstones – Petrophysical properties: Aapg Bulletin-American Association of Petroleum Geologists, v. 78, no. 3, p. 355-377.

Antonellini, M., Aydin, A., and Orr, L., 1999, Outcrop-aided characterization of a faulted hydrocarbon reservoir: Arroyo Grande Oil Field, California, USA, Faults and Subsurface Fluid Flow in the Shallow Crust, Volume 113: Washington, DC, AGU, p. 7-26.

Antonellini, M. A., Aydin, A., and Pollard, D. D., 1994, Microstructure of deformation bands in porous sandstones at Arches National Park, Utah: Journal of Structural Geology, v. 16, no. 7, p. 941-959.

Atkinson, B. K., 1987, Introduction to fracture mechanics and its geophysical applications, *in* Atkinson, B. K., ed., Fracture Mechanics of Rock: London, Academic Press, p. 1-26.

Aydin, A., 2000, Fractures, faults, and hydrocarbon entrapment, migration and flow: Marine and Petroleum Geology, v. 17, no. 7, p. 797-814.

Bally, A. W., Burbi, L., Cooper, C., and Ghelardoni, L., 1986, Balanced sections and seismic reflection profiles across the Central Apennines: Mem. Soc. Geol. It., v. 35, no. 257-310.

Barchi, M., De Feyter, A., Magnani, M., Minelli, G., Pialli, G., and Sotera, B., 1998a, Extensional tectonics in the Northern Apennines (Italy):Evidences from the CROP03 deep seismic reflection line: Mem. Soc. Geol. It., v. 52, p. 527-538.

Barchi, M., 1998b, The structural style of the Umbria-Marche fold and thrust belt: Mem. Soc. Geol. It., v. 52, p. 557-578.

Bellian, J. A., Kerans, C., and Jennette, D. C., 2005, Digital outcrop models: Applications of terrestrial scanning lidar technology in stratigraphic modeling: Journal of Sedimentary Research, v. 75, no. 2, p. 166-176.

Berg, S. S., and Skar, T., 2005, Controls on damage zone asymmetry of a normal fault zone: outcrop analyses of a segment of the Moab fault, SE Utah: Journal of Structural Geology, v. 27, no. 10, p. 1803-1822.

Billi, A., 2005, Attributes and influence on fluid flow of fractures in foreland carbonates of southern Italy: Journal of Structural Geology, v. 27, no. 9, p. 1630-1643.

Billi, A., Salvini, F., and Storti, F., 2003, The damage zone-fault core transition in carbonate rocks: implications for fault growth, structure and permeability: Journal of Structural Geology, v. 25, no. 11, p. 1779-1794.

Billi, A., Valle, A., Brilli, M., Faccenna, C., and Funiciello, R., 2007, Fracture-controlled fluid circulation and dissolutional weathering in sinkhole-prone carbonate rocks from central Italy: Journal of Structural Geology, v. 29, no. 3, p. 385-395.

Blenkinsop, T. G., 2008, Relationships between faults, extension fractures and veins, and stress: Journal of Structural Geology, v. 30, no. 5, p. 622-632.

Boncio, P., Brozzetti, F., and Lavecchia, G., 2000, Architecture and seismotectonics of a regional low-angle normal fault zone in central Italy: Tectonics, v. 19.

Boncio, P., Brozzetti, F., Ponziani, F., Barchi, M., Lavecchia, G., and Pialli, G., 1998, Seismicity and extensional tectonics in the Northern Umbia-Marche Apennines: Mem. Soc. Geol. It., v. 117, no. 52, p. 539-556.

Boncio, P., and Lavecchia, G., 2000, A structural model for active extension in Central Italy: Journal of Geodynamics, v. 29, no. 3-5, p. 233-244.

Bonson, C.G., Childs, C., Walsh, J.J., Schöpfer, M.P.J. & Carboni, V. 2007. Geometric and kinematic controls on the internal structure of a large normal fault in massive limestones: the Maghlaq Fault, Malta. Journal of Structural Geology 29, 336-354.

Bouvier, J. D., Kaars-Sijpesteijn, C. H., Kluesner, D. F., Onyejekwe, C. C., and van der Pal, R. C., 1989, Three-dimensional seismic interpretation and fault sealing investigations, Nun River Field, Nigeria: Aapg Bulletin, v. 73, no. 11, p. 1397-1414.

Brace, W. F., 1960, An Extension of the Griffith Theory of Fracture to Rocks: J. Geophys. Res., v. 65, no. 10, p. 3477-3480.

Broadbent, S. R., and Hammersley, J. M., 1957, Percolation processes. I. Crystals and Mazes: Proceedings of the Cambridge Philosophical Society, v. 53, no. 3, p. 629-641.

Bussolotto, M., Benedicto, A., Invernizzi, C., Micarelli, L., Plagnes, V., and Deiana, G., 2007, Deformation features within an active normal fault zone in carbonate rocks: The Gubbio fault (Central Apennines, Italy): Journal of Structural Geology, v. 29, no. 12, p. 2017-2037.

Byerlee, J., 1978, Friction of rocks: Pure and Applied Geophysics, v. 116, no. 4, p. 615-626.

Byerlee, J., 1993, Model for episodic flow of high-pressure water in fault zones before earthquakes: Geology, v. 21, no. 4, p. 303-306.

Caine, J. S., Evans, J. P., and Forster, C. B., 1996, Fault zone architecture and permeability structure: Geology, v. 24, no. 11, p. 1025-1028.

Chester, F. M., and Chester, J. S., 1998, Ultracataclasite structure and friction processes of the Punchbowl fault, San Andreas system, California: Tectonophysics, v. 295, no. 1-2, p. 199-221.

Chester, F. M., and Chester, J. S., 2000, Stress and deformation along wavy frictional faults: J. Geophys. Res., v. 105, no. B10, p. 23421-23430.

Chester, F. M., Chester, J. S., Kirschner, D. L., Schulz, S. E., and Evans, J. P., Structure of large-displacement, strike-slip fault zones in the brittle continental crust, *in*

Proceedings Meeting on Rheology and Deformation of the Lithosphere at Continental Margins, Snowbird, UT, Jan 23-26 2000, Columbia Univ Press, p. 223-260.

Chester, F. M., Evans, J. P., and Biegel, R. L., 1993, Iinternal structure and weakening mechanisms of the San-Andreas fault: Journal of Geophysical Research-Solid Earth, v. 98, no. B1, p. 771-786.

Chester, J. S., and Fletcher, R. C., 1997, Stress distribution and failure in anisotropic rock near a bend on a weak fault: Journal of Geophysical Research-Solid Earth, v. 102, no. B1, p. 693-708.

Childs, C., Nicol, A., Walsh, J. J., and Watterson, J., 1996, Growth of vertically segmented normal faults: Journal of Structural Geology, v. 18, no. 12, p. 1389-1397.

Childs, C., Watterson, J. & Walsh, J. J. 1996. A model for the structure and development of fault zones. Journal of the Geological Society, London 153, 337-340.

Collettini, C., 2002: University of Perugia.

Collettini, C., and Barchi, M. R., 2002, A low-angle normal fault in the Umbria region (Central Italy): a mechanical model for the related microseismicity: Tectonophysics, v. 359, no. 1–2, p. 97-115.

Collettini, C., De Paola, N., and Faulkner, D. R., 2009, Insights on the geometry and mechanics of the Umbria-Marche earthquakes (Central Italy) from the integration of field and laboratory data: Tectonophysics, v. 476, no. 1-2, p. 99-109.

De Paola, N., Collettini, C., Faulkner, D. R., and Trippetta, F., 2008, Fault zone architecture and deformation processes within evaporitic rocks in the upper crust: Tectonics, v. 27, no. 4, p. 21.

De Paola, N., Faulkner, D. R., and Collettini, C., 2009, Brittle versus ductile deformation as the main control on the transport properties of low-porosity anhydrite rocks: J. Geophys. Res., v. 114.

De Paola, N., Mirabella, F., Barchi, M. R., and Burchielli, F., 2006, Early orogenic normal faults and their reactivation during thrust belt evolution: the Gubbio Fault case study, Umbria-Marche Apennines (Italy): Journal of Structural Geology, v. 28, no. 11, p. 1948-1957.

Dershowitz, W., & Herda, H.H. , 1992. Interpretation of Fracture Spacing and Intensity. Proceedings of the 33rd U.S. Symposium on Rock Mechanics, Santa Fe, NM. 757-766.

Deschamps, A., Iannaccone, G., and Scarpa, R., 1984, The Umbrian earthquake (Italy) of 19 September 1979: Annales Geophysicae, v. 2, no. 1, p. 29-36.

Dewey, J. F., Helman, M. L., Knott, S. D., Turco, E., and Hutton, D. H. W., 1989, Kinematics of the western Mediterranean: Geological Society, London, Special Publications, v. 45, no. 1, p. 265-283.

Doglioni, C., 1995, Geological remarks on the relationships between extension and convergent geodynamic settings: Tectonophysics, v. 252, no. 1-4, p. 253-267.

Dziewonski, A. M., Franzen, J. E., and Woodhouse, J. H., 1985, Centroid-moment tensor solutions for April–June, 1984: Physics of the Earth and Planetary Interiors, v. 37, no. 2–3, p. 87-96.

Egeberg, P. K., and Saigal, G. C., 1991, North Sea chalk diagenesis – Cementation of chalks and healing of fractures: Chemical Geology, v. 92, no. 4, p. 339-354.

Ekström, G., Morelli, A., Boschi, E., and Dziewonski, A. M., 1998, Moment tensor analysis of the Central Italy Earthquake Sequence of September&October 1997: Geophys. Res. Lett., v. 25, no. 11, p. 1971-1974.

Engelder, T., 1989, Analysis of pinnate joints in the Mount Desert Island granite: Implications for postintrusion kinematics in the coastal volcanic belt, Maine: Geology, v. 17, no. 6, p. 564-567.

Evans, J. P., Forster, C. B., and Goddard, J. V., 1997, Permeability of fault-related rocks, and implications for hydraulic structure of fault zones: Journal of Structural Geology, v. 19, no. 11, p. 1393-1404.

Faulkner, D. R., 2004, A model for the variation in permeability of clay-bearing fault gouge with depth in the brittle crust: Geophys. Res. Lett., v. 31.

Faulkner, D. R., Lewis, A. C., and Rutter, E. H., 2003, On the internal structure and mechanics of large strike-slip fault zones: field observations of the Carboneras fault in southeastern Spain: Tectonophysics, v. 367, no. 3-4, p. 235-251.

Faulkner, D. R., Mitchell, T. M., Jensen, E., and Cembrano, J., 2011, Scaling of fault damage zones with displacement and the implications for fault growth processes: J. Geophys. Res., v. 116, no. B5, p. B05403.

Frykman, P., 2001, Spatial variability in petrophysical properties in Upper Maastrichtian chalk outcrops at Stevns Klint, Denmark: Marine and Petroleum Geology, v. 18, no. 10, p. 1041-1062.

Gaviglio, P., Bekri, S., Vandycke, S., Adler, P. M., Schroeder, C., Bergerat, F., Darquennes, A., and Coulon, M., 2009, Faulting and deformation in chalk: Journal of Structural Geology, v. 31, no. 2, p. 194-207.

Ghosh, K., and Mitra, S., 2009, Two-dimensional simulation of controls of fracture parameters on fracture connectivity: Aapg Bulletin, v. 93, no. 11, p. 1517-1533.

Gillespie, P. A., Howard, C. B., Walsh, J. J. & Watterson, J. 1993. Measurement and characterisation of spatial distributions of fractures. Tectonophysics 226, 113-141.

Gillespie, P.A., Walsh, J.J, Watterson, J., Bonson, C.G. & Manzocchi, T. 2001. Scaling relationships of joint and vein arrays from The Burren, Co. Clare, Ireland. Journal of Structural Geology 23, 183-201.

Graham, B., Antonellini, M., and Aydin, A., 2003, Formation and growth of normal faults in carbonates within a compressive environment: Geology, v. 31, no. 1, p. 11-14.

Groshong, R. H., 1988, Low-temperature deformation mechanisms and their interpretation: Geological Society of America Bulletin, v. 100, no. 9, p. 1329-1360.

Harding, T. P., and Tuminas, A. C., 1988, Interpretation of footwall (lowside) fault traps sealed by reverse faults and convergent wrench faults: Aapg Bulletin, v. 72, no. 6, p. 738-757.

Hawkins, T. R. W., and Aldrick, R. J., 1994, The pattern of faulting across the western sector of the Market Weighton Block, Vale of York: Proceedings of the Yorkshire Geological Society, v. 50, p. 125 - 128.

Hillis, R. R., 1995, Quantification of tertiary exhumation in the United Kingdom, Southern North Sea using sonic velocity data: Aapg Bulletin-American Association of Petroleum Geologists, v. 79, no. 1, p. 130-152.

Holland, M., and Urai, J. L., 2010, Evolution of anastomosing crack-seal vein networks in limestones Insight from an exhumed high-pressure cell, Jabal Shams, Oman Mountains: Journal of Structural Geology, v. 32, no. 9, p. 1279-1290.

Jaeger, J. C., and Cook, N. G. W., 1979, Fundamentals of Rock Mechanics, London, Chapman and Hall.

Jensenius, J., 1987, High temperature diagenesis in shallow chalk reservoir, Skjold oil field, Danish North Sea – Evidence from fluid inclusions and oxygen isotopes: Aapg Bulletin-American Association of Petroleum Geologists, v. 71, no. 11, p. 1378-1386.

Jones, R. R., McCaffrey, K. J. W., Clegg, P., Wilson, R. W., Holliman, N. S., Holdsworth, R. E., Imber, J., and Waggott, S., 2009, Integration of regional to outcrop digital data: 3D visualisation of multi-scale geological models: Computers & Geosciences, v. 35, no. 1, p. 4-18.

Jones, R. R., Wawrzyniec, T. F., Holliman, N. S., McCaffrey, K. J. W., Imber, J., and Holdsworth, R. E., 2008, Describing the dimensionality of geospatial data in the earth sciences--Recommendations for nomenclature: Geosphere, v. 4, no. 2, p. 354-359.

Jourde, H., Flodin, E. A., Aydin, A., Durlofsky, L. J., and Wen, X.-H., 2002, Computing Permeability of Fault Zones in Eolian Sandstone from Outcrop Measurements: Aapg Bulletin, v. 86, no. 7, p. 1187-1200.

Kim, Y.-S., and Sanderson, D. J., 2005, The relationship between displacement and length of faults: a review: Earth-Science Reviews, v. 68, no. 3–4, p. 317-334.

Kirby, G. A., and Swallow, P. W., 1987, Tectonism and sedimentation in the Flamborough Head region of north-east England: Proceedings of the Yorkshire Geological Society, v. 46, no. 4, p. 301-309.

Knipe, R. J., 1992, Faulting processes and fault seal, *in* Larsen, R. M., Brekke, H., Larsen, B. T., and Talleras, E., eds., Structural and tectonic modelling and its application to petroleum geology: Amsterdam, Elsevier, p. 325-342.

Knipe, R. J., Jones, G., and Fisher, Q. J., 1998, Faulting, fault sealing and fluid flow in hydrocarbon reservoirs: an introduction: Geological Society, London, Special Publications, v. 147, no. 1, p. vii-xxi.

Knott, S. D., Beach, A., Brockbank, P. J., Brown, J. L., McCallum, J. E., and Welbon, A. I., 1996, Spatial and mechanical controls on normal fault populations: Journal of Structural Geology, v. 18, no. 2-3, p. 359-372.

Kokkalas, S., Jones, R. R., McCaffrey, K. J. W., and Clegg, P., 2007, Quantitative fault analisys at Arkitsa, Central Greece, using Terrestrial Laser-Scanning (LiDAR): Bulletin of the Geological Society of Greece, v. 37.

Koukouvelas, I. K., and Papoulis, D., 2009, Fluid involvement in the active Helike normal Fault, Gulf of Corinth, Greece: Journal of Structural Geology, v. 31, no. 3, p. 237-250.

Lamplugh, G. W., 1895, Notes on the white chalk of Yorkshire: Proceedings of the Yorkshire Geological Society, v. 13, p. 65-87.

Lockner, D. A., and Beeler, N. M., 1999, Premonitory slip and tidal triggering of earthquakes: Journal of Geophysical Research-Solid Earth, v. 104, no. B9, p. 20133-20151.

Lucia, F. J., 1999, Carbonate Reservoir Characterization, New York, NY, USA, Springer.

Mallon, A. J., Swarbrick, R. E., and Katsube, T. J., 2005, Permeability of fine-grained rocks: New evidence from chalks: Geology, v. 33, no. 1, p. 21-24.

Manzocchi, T., 2002, The connectivity of two-dimensional networks of spatially correlated fractures: Water Resour. Res., v. 38, no. 9, p. 1162.

Manzocchi, T., Ringrose, P. S., and Underhill, J. R., 1998, Flow through fault systems in high-porosity sandstones, *in* Coward, M. P., Daltaban, T. S., and Johnson, H., eds., Structural Geology in Reservoir Characterization, Volume 127: Londin, Geological Society of London, p. 65-82.

McCaffrey, K. J. W., Feely, M., Hennessy, R., and Thompson, J., 2008, Visualization of folding in marble outcrops, Connemara, western Ireland: An application of virtual outcrop technology: Geosphere, v. 4, no. 3, p. 588-599.

McCaffrey, K.J.W, Sleight, J.M, Pugliese, S & Holdsworth, R.E 2003. Fracture formation and evolution in crystalline rocks: Insights from attribute analysis. In Hydrocarbons in Crystalline rocks. Petford, N. & McCaffrey, K. (eds) Geological Society of London, Special Publication 214, 109-124

McClay, K. R., 1987, The Mapping of Geological Structures, Milton Keynes, Open University Press, Geol. Soc. London Handbook Series.

McQuillan, H., 1973, Small-scale fracture density in Asmari formation of Southwest Iran and its relations to bed thickness and structural setting: Bull. Am. Ass. Petrol. Geol., v. 57, p. 2367-2385.

Micarelli, L., Benedicto, A., Invernizzi, C., Saint-Bezar, B., Michelot, J. L., and Vergely, P., 2005, Influence of P/T conditions on the style of normal fault initiation and growth in limestones from the SE-Basin, France: Journal of Structural Geology, v. 27, no. 9, p. 1577-1598.

Micarelli, L., Benedicto, A., and Wibberley, C. A. J., 2006a, Structural evolution and permeability of normal fault zones in highly porous carbonate rocks: Journal of Structural Geology, v. 28, no. 7, p. 1214-1227.

Micarelli, L., Moretti, I., and Daniel, J. M., 2003, Structural properties of rift-related normal faults: the case study of the Gulf of Corinth, Greece: Journal of Geodynamics, v. 36, no. 1-2, p. 275-303.

Micarelli, L., Moretti, I., Jaubert, M., and Moulouel, H., 2006b, Fracture analysis in the south-western Corinth rift (Greece) and implications on fault hydraulic behavior: Tectonophysics, v. 426, no. 1-2, p. 31-59.

Miller, S. A., Collettini, C., Chiaraluce, L., Cocco, M., Barchi, M., and Kaus, B. J. P., 2004, Aftershocks driven by a high-pressure CO2 source at depth: Nature, v. 427, no. 6976, p. 724-727.

Milsom, J., and Rawson, P. F., 1989, The Peak Trough – a major control on the geology of the North Yorkshire coast: Geological Magazine, v. 126, p. 699 - 705.

Mimran, Y., 1975, Fabric deformation induced in Cretaceous chalks by tectonic stresses: Tectonophysics, v. 26, no. 3-4, p. 309-316.

Mirabella, F., Ciaccio, M. G., Barchi, M. R., and Merlini, S., 2004, The Gubbio normal fault (Central Italy): geometry, displacement distribution and tectonic evolution: Journal of Structural Geology, v. 26, no. 12, p. 2233-2249.

Mitchell, T. M., and Faulkner, D. R., 2009, The nature and origin of off-fault damage surrounding strike-slip fault zones with a wide range of displacements: A field study from the Atacama fault system, northern Chile: Journal of Structural Geology.

Mizoguchi, K., Hirose, T., Shimamoto, T., and Fukuyama, E., 2008, Internal structure and permeability of the Nojima fault, southwest Japan: Journal of Structural Geology, v. 30, no. 4, p. 513-524.

Mollema, P. N., and Antonellini, M., 1999, Development of strike-slip faults in the dolomites of the Sella Group, Northern Italy: Journal of Structural Geology, v. 21, no. 3, p. 273-292.

Montanari, A., and Koeberl, C., 2000, Impact Stratigraphy The Italian Record.

Mort, K. & Woodcock, N. H. (2008) Quantifying fault breccia geometry: Dent Fault, NW England. *Journal of Structural Geology* 30, 701-709.

Needham, T., Li, A., Carr, C., Schorr, G., Benmahiddi, S., and Pena, J. L., 2008, Faulting and fault sealing in the TAGI Formation of the Ourhoud Field, Algeria: Petroleum Geoscience, v. 14, no. 4, p. 379-388.

Nicol, A., Walsh, J. J., Watterson, J., and Gillespie, P. A., 1996, Fault size distributions -- are they really power-law?: Journal of Structural Geology, v. 18, no. 2-3, p. 191-197.

Odling, N. E., 1992, Network properties of a two-dimensional natural fracture pattern: Pure and Applied Geophysics, v. 138, no. 1, p. 95-114.

Odling, N. E., 1997, Scaling and connectivity of joint systems in sandstones from western Norway: Journal of Structural Geology, v. 19, no. 10, p. 1257-1271.

Odling, N. E., Gillespie, P., Bourgine, B., Castaing, C., Chiles, J. P., Christensen, N. P., Fillion, E., Genter, A., Olsen, C., Thrane, L., Trice, R., Aarseth, E., Walsh, J. J., and Watterson, J., 1999, Variations in fracture system geometry and their implications for fluid flow in fractured hydrocarbon reservoirs: Petroleum Geoscience, v. 5, no. 4, p. 373-384.

Peacock, D. C. P., and Sanderson, D. J., 1994, Strain and scaling of faults in the chalk at Flamborough Head, U.K: Journal of Structural Geology, v. 16, no. 1, p. 97-107.

Peacock, D. C. P., and Sanderson, D. J., 1995, Pull-aparts, shear fractures and pressure solution: Tectonophysics, v. 241, no. 1–2, p. 1-13.

Petit, J. P., 1987, Criteria for the sense of movement on fault surfaces in brittle rocks: Journal of Structural Geology, v. 9, no. 5–6, p. 597-608.

Pialli, G., Barchi, M., and Minelli, G., 1998, Results of the crop03 deep seismic reflection profile: Mem. Soc. Geol. It., v. 52, p. 654.

Pollard, D. D., and Segall, P., 1987, Theoretical displacements and stresses near fractures in rock: with applications to faults, joints, veins, dikes, and solution surfaces, *in* Atkinson, B. K., ed., Fracture Mechanics of Rock: London, Academic Press, p. 227-349.

Price, M., 1987, Fluid flow in the Chalk of England: Fluid flow in sedimentary basins and aquifers: Geological society [London] Special Publication, no. 34, p. 141-156.

Questiaux, J.-M., Couples, G. D., and Ruby, N., 2010, Fractured reservoirs with fracture corridors: Geophysical Prospecting, v. 58, no. 2, p. 279-295.

Reynolds, P. J., Stanley, H. E., and Klein, W., 1980, Large-cell Monte Carlo renormalization group for percolation: Physical Review B, v. 21, no. 3, p. 1223-1245.

Rispoli, R., 1981, Stress fields about strike-slip faults inferred from stylolites and tension gashes: Tectonophysics, v. 75, no. 3–4, p. T29-T36.

Roberts, S. J., Nunn, J. A., Cathles, L., and Cipriani, F.-D., 1996, Expulsion of abnormally pressured fluids along faults: J. Geophys. Res., v. 101, no. B12, p. 28231-28252.

Rowland, J. V., and Sibson, R. H., 2004, Structural controls on hydrothermal flow in a segmented rift system, Taupo Volcanic Zone, New Zealand: Geofluids, v. 4, no. 4, p. 259-283.

Rudnicki, J. W., 1980, Fracture mechanics applied to the Earths crust: Annual Review of Earth and Planetary Sciences, v. 8, p. 489-525.

Salvini, F., Billi, A., and Wise, D. U., 1999, Strike-slip fault-propagation cleavage in carbonate rocks: the Mattinata Fault Zone, Southern Apennines, Italy: Journal of Structural Geology, v. 21, no. 12, p. 1731-1749.

Saucier, F., Humphreys, E., and Weldon, R., 1992, Stress near geometrically complex strike-slip faults – Application to the San Andreas fault at Cajon pass, Southern California: Journal of Geophysical Research-Solid Earth, v. 97, no. B4, p. 5081-5094.

Savage, H. M., and Brodsky, E. E., 2011, Collateral damage: Evolution with displacement of fracture distribution and secondary fault strands in fault damage zones: J. Geophys. Res., v. 116, no. B3, p. B03405.

Scholle, P. A., 1977, Chalk diagenesis and its relation to petroleum exploration – Oil from chalks, a modern miracle: Aapg Bulletin-American Association of Petroleum Geologists, v. 61, no. 7, p. 982-1009.

Scholz, C. H., 1987, Wear and gouge formation in brittle faulting: Geology, v. 15, no. 6, p. 493-495.

Scholz, C. H., Dawers, N. H., Yu, J. Z., and Anders, M. H., 1993, Fault growth and fault scaling laws – Preliminary results: Journal of Geophysical Research-Solid Earth, v. 98, no. B12, p. 21951-21961.

Schultz, R. A., and Fossen, H., 2002, Displacement-length scaling in three dimensions: the importance of aspect ratio and application to deformation bands: Journal of Structural Geology, v. 24, no. 9, p. 1389-1411.

Secor, D. T., 1965, Role of fluid pressure in jointing: Am J Sci, v. 263, no. 8, p. 633-646.

Seront, B., Wong, T.-F., Caine, J. S., Forster, C. B., Bruhn, R. L., and Fredrich, J. T., 1998, Laboratory characterization of hydromechanical properties of a seismogenic normal fault system: Journal of Structural Geology, v. 20, no. 7, p. 865-881.

Shipton, Z. K., and Cowie, P. A., 2001, Damage zone and slip-surface evolution over [mu]m to km scales in high-porosity Navajo sandstone, Utah: Journal of Structural Geology, v. 23, no. 12, p. 1825-1844.

Sibson, R. H., 1977, Fault rocks and fault mechanisms: Journal of the Geological Society, v. 133, no. 3, p. 191-213.

Sibson, R. H., 1992, Implications of fault-valve behaviour for rupture nucleation and recurrence: Tectonophysics, v. 211, no. 1-4, p. 283-293.

Sibson, R. H., 2000, Fluid involvement in normal faulting: Journal of Geodynamics, v. 29, no. 3-5, p. 469-499.

Sibson, R. H., 2004, Controls on maximum fluid overpressure defining conditions for mesozonal mineralisation: Journal of Structural Geology, v. 26, no. 6-7, p. 1127-1136.

Sibson, R. H., Moore, J. M. M., and Rankin, A. H., 1975, Seismic pumping—a hydrothermal fluid transport mechanism: Journal of the Geological Society, v. 131, no. 6, p. 653-659.

Sibson, R. H., and Rowland, J. V., 2003, Stress, fluid pressure and structural permeability in seismogenic crust, North Island, New Zealand: Geophysical Journal International, v. 154, no. 2, p. 584-594.

Singhal, B. B., and Gupta, R. P., 2010, Fractures and discontinuites, Applied Hydrogeology of Fractured Rocks: New York, Kluwer Academic Publishers (now Springer), p. 13-34.

Sleight, J. M., 2001, Fracture Characterisitics from Two Reactivated Basement Fault Zones: Examples from Norway and Shetland [PhD: Durham University.

Smith, D. A., 1980, Sealing and nonsealing faults in Louisiana Gulf Coast salt basin: Aapg Bulletin, v. 64, no. 2, p. 145-172.

Starmer, I. C., 1995, Deformation of the Upper Cretaceous Chalk at Selwicks Bay, Flamborough Head, Yorkshire: its significance in the structural evolution of north-east England and the North Sea Basin: Proceedings of the Yorkshire Geological Society, v. 50, part 3, p. 213-228.

Stauffer, D., 1985, Introduction to Percolation Theory, London, Taylor and Francis.

Stauffer, D., and Aharony, A., 1991, Introduction to Percolation Theory. (2nd ed.).

Stewart, S. A., and Bailey, H. W., 1996, The Flamborough Tertiary outlier, UK southern North sea: Journal of the Geological Society, v. 153, p. 163-173.

Tondi, E., 2007, Nucleation, development and petrophysical properties of faults in carbonate grainstones: Evidence from the San Vito Lo Capo peninsula (Sicily, Italy): Journal of Structural Geology, v. 29, no. 4, p. 614-628.

Torabi, A., and Berg, S. S., 2011, Scaling of fault attributes: A review: Marine and Petroleum Geology, v. 28, no. 8, p. 1444-1460.

Trinks, I., Clegg, P., McCaffrey, K., Jones, R., Hobbs, R., Holdsworth, B., Holliman, N., Imber, J., Waggott, S., and Wilson, R., 2005, Mapping and analysing virtual outcrops: Visual Geosciences, v. 10, no. 1, p. 13-19.

Twiss, R. J., and Moores, E. M., 1992, Structural geology, New York, W.H. Freeman, xii, 532 p p.:

Vermilye, J.M. & Scholz, C.H., 1995, Relation between vein length and aperture. Journal of Structural Geology 17, 3, 423-434.

Vermilye, J. M., and Scholz, C. H., 1998, The process zone: A microstructural view of fault growth: Journal of Geophysical Research-Solid Earth, v. 103, no. B6, p. 12223-12237.

Walker, R. J., 2010, The Structural Evolution of the Faroe Islands, NE Atlantic Margin [PhD: Durham University.

Wallace, R. E., and Morris, H. T., 1986, Characteristics of faults and shear zones in deep mines: Pure and Applied Geophysics, v. 124, no. 1, p. 107-125.

Wang, Z., 1997, Seismic Properties of Carbonate Rocks, Society of Exploration Geophysicists, Carbonate Seismology, v. 9781560802099.

Watts, N. L., 1987, Theoretical aspects of cap-rock and fault seals for single- and two-phase hydrocarbon columns: Marine and Petroleum Geology, v. 4, no. 4, p. 274-307.

Wawrzyniec, T. F., Jones, R. R., McCaffrey, K., Imber, J., Holliman, N., and Holdsworth, R. E., 2007, Introduction: Unlocking 3D earth systems--Harnessing new digital technologies to revolutionize multi-scale geological models: Geosphere, v. 3, no. 6, p. 406-407.

Wibberley, C. A. J., and Shimamoto, T., 2003, Internal structure and permeability of major strike-slip fault zones: the Median Tectonic Line in Mie Prefecture, Southwest Japan: Journal of Structural Geology, v. 25, no. 1, p. 59-78.

Willemse, E. J. M., Peacock, D. C. P., and Aydin, A., 1997, Nucleation and growth of strike-slip faults in limestones from Somerset, U.K: Journal of Structural Geology, v. 19, no. 12, p. 1461-1477.

Wilson, E. J., Friedmann, S. J., and Pollak, M. F., 2007, Research for deployment: Incorporating risk, regulation, and liability for carbon capture and sequestration: Environmental Science & Technology, v. 41, no. 17, p. 5945-5952.

Wilson, J. E., Chester, J. S., and Chester, F. M., 2003, Microfracture analysis of fault growth and wear processes, Punchbowl Fault, San Andreas system, California: Journal of Structural Geology, v. 25, no. 11, p. 1855-1873.

Woodcock, N. H., Dickson, J. A. D. & Tarasewicz, J. P. T. (2007) Transient permeability and reseal hardening in fault zones: evidence from dilation breccia textures. Special Publication of the Geological Society of London 270, 43-54.

Woodcock, N. H. and Mort, K. (2008) Classification of fault breccias and related fault rocks. Geological Magazine 145. 435-440.

Xu, X., Aiken, C. L. V., Bhattacharya, J. P., Corbeanu, R. M., Nielsen, K. C., McMechan, G. A., and Abdelsalam, M. G., 2000, Creating virtual 3-D outcrop: The Leading Edge, v. 19, no. 2, p. 197-202.

Xu, X., Aiken, C. L. V., and Nielsen, K. C., 1999, Real time and the virtual outcrop improve geological field mapping: Eos Trans. AGU, v. 80, no. 29, p. 317-324.

Yielding, G., Freeman, B., and Needham, D. T., 1997, Quantitative fault seal prediction: Aapg Bulletin-American Association of Petroleum Geologists, v. 81, no. 6, p. 897-917.

Zhang, Y., Gartrell, A., Underschultz, J. R., and Dewhurst, D. N., 2009, Numerical modelling of strain localisation and fluid flow during extensional fault reactivation: Implications for hydrocarbon preservation: Journal of Structural Geology, v. 31, no. 3, p. 315-327.

Zhu, W. L., and Wong, T. F., 1999, Network modeling of the evolution of permeability and dilatancy in compact rock: Journal of Geophysical Research-Solid Earth, v. 104, no. B2, p. 2963-2971.